Doctoral Thesis

Development of Electrochemical Devices for Utilization of Sustainable Fuel in the Atmosphere

Jeongwon Kim

School of Energy and Chemical Engineering
(Energy Engineering)

Ulsan National Institute of Science and Technology

2021

Development of Electrochemical Devices for Utilization of Sustainable Fuel in the Atmosphere

Jeongwon Kim

School of Energy and Chemical Engineering
(Energy Engineering)

Ulsan National Institute of Science and Technology

Development of Electrochemical Devices for Utilization of Sustainable Fuel in the Atmosphere

A thesis/dissertation submitted to
Ulsan National Institute of Science and Technology
in partial fulfillment of the
requirements for the degree of
Doctor of Philosophy

Jeongwon Kim

06.07.2021 of submission
Approved by

Advisor
Guntae Kim

Development of Electrochemical Devices for Utilization of Sustainable Fuel in the Atmosphere

Jeongwon Kim

This certifies that the thesis/dissertation of Jeongwon Kim is approved.

06.07.2021 of submission

Signature

Advisor: Guntae Kim

Signature

Jaephil Cho: Thesis Committee member #1

Signature

Youngkook Kwon: Thesis Committee member #2

Signature

Sang Kyu Kwak: Thesis Committee member #3

Signature

Ikwhang Chang: Thesis Committee member #4

Signature

Abstract

Since the Earth was formed, CO_2 level has steadily increased as mankind began using fossil fuels, now exceeding 408 ppm. The increased CO_2 has a significant impact on climate change by increasing the global temperature due to the greenhouse effect by approximately 1 ^oC, and it increased sea level by more than 30 cm for the last century. In response to this crisis, there have been great efforts to reduce and utilize CO_2 as a resource. The considerable research has been focused on the chemical conversion of CO_2 into high value-added carbon compounds and the electrochemical utilization on metal-CO_2 batteries adopting carbon capture, utilization and sequestration (CCUS) technology. However, it has been pointed out that it cannot be an effective greenhouse gas abatement technology due to low conversion rate with high energy requirement. In order to meet an energy society liberated from fossil fuels, we should be able to utilize and store energy using unlimited fuel which is environment friendly. This research focuses on developing advanced electrocatalysts for efficient utilization of oxygen *via* polymer electrolyte membrane fuel cell (PEMFC) and Meta (Li, Na, Zn)-air batteries. In addition to energy production, the rationally engineered electrochemical devices were further invented to efficiently reduce and utilize carbon dioxide in atmosphere.

Contents

List of Figures

List of Tables

Chapter 1 Introduction

1.1. Research background

Since the Earth was formed, CO_2 level has steadily increased as mankind began using fossil fuels, now exceeding 408 ppm (Figure 1-1a). The increased CO_2 has a significant impact on climate change by increasing the global temperature due to the greenhouse effect by approximately 1 ºC (Figure 1-1b), and it increased sea level by more than 30 cm for the last century.

The increasing concentration of greenhouse gas CO_2 in the atmosphere has caused serious anthropogenic climate changes.[1,2] Reducing the release of CO_2 into the environment is urgently needed. However, there is a dichotomy between power production and CO_2 emissions. Burning hydrocarbon releases a significant amount of CO_2 into the environment. Therefore, several renewable energy sources are being developed as alternative energy resources, such as solar and wind energy, hydropower and other renewable energy sources. The development of high energy storage systems is essential to save extra power for the increased demands and delivery to where it is required. The energy storage technologies available for largescale applications can be divided into four types: mechanical, electrical, electro-chemical and chemical. Among these, electrochemical energy storage approach is popular due to the mechanisms used to store energy. In general, electrochemical energy storage possesses a number of desirable features, including pollution free operation, high round trip efficiency, a long life cycle, low maintenance and energy characteristics such as quick response when the contingency occurs to meet different grid functions.[3] Batteries represent excellent energy storage technology for the integration of renewable resources. Fuel cells and super capacitors are also excellent mediums for electric energy with high power or energy density. Consequently, they are also receiving considerable attention. [4]

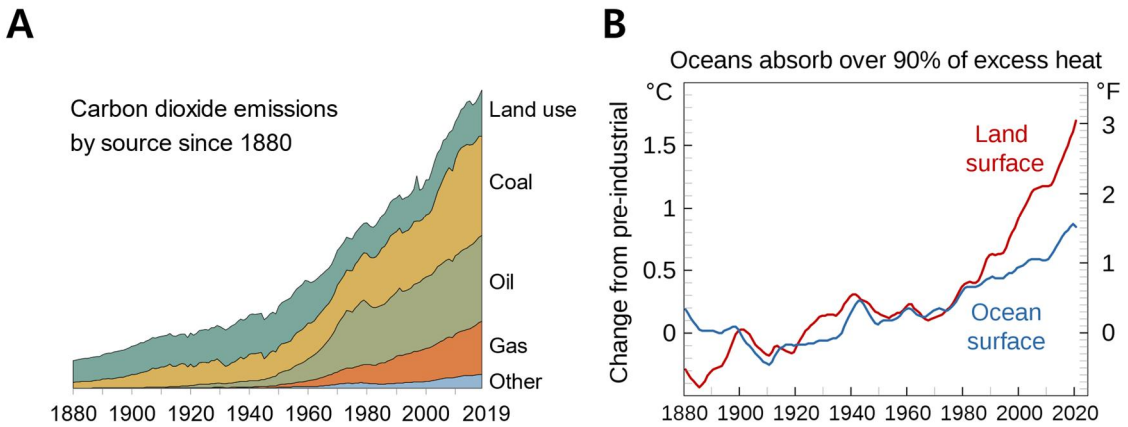

Figure 1-1 (a) CO_2 levels from the last three glacial cycles. (b) The change in global surface temperature relative to 1880-2020 average temperature. reproduced from Wikipedia under the terms of the CC BY-SA 3.0.

1.2. Polymer electrolyte membrane fuel cell

PEM (Polymer Electrolyte Membrane) fuel cell technologies have received world-wide attention in recent years owing to their high efficiencies and low emissions. PEM fuel cells are constructed using polymer electrolyte membranes (notably Nafion) as the proton conductor and electrochemical catalyst (usually Platinum-based materials) for electrochemical reactions under low temperature. Their noteworthy features include low operating temperature, high power density, and easy scale-up, making PEM fuel cells a promising candidate as the next generation of power sources for transportation, stationary, and portable applications. Figure 1-2 shows a PEM fuel cell structure and major components. To provide a sense of history, Sir William Robert Grove demonstrated the very first fuel cell in 1839 by showing that the electrochemical dissociation of water was almost reversible using platinized platinum (Pt) electrodes in dilute sulfuric acid[5]. Another milestone was the first practical fuel cell developed by General Electric Company (GE) for the Gemini space mission in 1962. The 1 kW Gemini fuel cell system had a Pt-loading of 35 mg/cm^2 and performance of 37 mA/cm^2 at 0.78 V[6]. Each stack consisted of 31 cells in series with an effective diameter about 22 cm for each cell, biporous nickel as electrodes (anode porous Ni and cathode lithiated NiO), and 70–85% potassium hydroxide solution as electrolyte. Waterand heat byproducts were removed by circulating hydrogen. The whole stack was enclosed in a thin metallic cylinder, and provided all the electric power for life support and drinking water in the two-week lunar mission. In the 1960s, improvements were made by incorporating Teflon in the catalyst layer directly adjacent to the electrolyte, as was done with the GE fuel cells at the time. Considerable improvements were made from the early 1970s onward with the adoption of the fully fluorinated Nafion membrane. However, research and development in PEM fuel cells didn't receive much attention and funding from the federal government, in particular the US Department of Energy (DOE), and industry until a few decades ago or so when breakthrough methods for reducing the Pt loading required for PEM fuel cells were developed and subsequently improved by Los Alamos National Laboratory (LANL)and others. Notably, Ian Raistrick[7–9]of LANL came up with a breakthrough technique by applying a

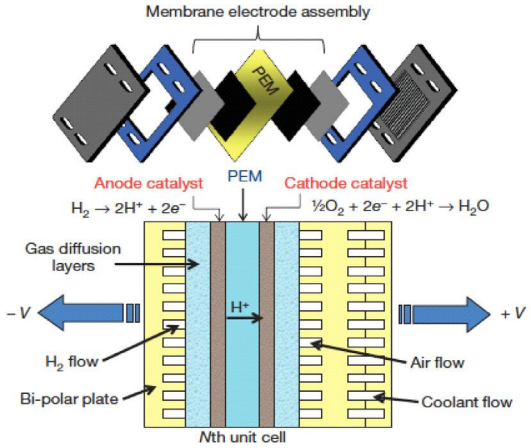

Figure 1-2 PEM fuel cell structure

solution containing dissolved Nafion material to the surface of a porous electrode. The electrodes were pressed to the membrane once the solution dried to produce an assembly that contains membrane and electrodes. Wilson[10,11], also of LANL, later invented methods for fabricating repeatable thin-film electrodes bonded to the proton-exchange membrane to generate a membrane electrode assembly (MEA). Combining Raistrick's and Wilson's techniques made it possible to dramatically lower the required precious-metal catalyst loadings by a factor of over 20 while simultaneously improving performance. Another contribution also due to LANL is that by Gottesfeld who proposed to inject a small amount of oxygen-containing air into the fuel stream to oxidatively remove CO from the catalyst surface[12]. This technique enables the direct use of hydrogen-rich gas streams derived from hydrocarbon fuels (such as gasolines, methanol, or natural gases) for PEM fuel cells. Recently, the concept of porous media flow fields was introduced to improve reactant supply and byproduct removal and fuel cell design[13,14]. In2017, Toyota launched its first commercial fuel cell vehicle,Mirai, at a price less than $59,000 with a total Pt loading of 0.365 mg/cm^2(anode loading of 0.05 mg/cm^2 and cathode of 0.315 mg/cm^2). The Toyota Mirai fuel cells adopt a carbon-coated Titanium-based porous flow field in the cathode. Though many technical and fundamental breakthroughs have been achieved during the last couple of decades, several challenges such as reducing cost and improving durability remain prior to the world-wide deployment of PEM fuel cells.

1.3. Metal-air batteries

The energy sources as for powering EVs require both high specific energy and high specific power. The feature of high specific energy is favorable for long driving range, while the high specific power is desirable for high acceleration rate and hill climbing capability.[15] The development of electric vehicles will decrease the dependency on fossil fuels and increase the deployment of renewable energy resources. Lead acid batteries are commonly used battery for electric vehicles propulsion in the 90s, but its applications are limited by relatively low energy density.[16] Other advanced battery systems such as nickel (Ni)-cadmium (Cd), nickel-metal hybrid, lithium-polymer, sodium sulfur, and sodium (Na)-metal chloride batteries are also being actively pursued for vehicle propulsion applications. Most of today's EVs, especially cars, are moving toward using lithium-ion batteries for propulsion. However, lithium-ion batteries powered EVs have a driving range limited to 160 kilometers on a single charge and the batteries account for nearly 65% of the total cost. It is known that the theoretical energy density of gasoline is 13,000 Wh kg^{-1} and the energy density of lithium-ion batteries is around 100–200 Wh kg^{-1}. Considering the energy conversion efficiency of tank-to-wheel of the fleet is 12.6%; therefore, the practical energy density of gasoline is 1700 Wh kg^{-1}, which is still much higher than that of lithium-ion batteries. Therefore, novel energy systems with higher energy densities are prominently desired. Metal-air batteries such as lithium-air, zinc-air, magnesium-air, and aluminum-air batteries are

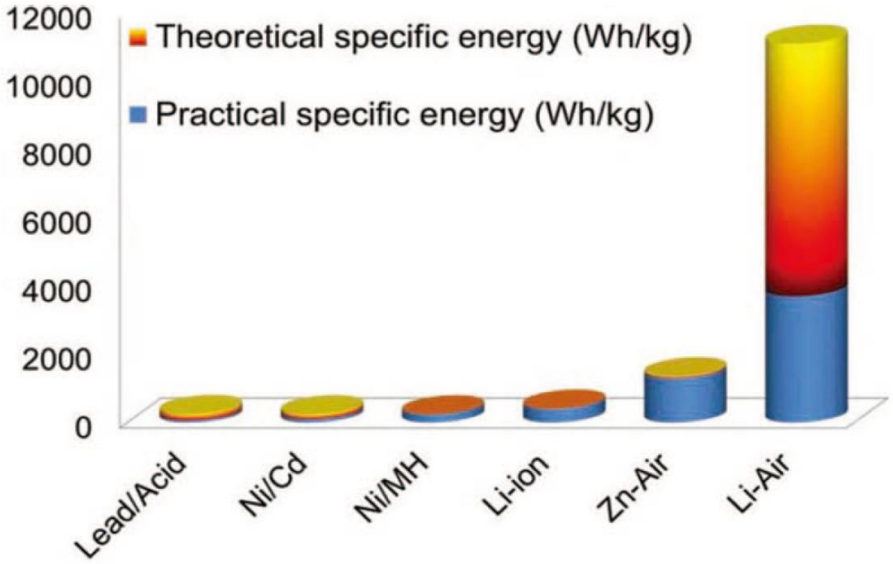

Figure 1-3 Theoretical and practical energy densities of batteries [17]

promising for future generations of EVs because they use oxygen from the air as one of the battery's main reactants, reducing the weight of the battery and freeing up more space devoted to energy storage. Among all these metal-air batteries, lithium-air battery shows the highest theoretical energy density, rivaling the gasoline engine (13000 $Whkg^{-1}$). It has a much greater energy density than other rechargeable batteries, as shown in Figure 1-3. But, there are many challenges facing the design of rechargeable lithium-air batteries such as incomplete discharge as porous carbon cathode blocking by discharge products, unstable anode in atmospheric moisture, inadequate understanding of catalysts effect, low electrical efficiency due to higher charge overpotential than discharge overpotential, carbonate based electrolytes decompose during discharge and produce lithium alkyl-carbonates and Li_2CO_3, which severely affects the rechargeability and cycle life of lithium-air batteries etc. There are also challenges for secondary Zn-air batteries such as requirement of closely controlled zinc precipitation, zinc anode dendrite formation, non-uniform zinc dissolution and limited solubility in electrolytes, higher charge overpotential than discharge overpotential, and necessity of bi-functional air cathode to liberate oxygen from discharge reaction products.

1.4. Metal-CO_2 batteries

The increasing concentration of greenhouse gas CO_2 in the atmosphere has caused serious anthropogenic climate changes. Reducing the release of CO_2 into the environment is urgently needed. However, energy is an important foundation for economic and social development. Capturing and converting CO_2 into a fuel has opened up the possibility of creating CO_2 emission reduction systems. In the past several years, both photochemical and electrochemical conversion of CO_2 have thus been globally investigated. In this regard, as for CO_2, in spite of its low concentration in ambient air (400

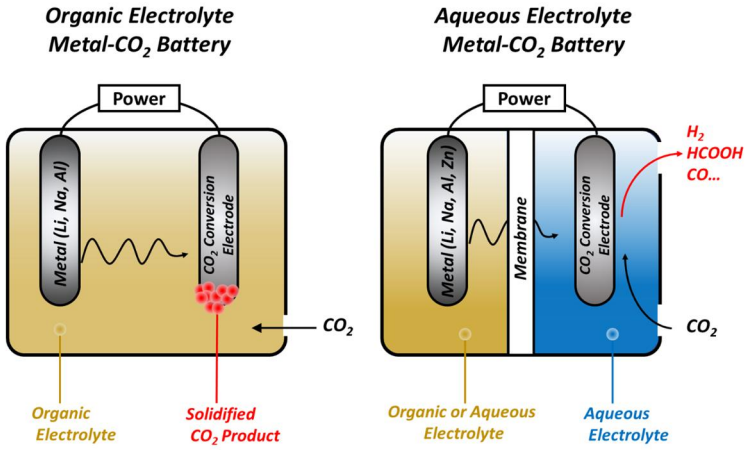

Figure 1-4 Scheme of Conventional Metal-CO_2 batteries

ppm), its solubility is 50 times larger than O_2 in organic solvents,[18] and CO_2 can react with the active intermediate species $O_2^{\bullet-}$ or the discharge products to form metal carbonates.[19] To develop actual metal–air batteries, it is critical to understand the potential impact of CO2 contamination on metal–O_2 batteries, and generally a mixture of O_2/CO_2 has been utilized as the reactant gas.[20–24] More interestingly, it has been proved that CO_2 itself can be utilized as the reactant gas, i.e., metal–CO_2 batteries.[25–28] The utilization of CO_2 in electrochemical energy storage devices provides a promising "clean" strategy for reducing fossil fuel consumption and consequently, lessening global warming. In addition, metal–CO_2 batteries are potential energy sources for scientific exploration and future immigration to Mars, for the air there contains 95% of CO_2. However, although Metal-CO_2 batteries based on organic electrolytes directly convert CO_2 feed into a solid product (*e.g.*, Li_2CO_3, Na_2CO_3, or $Al_2(CO_3)_2$), the products accumulate on the electrode surface to decrease the electrode electrochemical activity and hence create a limited discharge capacity (Figure 1-4). In addition, during the charge process, these solid products regenerate CO_2 gas, leading to inefficient storage of CO_2 feedstock. Therefore, there is a need to develop an advanced electrochemical device that can substantially reduce the concentration of carbon dioxide in the atmosphere with generating energy.

1.5 Electrochemical reaction in devices

1.5.1. The Sabatier principle and volcano plots

Since the early part of the 20th century, the Sabatier principle has provided a conceptual framework for our thinking about the optimum catalyst. The Sabatier principle is a dominating phenomena and rule in chemical or electrochemical catalysis. The idea is that the best catalysts should bind atoms and molecules with an intermediate strength: not too weakly in order to be able to activate the reactants, and not too strongly to be able to desorb the products. This important law in catalysis is found and named after the French chemist Paul Sabatier (Figure 1-5). In the 1920s, Sabatier studied the hydrogenation reaction using nickel element. At this time, he discovered that nickel had excellent activity because it

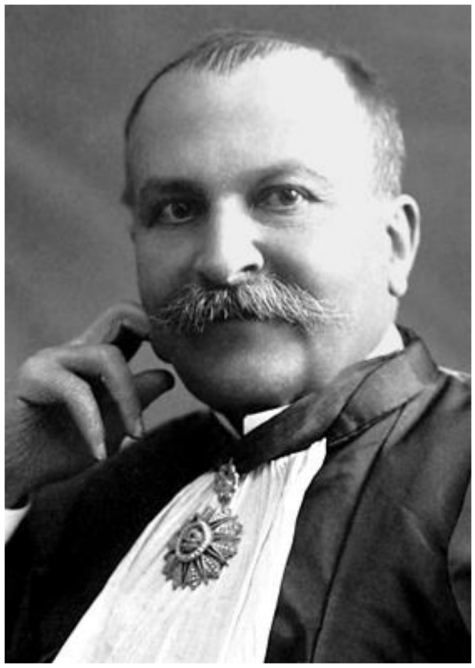

Figure 1-5 Paul Sabatier, reproduced from Wikipedia under the terms of the CC BY-SA 3.0.

could easily form intermediate hydrides during hydrogenation reactions, which is regenerated toward the free metal. From the research, he suggested that the adsorption energy must be adequate for an efficient catalyst.

From the Sabatier principle, a volcano plot could be obtained by plotting the activity index against the interaction force between catalyst and the reaction intermediates. This leads to a volcano-type relationship between activity and bond strength as illustrated in Figure 1-6. This picture has been very successful in providing a general qualitative understanding of why there might be an optimum catalyst. In the field of electrochemistry, activity of electrocatalyst is normally evaluated by the exchange current density, the overpotential at a specific current density, or the current density at a specific overpotential. Additionally, the interaction force can be evaluated as the adsorption energy. For each electro-process, there are various types of intermediate for whole electrochemical reactions. Therefore, the studies for detailed electrochemical mechanism with considering the Sabatier principle are needed.

1.5.2. Oxygen reduction reaction

In either proton exchange membrane fuel cells (PEMFCs) or Metal-air batteries (MAB), oxygen reduction reaction (ORR) is one of the important electrochemical process for efficiently operating whole devices. The ORR process has different mechanisms in acid and basic electrolytes, where multiple electron transfer is involved. The ORR process can be summarized in the following equations.

In acidic condition:

(4 electron pathway) $O_2 + 4H^+ + 4e^- \rightarrow 2H_2O$

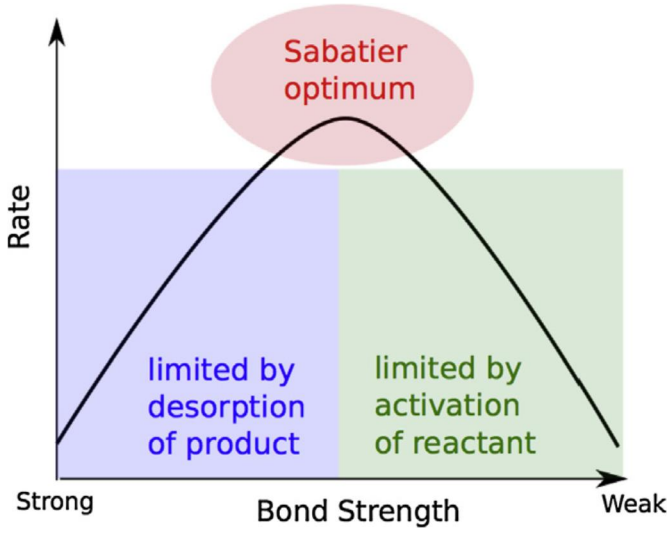

Figure 1-6 Schematic representation of the qualitative Sabatier principle.

(2 electron pathway 1) $O_2 + 2H^+ + 2e^- \rightarrow H_2O_2$

(2 electron pathway 2) $H_2O_2 + 2H^+ + 2e^- \rightarrow 2H_2O$

In alkaline condition:

(4 electron pathway) $O_2 + H_2O + 4e^- \rightarrow 4OH^-$

(2 electron pathway 1) $O_2 + H_2O + 2e^- \rightarrow HO_2^- + OH^-$

(2 electron pathway 2) $HO_2^- + H_2O + 2e^- \rightarrow 3OH^-$

Noteworthily, regardless the type of the electrolyte, there are only two pathways. One is the $4e^-$ transfer process to form either H_2O in acid electrolyte or OH^- in basic electrolyte, and the other is the two-step-$2e^-$-transfer pathway, where the first $2e^-$ reduction occurs to generate H_2O_2 or HO_2^-, following by the further reduction to H_2O or OH^- with another $2e^-$ transferred. It is desirable to adopt the direct $4e^-$ transfer pathway to achieve the maximal energy conversion efficiency.

For oxygen reduction activities of electrocatalyst, the volcano plot from Sabatier principle should be considered. The free energies of all the intermediate reactions have been calculated on a variety of close-packed metal surfaces, and a volcano plot was constructed relating the theoretical ORR activity and DEO, in which Pt located at the top (Figure 1-7a), indicating an efficient catalyst for catalyzing ORR. For metals that bind oxygen too strongly, the activity is limited by proton electron transfer to O* or OH*. In the contrary, for metals that bind oxygen too weakly, the activity is limited by proton electron transfer to O_2* or splitting of the O-O bond. Actually, there is no single polycrystalline metal catalyzes the ORR as effectively as Pt. However, the high cost and rather low durability hinder the potential

applications of Pt catalysts in metal-air batteries. Currently, three approaches are being pursed in order to reduce the costs for ORR: (i) reduction of the Pt-loading, (ii) development of non-noble metal catalysts and (iii) synthesis of metal-free catalysts. The reduction of Pt loading can be achieved by utilizing a support on which small Pt nanoparticles are deposited with a high dispersion, by alloying Pt with other metals, or by developing novel Pt structures. However, for commercialization of the electrocatalyst, these strategies cannot completely resolve with only reduction of the amount of Pt-loading. Thus, in order to realize the electrochemical devices for future commercialization, a long-term strategy should be dedicated to focusing the second and third approaches, especially metal-free electrocatalysts.

1.5.3. Oxygen evolution reaction

Oxygen evolution reaction (OER) is another key electrochemical reaction for the electrochemical devices including MAB and electricity-driven water splitting to produces hydrogen. However, due to the sluggish reaction kinetics of the four-electron transfer process, OER is actually the major bottleneck for improving the water splitting efficiency. OER is a complex multistep reaction involving with the O-H bond breaking and the O-O bond formation. Simply, the OER process is opposite reaction of ORR process. The general mechanism for OER can be described in the following equations.

In acidic electrolyte:

$* + H_2O \rightarrow {}^*OH + H^+ + e^-$

$* + H_2O \rightarrow {}^*O + H^+ + e^-$

$^*O + H_2O \rightarrow {}^*OOH + H^+ + e^-$

$^*OOH \rightarrow {}^*O_2 + H^+ + e^-$

$^*O_2 \rightarrow * + O_2$

In alkaline electrolyte:

$* + OH^- \rightarrow {}^*OH + e^-$

$^*OH^- + OH^- \rightarrow H_2O + {}^*O + e^-$

$^*OOH + OH^- \rightarrow {}^*O_2 + e^-$

$^*OOH + OH^- \rightarrow {}^*O_2 + e^-$

$^*O_2 \rightarrow * + O_2$

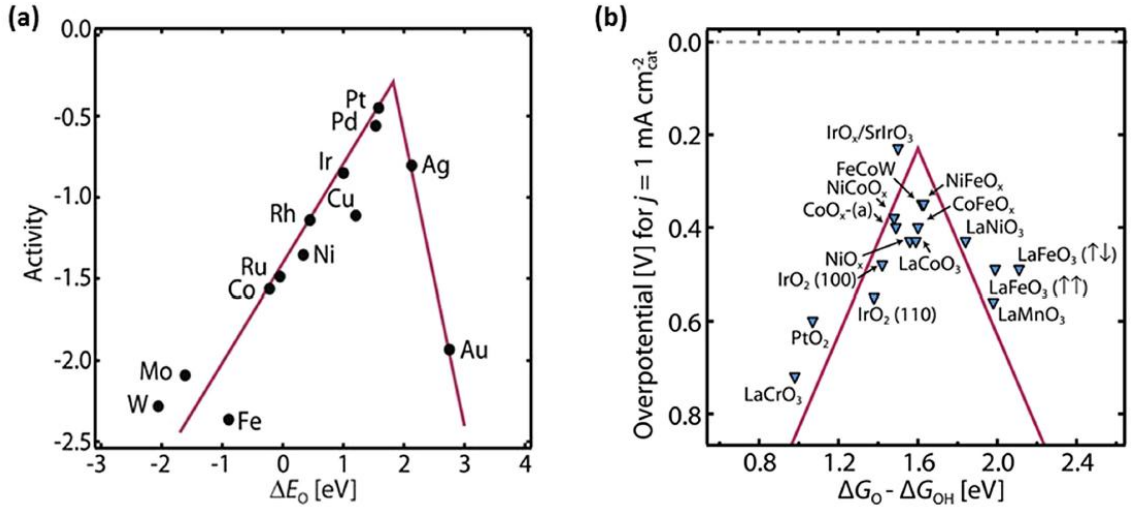

Figure 1-7 (a) ORR volcano plots for metals catalysts; (b) OER volcano plots for generally used metal oxides. Reproduced with permission. Copyright 2017, American Association for the Advancement of Science.

Like ORR, the appropriate binding energies of the oxygenated intermediates is favorable for OER, and the OER activity versus binding energy exhibited a volcano-shaped relationship as well (Figure 1-7). Though the remarkable electrocatalyst for oxygen reduction process has been variously investigated such as heteroatoms doped carbon catalyst, low amount of noble metal catalyst, and single-atom doped catalyst, the OER properties are not as good as those of commercial OER electrocatalysts such as Ir on carbon, IrO_2 or RuO_2. By employing ΔG_O - ΔG_{OH} as the descriptor, experimental overpotentials at 1 mA cm^{-2} cat are seen to follow well with the theoretical overpotential volcano constructed from a variety of metal oxide surfaces, as shown in Figure 1-7b. However, it is far from an ideal OER catalyst in terms of activity and is not completely stable under high oxidative potentials. Together, theoretical and experimental mechanistic studies will continue helping to design more advanced catalysts for electrical devices.

1.5.4. Hydrogen evolution reaction

Hydrogen (H_2) is regarded as a clean and high gravimetric density energy source to replace traditional fossil fuels. The hydrogen evolution reaction (HER) in electrochemical water splitting is one of the promising ways to economically produce high-purity hydrogen. Compared to ORR and OER process, the HER is a classic two-electron transfer reaction, plus its simple product and its paramount role in electrocatalysis, hence HER can serve a model to study the structure/function relationship of the electrocatalyst. The HER can follow either the Volmer- Heyrovsky or the Volmer-Tafel mechanism, as illustrated in Equations (Figure 1-8).

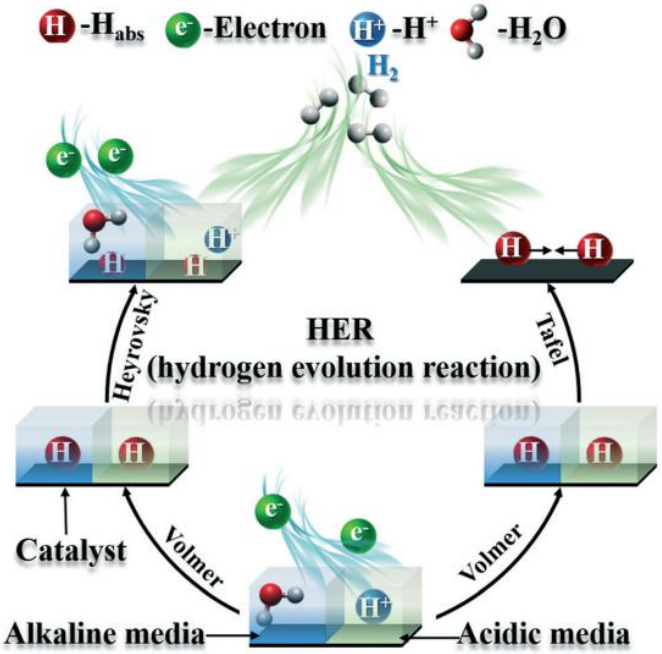

Figure 1-8 The illustration of the mechanism of the hydrogen evolution reaction on the surface of an electrode in acidic and alkaline solutions. Reprinted with permission. Copyright 2020, Royal Society of chemistry

Volmer-Heyrovsky mechanism:

The intermediate electrochemical hydrogen adsorption in acidic electrolyte:

$H_3O^+ + * + e^- \rightarrow H^* + H_2O$

In alkaline electrolyte:

$H_2O + * + e^- \rightarrow H^* + OH^-$

The electrochemical/chemical desorption of H_2:

$H^* + H_3O + e^- \rightarrow H_2 + H_2O$

Both the Volmer-Heyrovsky and the Volmer-Tafel pathways include two processes: intermediate electrochemical hydrogen adsorption and electrochemical/chemical desorption of H_2, and the difference between these two lies in the second step. The Tafel reaction is as follows:

$H^* + H^* \rightarrow H_2$

Using the Sabatier principle, in HER field, a volcano plot could be also obtained by plotting the activity index against the interaction force between catalyst and the reaction intermediates (Figure 1-9). The first volcano plot for HER was constructed by Trasatti, as shown in Figure 1-9 and he used the energy

of hydride formation instead of the adsorption energy to evaluate adsorption due to the unavailability of neither experimental nor theoretical data for the hydrogen adsorption energy ($\Delta G°_H$) at that time.

Currently, the state-of-the-art electrocatalyst for hydrogen production is composed of platinum (Pt)-based catalysts and it has several drawbacks such as high-cost, limited reserves, and poor electrochemical stability. Even though non-noble metal materials have been widely explored as enhanced catalysts for hydrogen production, the greatest challenge for the use of non-noble metal materials so far is that their HER activities still underperform Pt-based catalysts and they are susceptible to debase stability in a wide pH range. In view of the inevitable local pH change of the electrolyte near the electrode surface during the prolonged electrolysis process, the ideal catalyst should perform equally well in different pH conditions for energy-efficient water splitting. Though there has been some progress in recent years, the development of cost-effective catalysts with long-term stability and pH tolerance still remains challenging. Consequently, in order to reach a faster eco-friendly energy society, it is necessary to design an electrochemical catalyst efficiently with proper electrochemical devices.

1.6 Thesis structure

The structure of this thesis work is briefly outlined as follows:

Chapter 1 introduces the background of energy problems over the earth and the trend of direction of recent research.

Chapter 2 presents the electrocatalyst for oxygen reduction reaction for utilization of oxygen in air *via* polymer electrolyte membrane fuel cell (PEMFC).

Chapter 3 shows the bifunctional electrocatalyst for oxygen reduction and oxygen evolution reaction as alternative electrode for next generation batteries in Li-air and Zn-air battery.

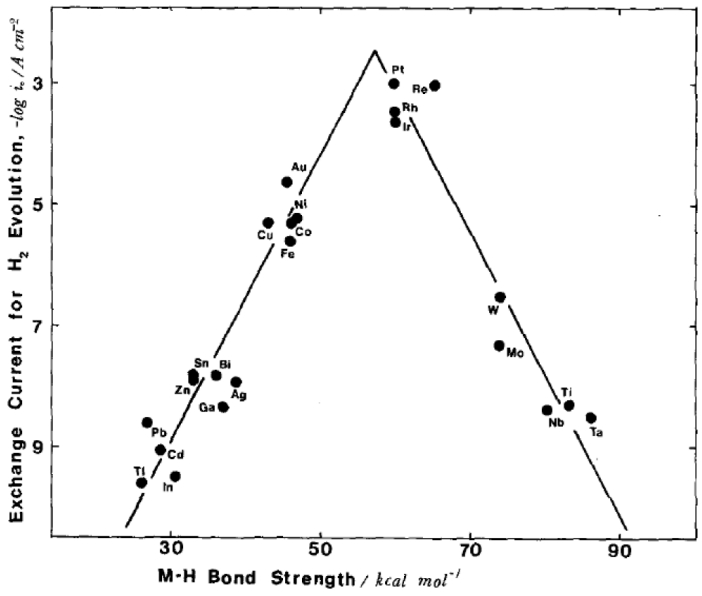

Figure 1-9 The first volcano plot for HER reported by Trasatti. Reproduced with permission. Copyright 1972. Published by Elsevier B.V.

Chapter 4 presents the rationally engineered electrochemical device for utilization of carbon dioxide denoted as hybrid Na-CO_2 system.

Chapter 5 shows the developed Metal (Zn & Al)-CO_2 system with indirect utilization of carbon dioxide for large scale of hydrogen (H_2) production.

Chapter 6 describes the membrane-free Mg-CO_2 system with production of hydrogen as well as electricity in quasi-neutral operating condition.

Chapter 7 presents the *in-operando* ammonia (NH_3) electrolysis protocol and Pt-based electrodes for commercialization compared to water-splitting.

References

[1] P. Friedlingstein, R. A. Houghton, G. Marland, J. Hackler, T. A. Boden, T. J. Conway, J. G. Canadell, M. R. Raupach, P. Ciais, C. Le Quere, *Nat. Geosci.* **2010**, *3*, 811.

[2] G. P. Peters, G. Marland, C. Le Quéré, T. Boden, J. G. Canadell, M. R. Raupach, Nat. Clim. Change 2012, 2, 2.

[3] M. A. Rahman, X. Wang, C. Wen, *Journal of The Electrochemical Society*, 160, A1759-A1771 (2013)

[4] M. Winter and R. J. Brodd, *Chem. Rev.* **104**, 4245 (2004).

[5] F.T. Bacon, Electrochim. *Acta* 14 (7) (1969) 569–585.

[6] A.J. Appleby, E.B. Yeager, *Energy* 11 (1–2) (1986) 137–152.

[7] I.D. Raistrick, Modified gas diffusion electrode for proton exchange membrane fuel cells, in: Proceedings of the Symposium on Diaphragms, Separators, and Ion-Exchange Membranes (Vol. 86), 1986, p. 172.

[8] I.D. Raistrick, U.S. Patent No. 4,876,115. Washington, DC: U.S. Patent and Trademark Office, 1989.

[9] I. Raistrick, Electrode Assembly for Use in a Solid Polymer Electrolyte Fuel Cell. U.S. Patent No. 4,876,115, 1989.

[10] M.S. Wilson, U.S. Patent No. 5,211,984. Washington, DC: U.S. Patent and Trademark Office, 1993.

[11] M.S. Wilson, UU.S. Patent No. 5,234,777. Washington, DC: U.S. Patent and Trademark Office, 1993.

[12] S. Gottesfeld, J. Pafford, *J. Electrochem. Soc.* 135 (10) (1988) 2651–2652.

[13] Y. Wang, *J. Electrochem. Soc.* 156 (10) (2009) B1134–B1141.

[14] Y. Wang, *J. Electrochem. Soc.* 156 (10) (2009) B1124–B1133.

[15] K. T. Chau, Y. S. Wong, and C. C. Chan, *Energy Convers. Manage.*, **40**(10), 1021 (1999).

[16] J. Larminie and J. Lowry, *Electric vehicle technology explained*, Wiley (2012).

[17] J.-S. Lee, S. T. Kim, R. Cao, N.-S. Choi, M. Liu, K. T. Lee, J. Cho, Adv. *Energy Mater.* 1, 34-50 (2011)

[18] J. D. Wadhawan, P. J. Welford, E. Maisonhaute, V. Climent, N. S. Lawrence, R. G. Compton, H. B. McPeak, C. E. W. Hahn, J. Phys. Chem. B 2001, 105, 10659.

[19] J. L. Roberts, T. S. Calderwood, D. T. Sawyer, J. Am. Chem. Soc. 1984, 106, 4667.

[20] K. Takechi, T. Shiga, T. Asaoka, Chem. Commun. 2011, 47, 3463.

[21] S. R. Gowda, A. Brunet, G. M. Wallraff, B. D. McCloskey, J. Phys. Chem. Lett. 2013, 4, 276.

[22] S. K. Das, S. Xu, L. A. Archer, Electrochem. Commun. 2013, 27, 59.

[23] Y. S. Mekonnen, K. B. Knudsen, J. S. G. Mýrdal, R. Younesi, J. Højberg, J. Hjelm, P. Norby, T. Vegge, J. Chem. Phys. 2014, 140, 121101.

[24] H. Lim, H. Lim, K. Park, D. Seo, H. Gwon, J. Hong, W. Goddard, H. Kim, K. Kang, J. Am. Chem. Soc. 2013, 135, 9733.

[25] Y. Liu, R. Wang, Y. Lyu, H. Li, L. Chen, Energy Environ. Sci. 2014, 7, 677.

[26] Z. Zhang, Q. Zhang, Y. Chen, J. Bao, X. Zhou, Z. Xie, J. Wei, Z. Zhou, Angew. Chem. Int. Ed. 2015, 54, 6550.

[27] X. Zhang, Q. Zhang, Z. Zhang, Y. Chen, Z. Xie, J. Wei, Z. Zhou, Chem. Commun. 2015, 51, 14636.

[28] X. Hu, J. Sun, Z. Li, Q. C. Chen, J. Chen, Angew. Chem. Int. Ed. 2016, 55, 6482.

Chapter 2 A New Strategy for Outstanding Performance and Durability in Acidic Fuel Cells: A Small Amount Pt Anchored on Fe,N co-Doped Graphene Nanoplatelets

This chapter has been published and has been cited in the thesis by co-author C. Kim.

Reproduced with permission from J. Kim, C. Kim, I.-Y. Jeon, J.-B. Baek, Y.-W. Ju, G. Kim, *ChemElectroChem* 2018, 5, 2857.

2.1. Introduction

Proton exchange membrane fuel cells (PEMFCs) are promising candidates for an alternative energy conversion system with low pollution, high power efficiency, and stable power generation at the low operating temperatures (55-95 oC).[1] Conventional electrode catalysts for PEMFCs are based on platinum (Pt) and Pt-alloy nanoparticles supported on carbon-based materials due to their excellent activity in cathodic oxygen reduction reaction (ORR) and anodic hydrogen oxidation reaction (HOR).[2,3] The major bottleneck of PEMFCs is related to the kinetically sluggish cathodic ORR rather than the anodic HOR.[4,5] Accordingly, use of Pt catalyst on the cathode is inevitable for the efficient electrochemical performance of PEMFCs. However, there are two major problems for using Pt catalysts in PEMFCs: (i) The high cost of Pt-based catalysts contributed over 55 % of the total cost [6,7] (ii) A poor durability from a self-agglomeration and a dissolution from the carbon substrate during long operation.[8–10]

To achieve both low cost and high durability, alternative electrochemical active substrates have been extensively investigated such as oxide-based, carbon nanotube, and graphene-like.[11–16] Among them, graphene is regarded as a promising supporting substrate for the precious metal catalysts because of its unique electrical and structural properties, such as high surface area (2,630 m2 g-1), tremendous electron mobility (~200,000 cm2 V-1 s-1), good chemical and electrochemical stability.[17] Despite these advantages, the catalysts based on graphene substrate possess insufficient electrochemical activity toward the ORR when they compare with that of commercial Pt/C so that these need to be further developed for acidic PEM fuel cells.[18] In order to enhance the electrochemical activity and durability of the catalysts on the graphene, the heteroatom-modified (e.g., nitrogen, sulfur, or iodine, etc.) graphene structures have been suggested as promising catalyst supports.[19–22] Among them, nitrogen-doped graphene has a beneficial interaction between nitrogen atoms and Pt-catalysts, thereby resulting in enhancing catalytic activity and stability.[23] Recently, several research groups have reported that transition metal (Fe, Co) substitution in the nitrogen-doped carbon-based material (M-N-C) could improve ORR activities.[24,25] In electrocatalysts with M-N-C functionalized group, two crucial factors govern the better performance of ORR, i.e., (i) the elemental composition and the interaction

between different components, which determine the intrinsic nature of active site; and (ii) interplanar spacing of the neighboring graphene sheets allowing both sides of each graphene sheet to be accessible to the ORR-relevant species (H+, O2, H2O).[24,26]

In these regards, we designed a new catalyst by anchoring low amount of Pt on the substrate of iron (Fe) and nitrogen (N) co-doped graphene nanoplatelets (FeN-GnPs). Fe-N-C functional groups in the graphene network offering the additional catalytic active sites for ORR can lower the amount of Pt while maintaining ORR performances. Moreover, an anchoring of nanoscale Pt on the FeN-GnPs induces much higher durability contributed by nitrogen atoms in the graphene crystals and provides favorable binding interaction with Pt.[17,27] To better understand the interaction between Pt nanoparticles and FeN-GnPs, the specific interaction related to Pt-N interaction was identified by X-ray photoemission spectroscopy (XPS). This interaction could prevent the agglomeration of Pt and disperse Pt in nanoscale on the graphene sheets, resulting in both excellent durability and enhanced ORR activity. With these favorable properties, nanoscale Pt anchored on Fe and N co-doped graphene nanoplatelets (Pt/FeN-GnPs) exhibits excellent electrochemical activities toward ORR, remarkable cell performance, and high durability for acidic PEM fuel cells.

2.2. Experimental

2.2.1. Preparation of Pt/FeN-GnPs composite

FeN-GnPs was synthesized by the ball-milling process using the pristine graphite flake in the ball-mill machine (Pulverisette 6, Fritsch) in the presence of nitrogen (N2). The stainless steel balls (500.0 g, diameter 5 mm) and the pristine graphite (5.0 g, Alfa Aesar, natural graphite, 100 mesh (< 150 μm), 99.9995% metals basis, Lot#14735) were put into a stainless steel ball-mill capsule (500 mL). After five charging-discharging cycles with N_2, the capsule was sealed and fully charged with N2 (8 bar of cylinder pressure). It was placed on the planetary ball-mill instrument and operated at 500 rpm for 48 h. The product was Soxhlet extracted with methanol and 1 M aq. HCl solution to get rid of impurities. The final product (FeN-GnPs) was freeze-dried at -120 ^{o}C under reduced pressure (0.05 mmHg) for 48h. The source of iron (Fe) is the ball-mill capsules and stainless steel balls.[25] In sequence, FeN-GnPs of 550 mg and H_2PtCl_6 of 623.4 mg (5.0 g, Alfa Aesar, 99.9 % metals basis) were mixed in aqueous solution with ultrasonication at pH=10 adjusted by ammonia. And then, an excessive NaBH4 aqueous solution with a concentration of 2 mg mL^{-1} was slowly added and stirred for 12h under the room temperature. The solution was filtered via vacuum filtration using Buchner funnel and further washed with distilled water.

2.2.2. Characterization of electrochemical measurements

Transmission electron microscopy (TEM) images were obtained using a high-resolution TEM (JEOL, JEM-2100F). Thermogravimetric analysis (TGA) was conducted from 100 to 800 oC using an SDT-

Q600 (TA instrument, USA) with a heating/cooling rate of 2 oC min-1 in the air. The phase identification of Pt/FeN-GnPs was confirmed by X-ray powder diffraction (XRD) (Rruker diffractometer, Cu Kα radiation) with a scanning rate of 1 o min-1 in the 2 range of 20 to 60 o. XRD was employed to verify the graphene phase and existence of platinum in Pt/FeN-GnPs.

RRDE test was carried out using a computer controlled potentiostat (Biologic VMP3) with a typical three-electrodes cell. In the RRDE test, a carbon electrode was used as a counter electrode and Ag/AgCl (1 M NaOH filled) electrode was used as a reference electrode in the acidic media 0.1 M HClO4. The system was saturated by continuous purging with pure oxygen gas (99.995% purity) before each measurement for 20 min. Each sample was stabilized by running cyclic voltammetry (CV) scans between 0.2 V and 1.1 V vs. RHE at a scan rate of 20 mV s-1 until reproducible CV polarization curves were observed. In succession, polarization curves were measured at a scan rate of 10 mV s-1. For the hydrogen underpotential deposition (Hupd), we performed cyclic voltammetry at 50 mV s-1 in N2 saturated electrolyte. The working electrodes were prepared by applying each of the catalyst inks onto a pre-polished glassy carbon disk electrode. Preparing the catalyst ink was first dispersed in an ethanol/isopropyl alcohol solution (10 mg mL-1) and a Nafion (25 wt. %) stock solution (10 μL) in ethanol was added to the catalyst ink by bath sonication. A total of 5μL of well-dispersed catalyst ink was applied onto the pre-polished glassy carbon (GC) disk electrode (5 mm in diameter). The prepared electrodes were fully dried at room temperature before the electrochemical tests.

2.2.3. Polymer electrolyte membrane fuel cell tests

For the MEA fabrication, the gas diffusion layers (GDLs) for anode and cathode were prepared with Freudenberg H23C8 carbon paper (FuelCellsEtc). For the FeN-GnPs based cathodes, the loading density of the catalyst was 1.5 mg cm-2 and binder was 1 mg cm-2. For the Pt/FeN-GnPs based cathodes, the loading density of the catalyst was 0.23 mg_{Pt} cm^{-2} and binder was 1 mg cm-2. For the 40 wt. % Pt/C (5.0 g, nominally 40 % on carbon black, Alfa Aesar) based cathodes, the loading density of Pt/C was 0.4 mg_{Pt} cm^{-2} and binder was 1 mg cm^{-2}. The anode was Pt/C (40 wt. %) with an excessive Pt loading of 0.4 mg_{pt} cm^{-2} to ensure sufficient proton supply from the anode. A pair of cathode and anode was hot pressed onto two sides of a Nafion NRE-212 membrane (0.05 mm thick, Alfa Aesar) at 130 ^{o}C for 2.5 min firstly, then under pressure 1 MPa for 2.5 min. The membrane electrode assembly (MEA) thus produced was tested in a 1 cm^2 PEM fuel cell at 80 ^{o}C and the humidified H_2 (60 mL min^{-1}) and O_2 (100 mL min^{-1}) were used as anode and cathode fuels, respectively.

2.3. Result and discussion

2.3.1. Characterization of Pt/FeN-GnPs catalyst

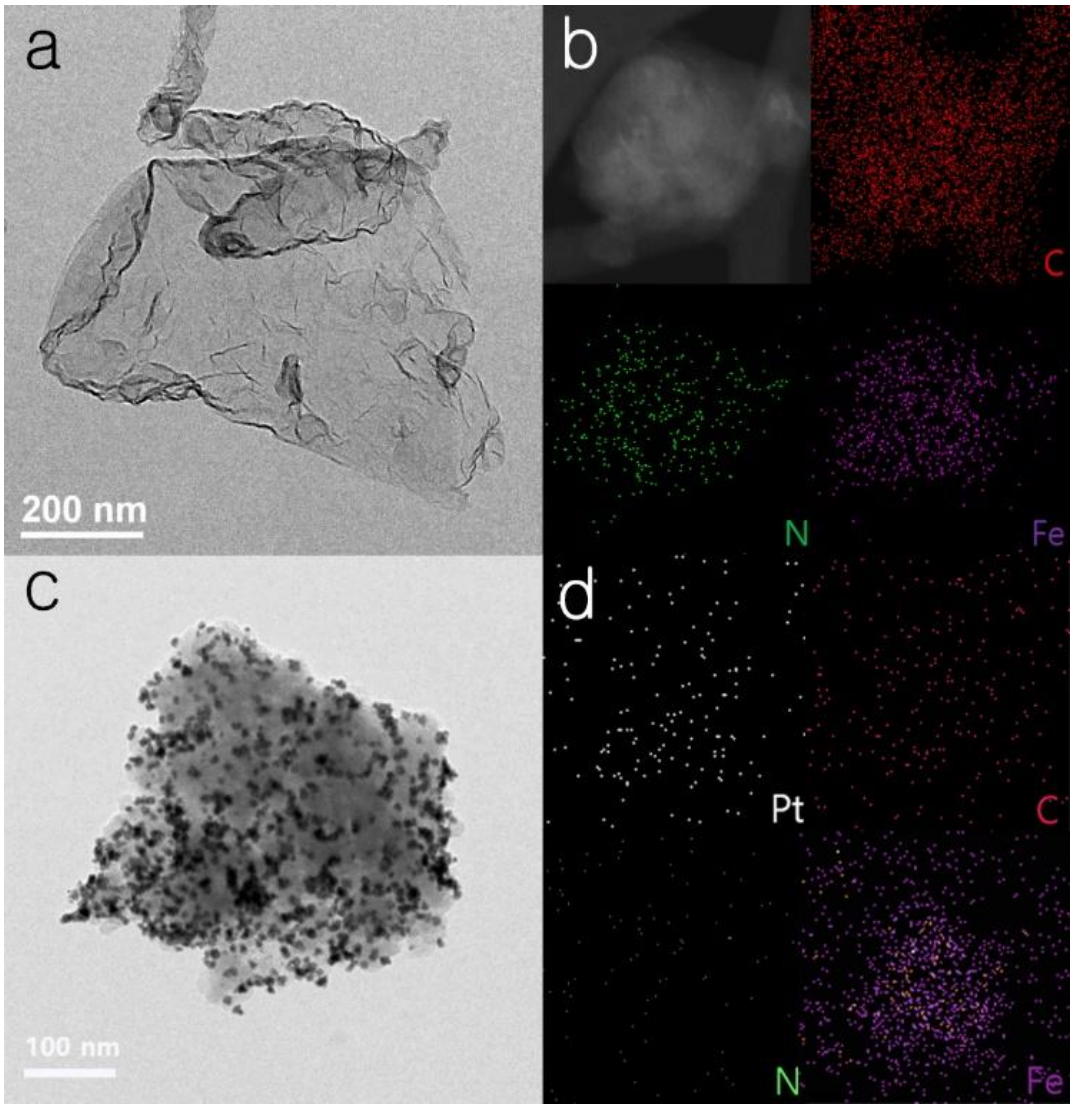

Figure 2-1 TEM images of (a) FeN-GnPs and (c) Pt/FeN-GnPs. Elemental mapping by EDS for (b) FeN-GnPs and (d) Pt/FeN-GnPs.

Iron (Fe) and nitrogen (N) co-doped graphene nanoplatelets (FeN-GnPs) were synthesized by the ball-milling process.[28-30] The transmission electron microscopy (TEM) image shows the morphology of FeN-GnPs after the ball-milling process (Figure 2-1a) and energy dispersive X-ray spectroscopy (EDS) shows the elements of Fe and N atoms in FeN-GnPs (Figure 2-1b). In Figure 2-1c, nitrogen atoms in the Pt/FeN-GnPs could hold Pt particles, resulting in well-dispersed Pt nanoparticles over the graphene sheet. It has been demonstrated that nitrogen-doped carbon substrates can increase the activity and stability of Pt catalyst.[31,32] EDS images (Figure 2-1d) shows the elements of Pt, Fe, N, and C in the

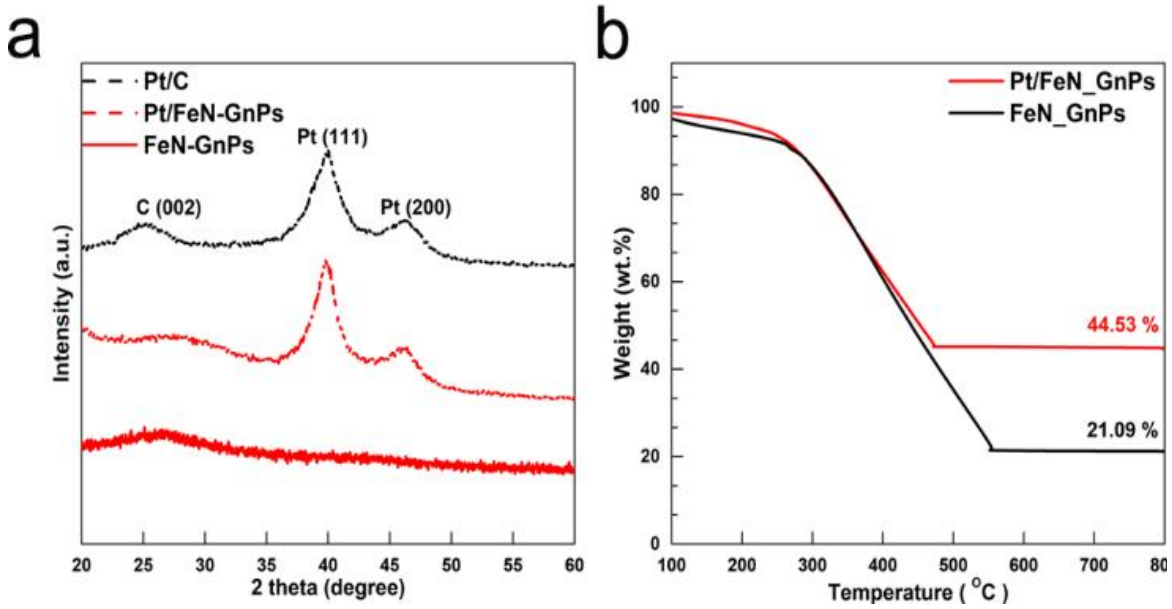

Figure 2-2 (a) X-ray diffraction (XRD) patterns of Pt/FeN-GnPs, Pt/C, and FeN-GnPs. (b) Thermogravimetric analysis (TGA) of Pt/FeN-GnPs and FeN-GnPs.

Pt/FeN-GnPs in Figure 2-1c. The EDS results also confirm that Pt particles are uniformly distributed over the FeN-GnPs (Figure 2-1d).

XRD patterns of Pt/FeN-GnPs and FeN-GnPs are shown in Figure 2-2a. The facet C (002) at 2θ of 20-30 o in the XRD patterns of FeN-GnPs and Pt/FeN-GnPs indicates graphite plane. Face-centered cubic (fcc) crystalline platinum is measured as Pt (111) and Pt (200) facets along with the graphitic carbon peak in the XRD patterns of Pt/FeN-GnPs. The mean particle sized can be calculated through XRD patterns according to Scherrer's formula (equation 2-1)[6]

$$\bar{d}_{xrd} = \frac{0.9\ \lambda}{\beta_{1/2} \cos\theta} \tag{2-1}$$

Where $\bar{d}_{xrd}$ is the average particle size (nm), λ is the wavelength of X-ray (0.154 nm), θ is the angle at the peak maximum, and $\beta_{1/2}$ is the width (radians) of the peak at half height. The calculated average particle size is found to be 4.29 nm for Pt/FeN-GnPs, which is suitable Pt particles size for favorable ORR though the little bit larger size compared to that of commercial Pt/C (2.7 nm).[33,34] As shown in Figure 2-2b, the weight loss of Pt/FeN-GnPs and FeN-GnPs is investigated by TGA from room temperature to 800 ºC in the air. There is a significant drop in mass at 300~600 ºC, indicating the evolution of CO and CO_2 from carbon in graphene sheets. After combustion, the difference of values between Pt/FeN-GnPs and FeN-GnPs could be assigned as loading amount of platinum catalyst in

Pt/FeN-GnPs (23.4 wt.%). Moreover, the weight ratio of Pt and each element in FeN-GnPs and Pt/FeN-GnPs were quantified from the EDS in Table 2-1.

Table2-1. Element weight ratio (wt. %) of the catalysts from EDS

	Pt	C	N	Fe	O
FeN-GnPs	-	80.61	2.88	10.98	5.53
Pt/FeN-GnPs	20.7	65.6	2.7	5.3	5.8

2.3.2. Electrochemical properties for oxygen reduction reaction

The oxygen reduction activities of commercial 40 wt.% Pt/C and Pt/FeN-GnPs were investigated by cyclic voltammograms (CVs) and rotating disk electrode (RDE) experiments in O_2 or N_2-saturated 0.1 M $HClO_4$. Figure 2-3a shows the polarization curves of Pt/FeN-GnPs by CVs in O_2 or N_2-saturated 0.1 M $HClO_4$ at the scan rate of 0.01 V s-1 from 0.25 V to 1.15 V (vs. RHE). As shown in Figure 2-3a, Pt/FeN-GnPs catalyst cannot show any redox peak over a potential range from 0.25 V to 1.15 V in the N_2-saturated solution. In contrast, Pt/FeN-GnPs catalyst exhibited ORR peak with an onset and peak potentials at 0.9 V and 0.8 V, respectively, in the O_2-saturated solution. To gain further insight into the ORR electrochemical properties, we performed RDE experiment at a rotation rate of 1600 rpm and a scan rate of 0.01 V s-1 (Figure 2-3b). Although FeN-GnPs showed poor ORR catalytic activities compared to Pt-based catalysts (Pt/C and Pt/FeN-GnPs), the onset potential for oxygen reduction of Pt/FeN-GnPs is +0.87 V, which is slightly higher than commercial Pt/C (+0.8 V). Furthermore, the limiting current of Pt/FeN-GnPs is even larger than that of the commercial Pt/C at the high overpotential area. The high catalytic activity of Pt/FeN-GnPs can be attributed to the apparently synergistic effect of Fe, N co-doped carbon substrate and the high activated Pt with the suitable size for ORR.[33,34] Hence, the Pt/FeN-GnPs (23.4 wt. %) presented better ORR activities with even lower amounts of Pt catalysts than the commercial Pt/C (40 wt. %). The polarization curves of Pt/FeN-GnPs are shown in Figure 2-3c at different rotation rates from 100 rpm to 2500 rpm. According to the Koutecky-Levich equation as below,

$$1/i = 1/i_k + 1/(B\,\omega^{0.5}) \quad (2\text{-}2)$$

Where i is the observed total current density, i_k is the kinetically limited current density, ω is the rotation speed of the electrode, and B is the Levich slope, we can obtain four J^{-1}-$\omega^{-1/2}$ lines (Figure 2-3d). The Levich slope B is given by the equation 2-3.

$$B = 0.62 \bullet n \bullet F \bullet [O_2] \bullet D^{2/3}{}_{O2} \bullet \nu^{-1/6} \quad (2\text{-}3)$$

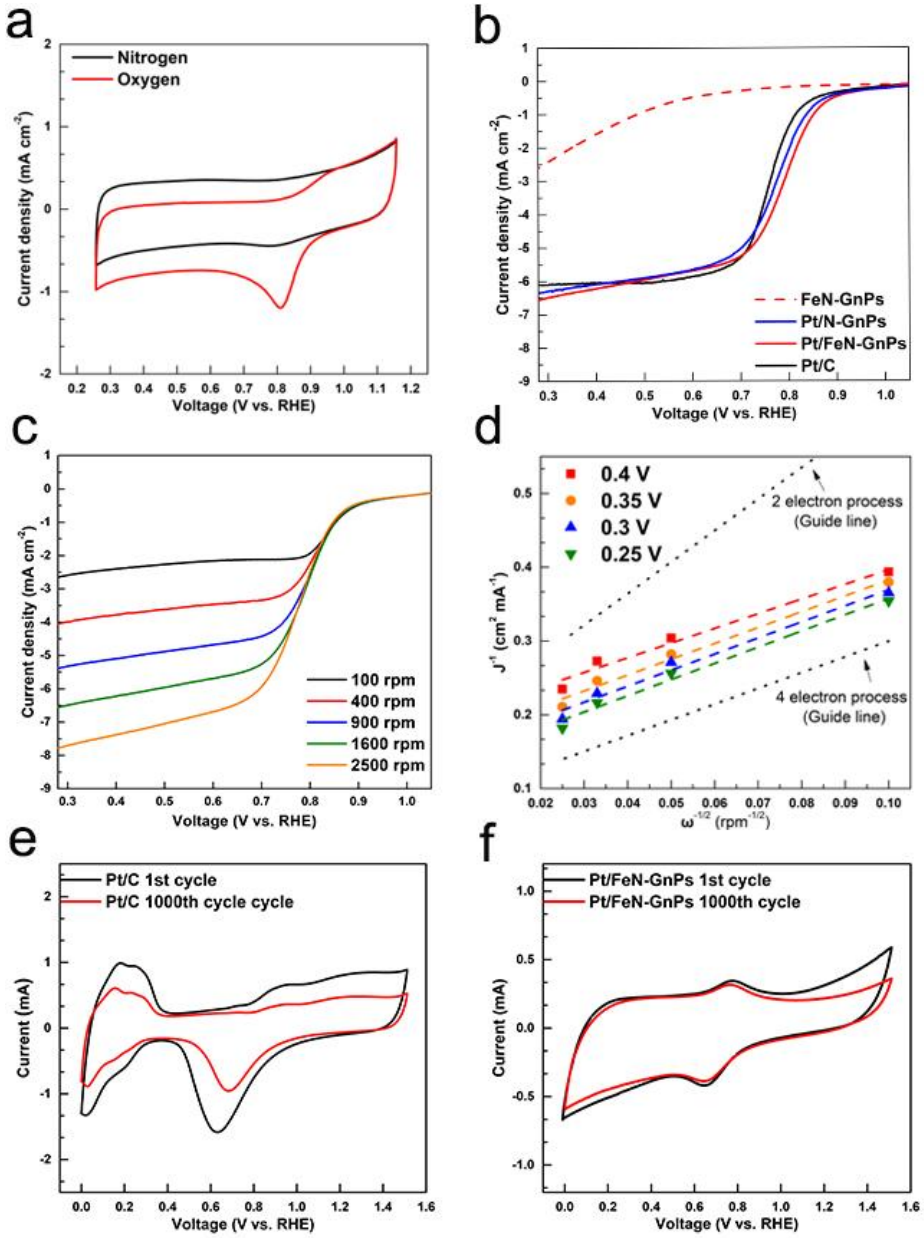

Figure 2-3 (a) Cyclic voltammograms of Pt/FeN-GnPs in O_2- or N_2-saturated 0.1 M $HClO_4$. (b) Linear sweep voltammetry (LSV) curves for ORR polarization curves of Pt/C, FeN-GnPs, and Pt/FeN-GnPs by RDE in O_2-saturated 0.1 M $HClO_4$. (c) RDE voltammograms for Pt/FeN-GnPs in 0.1 M $HClO_4$ saturated with O_2. (d) Koutecky-Levich plots obtained from the RDE results. CVs of (e) Pt/C and (f) Pt/FeN-GnPs in N_2-saturated 0.1 M $HClO_4$ for the 1st and 1000th cycles.

Where n is the number of electrons transferred during the ORR, F is the Faraday constant (F= 96,485 C), D is the diffusion coefficient of O_2 in the 0.1 M $HClO_4$ electrolyte ($D=1.93 \times 10^{-5}$ cm^2 s^{-1}), C is the bulk concentration of O_2 ($C=1.26 \times 10^{-3}$ mol L^{-1}), and ν is the kinetic viscosity of the electrolyte of 0.1 M $HClO_4$ ($v= 1.009 \times 10^{-2}$ cm^2 s^{-1}).[35] Using the equation (2), we can calculate the electron transfer number n from the slope of each line as 3.98 and 3.925 at 0.35 V and 0.3 V, respectively. These results revealed that the oxygen reduction on Pt/FeN-GnPs catalyst followed almost four electrons transfer pathway. Moreover, we investigated the stability of the Pt/FeN-GnPs and Pt/C by cyclic

voltammograms in O_2-saturated 0.1 M $HClO_4$ at a scan rate of 50 mV s^{-1}. The electrochemical surface area (ECSA) was calculated by measuring the Coulombic charge for hydrogen desorption in the range of 0.05 V to 0.4 V vs. RHE.[36] The specific values of the ECSA of Pt/FeN-GnPs and commercial Pt/C based on the mass of Pt were 74.2 and 76.7 m^2 g^{-1}, respectively, before durability test. The ECSA of the commercial Pt/C significantly decreased by 39 % compared to 1 cycle after 1000 continuous cycles between 0 V and 1.5 V vs. RHE (Figure 2-3e). Interestingly, Pt/FeN-GnPs maintained high electrochemical catalytic activity even after 1000 continuous cycles with 92.9 % activities (Figure 2-3f). The interaction between nitrogen atoms and Pt particles in Pt/FeN-GnPs prevented the agglomeration of Pt particles and led to the excellent durability in acidic media.[21,29,37] These results reveal that the Pt/FeN-GnPs is a highly promising electrocatalyst in acidic media due to its excellent ORR activity, stability, and cost-effectiveness compared to the commercial Pt/C catalyst

2.3.3. Structural analysis between before and after operation for ORR

TEM images of Pt/FeN-GnPs and Pt/C catalysts are shown in Figure 2-4. Figure 2-4a shows TEM images of Pt/FeN-GnPs before cycle test in O_2 saturated 0.1 M $HClO_4$ by CVs. The platinum particles of Pt/FeN-GnPs (Figure 2-4a) are uniformly dispersed on the FeN-GnPs and the mean platinum particle shows the diameter of 4.64 nm corresponding to XRD analysis (inset of Figure 2-4a). After continuous 10000 cycles by CVs in acidic media, the morphology of Pt/FeN-GnPs (Figure 2-4b) shows slight changes in platinum particles size of 7.03 nm and FeN-GnPs substrate. However, from the Pt/C, there

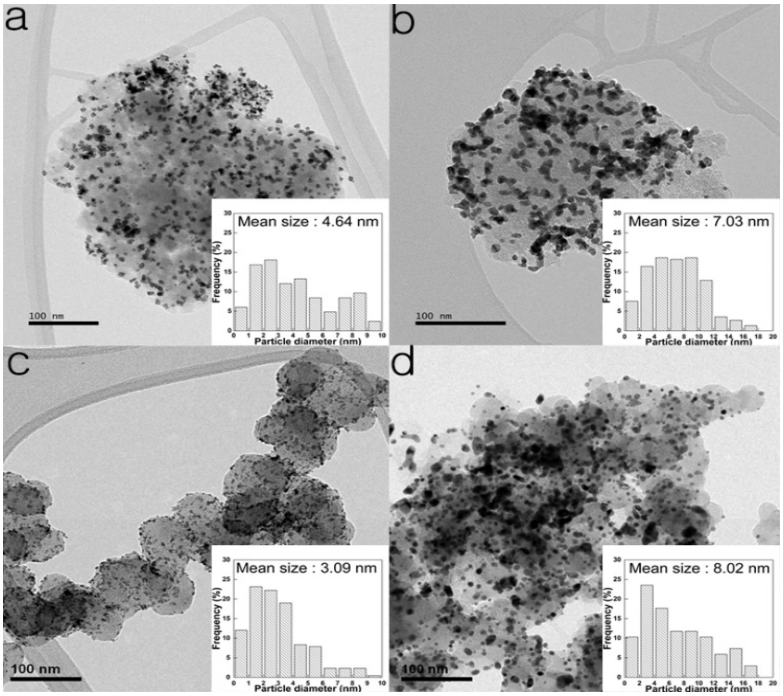

Figure 2-4 TEM images of Pt/FeN-GnPs (a) before and (b) after cycles in O_2 saturated 0.1 M $HClO_4$ by CVs. TEM images of commercial Pt/C (c) before and (d) after cycles in O_2 saturated 0.1 M $HClO_4$ by CVs.

is obvious changes in morphology and Pt particles size from the significant agglomeration after cycle test from 3.09 nm to 8.02 nm (Figure 2-4c and 2-4d).[18,38] These results also show that FeN-GnPs substrate improves the durability of the Pt catalysts due to the interaction between Pt particles and nitrogen atoms in FeN-GnPs substrate.[39]

2.3.4. Electric configuration of targe catalyst

To further investigate the iron and nitrogen doping effects in Pt/FeN-GnPs, X-ray photoelectron spectroscopy (XPS) measurements were carried out. There are signals of Pt, Fe, N, O and C elements (Figure 2-5a). The high-resolution C1s XPS spectrum of Pt/FeN-GnPs sample (Figure 2-5b) shows a main peak at 284.6 eV corresponding to the graphite-like sp^2 C. The sp^2-hybridized carbon in graphitic layers could provide facile electron pathway enhancing the catalytic activity of platinum.[7] The two weak peaks observed at 286.1 eV and 288.0 eV reflect the presence of carbon-nitrogen bonds, indicating sp^2 C-N and sp^3 C-N bonds, respectively.[40,41] These two peaks indicate substitution of the nitrogen atoms, defects or the edge of the graphene sheets.[42,43] The Fe 2p XPS spectra of Pt/FeN-GnPs is shown in Figure 2-5c. The photoelectron peaks at 727.5 eV correspond to the binding energy of 2p1/2 of Fe^{3+} and Fe^{2+} ion, and the peak at 724.5 eV is attributed to the binding energies of 2p1/2 of Fe^{2+} ion. The peaks at 712.2 eV and 710.3 eV are assigned to the binding energies of 2p3/2 of Fe^{3+} ion and Fe^{2+} ion, respectively.[44] These characterizations confirmed that the iron atoms had been successfully substituted at the edge of GnPs by the ball-milling process. The successful substitution of Fe-N-C functional group gives catalytic active sites of interplanar spacing in graphene sheets, resulting in the high catalytic activity of Pt/FeN-GnPs with low contents of Pt catalysts. Regarding the Pt 4f region (Figure 2-5d), the spectra contain Pt 4f7/2 and 4f5/2 states from the spin-orbital splitting. Each peak is deconvoluted into three different oxidation states of Pt (Pt^0, Pt^{2+}, and Pt^{4+}). The peaks of Pt^{2+} 4f5/2 and 4f7/2 in Pt/FeN-GnPs sample could be interpreted as an evidence of the Pt-N interaction.[45] The resolution N1s spectrum of FeN-GnPs (Figure 2-5e) and Pt/FeN-GnPs (Figure 2-5f) has been deconvoluted into four peaks as pyridinic N, pyrrolic N, graphitic N and oxidized N. Pyridinic and pyrrolic N 1s XPS spectra are observed from both FeN-GnPs and Pt/FeN-GnPs. These two nitrogen edge sites have a high ORR activity by itself and can also provide interaction with the Pt particles in the Pt/FeN-GnPs substrate, reducing aggregation of the Pt particles.[46] In the case of the N1s spectra in Pt/FeN-GnPs sample (Figure 2-5f), an additional peak at 397.9 eV confirmed the Pt-N interaction in Pt/FeN-GnPs. This new Pt-N interaction helps to synthesize the Pt nanoparticles on the FeN-GnPs and have excellent stability without degradation during ORR.

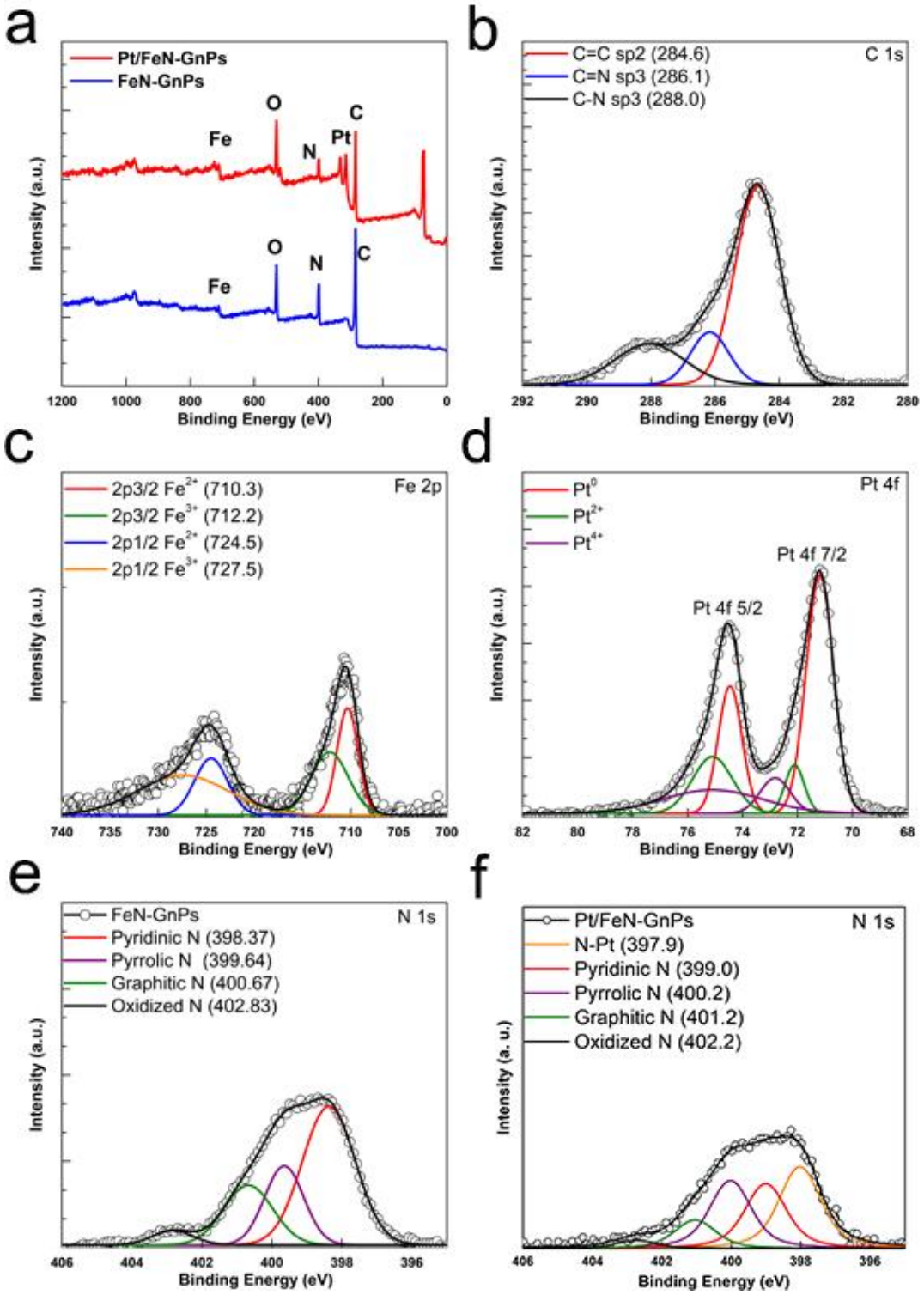

Figure 2-5 (a) XPS survey scan spectrum of FeN-GnPs and Pt/FeN-GnPs. XPS images of (b) C 1s, (c) Fe 2p, (d) Pt 4f, N 1s for (e) FeN-GnPs and (f) Pt/FeN-GnPs.

2.3.5. Electrochemical performances in an acidic PEM fuel cell

The electrochemical performances of Pt/C, FeN-GnPs, and Pt/FeN-GnPs catalyst were evaluated in an acidic PEM fuel cell with Nafion electrolyte and humidified H_2/O_2 gas (gas pressure ratio: Anode/Cathode = 1/1.7). In Figure 2-6a, the maximum power density of Pt/FeN-GnPs catalyst was 0.7 W cm^{-2}, which is outperforming about 70% power density of Pt/C and 352 % power density of FeN-GnPs. Even though the amount of Pt catalyst in Pt/FeN-GnPs is reduced by almost half, the performance of Pt/FeN-GnPs exhibits higher than 70 % than that of Pt/C. The single cell performances with Pt/C and Pt/FeN-GnPs per loaded Pt catalyst are shown in Figure 2-6b. Pt/FeN-GnPs exhibits maximum power density of 3.0 W mg_{pt}^{-1} and it even showed better performance than that of commercial Pt/C.

2.3.6. Stability measurements in an acidic PEM fuel cell

For long-term stability (Figure 2-7), the chronopotentiometry in single cell condition of Pt/FeN-GnPs displays a stable potential over 200 hours without degradation of cell voltage at the current density of 0.5 A cm^{-2} whereas the degradation of Pt/C begins to appear after 100 hours. These results also demonstrate the synergistic catalytic effect of the Pt-N interaction and Fe-N-C functional group in accordance with the XPS analysis. The composite structure of Pt nanoparticles on the FeN-GnPs substrate not only prevents dissolution and agglomeration of Pt nanoparticles but also provides catalytic active sites toward ORR, contributing to the improvement in both stability and catalytic activity of the catalyst. The present study shows doping effects of Fe and N atoms and analyzes the specific interactions between Pt catalyst and FeN-GnPs substrate. Consequently, Pt/FeN-GnPs catalyst is an efficient ORR catalyst with comparable performance to benchmark Pt/C for acidic PEM fuel cells.

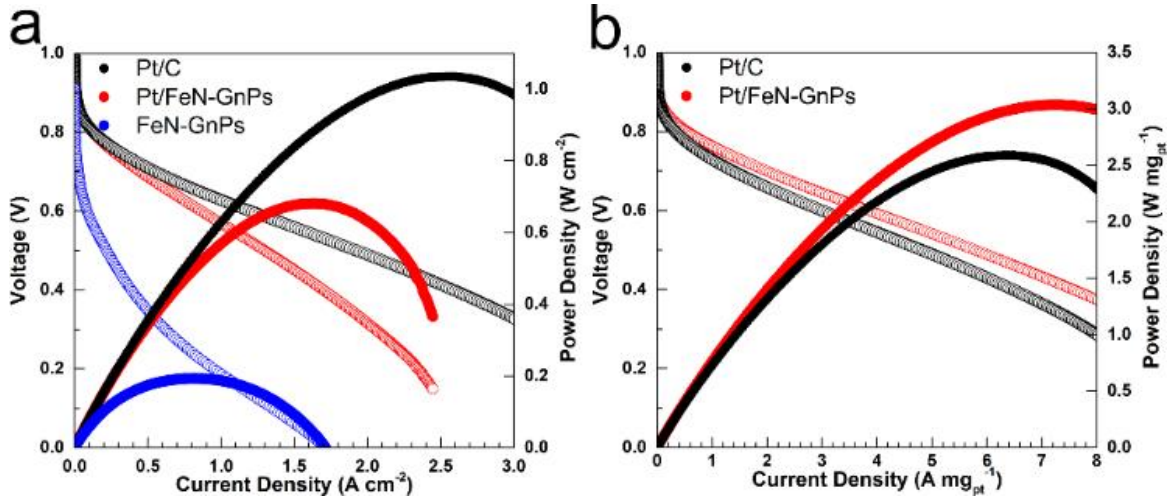

Figure 2-6 (a) Comparison of single cell performances with the commercial 40 wt.% Pt/C, FeN-GnPs, and Pt/FeN-GnPs as the cathode catalysts at a catalyst loading of 1 mg cm^{-2}. Commercial 0.4 mg_{pt} cm^{-2} Pt/C as anode; H_2/O_2 at 80 °C (gas pressure ratio: Anode/Cathode = 1/1.7); Nafion 112 membrane; 60/100 mL min^{-1} anode and cathode flow rates, respectively.

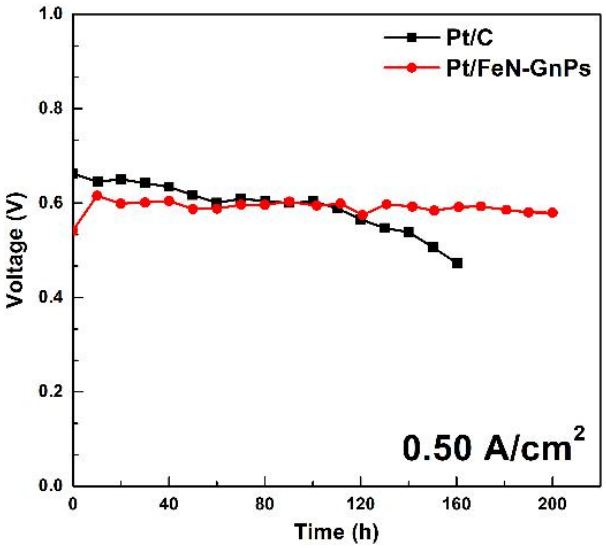

Figure 2-7 Stability of single cell performance with Pt/FeN-GnPs catalyst at constant current density of 0.5 A cm^{-2}.

2.4. Conclusions

In summary, we have fabricated nanoscale platinum anchored on iron and nitrogen co-doped graphene nanoplatelets (Pt/FeN-GnPs) for efficient electrocatalysts of acidic fuel cells. When nanoscale Pt is anchored with nitrogen in FeN-GnPs, it has much higher durability. Moreover, Fe-N-C functional groups in the graphene network offer the additional catalytic active sites for ORR, lowering the amount of Pt while maintaining ORR performances. The Pt-N interaction confirmed by XPS could help to disperse the Pt nanoparticles on the FeN-GnPs and provides an excellent stability without performance degradation. The acidic PEM fuel cells confirmed that Pt/FeN-GnPs possess the good electrochemical performance and higher durability than that of commercial Pt/C. This work reveals that the anchoring of Pt on Fe and N co-doped graphene sheets is excellent strategy to achieve high performance and durability for the acidic fuel cells

References

[1] X. Yu and S. Ye, *J. Power Sources*, **172**, 145 (2007)

[2] J. Wu and H. Yang, *Acc. Chem. Res*., **46**, 1848 (2013)

[3] M. K. Debe, *Nature*, **486**, 43 (2012)

[4] W. Sheng, H. A. Gasteiger, and Y. Shao-Horn, *J. Electrochem. Soc*., **157**, B1529 (2010)

[5] Y. Bing, H. Liu, L. Zhang, D. Ghosh, and J. Zhang, *Chem. Soc. Rev*., **39**, 2184 (2010)

[6] R. Bashyam and P. Zelenay, *Nature*, **443**, 63 (2006)

[7] Y. Bing, H. Liu, L. Zhang, D. Ghosh, and J. Zhang, *Chem. Soc. Rev*., **39**, [2184 (2010)

[8] . Ma, A. Habrioux, and N. Alonso-Vante, *ChemElectroChem*, **1**, 37 (2014)

[9] Y.-C. Park, K. Kakinuma, M. Uchida, D. A. Tryk, T. Kamino, H. Uchida, and M. Watanabe, *Electrochim. Acta*, **91**, 195 (2013)

[10] F. Hasché, M. Oezaslan, and P. Strasser, *Phys. Chem. Chem. Phys*., **12**, 15251 (2010)

[11] M. Liu, R. Zhang, and W. Chen, *Chem. Rev*., **114**, 5117 (2014)

[12] A. Lewera, L. Timperman, A. Roguska, and N. Alonso-Vante, *J. Phys. Chem. C*, **115**, 20153 (2011)

[13] J. Ma, A. Habrioux, and N. Alonso-Vante, *J. Solid State Electrochem*., **17**, 1913 (2013)

[14] V. T. T. Ho, C.-J. Pan, J. Rick, W.-N. Su, and B. J. Hwang, *J. Am. Chem. Soc*., **133**, 11716 (2011)

[15] Z. Li, Q. Gao, H. Zhang, W. Tian, Y. Tan, W. Qian, and Z. Liu, *Sci. Rep.*, **7**, 43352 (2017)

[16] L. Xin, F. Yang, S. Rasouli, Y. Qiu, Z.-F. Li, A. Uzunoglu, C.-J. Sun, Y. Liu, P. Ferreira, W. Li, Y. Ren, L. A. Stanciu, and J. Xie, *ACS Catal.,* **6**, 2642 (2016)

[17] H. Wang, T. Maiyalagan, and X. Wang, *ACS Catal*., **2**, 781 (2012)

[18] B. P. Vinayan and S. Ramaprabhu, *Nanoscale*, **5**, 5109 (2013)

[19] I.-Y. Jeon, S.-Y. Bae, J.-M. Seo, and J.-B. Baek, *Adv. Funct. Mater*., **25**, 6961 (2015)

[20] I.-Y. Jeon, C. Kim, G. Kim, and J.-B. Baek, *Carbon*, **93**, 465 (2015)

[21] Y. Chen, J. Wang, H. Liu, M. N. Banis, R. Li, X. Sun, T.-K. Sham, S. Ye, and S. Knights, *J. Phys. Chem. C*, **115**, 3769 (2011).

[22] J. Xu, I.-Y. Jeon, J.-M. Seo, S. Dou, L. Dai, and J.-B. Baek, *Adv. Mater*., **26**, 7317 (2014)

[23] D. C. Higgins, D. Meza, and Z. Chen, *J. Phys. Chem. C*, **114**, 21982 (2010)

[24] F. Jaouen, E. Proietti, M. Lefèvre, R. Chenitz, J.-P. Dodelet, G. Wu, H. T. Chung, C. M. Johnston, and P. Zelenay, *Energy Environ. Sci*., **4**, 114–130 (2011)

[25] Y.-W. Ju, S.Yoo, C. Kim, S. Kim, I.-Y. Jeon, J. Shin, J.-B. Baek, and G. Kim, *Adv. Sci*., **3**, 1500205 (2016)

[26] U. I. Kramm, J. Herranz, N. Larouche, T. M. Arruda, M. Lefèvre, F. Jaouen, P. Bogdanoff, S. Fiechter, I. Abs-Wurmbach, S. Mukerjee, and J.-P. Dodelet, *Phys. Chem. Chem. Phys*., **14**, 11673 (2012)

[27] A. Zahoor, M. Christy, Y. J. Hwang, Y. R. Lim, P. Kim, and K. S. Nahm, *Appl. Catal. B Environ*., **147**, 633 (2014)

[28] I.-Y. Jeon, H.-J. Choi, M. J. Ju, I. T. Choi, K. Lim, J. Ko, H. K. Kim, J. C. Kim, J.-J. Lee, D. Shin, S.-M. Jung, J.-M. Seo, M.-J. Kim, N. Park, L. Dai, and J.-B. Baek, *Sci. Rep.,* **3**, 2260 (2013)

[29] D. W. Chang, H. J. Choi, I.-Y. Jeon, and J.-B. Baek, *Chem. Rec*., **13**, 224 (2013)

[30] C. Kim, O. Gwon, I.-Y. Jeon, Y. Kim, J. Shin, Y.-W. Ju, J.-B. Baek, and G. Kim, *J. Mater. Chem. A*, **4**, 2122 (2016)

[31] Y. Shao, G. Yin, and Y. Gao, *J. Power Sources*, **171**, 558 (2007)

[32] Y. Chen, J. Wang, H. Liu, R. Li, X. Sun, S. Ye, and S. Knights, *Electrochem. commun*., **11**, 2071 (2009)

[33] F. J. Perez-Alonso, D. N. McCarthy, A. Nierhoff, P. Hernandez-fernandez, C. Strebel, I. E. L. Stephens, J. H. Nielsen, and I. Chorkendorff, *Angew. Chem. Int. Ed*., **51**, 4641 (2012)

[34] K. Kinoshita, *J. Electrochem. Soc*., **137**, 845 (1990)

[35] H. Peng, Z. Mo, S. Liao, H. Liang, L. Yang, F. Luo, H. Song, Y. Zhong, and B. Zhang, *Sci Rep*.,**3**, 1765 (2013)

[36] T. Binninger, E. Fabbri, R. Kotz, and T. J. Schmidt, *J. Electrochem. Soc.*, **161**, H121–H128 (2014)

[37] K. Mamtani, D. Jain, D. Dogu, V. Gustin, S. Gunduz, A. C. Co, and U. S. Ozkan, *Appl. Catal. B Environ*., **220**, 88 (2018)

[38] A. V. Virkar and Y. Zhou, *J. Electrochem. Soc.*, **154**, B540 (2007)

[39] Y. Zhou, K. Neyerlin, T. S. Olson, S. Pylypenko, J. Bult, H. N. Dinh, T. Gennett, Z. Shao, and R. O'Hayre, *Energy Environ. Sci*., **3**, 1437 (2010)

[40] D. Wei, Y. Liu, Y. Wang, H. Zhang, L. Huang, and G. Yu, *Nano Lett*., **9**. 1752 (2009)

[41] H. Wang, C. Zhang, Z. Liu, L. Wang, P. Han, H. Xu, K. Zhang, S. Dong, J. Yao, and G. Cui, *J. Mater. Chem*., **21**, 5430 (2011)

[42] C. Ronning, H. Feldermann, R. Merk, H. Hofsass, P. Reinke, and J.-U. Thiele, *Phys. Rev. B*, **58**, 2207 (1998)

[43] J. W. Jang, C. E. Lee, S. C. Lyu, T. J. Lee, and C. J. Lee, *Appl. Phys. Lett*., **84**, 2877 (2004)

[44] Q. Dong, X. Zhuang, Z. Li, B. Li, B. Fang, C. Yang, H. Xie, F. Zhang, and X. Feng, *J. Mater. Chem. A*, **3**, 7767 (2015)

[45] J. Ma, A. Habrioux, Y. Luo, G. Ramos-Sanchez, L. Calvillo, G. Granozzi, P. B. Balbuena, and N. Alonso-Vante, *J. Mater. Chem. A*, **3**, 11891 (2015)

[46] X. Ning, H. Yu, F. Peng, and H. Wang, *J. Catal*., **325**, 136 (2015)

Chapter 3 Synergistic Coupling Derived Cobalt Oxide with Nitrogenated Holey Two-Dimensional Matrix as an Efficient Bifunctional Catalyst for Metal-Air Batteries

This chapter has been published.

3.1. Introduction

Intensive energy demands have stimulated considerable interest in alternative energy conversion and storage systems with a low cost, environment-friendly processing, and a high energy density.[1–4] The oxygen reduction reaction (ORR) and oxygen evolution reaction (OER) are key processes in renewable-energy devices, including fuel cells and metal-air batteries.[5-8] Despite tremendous efforts, the sluggish ORR and OER processes remain the current bottleneck in the advancement of this technology.[9-13] For efficient ORR and OER processes in alkaline media, noble metal catalysts such as Pt, iridium oxide (IrO_2), and ruthenium oxide (RuO_2) are commonly used owing to their excellent catalytic activities. Precious-metal-based catalysts, however, are not suitable for large-scale applications owing to their high cost, lack of bifunctional catalytic activity, and limited material options.[14,15]

Therefore, transition metal oxides have been considered as alternatives because of their promising catalytic, electrical, and electrochemical properties in alkaline solutions.[16,17] Among the available metal oxides, the Co_3O_4 spinel catalyst has attracted considerable interest for designing structures with certainly exposed crystal planes and surface-sensitive electrochemical properties owing to various atomic configurations.[18,19] Following the report by Han *et al.* on controlling the Co_3O_4 morphology of catalysts for the ORR and OER, the crystal-plane-dependent catalytic activities of Co_3O_4 nanostructures are well known to follow the order of NPs, nanotruncated octahedrons, and nanocubes, which is consistent with having more exposed planes in the order {111} > {112} > {110} > {100}.[18,20] Therefore, uniformly controlled Co_3O_4 with a specific atomic arrangement, which contributes to its electrocatalytic activity and overall performance, deserves a great deal of attention for designing bifunctional catalysts. However, Co_3O_4 nanoparticles alone are well known to have poor electrochemical activity; thus, many recent studies have been carried out on the synergistic or cooperative effects of nanoparticles grown on carbon-based supports on both the ORR and the OER in alkaline solutions.[21-25] These effects could be expected if the Co_3O_4 nanoparticles are well dispersed on the carbon matrix. Recently, Mahmood *et al.* fabricated an Fe@C_2N catalyst, that is, Fe encapsulated by graphitic layers on a nitrogenated, porous two-dimensional (2D) structure (C_2N matrix), *via* the *in situ* sandwiching of Fe^{3+} precursors in the C_2N layer.[26,27] The Fe@C_2N catalyst showed favorable oxygen diffusion and electron tunneling with the

polar C_2N matrices, and its ORR performance showed outstanding stability owing to the Fe nanoparticle cores protected by nitrogenated graphitic shells, rendering it a suitable cocatalyst.

Against this background, we rationally designed nanopolyhedron (NP) Co_3O_4 on an $Fe@C_2N$ structure (NP Co_3O_4/$Fe@C_2N$) with excellent bifunctional activities toward both the ORR and the OER, which we grew *via* a hydrothermal process. The exposed planes of the Co_3O_4 phase on the $Fe@C_2N$ structure with NP morphology are well controlled to be (111) plane, which lead to superior bifunctional activities for the ORR and the OER in comparison with those of their counterpart catalysts with different exposed planes (*e.g.*, the cubic and octahedral nanostructures of Co_3O_4). Furthermore, this is the report confirming the specific binding interaction between NP Co_3O_4 particles and the C_2N framework generated by a hydrothermal process, as well as the synergistic coupling between the NP Co_3O_4 and the C_2N framework, thus leading to a better electrochemical performance than those of Co_3O_4 or $Fe@C_2N$ alone. The NP Co_3O_4/$Fe@C_2N$ catalyst shows a comparable Tafel slope for both the ORR and the OER to that of commercial Pt/C and IrO_2 catalysts, as well as excellent electrochemical stability caused by the binding interaction between the NP Co_3O_4 and the C_2N framework. The NP Co_3O_4/$Fe@C_2N$ electrocatalyst shows an exceptionally high stability over 700 min and 30 h in Zn–air and hybrid Li-air batteries, respectively, as well as an even lower charge-discharge overpotential gap at 15 mA cm^{-2} in Zn–air batteries (0.85 V) than that of the Pt/C+IrO_2 catalyst (1.01 V). Along with these favorable properties, we demonstrated that the NP Co_3O_4/$Fe@C_2N$ catalyst is a promising bifunctional catalyst for metal-air batteries, and the synergistic coupling of a metal oxide with the C_2N framework represents an approach for developing advanced catalysts for energy conversion.

3.2. Experimental

3.2.1. Synthesis of $Fe@C_2N$

The powder FeCl3 of 1.17 g was added in 35 mL NMP with an ice bath. Hexaketocyclohexane octahydrate of 1.13 g was added in the solution, and then Hexaaminobenzene trihydrochloride of 1.0 g was added in nitrogen (N2) condition. The flask was maintained to ambient temperature for 120 minutes. The ice bath was taken the place of an oil bath and the flask was maintained to 175 °C with reflux during 8 hours. After finishing the refluxing, the solution was turned down the heat to 80 °C and sodium borohydride (NaBH4) powder was slowly added. The solution was maintained at reflux for 180 minutes. The solution was turned down the heat to room temperature and then distilled water was slowly added. PTFE (0.5 μm) membrane was used to collect the precipitated solid product by suction filtration. The black powder was extracted followed Soxhlet with distilled water (3 days) and methanol (3 days). After that, it was rapidly cooled down below -120 oC using freeze-dried method. After drying, the powder was annealed at 600 oC for 120 minutes in argon (Ar) condition. The final product was washed several times with 4 M HCl and distilled water.

3.2.2. Synthesis of NP Co_3O_4/Fe@C_2N

Fe@C_2N was dispersed in the anhydrous ethanol (EtOH) with the concentration of the Fe@C_2N in EtOH solution was ~0.3 mg/mL. For the first step synthesis, 2.4 ml of 0.125 M Co(Ac)2 aqueous solution was mixed with 48 ml of Fe@C_2N EtOH solution, and then 1.2 ml distilled water was added at ambient temperature. Then, the product was maintained at 80 oC with stirring for 10 hours. After finishing the dispersion, the solution (~40 ml) was moved to the autoclave for the hydrothermal process at 150 oC for 180 minutes. After filtration, the product was obtained and then washed several times with distilled water and ethanol, respectively. The resulting NP Co_3O_4/ Fe@C_2N catalyst was ~20 mg after filtration. To prepare 0.2 M, 0.15 M, and 0.1 M Co_3O_4/ Fe@C_2N, 2.4 ml of 0.2 M, 0.15 M, and 0.1 M Co(Ac)2 solution was added to 48 ml of Fe@C_2N EtOH solution, respectively. The following steps were the same as above. To prepare NP Co_3O_4/C2N catalyst, 2.4 ml of 0.125 M Co(Ac)2 aqueous solution was added to 48 ml of C2N EtOH suspension. The following steps were the same as above.

3.2.3. Structural characterization and electrochemical tests

The micromorphology was investigated using scanning electron microscopy (Nova FE-SEM) instrument. The transmission electron microscopy was conducted using a JEOL 2100F with a probe-side spherical aberration (Cs) corrector at an accelerating voltage of 200 kV. HAADF-STEM images and EELS spectra were taken using a FEI Titan3 G2 60-300 microscope equipped with a double-sided Cs corrector operating at 200 kV. X-ray photoelectron spectroscopy (XPS) measurement was conducted on an X-ray Photoelectron Spectrometer Thermo Fisher K-alpha (UK). The crystal structure of NP Co_3O_4/Fe@C_2N and Fe@C_2N was investigated by using X-ray powder diffraction (XRD) (Rigagu-diffractometer, Cu Ka radiation) and a scan rate is 0.03 ^{o} s^{-1} for measurements. In a three-electrode system, graphite rod was used to serve as the counter-electrode and the reference electrode was a commercial Ag/AgCl in saturated KCl. The working electrode was the glassy carbon (GC) electrode which was coated by each catalyst. The 10 mg catalyst was firstly added in mixture solution with EtOH/isopropyl alcohol (IPA) with a 1:1 ratio and the 54 L Nafion solution (5 wt. %, Sigma-Aldrich) was added. The addition of the Nafion could lead as a well-dispersed catalyst solution and act binder between the catalyst and GC electrode. In the case of composite Co_3O_4+Fe@C_2N catalyst, 5 mg commercial Co_3O_4 (<50nm particle size, Sigma Aldrich, Lot# MKBR1914V) and 5 mg Fe@C_2N were physically mixed. A 5 L catalyst solution was loaded on the GC disk electrode with controlled 0.125 cm^2. The working electrode was dried at ambient temperature for all the electrochemical measurements. In RRDE measurements, the number of transferred electrons (n) and hydroperoxide yields (%) were investigated as follows equations

$$n = 4 \times \frac{I_d}{\text{-a} \quad \text{/ A}}$$

$$\% HO_2^- = 200 \times \frac{I_r/N}{-a \cdot \ / N}$$

where I_d means the value of disk current, I_r means the value of the ring current and N means the efficiency of the current collection on the Pt ring in the RRDE. Abbreviation of N was measured to be 0.41 by the reduction of $K_3Fe[CN]_6$. All the electrochemical test was conducted using a potentiostat (Biologic VMP3).

3.2.4. Zinc (Zn)-air cell assembly and measurements

A Zn-air cell is composed of Zinc metal / aqueous electrolyte / cathode. 0.2 M zinc acetate in 6 M aq. KOH solution was used as the aqueous electrolyte between the anode and cathode, and carbon paper was served as a current collector. The zinc acetate material was used for the rechargeable one Zn metal with 0.25 mm thickness (Alfa Aesar) was selected as the anode and gas diffusion layer (Toray TGP-H-090) was used as the air electrode. Zinc plate and air electrode were separated by a glass fiber separator (EL-CELL, 18 mm x 1mm). The catalyst (10 mg) was dispersed in a 0.95 mL IPA/EtOH mixed solution (1/1) with Nafion (5 wt.%) stock solution (54 uL) for the catalyst ink. The active area was controlled to be 16 mm in diameter and the catalyst solution ink was loaded on the carbon paper. The catalyst loading density was 1 mg cm-2 and binder content in the cathode was 20 wt. %. In the case of Pt/C+IrO2 sample, 5 mg commercial Pt/C (20 wt.%) and 5 mg IrO2 were physically mixed. Battery test was conducted using a meshed CR2032 coin cell (CR2032-CASE-304-MESH, MTI Co.). Full-cell measurements were investigated at room temperature using a Biologic VMP3.

3.2.5. Hybrid lithium (Li)-air cell assembly and measurements

A Li metal (0.2 mm thickness) was used from Honjo metal, cut for use the anode electrode of 1cm. An organic electrolyte was selected as 1 M LiPF6 in tetraethylene glycol dimethyl ether (TEGDME), and an aqueous electrolyte was selected as 1 M LiNO3 + 0.5 M LiOH solution. The solid electrolyte (Li1+x+yTi2-xAlxP3-ySiyO12, 0.15 mm thickness, OHARA Inc., Japan) between anode and cathode was applied as solid lithium super ionic conductor (LISICON). The cathode was controlled by drop-coating each catalyst inks with Nafion binder onto the carbon paper (Toray TGP-H-090). 1 mg cm-2 catalyst was loaded and Nafion binder content in the cathode was 20 wt. %. Full-cell measurements were investigated on a computer controlled potentiostat (Biologic VMP3).

3.3. Result and discussion

3.3.1. Structural Characterization

As schematically shown in Figure 3-1a, the nitrogenated, porous 2D network (denoted by C2N for the empirical formula of repeating units in its basal area) is composed of uniformly distributed holes with six nitrogen atoms facing the center of each hole.[28] The structure of the Fe@C_2N catalyst is composed of an Fe nanoparticle core encapsulated in an N-doped graphitic shell (Fe@C_2N nanoparticles) decorating the C2N framework. The polar C2N in the Fe@C_2N catalyst plays several crucial roles: (i) it provides coordination sites for interactions with Fe; (ii) it prevents catalytic nanoparticles from leaching out, thus imparting long-term stability; and (iii) it provides oxygen diffusion and electron pathways. NP Co_3O_4 on the Fe@C_2N structure (NP Co_3O_4/ Fe@C_2N) was self-grown via a hydrothermal process, and facet-controlled Co_3O_4 nanoparticles are well distributed on the C2N framework. The synthetic processes are described in detail in the Experimental section. The crystalline structures of Fe@C_2N and NP Co_3O_4/ Fe@C_2N were measured using powder X-ray diffraction. As shown in Figure 3-1b, the peaks at 44.7 and 65.0° are characteristic of metallic Fe in Fe@C_2N (JCPDS: 87-0721).29 The minor peaks indicate the formation of iron carbide (Fe3C) (JCPDS: 72-1110), which forms during the synthesis of Fe@C_2N.30 In Figure 3-1c, seven diffraction peaks appear in the X-ray diffraction patterns of NP Co_3O_4/ Fe@C_2N, located at 2θ = 31.3°, 36.8°, 38.5°, 44.8°, 55.6°, 59.3°, and 65.2°, corresponding to (220), (311), (222), (400), (422), (511), and (440) planes of face-centered cubic (fcc) spinel Co_3O_4, respectively. The peak at 26.1° indicates the (002) plane of the graphitic layer in both Figure 3-1b and 3-1c. Notably, the Fe nanoparticle core encapsulated in the N-doped graphitic shell is well preserved, even after loading Co_3O_4 onto the C2N framework via the hydrothermal process. As observed in bright-field (BF)-scanning transmission electron microscope (STEM) image, nanoparticles with a uniform particle size of ~15nm are well dispersed on the C2N matrix (Figure 3-2a). To investigate the chemical information of each nanoparticles, we performed an electron energy loss spectroscopy (EELS) spectrum image (SI) analysis. Figure 3-2b shows the EELS elemental mapping images of C-K, N-K, Fe-$L_{2,3}$, Co-$L_{2,3}$, and O-K edges. Fe and Co oxide nanoparticles on the carbon matrix with a nitrogen is clearly identified. The energy dispersive X-ray spectroscopy (EDS) investigation also shows the corresponding elemental distribution of NP Co_3O_4/ Fe@C_2N in Figure 3-3. The mass percentages of Co and Fe atoms in NP Co_3O_4/ Fe@C_2N are determined to be approximately 40.5 wt.% and 3.9 wt.%, respectively, based on inductively coupled plasma mass spectrometry measurements. The HR-TEM images present the NP Co_3O_4/ Fe@C_2N in Figure 3-2c, and nanoparticle Co_3O_4 (red circle) and Fe@C_2N (blue circle) in Figure 3-2d and 3-2e, respectively. In Figure 3-2d, the measured adjacent interlayer distance of 0.47 nm corresponds to the spacing of the (111) planes of Co_3O_4, which is consistent with XRD result. Combining the structural and morphological information confirmed by HR-TEM and STEM in Figure 3-2b, 3-2c and 3-2d, the Co_3O_4 nanostructures on the C2N

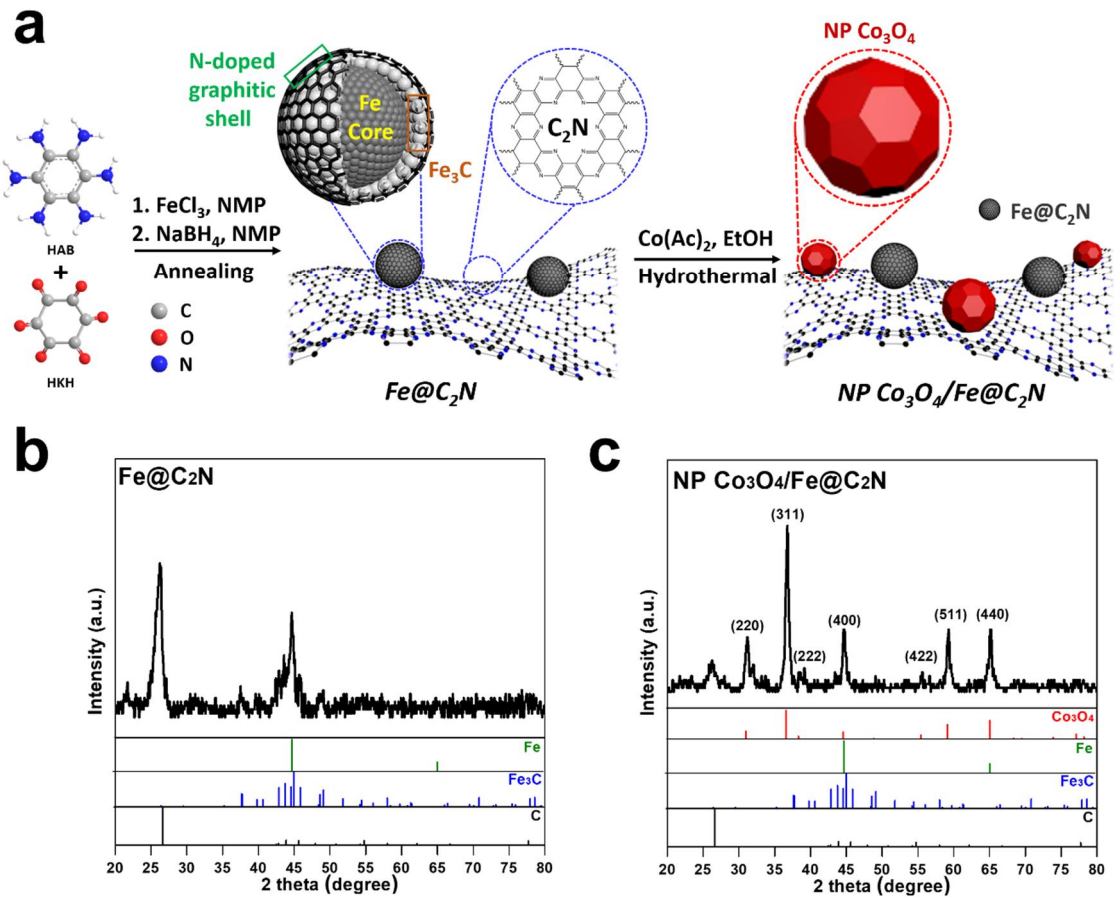

Figure 3-1 (a) Schematic illustration of the fabrication of Fe@C_2N and NP Co¬3O4/ Fe@C_2N nanocomposites via an annealing and hydrothermal strategy. XRD patterns of (b) Fe@C_2N and (c) NP Co_3O_4/ Fe@C_2N.

framework are well-distributed. Figure 3-2e presents the neighboring interlayer distance of 0.206 nm, which is well matched to the (110) planes of metallic Fe. Moreover, the d-spacing of the encapsulating shells is 0.346 nm, which matches that of the graphitic layer. The structural analysis, thus, confirms that Fe nanoparticles encapsulated in the N-doped graphitic shell and NP Co_3O_4 are uniformly distributed and successfully loaded on the C2N framework.

3.3.2. Electrocatalytic activities

To evaluate the electrochemical properties for ORR of the successfully synthesized NP Co_3O_4/Fe@C_2N, rotating ring-disk electrode investigation was performed in an O_2- or N_2-saturated 0.1 M KOH solution. In Figure 3-4a, cyclic voltammetry (CV) was conducted on Fe@C_2N, NP Co_3O_4/Fe@C_2N, and commercial Pt/C. The apparent cathodic reduction peaks in Figure 3-4a are the effects on the catalyzed ORR, in contrast with the curves recorded in the N_2 atmosphere, which exhibited no peaks. Fe@C_2N and NP Co_3O_4/Fe@C_2N show reduction peaks at 0.847 V and 0.870 V, respectively, which are comparable with that of Pt/C (0.862 V). The CV results agree well with those of linear sweep voltammetry (LSV), with 1,600 round per minute (rpm) at a scan rate of 10 mV s^{-1} (Figure 3-4b). The onset and half-wave potentials of NP Co_3O_4/Fe@C_2N are comparable to those of benchmark Pt/C (namely, 0.93 V *versus* 0.94 V and 0.89 V *versus* 0.87 V, respectively). Interestingly, anchoring NP Co_3O_4 with Fe@C_2N slightly increased the onset and half-wave potentials compared to those of

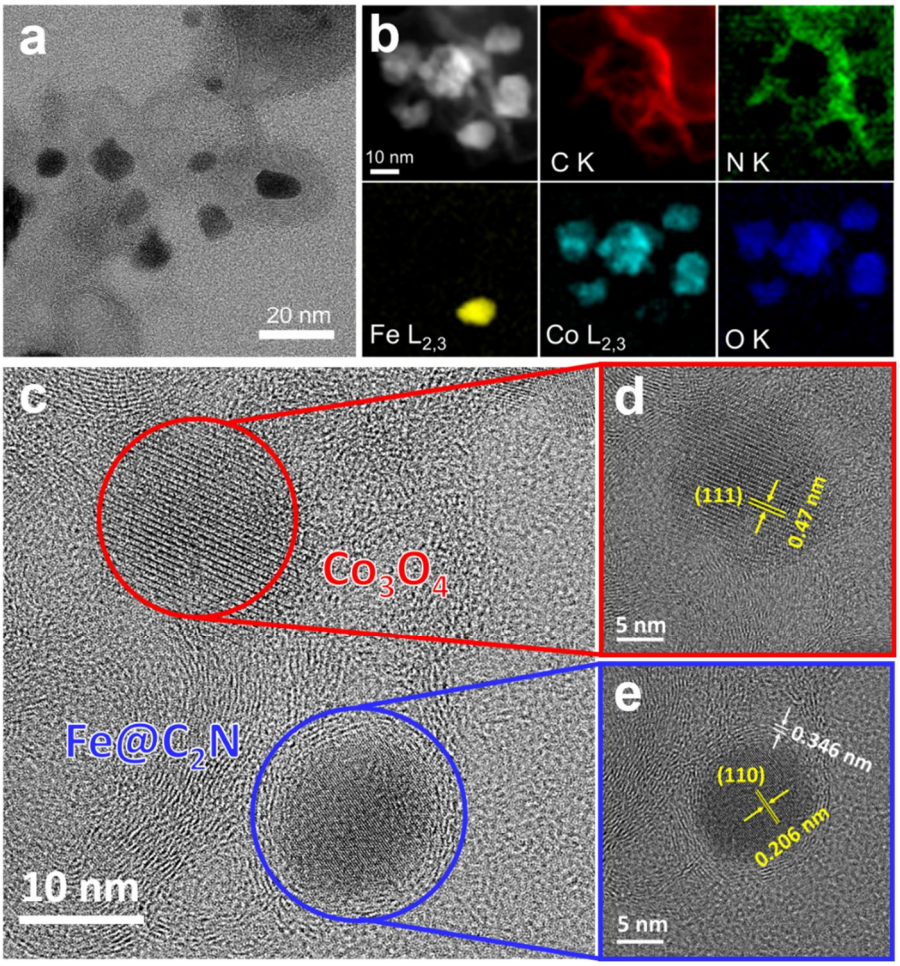

Figure 3-2 (a) Bright-field (BF) STEM image of Co_3O_4/ Fe@C_2N. (b) High-angle annular dark-field (HAADF) STEM image and electron energy loss spectroscopy (EELS) elemental mapping images of C K, N K, Fe $L_{2,3}$, and Co $L_{2,3}$ edges of Co_3O_4/ Fe@C_2N. (c) High-resolution (HR) TEM image of Co_3O_4/ Fe@C_2N. Magnified images of (d) Co_3O_4 and (e) Fe@C_2N.

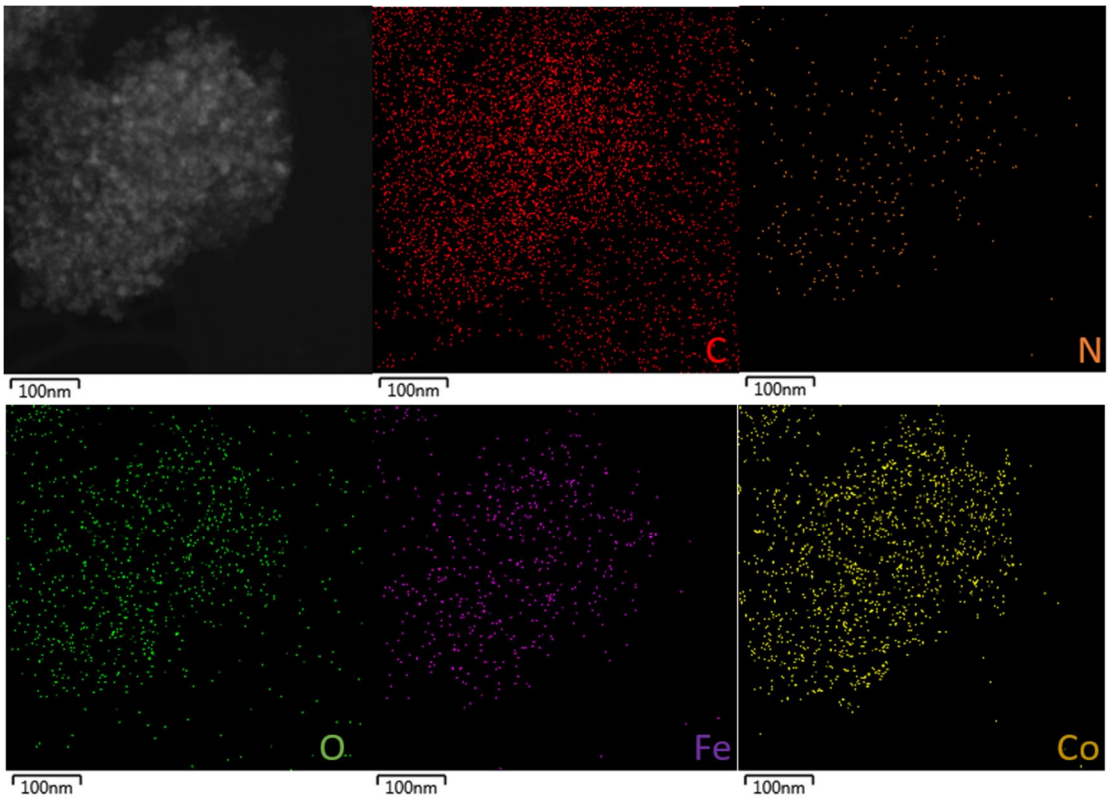

Figure 3-3 (a) Schematic illustration of the fabrication of Fe@C_2N and NP Co_3O_4/Fe@C_2N nanocomposites via an annealing and hydrothermal strategy. XRD patterns of (b) Fe@C_2N and (c) NP Co_3O_4/Fe@C_2N.

Fe@C_2N or Co_3O_4 alone (Figure 3-5); thus, this is the report on the synergistic coupling between NP Co_3O_4 and the C_2N network to increase the ORR activity of the hybrid catalyst. In addition, the ORR electrochemical activities vary depending on the amount of Co_3O_4 loaded onto the Fe@C_2N framework, as shown in Figure 3-6; thus, we selected the 0.125 M Co_3O_4/Fe@C_2N as the optimized NP Co_3O_4/Fe@C_2N catalyst concentration. In order to gain further insights into the ORR electrochemical properties, the catalytic activities of each catalyst were further analyzed using Tafel plots, as shown in Figure 3-4c. NP Co_3O_4/Fe@C_2N exhibits a smaller Tafel slope and overpotential than those of Fe@C_2N. Notably, the Tafel slope of NP Co_3O_4/Fe@C_2N (83 mV dec^{-1}) is comparable to that of Pt/C (68 mV dec^{-1}), indicating that NP Co_3O_4/Fe@C_2N with a small Tafel slope can reach quickly to the limiting current region. The yield of peroxide species (HO_2^-) for the NP Co_3O_4/Fe@C_2N catalyst remained below ~10% over the entire potential range, and the calculated *n* value was above 3.84 within the potential window of 0.3–0.8 V *versus* RHE, indicating that the NP Co_3O_4/Fe@C_2N exhibits a highly efficient four-electron ORR, even more efficient than that of Fe@C_2N or Co_3O_4 (Figure 3-7). Although Fe@C_2N has a larger surface area from Brunauer-Emmett-Teller (BET) (338.13 $m^2 g^{-1}$, Figure 3-8) than that of NP Co_3O_4/Fe@C_2N (121.33 $m^2 g^{-1}$, Figure 3-8), the electrochemically effective surface area (ECSA) of NP Co_3O_4/Fe@C_2N is nearly 25% larger than that of Fe@C_2N, as estimated from the electrochemical double-layer capacitances, C_{dl} (4.25 mF cm^{-2} and 3.42 mF cm^{-2} for NP Co_3O_4/Fe@C_2N

and Fe@C_2N, respectively), from the CV analysis, as shown in Figure 3-9.[31] Recent researches suggest that the junction sites where Co_3O_4 is anchored onto a N-doped carbon species are responsible for the high electrochemical activities. Such the charge transfer in the junction sites is believed to be the main reason why the metal oxide-carbon catalysts possess high electrochemical activity such as Co_3O_4/GN, CoO/CNT, and Co_3O_4/ON-CNW.[21,22,32] Therefore, the different ECSA values of NP Co_3O_4/Fe@C_2N can be ascribed to not simply the increased electrical conductivity, but also the induced junction sites from the synergistic interaction between strongly interacted Co_3O_4 and carbon species.[33] These increased ECSA values indicate that anchoring Co_3O_4 nanoparticles onto the C_2N framework is likely to induce more electrochemically active sites, which accelerate the overall catalytic performance. In addition to the high activity, NP Co_3O_4/Fe@C_2N also exhibits considerable catalytic electrochemical

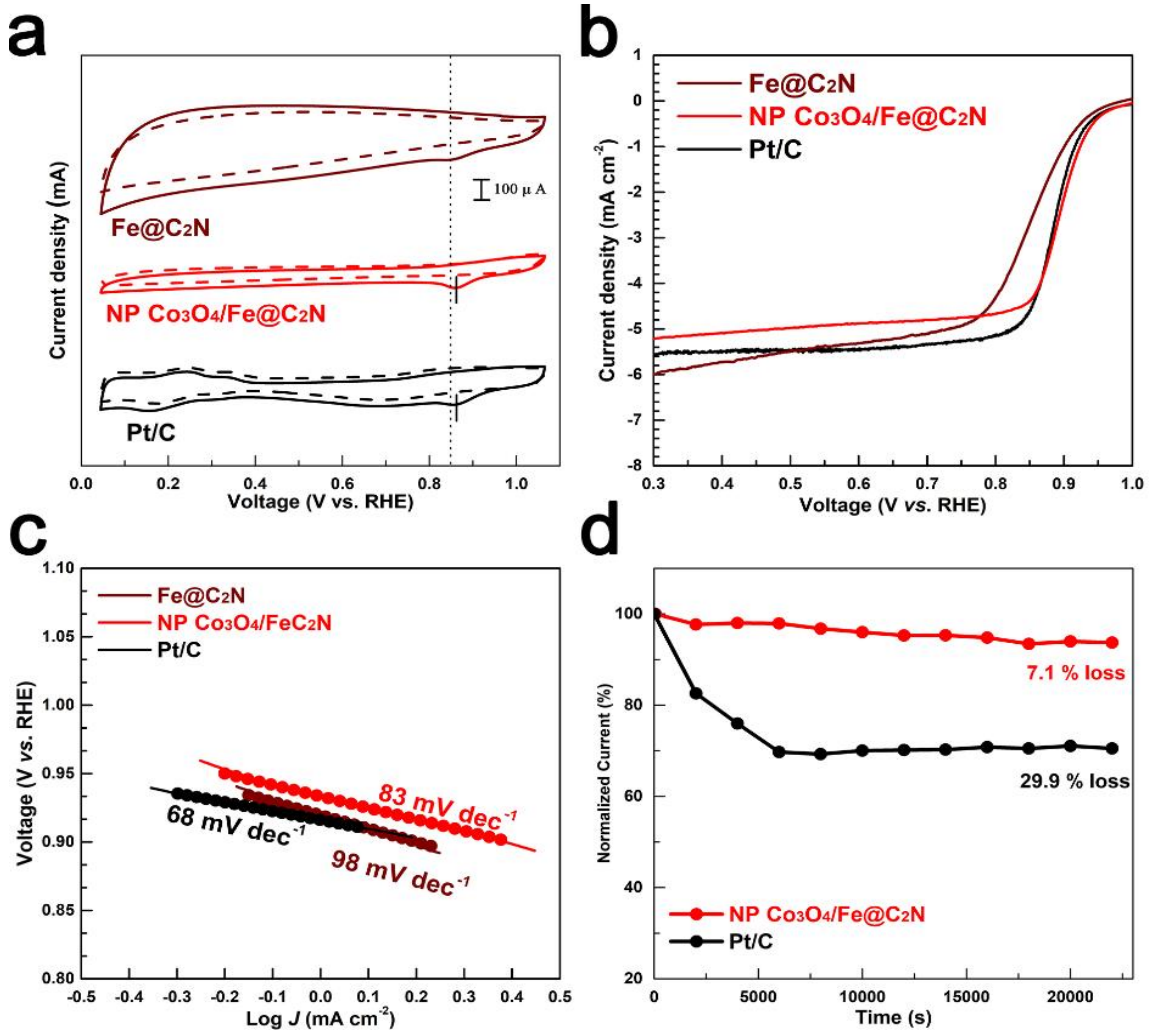

Figure 3-4 (a) CV curves in N_2-saturated (dash line) and O2-saturated (solid line) 0.1 M KOH solution, (b) LSV at 1600 rpm in O_2-saturated 0.1 M KOH solution and (c) Tafel plots for Fe@C_2N, NP Co_3O_4/ Fe@C_2N, and Pt/C. (d) chronoamperometric profile of NP Co_3O_4/ Fe@C_2N compared to that of Pt/C at 0.6 V vs. RHE.

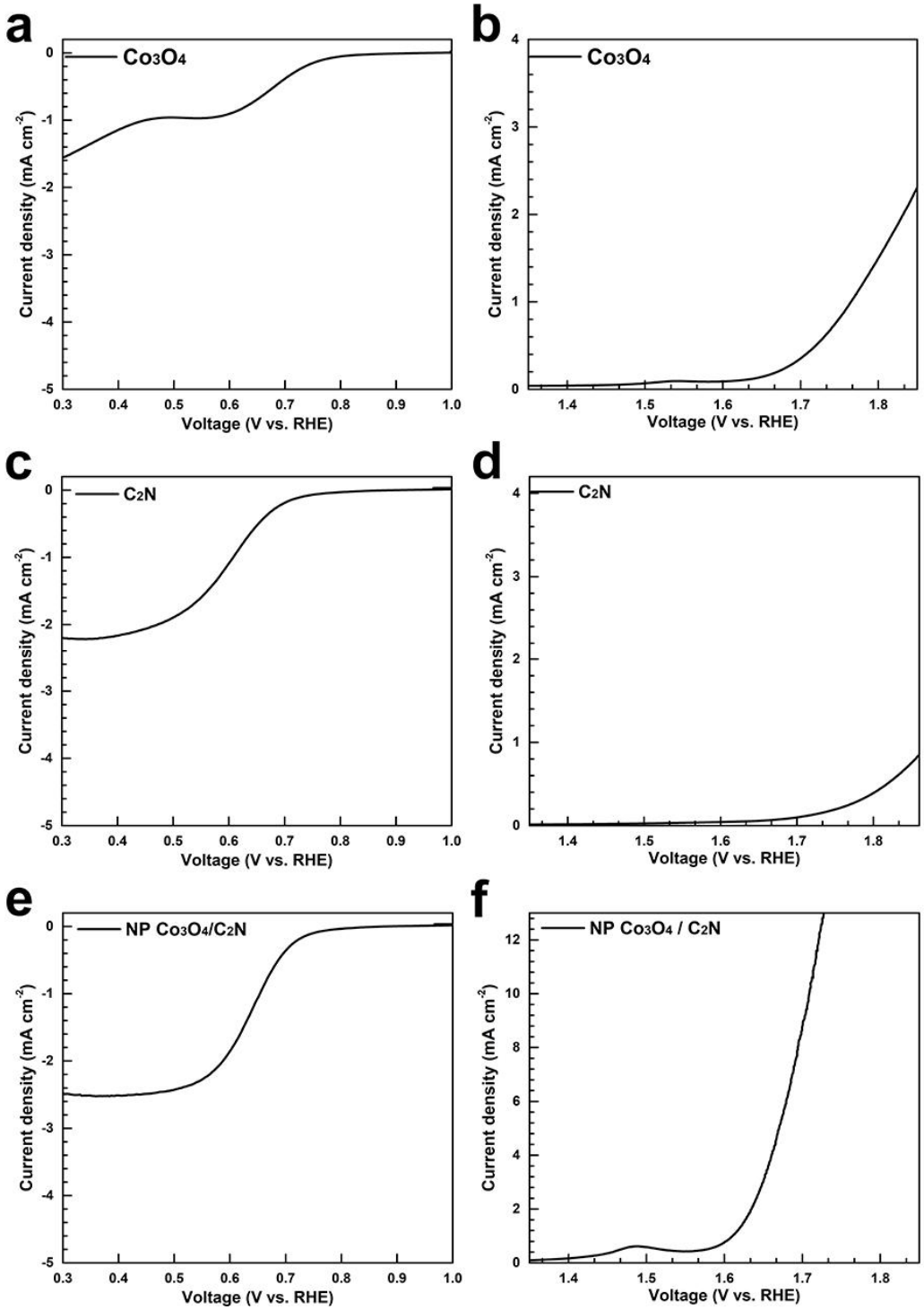

Figure 3-5 LSV at 1600 rpm in O_2-saturated 0.1 M KOH solution for ORR of a) Co_3O_4, c) C_2N, and e) NP Co_3O_4/C_2N, and for OER of b) Co_3O_4 , d) C_2N, and f) NP Co_3O_4/C_2N catalyst.

tolerance. The chronoamperometric ORR current of NP Co_3O_4/Fe@C_2N maintains about 93% of its initial value after a consecutive polarization period of 22,500 s, thus outperforming commercial Pt/C (~70 %, Figure 3-4d). The excellent activity and durability of NP Co_3O_4/Fe@C_2N result from the synergistic contribution of the well-ordered nitrogenated graphitic shells protecting the Fe nanoparticle cores and the specific interaction between nitrogen and NP Co_3O_4 particles (as shown in further detail

in Figure 3-10).

Regarding the development of bifunctional catalysts for rechargeable metal-air batteries (Zn and Li), the OER electrochemical performance of the catalyst was also investigated under the same conditions as those of the ORR measurements. In Figure 3-10a and 3-5b, two oxidation curves can be seen at 1.45–1.55 V and above 1.6 V, assigned to the $Co^{4+/3+}$ oxidation and OER processes, respectively.[34] In the LSV profiles for the OER, NP Co_3O_4/Fe@C_2N presents an overpotential of 0.43 V at a current density of 10 mA cm^{-2}, which is 86 mV smaller than that of IrO_2 (Table 3-1). Moreover, as indicated by the Tafel plots in Figure 3-10b, the Tafel slopes of NP Co_3O_4/Fe@C_2N, Fe@C_2N, and IrO_2 are 103, 312, and

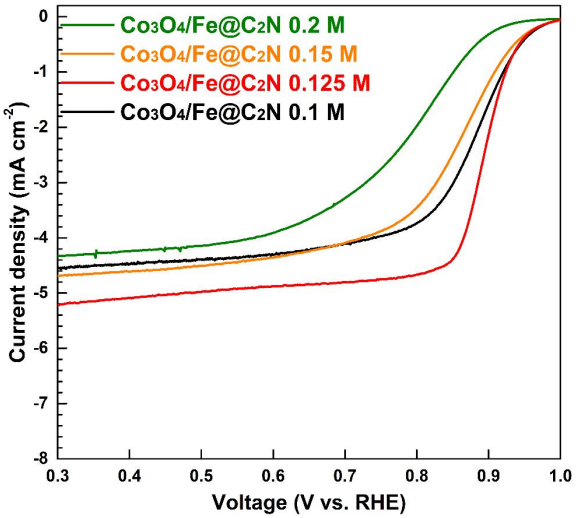

Figure 3-6 LSV at 1600 rpm in O_2-saturated 0.1 M KOH solution with the different concentration of $Co(Ac)_2$ aqueous solution.

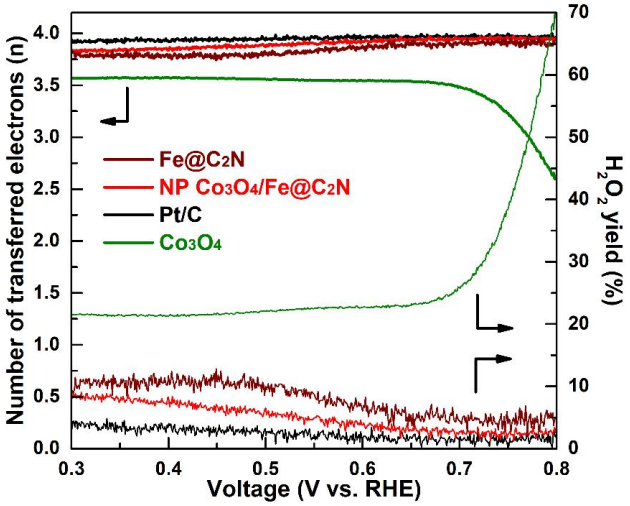

Figure 3-7 The number of transferred electrons (n) and peroxide yield recorded with Fe@C_2N, NP Co_3O_4/Fe@C_2N, Pt/C, and Co_3O_4 catalysts at 1600 rpm in O_2-saturated 0.1 M KOH solution.

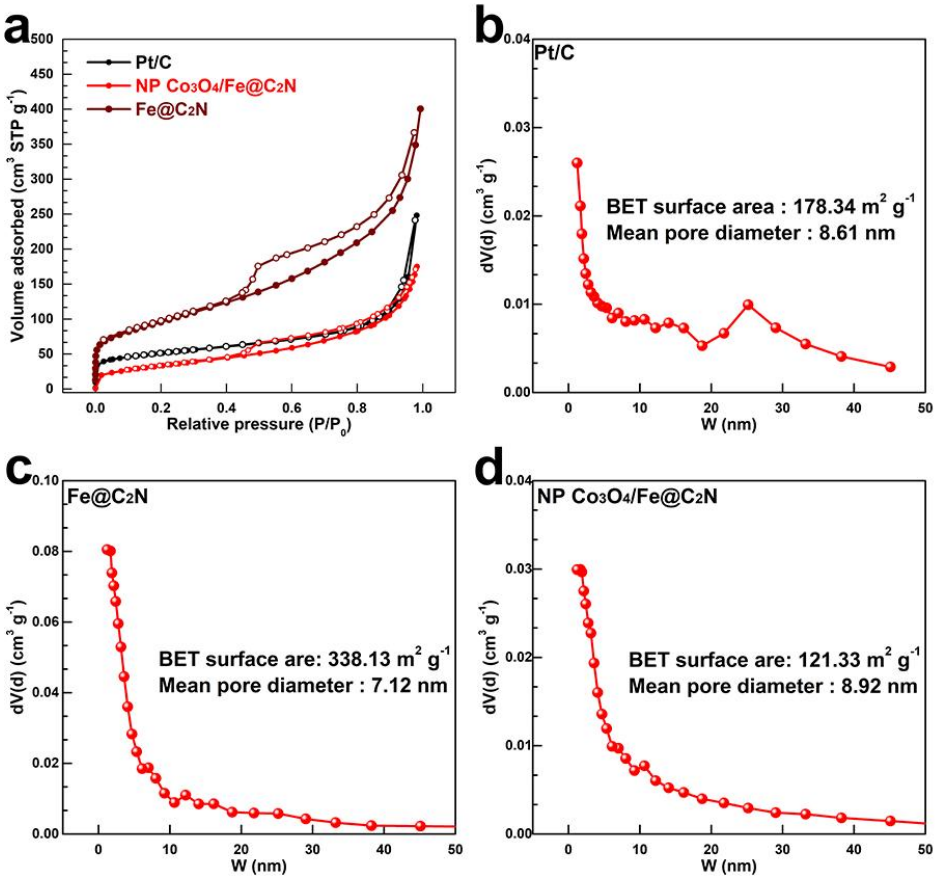

Figure 3-8 a) N_2 adsorption/desorption isotherms of Fe@C_2N, NP Co_3O_4/Fe@C_2N, and Pt/C. b-d) the pore size distribution of Pt/C, Fe@C_2N, and NP Co_3O_4/Fe@C_2N. The Brunauer-Emmett-Teller (BET) specific surface areas are 178.3, 338.1, and 121.3 m^2 g^{-1} for Pt/C, Fe@C_2N, and NP Co_3O_4/Fe@C_2N, which are calculated by the results of N_2 adsorption/desorption isotherms.

114 mV dec^{-1}, respectively, corresponding to electroactivities following the order of NP Co_3O_4/Fe@C_2N > IrO_2 > Fe@C_2N. In OER electrochemical process, the Fe@C_2N and C_2N show low electrochemical activities for OER in Figure 3-10a and 3-5d. However, after loading the Co_3O_4 on each catalyst, the electrochemical performance of both of them is improved, indicating that the Co_3O_4 is the main active sites for the OER process. Therefore, for the NP Co_3O_4/Fe@C_2N catalyst, the ORR progress is mainly caused by Fe@C_2N and supported by Co_3O_4 on C_2N substrate whereas the OER progress is mainly caused by Co_3O_4 on C_2N substrate. Interestingly, the OER performance stability results of the physical mixture of commercial Co_3O_4 and Fe@C_2N (denoted by composite Co_3O_4+Fe@C_2N) and hydrothermally synthesized NP Co_3O_4/Fe@C_2N show totally different tendencies (Figure 3-4c and 3-4d) in spite of similar morphology (Figure 3-11). The current density of composite Co_3O_4+Fe@C_2N at 1.7 V continuously decreases over 100 sequential scans in the range of 1.25–1.7 V *versus* RHE (Figure 3-10c) by a total of 21%. In striking contrast, the hydrothermally synthesized catalyst, NP Co_3O_4/Fe@C_2N, exhibits no degradation under the same conditions. These results represent evidence of its superior electrochemical tolerance for long-term electrochemical operation. Charge-transfer

resistance (R_{ct}) values of 2.5, 173.4, and 21.5 Ω cm^{-2} were fitted from the electrochemical impedance spectrum for NP Co_3O_4/Fe@C_2N, Fe@C_2N, and IrO_2, respectively (Table 3-1). This coinciding tendency indicates that the enhanced charge-transfer property of NP Co_3O_4/Fe@C_2N is strongly correlated with its superior catalytic activity and reaction kinetics for the OER process. Moreover, the chronopotentiometric profile of each catalyst was measured at a constant current density of 1.0 mA cm^{-2} in order to observe their long-term stabilities, as shown in Figure 3-10f. The overpotential of NP Co_3O_4/Fe@C_2N catalyst did not obviously change, whereas those of IrO_2 and Fe@C_2N increased after 5,000 s, thus confirming the structural stability of NP Co_3O_4/Fe@C_2N. The electrochemical performance of NP Co_3O_4/Fe@C_2N for both the OER and the ORR suggests its prospect as a bifunctional electrochemical catalyst.

Table 3-1. Comparison of electrocatalytic performance of each catalyst

catalyst	ORR[a]				OER[b]			
	E_{onset} [V]	E_{half} [V]	I_d [mA cm^{-2}]	*Tafel slope* [mV dec^{-1}]	η [mV]	I_S [mA cm^{-2}]	*Tafel slope* [mV dec^{-1}]	R_{ct} [Ω]
Fe@C_2N	0.89	0.84	-5.96	98	-	0.59	312	173.4
NP Co_3O_4/Fe@C_2N	0.93	0.89	-5.22	83	432	21.5	103	2.5
Pt/C	0.94	0.87	-5.54	68	-	-	-	-
IrO_2	-	-	-	-	518	6.92	114	21.5

[a] E_{onset}, E_{half}, and I_d presents onset potential, half-wave potential, and limiting current density in ORR progress. [b] η is the overpotential (mV) at 10 mA cm^{-2} from 1.23 V *vs.* RHE, I_s is the specific OER current density and R_{ct} is the charge-transfer resistance at 1.70 V *vs.* RHE.

3.3.3. Electrochemical characterization

To identify the synergistic contribution of NP Co_3O_4 and Fe@C_2N in improving the ORR/OER electrochemical performance, X-ray photoelectron spectroscopy (XPS) was carried out (Figure 3-12). The oxidation states or the electronic configuration of each element are normally investigated by XPS measurements. The XPS spectrum of NP Co_3O_4/Fe@C_2N in Figure 3-12a shows the elemental composition of C, N, O, Fe, and Co. The high-resolution XPS spectrum for C 1s was deconvoluted into three major peaks at 284.3 eV (C=C sp^2), 286.0 eV (C–N), and 288.3 eV (C-heteroatom), as shown in Figure 3-12b.[26,35] In Figure 3-12c, the peaks at 720.0 eV for Fe $2p_{1/2}$ and 707.1 eV for Fe $2p_{3/2}$ indicate the presence of metallic Fe in the Fe@C_2N.[26] These characterizations confirmed that the C_2N framework and Fe encapsulated in graphitic layers were successfully synthesized. In order to investigate the specific interaction between Co_3O_4 and the C_2N network *via* hydrothermal synthesis, we compared NP Co_3O_4/Fe@C_2N to the composite Co_3O_4+Fe@C_2N (Figure 3-12d,e,f). The deconvoluted high-resolution XPS spectrum of N 1s (Figure 3-12d) shows that the deconvoluted two peaks, namely, N-

pyrazine like coordinated with metal at 400.2 eV and N-pyrazine like at 398.1 eV, which is similar to the results in our previous research.[35] Interestingly, considering the intensity of the peaks, the N-pyrazine like coordinated with a metal peak in NP Co_3O_4/Fe@C_2N shows a ratio of 52.6%, which is higher than that of composite Co_3O_4+Fe@C_2N (47.6%). During the hydrothermal synthesis loading Co_3O_4 on C_2N framework, the nitrogen-doped carbon support, C_2N, provides responsible anchoring sites for the self-growth of metal oxide nuclei, resulting in a higher ratio of N-pyrazine like coordinated with a metal peak than a physically mixed composite Co_3O_4+Fe@C_2N.[36-38] In addition, we have further investigated the XPS spectrum of N 1s for the detailed comparison as shown in Figure 3-13. In Figure 3-13a-c, we compared the ratio of N-pyrazine like coordinated with a metal peak from the XPS results of NP Co_3O_4/Fe@C_2N, Fe@C_2N, and C_2N material. After loading Co_3O_4 on Fe@C_2N *via* hydrothermal process, the ratio of N-pyrazine like coordinated with a metal in NP Co_3O_4/Fe@C_2N catalyst is increased to 52.6 % from 37.1 % for that of Fe@C_2N. Although the ratio of N-pyrazine like coordinated with a metal has increased after doping with Fe in C_2N compared to C_2N, the increased ratio for NP

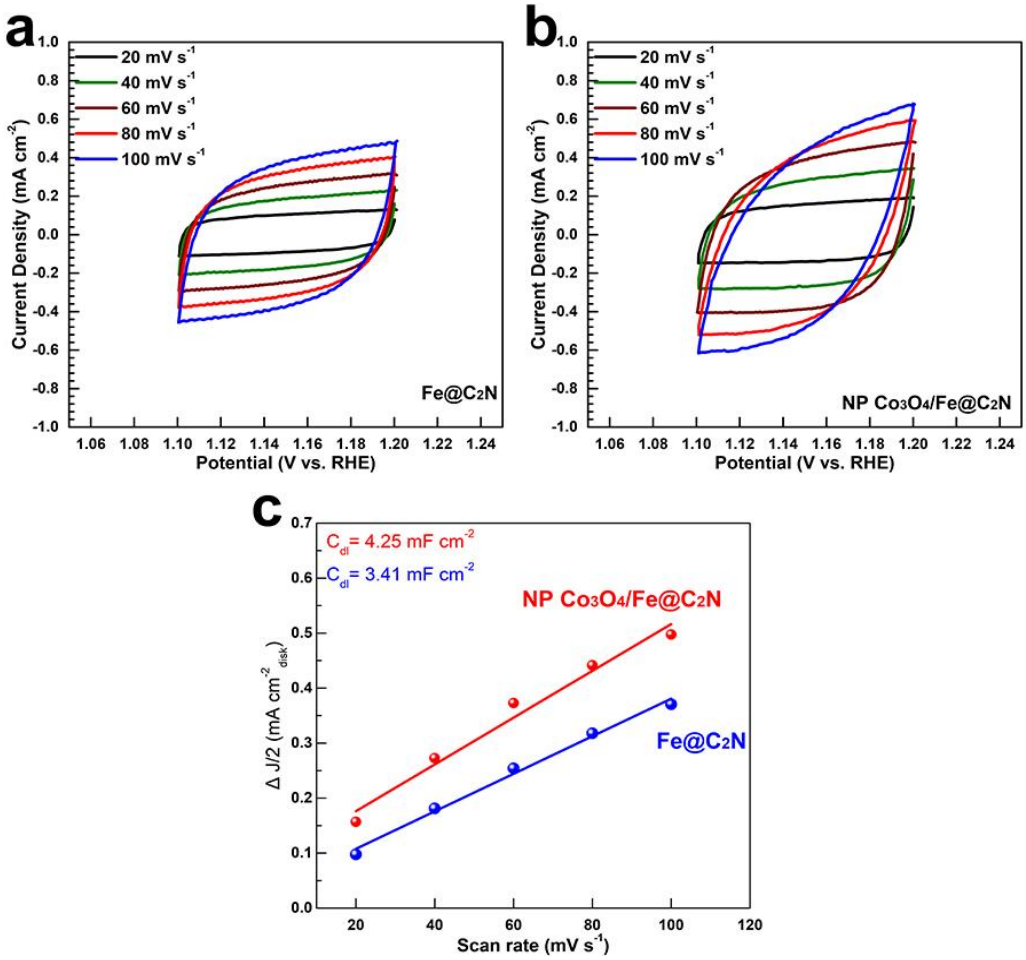

Figure 3-9 Electrochemical CV scans recorded for a) Fe@C_2N and b) NP Co_3O_4/Fe@C_2N catalysts at different potential scanning rates. Scan rates are 20, 40, 60, 80, and 100 mV s^{-1}. The selected potential range where no faradic current was observed is 1.10 to 1.20 V vs. RHE. c) plot of half of the current density at 1.15 V *vs.* the scan rate.

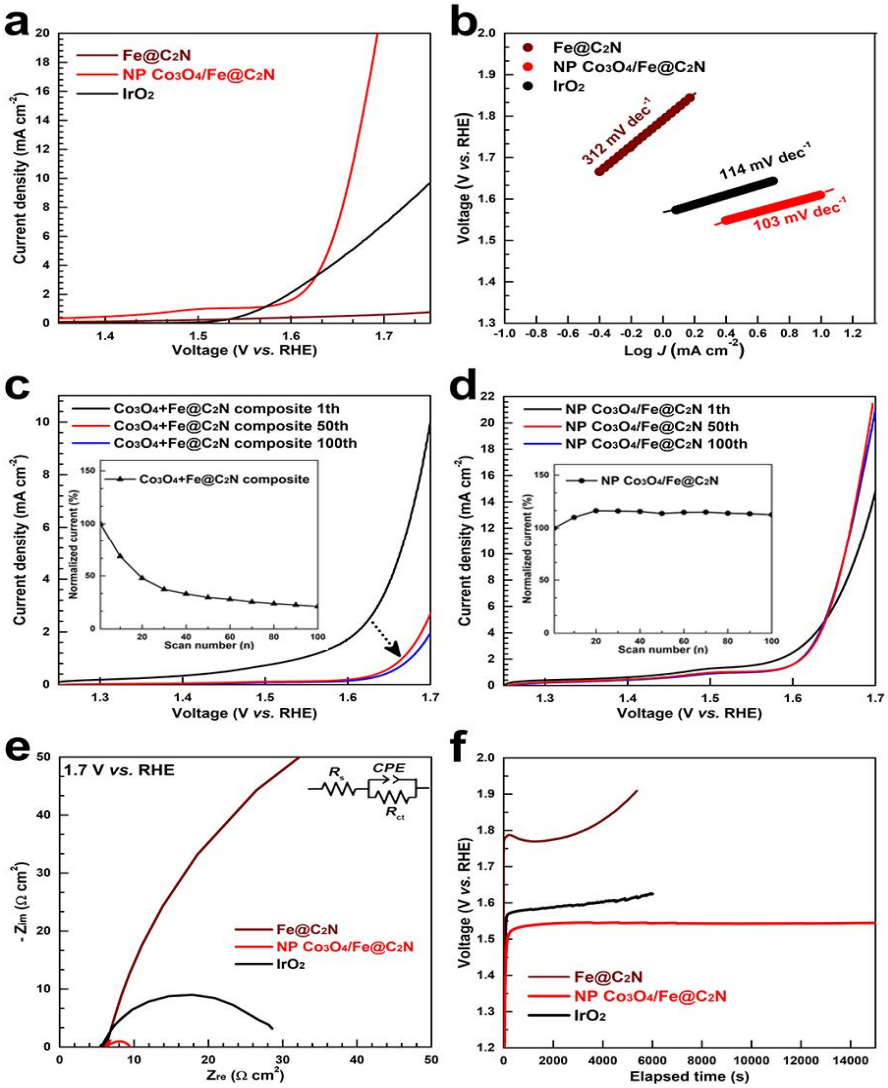

Figure 3-10 a) LSV plots for OER and b) Tafel plots of Fe@C_2N, NP Co_3O_4/ Fe@C_2N, and IrO2 after ten consecutive scans. LSV curves for OER of c) Co_3O_4+ Fe@C_2N composite and d) NP Co_3O_4/ Fe@C_2N for 100 cycle measurements. The insets in (c) and (d) show the normalized current densities along 100 consequent scans at 1.7 V vs. RHE at each sample. e) EIS curves at 1.7 V vs. RHE of Fe@C_2N, NP Co_3O_4/ Fe@C_2N, and IrO2. Inset represents the equivalent circuit used to fit the experimental data where Rs is electrolyte resistance, CPE is double layer capacity, and Rct is charge transfer resistance). f) Chronopotentiometry profile of NP Co_3O_4/ Fe@C_2N, and IrO2 at a constant current density of 1.0 mA cm^{-2}.

Co_3O_4/Fe@C_2N after loading C o_3O_4 on Fe@C_2N is evidence of the additional specific interaction between Co_3O_4 and the C_2N network through hydrothermal synthesis, which increases the electrochemical activities and stabilities during the ORR and OER processes. Furthermore, in Figure 3-13d-f, there is no change of the ratio after hydrothermal process without Co_3O_4 with Fe@C_2N (denoted by hydrothermal Fe@C_2N) compared to Fe@C_2N catalyst. Therefore, it can be concluded the different ratio between NP Co_3O_4/Fe@C_2N and Fe@C_2N is caused by anchoring between the Co_3O_4 and C_2N framework. Moreover, the comparing level of Fe and N contents between Fe@C_2N and NP

Co_3O_4/Fe@C_2N is important to clarify the electrochemical activities. Based on the XPS measurements, we have compared the ratio of elements in each sample and all elements atomic ratio were shown in the Table 3-2. After the hydrothermal process with Co_3O_4 and Fe@C_2N, the ratio of C, N, Fe decreases slightly, which is caused by loading Co_3O_4 on the substrate. The ratio of C/Fe shows similar values between Fe@C_2N and NP Co_3O_4/Fe@C_2N, and it means that there is no amount of loss of Fe during the loading Co_3O_4 synthesis. However, the ratio of Fe/N and C/N is small increased after the hydrothermal process, which is indicating the partial loss of N in the substrate during loading Co_3O_4 process. Fe-Nx or Nx-C is well known as an ORR active sites, and although there is a slight loss of N in NP Co_3O_4/Fe@C_2N, interestingly, the ORR performance of NP Co_3O_4/Fe@C_2N catalyst was improved than Fe@C_2N.[14,26,27] This improved electrochemical activities in this study may have been attributed to the junction sites at which Co_3O_4 is anchored onto a N-doped carbon substrate. Meanwhile, the Co 2p spectrum of each sample displays two major peaks at 795 and 780 eV, corresponding to the binding energies of Co $2p_{1/2}$ and Co $2p_{3/2}$, respectively (Figure 3-12e). Co $2p_{1/2}$ peak has deconvoluted to the binding energies of $2p_{1/2}$ of Co^{2+} and Co^{3+} and the Co $2p_{3/2}$ peak also has deconvoluted to the binding energies of $2p_{1/2}$ of Co^{2+} and Co^{3+}. The relative area ratio of Co^{3+} t o Co^{2+} in NP Co_3O_4/Fe@C_2N is slightly higher (2.3) than that of composite Co_3O_4+Fe@C_2N (2.2), indicating that more exposed Co atoms are in the oxidation state of Co^{3+} on the surface of Co_3O_4 in NP Co_3O_4/Fe@C_2N. The high ratio of Co^{3+} on the surface of Co_3O_4 indicates that a strong interaction exists between Co_3O_4 and C_2N framework and consequently leads to a lower electron density at the Co atom through interfacial Co-N-C bonding.[39] The migration of Co electron could be induced by the strong electronegative between C

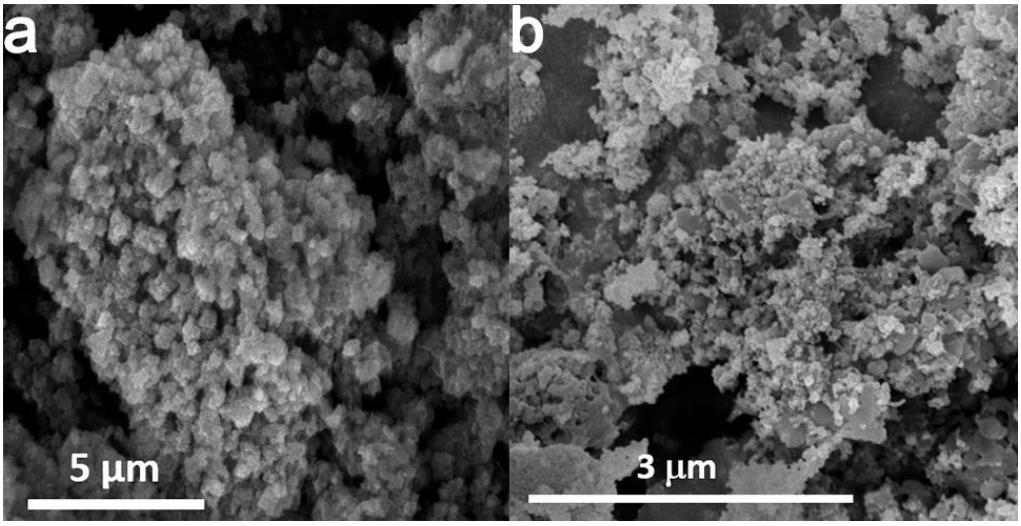

Figure 3-11 SEM image of a) the NP Co_3O_4/Fe@C_2N and b) Co_3O_4+Fe@C_2N composite.

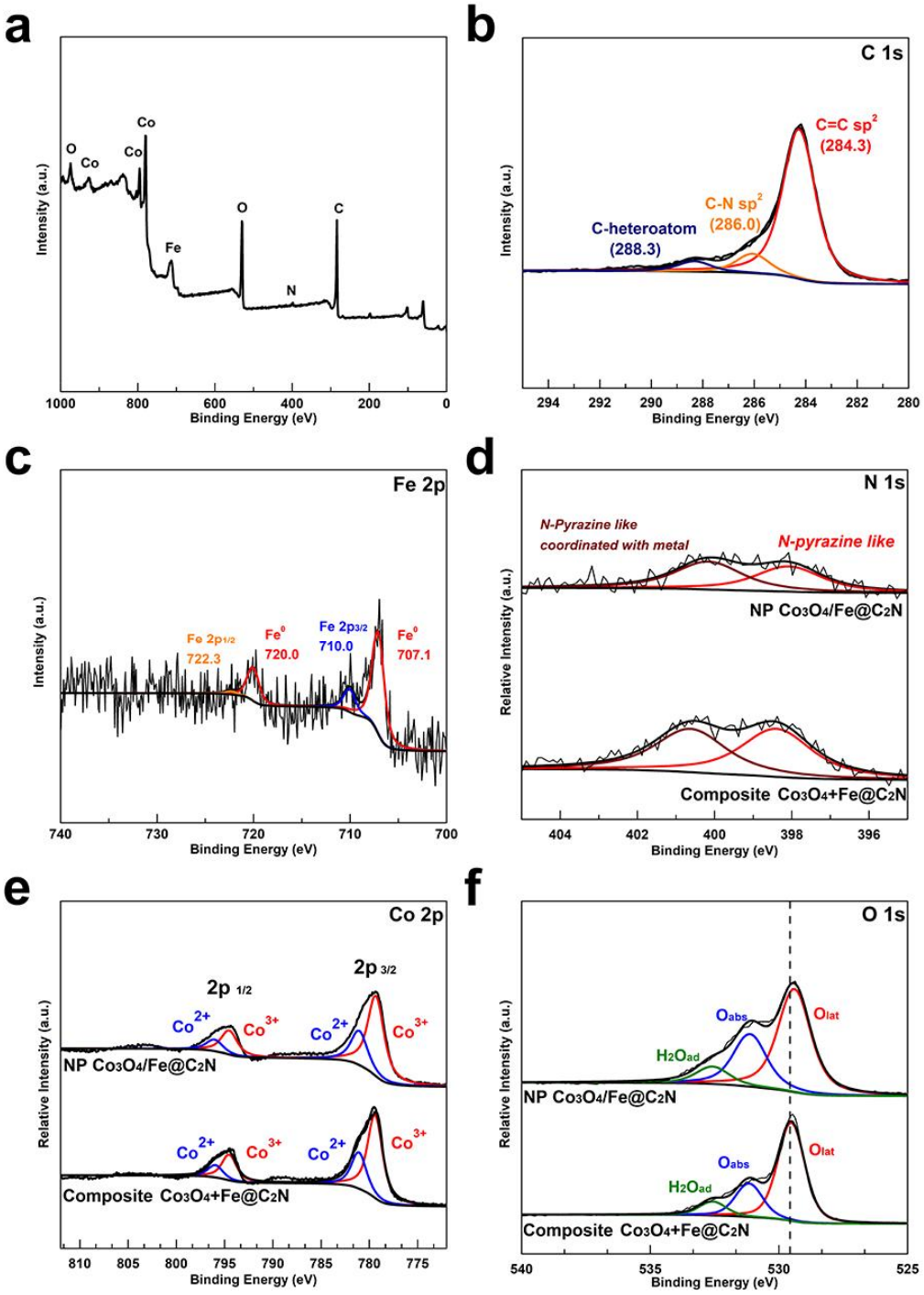

Figure 3-12 a) XPS survey spectrum, high-resolution XPS spectra of the b) C 1s, and c) Fe 2p in NP Co_3O_4/ Fe@C_2N, d) high-resolution XPS spectra of the d) N 1s, e) O 1s, and f) Co 2p in NP Co_3O_4/ Fe@C_2N and composite Co_3O_4+ Fe@C_2N.

and N, demonstrating the coupling electronic effect NP Co_3O_4 with C_2N framework.[20] This increased ratio of oxidation Co state is consistent with the specific interaction between Co_3O_4 and C_2N from XPS spectrum of N 1s. Therefore, the higher ratio of Co^{3+}/Co^{2+} provides more donor-acceptor reduction sites, which is an important factor for the ORR and OER, and is expected to increase the catalytic activities of NP Co_3O_4/Fe@C_2N.[4,40] The O 1s spectra show three main peaks representing lattice oxygen ($O_{lattice}$),

adsorbed oxygen species (O_{ad}), and adsorbed H_2O (H_2O_{ad}), as shown in Figure 3-12f. Based on the fitted results, the relative contents ($O_{lattice}/O_{ad}$) of NP Co_3O_4/Fe@C_2N and composite Co_3O_4+Fe@C_2N are 1.94 and 2.93, respectively. According to the electroneutrality principle, an increase in the Co^{3+} ratio means a rise in the amount of oxygen vacancies and lead decreased ratio of $O_{lattice}/O_{ad}$, which is consistent with XPS spectrum analysis of N 1s and Co 2p in Figure 3-12d and 3-5e.[42,42] Notably, the lower $O_{lattice}/O_{ad}$ ratio in NP Co_3O_4/Fe@C_2N indicates that the interaction between the NP Co_3O_4/Fe@C_2N and surface oxygen-adsorbed species is strong, which facilitates the oxygen adsorption process, thus increasing the electrocatalytic reactivity.[43] Furthermore, the lower $O_{lattice}$ binding energy of NP Co_3O_4/Fe@C_2N is expected to improve the electron donor ability associated with the increased catalytic activity for the ORR, leading to synergistic coupling between NP Co_3O_4 and the C_2N network and high ORR activity.[40,44] These results reveal that NP Co_3O_4/Fe@C_2N exhibits specific interactions between the NP Co_3O_4 nanoparticles and the C_2N network, thus demonstrating synergistic electrochemical performance for both ORR and OER processes.

Table 3-2. Elemental atomic composition from XPS measurements

Sample	C %	N %	Fe %	Co %	O %	Total	Fe/N	C/N	C/Fe
Fe@C2N	66.25	13.35	2.93	-	17.47	100	0.22	4.96	22.61
NP Co3O4/Fe@C2N	61.73	7.67	2.72	7.74	20.14	100	0.35	8.05	22.69

3.3.4. Alkaline Metal (Zn, Li) -Air Batteries

The electrochemical performance of NP Co_3O_4/Fe@C_2N was evaluated with Zn–air batteries and hybrid Li-air batteries and compared with that of Pt/C+IrO_2 and Co_3O_4+Fe@C_2N composites for reference. All catalyst loading density was the same as 1 mg cm^{-2}, which is addressed in detail in Supporting information. Figure 3-14a shows the discharge and charge profiles of Zn–air batteries at various current densities in the range of 5–15 mA cm^{-2}. The Zn-air battery was assembled by using the gas diffusion layer loaded with each catalyst as the cathode, the metallic Zn plate as the anode, and a mixed aqueous solution of 6.0 M KOH and 0.2 M $Zn(ac)_2$ as the electrolyte (Figure 3-15a). The discharge voltage of NP Co_3O_4/Fe@C_2N is comparable to that of Pt/C+IrO_2, and the charge voltage of NP Co_3O_4/Fe@C_2N is even lower than that of Pt/C+IrO_2. At the highest current density (15 mA cm^{-2}), the NP Co_3O_4/Fe@C_2N catalyst exhibits an even lower charge–discharge overpotential gap (0.85 V) than that of the Pt/C+IrO_2 catalyst (1.01 V), which means that NP Co_3O_4/Fe@C_2N is more efficient during the charging process than Pt/C+IrO_2 and is comparable to the benchmark Pt/C+IrO_2, even in the high-

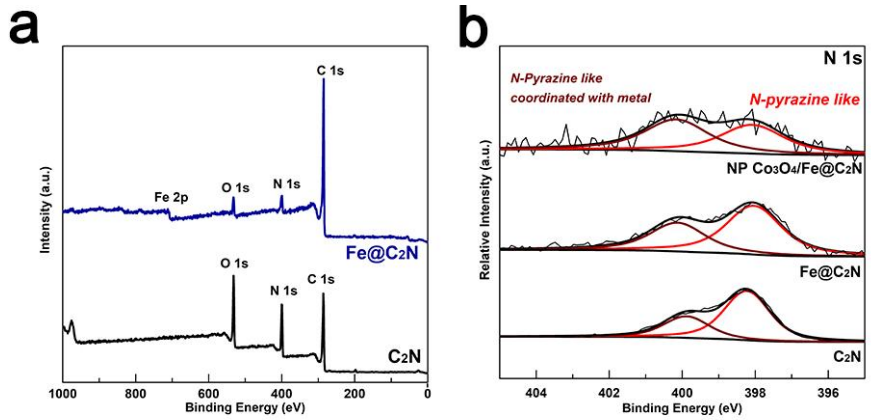

c

Sample	N-pyrazine like coordinated with metal	N-pyrazine like
NP Co3O4/Fe@C2N	52.64 %	47.36 %
Fe@C2N	37.12 %	62.88 %
C2N	30.47 %	69.53 %

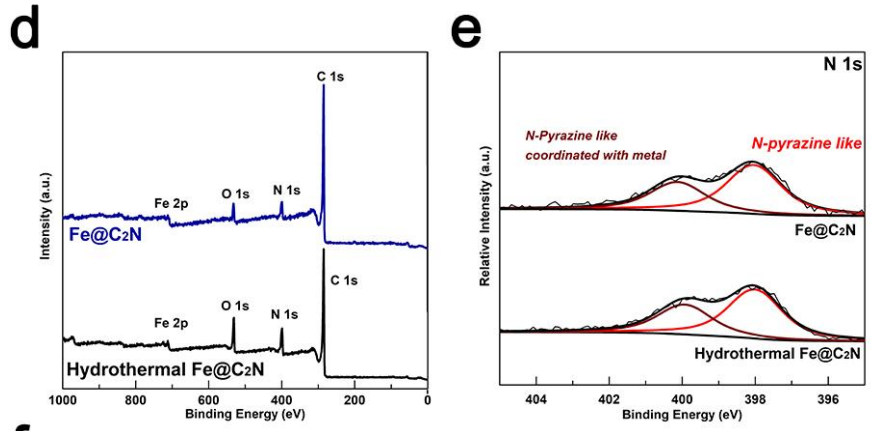

f

Sample	N-pyrazine like coordinated with metal	N-pyrazine like
Fe@C2N	37.12 %	62.88 %
Hydrothermal Fe@C2N	37.94 %	62.06 %

Figure 3-13 a) XPS survey spectrum for Fe@C_2N and C_2N. b) High-resolution XPS spectra of the N 1s in NP Co_3O_4/Fe@C_2N, Fe@C_2N, and C_2N. c) Detailed peak ratio in b). d) XPS survey spectrum and e) high-resolution XPS spectra of the N 1s for Fe@C_2N and Hydrothermal Fe@C_2N. f) Detailed peak ratio in e). 2p in NP Co_3O_4/ Fe@C_2N, d) high-resolution XPS spectra of the d) N 1s, e) O 1s, and f) Co 2p in NP Co_3O_4/ Fe@C_2N and composite Co_3O_4+ Fe@C_2N.

current-density region. Figure 3-14b shows the cycling performance of NP Co_3O_4/Fe@C_2N and Pt/C+IrO_2 at a constant current density of 2 mA cm^{-2} in ambient air. The Pt/C+IrO_2 catalyst shows continuous degradation over 350 min, with a substantial increase in the charge-discharge voltage gap from 0.64 to 0.85 V. This result is well matched with the vulnerability of Pt/C and IrO_2 during the ORR

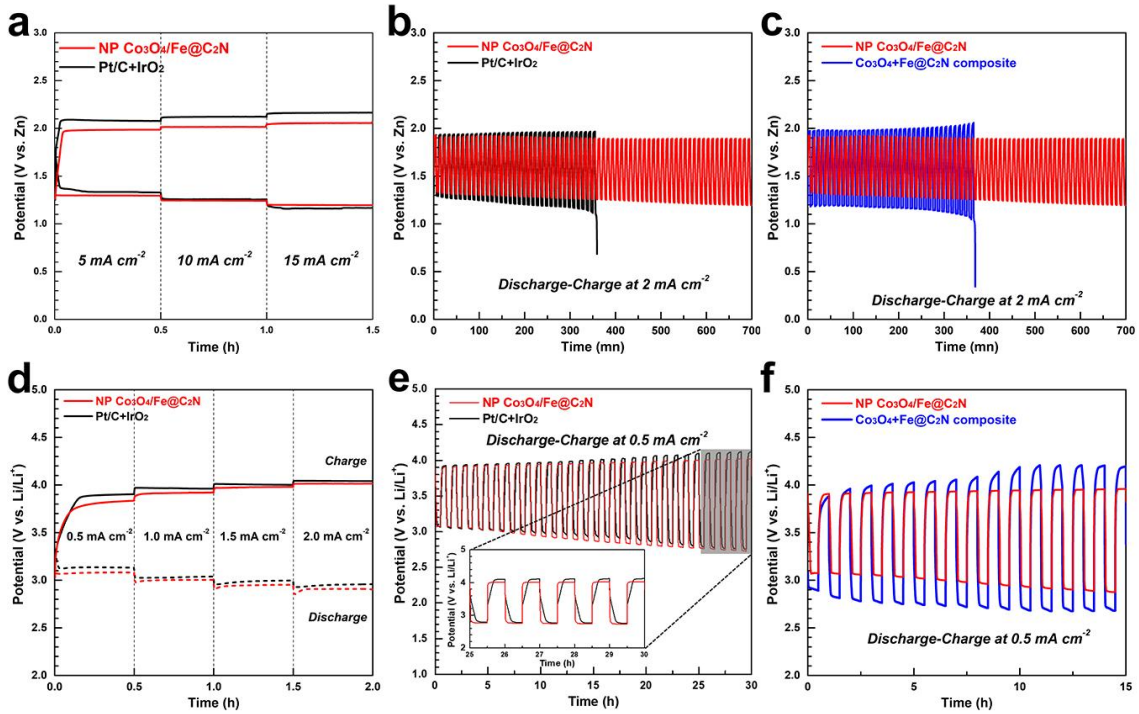

Figure 3-14 Full-cell performance of the NP Co_3O_4/ Fe@C_2N and Pt/C+IrO2 catalyst. a) First discharge-charge curves of Zinc-air cells for the NP Co_3O_4/ Fe@C_2N and Pt/C+IrO2 with different current densities in the range of 5-15 mA cm-2. b) Cycling performance of Zinc-air cells using b) NP Co_3O_4/ Fe@C_2N and Pt/C+IrO2, and c) NP Co_3O_4/ Fe@C_2N and Co_3O_4+ Fe@C_2N composite at a current density of 2 mA cm^{-2}. d) First discharge-charge curves of hybrid Li-air cells for the NP Co_3O_4/ Fe@C_2N and Pt/C+IrO2 with different current densities in the range of 0.5 – 2.0 mA cm-2. Cycling performance of hybrid Li-air cells using e) NP Co_3O_4/ Fe@C_2N and Pt/C+IrO2, and f) NP Co_3O_4/ Fe@C_2N and Co_3O_4+ Fe@C_2N composite at a current density of 0.5 mA cm^{-2}.

and OER processes. For NP Co_3O_4/Fe@C_2N, in contrast, an outstanding cycling performance was attained over 700 min without significant degradation of the charge-discharge voltage gap (from 0.57 to 0.63 V during a period of 700 min). The first discharge-charge curves and cycling performance without catalyst were also investigated as a reference (Figure 3-15b and 3-15c). In Figure 3-14c, the Co_3O_4+Fe@C_2N composite is also evaluated and compared to the NP Co_3O_4/Fe@C_2N catalyst. Similar to the ORR and OER electrochemical properties, the mixed Co_3O_4+Fe@C_2N composite continuously degrades during a cyclic test over 360 min. This electrochemical performance corresponds well with the results from the LSV curves. The discharge polarization curves and the corresponding power densities based on Pt/C+IrO_2, NP Co_3O_4/Fe@C_2N, and without catalyst were obtained in Figure 3-15d. The maximum power density using NP Co_3O_4/Fe@C_2N catalyst was 186.3 mW cm^{-2} at 189.5 mA cm^{-2}, which is even better than that of Pt/C+IrO_2 (177.9 mW cm^{-2} at 165.8 mA cm^{-2}). The specific capacity normalized to the mass of reacted Zn was 790.1 mAh g^{-1}_{Zn} for NP Co_3O_4/Fe@C_2N catalyst. This specific capacity was also comparable to that of Pt/C catalyst (776.1 mAh g^{-1}_{Zn}). The further cycling stability measurements at large current density, 10 mA cm^{-2} were investigated in Figure 3-15f. Impressively, the

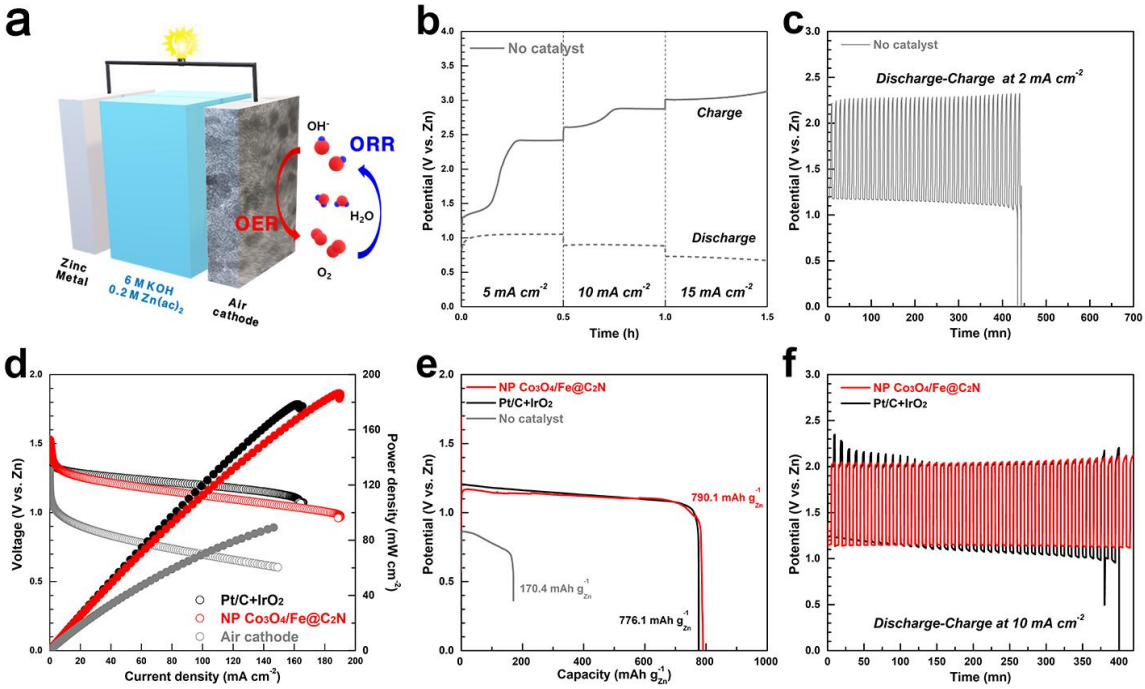

Figure 3-15 a) The schematic configuration of the assembled Zn-air battery. b) First discharge-charge curves without catalyst with different current densities in the range of 5-15 mA cm^{-2}. c) Cycling performance without catalyst at a current density of 2 mA cm^{-2}. d) Discharging polarization curves and the corresponding power densities based on Pt/C+IrO_2, NP Co_3O_4/Fe@C_2N and without catalyst. e) Discharge curves of Zn-air battery with Pt/C+IrO_2, NP Co_3O_4/Fe@C_2N and without catalyst under continuous discharge until complete consumption of Zn. f) Cycling performance for Pt/C+IrO_2 and NP Co_3O_4/Fe@C_2N at a current density of 10 mA cm^{-2}.

cell catalyzed by NP Co_3O_4/Fe@C_2N shows superior rechargeability compared to Pt/C+IrO_2 over 400 mn. Therefore, these results indicated that the synergistic effects from junction sites between NP Co_3O_4 and C_2N framework attributed the excellent electrochemical activities as well as preventing the degradation of electrochemical performance such as agglomeration or detaching.

The electrochemical performances of the NP Co_3O_4/Fe@C_2N and Pt/C+IrO_2 catalysts were also evaluated in hybrid Li-air batteries. The schematic configuration of the assembled Li-air battery was shown in Figure 3-16a. The discharge-charge profiles of hybrid Li-air batteries were recorded at a current density of 0.5–2.0 mA cm^{-2} (Figure 3-14d). The charge and discharge voltages of NP Co_3O_4/Fe@C_2N are comparable with those of Pt/C+IrO_2, which agrees with the results for Zn–air batteries. Figure 3-14e shows the cycling performance of NP Co_3O_4/Fe@C_2N and Pt/C+IrO_2 at a constant current density of 0.5 mA cm^{-2}. Although the charge-discharge voltage gap of NP Co_3O_4/Fe@C_2N is relatively higher, it is still comparable to or even better than that of the noble Pt/C+IrO_2 catalyst after 25 h (inset in Figure 3-14e). Figure 3-14f compares the cycling performance of the Co_3O_4+Fe@C_2N composite to that of the NP Co_3O_4/Fe@C_2N catalyst at a current density of 0.5 mA cm^{-2}. The mixed Co_3O_4+Fe@C_2N composite obviously degrades over 15 h, showing poor

electrochemical stability under these operating conditions. These results corroborate the results for each sample during the ORR and OER processes. The first discharge-charge curves and cycling performance without catalyst were also investigated as a reference (Figure 3-16b and c). Consequently, NP Co_3O_4/Fe@C_2N is an efficient bifunctional catalyst with comparable performance and stability comparable to those of benchmark materials, such as Pt/C and IrO_2, for hybrid metal (Zn, Li)–air batteries.

3.4. Conclusions

In summary, we rationally designed NP Co_3O_4 on Fe@C_2N (NP Co_3O_4/Fe@C_2N) as a bifunctional catalyst for both the ORR and the OER, which we grew hydrothermally. Although the Co_3O_4 nanostructure alone has a scarce catalytic activity toward the ORR and OER, in hybrid materials with the C_2N matrix, it exhibits unexpectedly high ORR and OER activities in alkaline solutions, superior to those of the benchmark Pt/C and IrO_2 catalysts. Further investigation demonstrates that the NP Co_3O_4 structures on the C_2N framework show specific interactions, which synergistically contribute to the overall electrochemical performance for both ORR and OER processes. The specific exposed facets on the NP Co_3O_4 nanostructure present a superior bifunctional electrochemical activity on the Fe@C_2N framework. In addition, metal (Zn, Li)–air batteries based on NP Co_3O_4/Fe@C_2N display a charge-discharge overpotential similar to that of the Pt/C+IrO_2 catalyst at various current densities. Moreover, NP Co_3O_4/Fe@C_2N demonstrates higher stability under operating conditions than that of the Co_3O_4+Fe@C_2N composite and Pt/C+IrO_2 catalysts. Therefore, this work presented a highly promising bifunctional electrochemical catalyst for metal-air batteries and an approach for advanced catalyst engineering by introducing synergistic effects between the metal oxide and the C_2N framework.

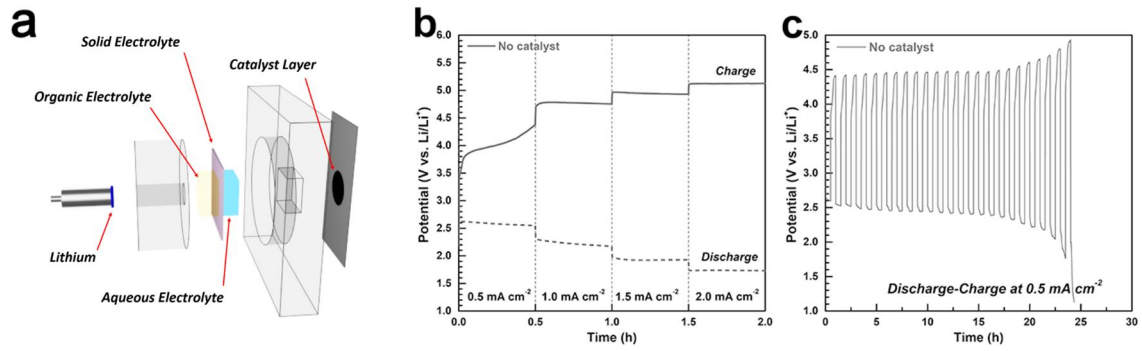

Figure 3-16 a) The schematic configuration of the assembled Li-air battery. b) First discharge-charge curves without catalyst with different current densities in the range of 0.5-2.0 mA cm^{-2}. c) Cycling performance without catalyst at a current density of 0.5 mA cm^{-2}.

References

1. Wang, Z.-L.; Xu, D.; Xu, J.-J.; Zhang, X.-B. Oxygen Electrocatalysts in Metal-Air Batteries: From Aqueous to Nonaqueous Electrolytes. *Chem. Soc. Rev.* **2014**, *43*, 7746–7786.
2. Kim. C.; Kim, J.; Joo, S.; Bu, Y.; Liu, M.; Cho, J.; Kim, G. Efficient CO_2 Utilization *via* a Hybrid Na-CO_2 System Based on CO_2 Dissolution. *iScience* **2018**, *9*, 278-785.
3. Kim, C.; Gwon, O.; Jeon, I.-Y.; Kim, Y.; Shin, J.; Ju, Y.-W.; Baek, J.-B.; Kim, G. Cloud-Like Graphene Nanoplatelets on $Nd_{0.5}Sr_{0.5}CoO_{3-\delta}$ Nanorods as an Efficient Bifunctional Electrocatalyst for Hybrid Li-Air Batteries. *J. Mater. Chem. A* **2016**, *4*, 2122-2127.
4. Gwon, O.; Kim, C.; Kwon, O.; Jeong, H. Y.; Park, H.-K.; Shin, J.; Ju, Y.-W.; Kim, G. An Efficient Oxygen Evolution Catalyst for Hybrid Lithium Air Batteries: Almond Stick Type Composite of Perovskite and Cobalt Oxide. *J. Electrochem. Soc*. **2016**, *163* , A1893–A1897.
5. Christensen, J.; Albertus, P.; Sanchez-Carrera, R. S.; Lohmann, T.; Kozinsky, B.; Liedtke, R.; Ahmed, J.; Kojic, A. A Critical Review of Li/Air Batteries. *J. Electrochem. Soc*. **2012**, *159*, R1-R30.
6. Gewirth, A. A.; Thorum, M. S. Electroreduction of Dioxygen for Fuel-Cell Applications: Materials and Challenges. *Inorg. Chem.* **2010**, *49*, 3557–3566.
7. Pei, Z.; Li, H.; Huang, Y.; Xue, Q.; Huang, Y.; Zhu, M.; Wang, Z.; Zhi, C. Texturing *in situ*: N,S-Enriched Hierarchically Porous Carbon as a Highly Active Reversible Oxygen Electrocatalyst. *Energy Environ. Sci*. **2017,** *10*, 742-749.
8. Pei, Z.; Tang, Z.; Liu, Z.; Huang, Y.; Wang, Y.; Li, H.; Xue, Q.; Zhu, M.; Tang, D.; Zhi, C. Construction of a Hierarchical 3D Co/N-Carbon Electrocatalyst for Efficient Oxygen Reduction and Overall Water Splitting, *J. Mater. Chem. A*. **2018**, *6*, 489-497.
9. Ma, L.; Chen, S.; Pei, Z.; Huang, Y.; Liang, G.; Mo, F.; Yang, Q.; Su, J.; Gao, Y.; Zapien, J. A.; *et al*. Single-Site Active Iron-Based Bifunctional Oxygen Catalyst for a Compressible and Rechargeable Zinc-Air Battery. *ACS Nano* **2018**, *12*, 1949-1958.
10. Pei, Z.; Huang, Y.; Tang, Z.; Ma, L.; Liu, Z.; Xue, Q.; Wang, Z.; Li, H.; Chen, Y.; Zhi, C. Enabling Highly Efficient, Flexible and Rechargeable Quasi-Solid-State Zn-Air Batteries *via* Catalyst Engineering and Electrolyte Functionalization. *Energy Storage Materials* DOI: 10.1016/j.ensm.2018.11.010.
11. Wang, T.; Kou, Z.; Mu, S.; Liu, J.; He, J.; He, D.; Amiinu, I. S.; Meng, W.; Zhou, K. Luo, Z.; Chaemchuen, S.; *et al*. 2D Dual-Metal Zeolitic-Imidazolate-Framework-(Zif)-Derived Bifunctional Air Electrodes with Ultrahigh Electrochemical Properties for Rechargeable Zinc-Air Batteries. *Adv. Funct. Mater*. **2018,** *28*, 1705048.
12. Guo, Y.; Yuan, P.; Zhang, J.; Hu, Y.; Amiinu, I. S.; Wang, X.; Zhou, J.; Xia, H.; Song, Z.; Xu, Q.; *et al*. Carbon Nanosheets Containing Discrete Co-N_x-B_y-C Active Sites for Efficient Oxygen Electrocatalysis and Rechargeable Zn-Air Batteries. *ACS Nano* **2018**, *12*, 1894-1901.

13. Amiinu, I. S.; Pu, Z.; Liu, X.; Owusu, K. A.; Monestel, H. G. R.; Boakye, F. O.; Zhang, H.; Mu, S. Multifunctional Mo-N/C@MoS_2 Electrocatalysts for HER, OER, ORR, and Zn-Air Batteries, *Adv. Funct. Mater*. **2017,** *27*, 1702300.
14. Ju, Y.-W.; Yoo, S.; Kim, C.; Kim, S.; Jeon, I.-Y.; Shin, J.; Baek, J.-B.; Kim, G. Fe@N-Graphene Nanoplatelet-Embedded Carbon Nanofibers as Efficient Electrocatalysts for Oxygen Reduction Reaction. *Adv. Sci.* **2016**, *3*, 1500205.
15. Chen, Z.; Yu, A.; Higgins, D.; Li, H.; Wang, H.; Chen, Z. Highly Active and Durable Core-Corona Structured Bifunctional Catalyst for Rechargeable Metal-Air Battery Application. *Nano Lett.* **2012**, *12*, 1946–1952.
16. Yi, J.; Wang, Y.; Jiang, Y.; Jung, I. W.; Liu, W.; De Andrade, V.; Xu, R.; Parameswaran, R.; Peters, I. R.; Divan, R.; *et al*. 3D Calcite Heterostructures for Dynamic and Deformable Mineralized Matrices. *Nat. Commun.* **2017**, *8*, 509
17. Rui, M.; Li, X.; Gan, L.; Zhai, T.; Zeng, H. Ternary Oxide Nanocrystals: Universal Laser-Hydrothermal Synthesis, Optoelectronic and Electrochemical Applications. *Adv. Funct. Mater*. **2016**, *26* , 5051–5060.
18. Su, D.; Dou, S.; Wang, G. Single Crystalline Co_3O_4 Nanocrystals Exposed with Different Crystal Planes for Li-O_2 Batteries. *Sci. Rep*. **2015**, *4*, 5767.
19. Xie, X.; Li, Y.; Liu, Z. Q.; Haruta, M.; Shen, W. Low-Temperature Oxidation of CO Catalysed by Co_3O_4 Nanorods. *Nature* **2009**, *458*, 746–749.
20. Han, X.; He, G.; He, Y.; Zhang, J.; Zheng, X.; Li, L.; Zhong, C.; Hu, W.; Deng, Y.; Ma, T.-Y. Engineering Catalytic Active Sites on Cobalt Oxide Surface for Enhanced Oxygen Electrocatalysis. *Adv. Energy Mater*. **2018**, *8*, 1702222.
21. Sun, C.; Li, F.; Ma, C.; Wang, Y.; Ren, Y.; Yang, W.; Ma, Z.; Li, J.; Chen, Y.; Kim, Y.; *et al*. Graphene–Co_3O_4 Nanocomposite as an Efficient Bifunctional Catalyst for Lithium–Air Batteries. *J. Mater. Chem. A* **2014**, *2*, 7188-7196.
22. Liang, Y.; Li, Y.; Wang, H.; Zhou, J.; Wang, J.; Regier, T.; Dai, H. Co_3O_4 Nanocrystals on Graphene as a Synergistic Catalyst for Oxygen Reduction Reaction. *Nat. Mater*. **2011**, *10*, 780–786.
23. Wang, Y.; Zhang, H. J.; Lu, L.; Stubbs, L. P.; Wong, C. C.; Lin, J. Designed Functional Systems from Peapod-Like Co@Carbon to Co_3O_4@Carbon Nanocomposites. *ACS Nano* **2010**, *4*, 4753–4761.
24. Hao, F.; Zhang, Z.; Yin, L. Co_3O_4 /Carbon Aerogel Hybrids as Anode Materials for Lithium-Ion Batteries with Enhanced Electrochemical Properties. *ACS Appl. Mater. Interfaces* **2013**, *5*, 8337–8344.
25. Shen, L.; Wang, C. Hierarchical Co_3O_4 Nanoparticles Embedded in a Carbon Matrix for Lithium-Ion Battery Anode Materials. *Electrochim. Acta* **2014**, *133*, 16–22.
26. Mahmood, J.; Li, F.; Kim, C.; Choi, H. J.; Gwon, O.; Jung, S. M.; Seo, J. M.; Cho, S. J.; Ju, Y. W.;

Jeong, H. Y.; *et al*. Fe@C_2N: A Highly-Efficient Indirect-Contact Oxygen Reduction Catalyst. *Nano Energy* **2018**, *44*, 304–310.

27. Kim, S.-J.; Mahmood, J.; Kim, C.; Han, G.-F.; Kim, S.-W.; Jung, S.-M.; Zhu, G.; De Yoreo, J. J.; Kim, G.; Baek, J.-B. Defect-Free Encapsulation of Fe^0 in 2D Fused Organic Networks as a Durable Oxygen Reduction Electrocatalyst. *J. Am. Chem. Soc*. **2018**, *140*, 1737-1742
28. Mahmood, J.; Lee, E. K.; Jung, M.; Shin, D.; Jeon, I. Y.; Jung, S. M.; Choi, H. J.; Seo, J. M.; Bae, S. Y.; Sohn, S. D.; *et al*. Nitrogenated Holey Two-Dimensional Structures. *Nat. Commun.* **2015**, *6*, 6486.
29. Wang, H.; Shrestha, T. B.; Basel, M. T.; Dani, R. K.; Seo, G. M.; Balivada, S.; Pyle, M. M.; Prock, H.; Koper, O. B.; Thapa, P. S.; *et al*. Magnetic-Fe/Fe_3O_4-Nanoparticle-Bound SN38 as Carboxylesterase-Cleavable Prodrug for the Delivery to Tumors within Monocytes/Macrophages. *Beilstein J. Nanotechnol*. **2012**, *3*, 444–455.
30. Wu, A.; Liu, D.; Tong, L.; Yu, L.; Yang, H. Magnetic Properties of Nanocrystalline Fe/Fe_3C Composites. *CrystEngComm* **2011**, *13*, 876–882.
31. Xu, X.; Chen, Y.; Zhou, W.; Zhu, Z.; Su, C.; Liu, M.; Shao, Z. A Perovskite Electrocatalyst for Efficient Hydrogen Evolution Reaction. *Adv. Mater*. **2016**, *28*, 6442–6448.
32. Liang, Y.; Wang, H.; Diao, P.; Chang, W.; Hong, G.; Li, Y.; Gong, M.; Xie, L.; Zhou, J.; Wang, J.; *et al*. Oxygen Reduction Electrocatalyst Based on Strongly Coupled Cobalt Oxide Nanocrystals and Carbon Nanotubes. *J. Am. Chem. Soc.* **2012**, *134*, 15849-15857
33. Ma, T. Y.; Dai, S.; Jaroniec, M.; Qiao, Z. Metal-Organic Framework Derived Hybrid Co_3O_4-Carbon Porous Nanowire Arrays as Reversible Oxygen Evolution Electrodes. *J. Am. Chem. Soc.* **2014**, *136*, 13925-13931
34. Liu, X.; Chang, Z.; Luo, L.; Xu, T.; Lei, X.; Liu, J.; Sun, X. Hierarchical $Zn_xCo_{3-x}O_4$ Nanoarrays with High Activity for Electrocatalytic Oxygen Evolution. *Chem. Mater.* **2014**, *26*, 1889–1895.
35. Mahmood, J.; Jung, S.; Kim, S.; Park, J.; Yoo, J.; Baek, J.-B. Cobalt Oxide Encapsulated in C_2N-h 2D Network Polymer as a Catalyst for Hydrogen Evolution. *Chem. Mater.* **2015**, *27*, 4860-4864.
36. Yin, H.; Zhang, C.; Liu, F.; Hou, Y. Hybrid of Iron Nitride and Nitrogen-Doped Graphene Aerogel as Synergistic Catalyst for Oxygen Reduction Reaction. *Adv. Funct. Mater.* **2014**, *24*, 2930-2937.
37. Bu, Y.; Nam, G.; Kim, S.; Choi, K.; Zhong, Q.; Lee, J.; Qin, Y.; Cho, J.; Kim, G. A Tailored Bifunctional Electrocatalyst: Boosting Oxygen Reduction/Evolution Catalysis *via* Electron Transfer Between N-Doped Graphene and Perovskite Oxides. *Small* **2018**, 1802767
38. Kim, J.; Kim, C.; Jeon, I.-Y.; Baek, J.-B.; Ju, Y.-W.; Kim, G. A New Strategy for Outstanding Performance and Durability in Acidic Fuel Cells: A Small Amount Pt Anchored on Fe, N Co-Doped Graphene Nanoplatelets. *ChemElectroChem* **2018**, *5*, 2857-2862.
39. Nie, R.; Shi, J.; Du, W.; Ning, W.; Hou, Z.; Xiao, F.-S. A Sandwich N-Doped Graphene/Co_3O_4 Hybrid: An Efficient Catalyst for Selective Oxidation of Olefins and Alcohols. *J. Mater. Chem. A,*

2013, *1*, 9037-9045.

40. Kim, S.; Kwon, O.; Kim, C.; Gwon, O.; Jeong, H. Y.; Kim, K. H.; Shin, J.; Kim, G. Strategy for Enhancing Interfacial Effect of Bifunctional Electrocatalyst: Infiltration of Cobalt Nanooxide on Perovskite. *Adv. Mater. Interfaces* **2018**, *5*, 1800123.
41. Xie, S.; Dai, H.; Deng, J.; Liu, Y.; Yang, H.; Jiang, Y.; Tan, W.; Ao, A.; Guo, G. Au/3DOM Co_3O_4: Highly Active Nanocatalysts for the Oxidation of Carbon Monoxide and Toluene. *Nanoscale*, **2013**, *5*, 11207
42. Xu, L.; Wang, Z.; Wang, J.; Xiao, Z.; Huang, X.; Liu, Z.; Wang, S. N-Doped Nanoporous Co_3O_4 Nanosheets with Oxygen Vacancies as Oxygen Evolving Electrocatalysts. *Nanotechnology* **2017**, *28*, 165402
43. Li, C.; Han, X.; Cheng, F.; Hu, Y.; Chen, C.; Chen, J. Phase and Composition Controllable Synthesis of Cobalt Manganese Spinel Nanoparticles Towards Efficient Oxygen Electrocatalysis. *Nat. Commun.* **2015**, *6*, 7345.
44. Dimitrov, V.; Komatsu, T.; Sato, R. Optical Basicity and O1s Binding Energy of Simple Oxides. *J. Ceram. Soc. Japan* **1999**, *107*, 21–26.

Chapter 4 Efficient CO_2 utilization *via* a hybrid Na-CO_2 system based on CO_2 dissolution

This chapter has been published and has been cited in the thesis by co-author C. Kim.

Reproduced with permission from C. Kim, J. Kim, S. Joo, Y. Bu, M. Liu, J. Cho, G. Kim, *iScience* 2018, 9, 278-285.

4.1. Introduction

Many researchers believe that global warming and climate change are the result of carbon dioxide (CO_2) generated by human activities over the centuries (Jenkinson et al., 1991; Obama, 2017). Thus, many countries and organizations have made great efforts to reduce their carbon footprint, and recently, carbon capture, utilization and storage/sequestration (CCUS) technology has been studied to recycle CO_2 as a resource (Keith et al., 2018; Andersen, 2017; Dowell et al., 2017). In this regard, considerable research has been focused on the chemical conversion of CO_2 into high value-added carbon compounds, such as methanol, organic materials, and plastics (Liu et al., 2015; Li et al., 2016; Angamuthu et al., 2010; Darensbourg, 2007). However, due to the low conversion efficiency, it has been pointed out that it cannot be an effective greenhouse gas abatement technology (Bourzac, 2017; Markewitz et al., 2012; Mikkelsen et al., 2010). Recently, aprotic (non-aqueous) metal-CO_2 batteries have also been studied for the production of electrical energy using CO_2 (Zhang et al., 2015; Qie et al., 2017; Hu et al., 2016; Al Sadat and Archer, 2016; Das et al., 2013). However, during the generation of electric energy, solid carbonate products accumulate on the surface of the electrode, which deteriorates the performance and discharge capacity. Additionally, because CO_2 is regenerated in the charging process, aprotic metal-CO_2 batteries are not an efficient CCUS technology for utilizing and reducing CO_2. Thus, we have devised a hybrid Na-CO_2 that produces continuously both electric energy and hydrogen simultaneously through efficient CO_2 conversion with highly stable operation over 1,000 hours from the nature of spontaneous CO_2 dissolution in an aqueous solution. We further show that unlike existing aprotic metal-CO_2 batteries (Zhang et al., 2015; Qie et al., 2017; Hu et al., 2016; Al Sadat and Archer, 2016), the proposed system does not regenerate CO_2 during charging process. Therefore, this hybrid Na-CO_2 cell, which adopts efficient CCUS technologies, not only utilizes CO_2 as the resource for generating electrical energy, but also produces the clean energy source, hydrogen.

4.2. Experimental

4.2.1. Half-cell configured electrochemical analysis.

In three-electrode half-cell measurements, a platinum wire was used as both of working electrode and

counter electrode with Ag/AgCl (saturated KCl filled) reference electrode in 0.1 M sodium hydroxide (NaOH, Sigma-Aldrich Co.) in pure water and seawater (taken from sea of Ulsan and filtered to remove visible impurities). To estimate pH and hydrogen evolution potential in the solution, a reversible hydrogen electrode (RHE) calibration was conducted in H_2-saturated solutions where platinum wires were used as the working, counter electrodes and Ag/AgCl as a reference electrode at a scan rate of 1 mV s^{-1}. For all half-cell configured experiments, iR correction was applied by measuring the resistance of solution (0.1 M NaOH, CO_2-saturated 0.1 M NaOH, seawater, CO_2-saturated seawater). The ohmic resistances of before CO_2-saturated 0.1 M NaOH, after CO_2-saturated 0.1 M NaOH, before CO_2-saturated seawater, and after CO_2-saturated seawater have been confirmed as 12.5, 35.8, 4.2 and 4.0 , respectively. A rotating disk electrode testing was conducted by using a mixture of 20wt.% Pt/C and IrO_2 catalyst (Sigma-Aldrich Co., mixed in 1 : 1 gravimetric ratio) on RRDE-3A (ALS Co.). The mixture of catalyst was prepared into a catalyst ink by dispersing 10 mg of the catalyst in 1 mL of a binder solution (45 : 45 : 10 = ethanol : isopropyl alcohol : 5 wt.% Nafion solution (Sigma-Aldrich Co.), volumetric ratio) followed by a bath sonication process. The oxidation RDE profiles were measured by 5 μL of the catalyst ink drop-coated glassy carbon disk electrode, where area is 0.1256 cm^2, at a scan rate of 10 mV s^{-1}. All electrochemical tests were carried out using Biologic VMP3.

4.2.2. Characterization techniques

The soluble solid products after discharge process in CO_2-saturated 0.1 M NaOH were obtained through various drying process such as freeze-drying, natural drying at room-temperature, high temperature drying at 70^{o}C oven. The phase identification of the obtained products was confirmed by X-ray powder diffraction (XRD) (Bruker diffractometer, Cu Kα radiation) at a scan rate of 1^o min^{-1}. The power patterns were analyzed using JADE 6.5 software. The generated gas from discharge process was collected using three-electrode configuration in CO_2-saturated seawater and 0.1 M NaOH by water substitution method using U tube. Then the gas was analyzed by gas chromatograph (Agilent 7820A GC instrument) with a thermal conductivity detector (TCD) and a packed column (Agilent carboxen 1000). The gas used for GC measurement were controlled using a mass flow controller (MFC) (Atovac GMC1200) and the exact volume value of gas was calibrated through a bubble flow meter. The gas evolved from the charging process were also collected by three-electrode configuration (Pt wires as a counter electrode, Pt/C+IrO_2 catalyst loaded carbon felt as a working electrode, and Ag/AgCl as a reference electrode) in 0.1 M NaOH. The gas was analyzed by 450-GC chromatograph and 320-MS (Bruker Co.). The morphological analysis of the working electrode before and after discharge process in hybrid Na-CO_2 system was examined by scanning electron microscopy (Nova FE-SEM, FEI Co.).

4.2.3. Full-cell measurments

For testing the hybrid Na-CO_2 system, the commercial Na-air battery (seawater battery) system was

purchased at 4TOONE Co. and we modified the system into hybrid Na-CO_2 system. The hybrid Na-CO_2 system is composed of Na metal / organic electrolyte / solid electrolyte / aqueous electrolyte / cathode. For the organic electrolyte, 1 M Sodium trifluoromethanesulfonate ($NaCF_3SO_3$, Sigma-Aldrich Co.) in tetraethylene glycol dimethyl ether (TEGDME, Sigma-Aldrich Co.) was used. And NASICON-type (NASICON: Na super ionic conductor) $Na_3Zr_2Si_2PO_{12}$ with a thickness of 1 mm and a diameter of 16 mm was used as the solid electrolyte. The anode coin cell was assembled in Ar-filled glove box where the water and oxygen concentrations were kept less than 1 ppm. The sodium metal (Sigma-Aldrich Co.) with a diameter of 16 mm and a thickness of 0.5 mm was loaded on the stainless-steel metal support and the prepared organic electrolyte was filled between sodium metal and NASICON. After assembling the anode coin cell with proper sealing, the assemblage was moved out from the glove box. The assembled coin cell is 24 mm in diameter and 6.5 mm in thickness (2465 size). For the aqueous electrolyte, 150 mL of 0.1 M NaOH and seawater were used. The cathode was prepared by drop-coating the catalyst ink (Pt/C+IrO_2 ink) in a carbon felt electrode (Fuel Cell Store Co.) with a loading density of 2 mg cm^{-2}. The current density was normalized with the loading density of the catalysts. A titanium wire was used as a current collector of the cathode and the aqueous electrolytes were saturated by CO_2 at a rate of 50 mL min^{-1} at the ambient air condition for electrochemical measurements in hybrid Na-CO_2 system. All electrochemical tests were conducted using Biologic VMP3.

4.3. Result and discussion

Figure 4-1 Schematic illustration of hybrid Na-CO_2 system and its reaction mechanism.

4.3.1. The proposed hybrid Na-CO_2 cell and its reaction mechanism

A schematic illustration of the proposed hybrid Na-CO_2 cell is presented in **Figure 4-1**. The digital photographs of the system are also presented in **Figure 4-2**. This system could work continuously with Na metal and CO_2 as fuel at the anode and feedstock gas at the cathode, respectively. Na is regarded as a promising candidate as a substitute for Li in terms of its electrochemically similar behavior along with low cost (30 times cheaper than Li) from natural abundance and environmental friendliness (Noorden, 2014; Kwak et al., 2015). The Na metal anode is kept in an organic electrolyte to prevent a direct corrosion from an aqueous electrolyte separating by Na super ionic conductor (NASICON) membrane. The overall reaction mechanisms are composed of a chemical reaction and an electrochemical reaction. The chemical reaction of CO_2 dissolution mechanism is as follows:

$$CO_2(aq) + H_2O(l) \rightleftharpoons H_2CO_3(aq), \qquad K_h = 1.70 \times 10^{-3} \qquad (1)$$

$$H_2CO_3(aq) \rightleftharpoons HCO_3^-(aq) + H^+(aq), \qquad pK_{a1} = 6.3 \qquad (2)$$

When CO_2 is purged into an aqueous solution (*e.g.*, distilled water, seawater, NaOH solution), CO_2 dissolution proceeds and carbonic acid ($H_2CO_3(aq)$) is formed through the hydration of CO_2 (**Equation 1**). For a standard state condition in pure water, this spontaneous chemical equilibrium of CO_2 hydration is determined by the hydration equilibrium constant ($K_h = 1.70 \times 10^{-3}$) (Housecroft and Sharpe, 2005). Then, the carbonic acid dissociates into HCO_3^- and H^+ determined by the first acid dissociation constant ($K_{a1} = 4.46 \times 10^{-7}$), shown in **Equation 2** (Harris, 2010). Because carbonic acid is a polyprotic acid dissociating multiple steps, an in-depth understanding of CO_2 dissolution requires that the second acid dissociation step, *i.e.*, $HCO_3^-(aq) \rightleftharpoons CO_3^{2-}(aq) + H^+(aq)$ ($K_{a2} = 4.69 \times 10^{-11}$), be considered (Harris, 2010). However, the second acid dissociation constant is significantly smaller than the first ($K_{a1} >> K_{a2}$), making it negligible in calculating the proton concentration. Thus, when CO_2 dissolved in water, it acidifies the aqueous solution and $HCO_3^-(aq)$ is predominant over $CO_3^{2-}(aq)$. The concentration of carbonate ions when CO_2 dissolves in water at normal atmospheric pressure is provided at **Table 4-1**. The mole fractions of carbonate ions depending on the pH of solution is shown in **Figure 4-3**.

The electrochemical reactions are composed of anodic reaction of sodium metal oxidation (**Equation 3**) and cathodic reaction of hydrogen evolution (**Equation 4**):

$$\text{Anodic reaction:} \quad 2Na \rightarrow 2Na^+ + 2e^- \qquad E^o = -2.71\ V \qquad (3)$$

$$\text{Cathodic reaction:} \quad 2H^+ + 2e^- \rightarrow H_2(g) \qquad E^o = 0.00\ V \qquad (4)$$

$$\text{Net equation:} \quad 2Na + 2H^+ \rightarrow 2Na^+ + H_2(g) \qquad E^o = 2.71\ V \qquad (5)$$

Then, the electrochemical net equation is simply given as the oxidation of Na metal and the spontaneous

evolution of hydrogen (**Equation 5**). Because the potential of cathodic reaction is closely influenced by the pH of aqueous solution, the dissolution of CO_2 renders a favorable electrochemical reaction environment by acidifying the aqueous solution.

Table 4-1. Concentration of various ions when CO_2 dissolves in water at normal atmospheric pressure.

pCO_2 (atm)	$[CO_2(aq)]$ (mol L^{-1})	$[H_2CO_3(aq)]$ (mol L^{-1})	$[HCO_3^-(aq)]$ (mol L^{-1})	$[CO_3^{2-}(aq)]$ (mol L^{-1})	$[H^+(aq)]$ (mol L^{-1})	pH
3.5×10^{-4}	1.18×10^{-5}	1.41×10^{-8}	2.29×10^{-6}	4.69×10^{-11}	2.29×10^{-6}	5.64

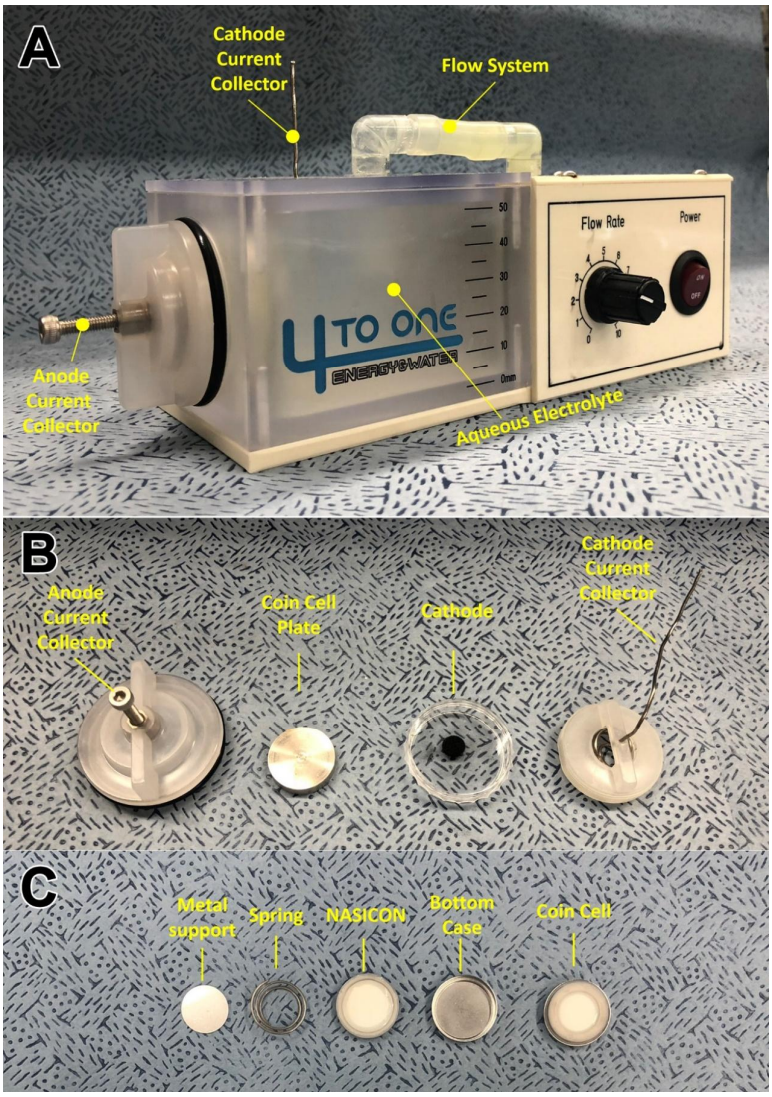

Figure 4-2 The components of hybrid Na-CO_2 cell. Related to Figure 1. (A) The digital photograph of hybrid Na-CO_2 cell. (B) The anode and cathode assembly of Na-CO_2 cell. (C) The components of anode coin cell. Details are available in Transparent Methods. Related to Figure 4-1.

4.3.2. Half-cell configured electrochemical analysis.

The cathodic electrochemical profiles were closely examined using a cyclic voltammetry (CV) technique on the Pt electrode (**Figure 4-4A**). An apparent cathodic peak in O_2-saturated NaOH was observed near of -0.1 V vs. Ag/AgCl, which could be ascribed to oxygen reduction reaction (ORR) on the Pt electrode (Park et al., 1986; Kim et al., 2016). When ORR is occurred, a diffusion-controlled region was found near of -0.2 V and a limiting current was observed due to the typical O_2 mass transfer limitation in ORR profiles (Kim et al.,2016; Bu et al., 2017). At the lower potential, a cathodic peak corresponding to hydrogen evolution reaction (HER) was observed around -0.95 V in O_2- and N_2-saturated conditions (Mahmood et al., 2017; Xu et al., 2016; Ahn et al., 2018). Meanwhile, in the case of CO_2 saturated condition, hydrogen evolution occurs more positively by 0.35 V due to the higher concentration of H^+. In addition, HER profiles, contrary to ORR profiles, presented sharply increasing cathodic curves without a mass transfer limitation. For depth analysis, the kinetics of these electrochemical reactions were interpreted by an analysis of the Tafel slope (**Figure 4-4B**). Because ORR is one of the most complex electrochemical reactions, involving 4 electrons with 2 reactants (O_2 and H_2O), the reaction kinetics is sluggish, even on a state-of-the-art Pt electrode, with a value of 78 mV dec.$^{-1}$. However, HER only involves 2 electrons with 1 reactant (H^+ or H_2O depending on pH) and thus presented a low Tafel slope of 48 mV dec.$^{-1}$ near the onset potential. Furthermore, the Tafel slope is more decreased to 28 mV dec.$^{-1}$ at an activation controlled Tafel region, indicating a highly efficient cathodic reaction. Further, the cathodic CVs and corresponding Tafel plots were investigated in seawater (**Figure 4-4C and 4-4D**). Likewise, it has been confirmed that CO_2 dissolution in seawater provides the electrochemically favorable environment toward HER. The hydrogen evolution potential based on pH is described in **Figure 4-4E, F, G, H, and I**. These electrochemical profiles have significant implications; the less corrosive environment of the quasi-neutral condition (pH ~ 7) could potentially

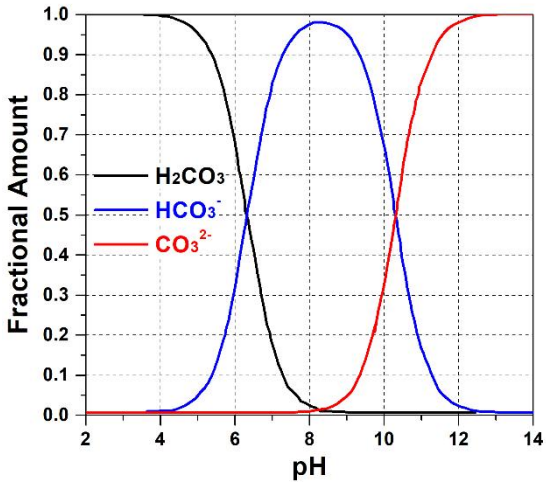

Figure 4-3 Mole fractions of the three different carbonate forms, *i.e.*, carbonic acid ion, bicarbonate ion, and carbonate ion, as a function of pH of dissolved solution (Note: carbonic acid ion here includes ionic carbon dioxide).

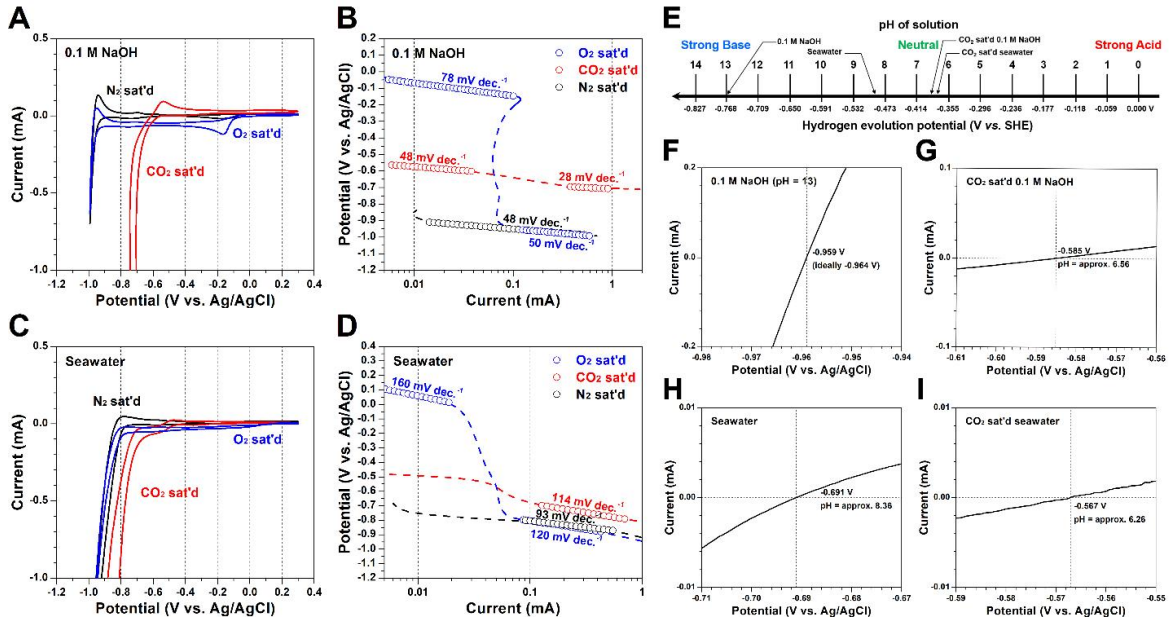

Figure 4-4 (A) Cathodic CV profiles measured in O_2, N_2, and CO_2-saturated 0.1 M NaOH at 10 mV s^{-1}, where Pt as a working and counter electrode and Ag/AgCl electrode as a reference electrode. A reference potential is described with Ag/AgCl instead of RHE for the clarification of potential difference in relationship between purging gases and pH. (B) Tafel analysis of the cathodic profiles. (C) Cathodic CV profiles measured in O_2 and CO_2 saturated seawater. (D) Corresponding Tafel plots. (E) Schematics diagram of hydrogen evolution potential related to pH. RHE calibration profile corresponding to hydrogen evolution potential measured in (F) 0.1 M NaOH (G) CO_2 saturated 0.1 M NaOH (H) seawater and (I) CO_2 saturated seawater.

allow adoption of abundant and non-noble metal-based electrocatalysts. Thus, notably, this combined cathodic reaction not only utilizes CO_2 to generate H_2, but also possesses highly efficient reaction kinetics, possibly overcoming the key issue of sluggish discharge rates for common metal-air batteries (Wang et al., 2014).

4.3.3. Performance and stability of hybrid Na-CO_2 cell

The actual working performance of hybrid Na-CO_2 cell is evaluated using a composite of Pt/C and IrO_2 (Pt/C+IrO_2) as a catalyst. **Figure 4-5A** presents the chronopotentiometric discharge profiles at the current density of 50 to 200 mA g^{-1} under N_2- or CO_2-saturated 0.1 M NaOH. Discharging CV profiles measured in various gas-saturated conditions were also investigated and three distinctive reduction peaks were found as similarly observed in the half-cell CV profiles (**Figure 4-6**). These findings confirmed that the dissolution of CO_2 led to a favorable HER environment in both NaOH solution and seawater. The full discharge profile was investigated in a CO_2-saturated NaOH solution (**Figure 4-5B**) with a mechanical recharge by replacing the Na metal anode. As shown in **Figure 4-5B**, the highly stable operation over 1,000 hours was achieved because only a gas phase H_2(g) was produced during the discharge process suggesting its similar nature of fuel cell systems (Park et al., 2000; Sengodan et al., 2015; Yang et al., 2009). Also, the full discharge profile measured under CO_2-saturated seawater

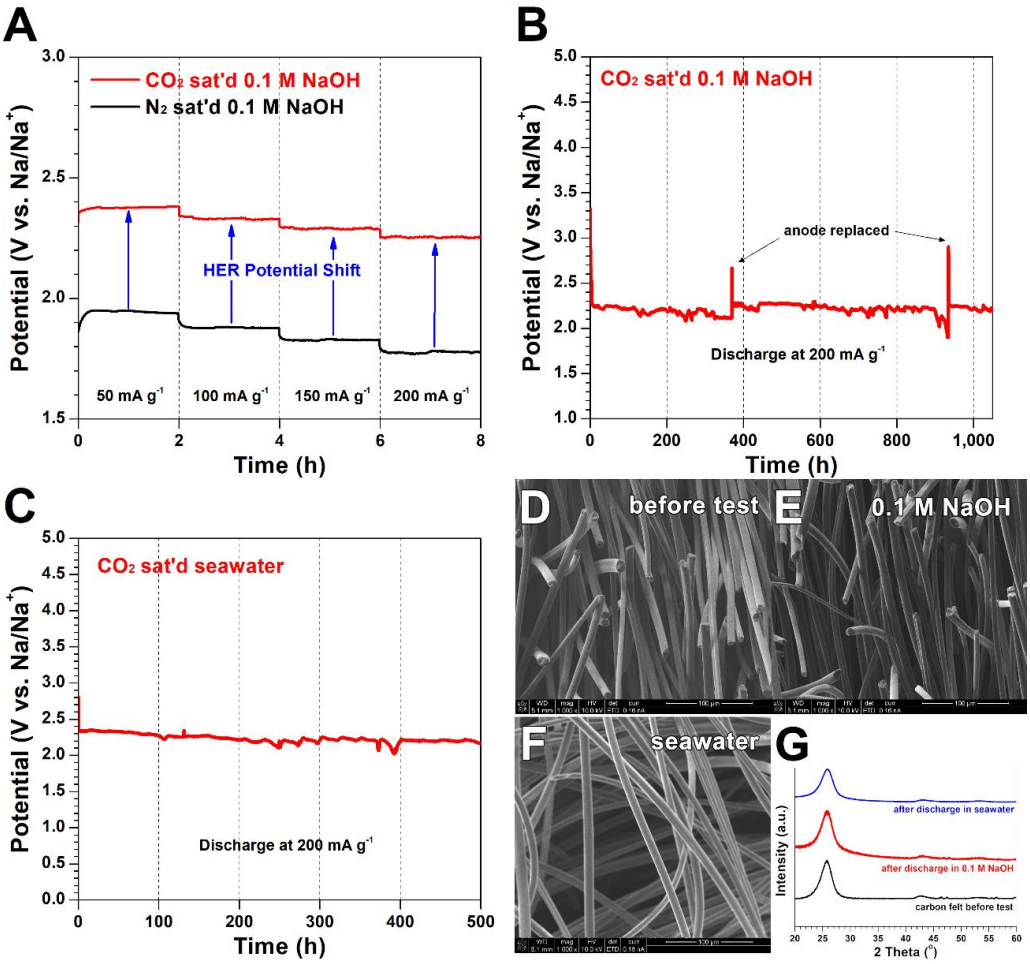

Figure 4-5 (A) Chronopotentiometric potential profiles on the hybrid Na-CO_2 system under various current densities. Discharge processes are conducted in CO_2, N_2 saturated 0.1 M NaOH to observe the effects of CO_2 dissolution. (B) The chronopotentiometric discharge profile of Pt/C+IrO_2 catalyst at 200 mA g^{-1} in CO_2-saturated 0.1 M NaOH. (C) Discharge profile of hybrid Na-CO_2 system measured in CO_2 saturated seawater. Surface observation of carbon felt cathode before and after test. (D) Scanning Electron Microscopy (SEM) image of carbon felt before discharge (E) after discharge in 0.1 M NaOH, (F) after discharged in seawater. (G) XRD profiles of carbon felt electrode before and after discharge in 0.1 M NaOH and seawater.

presented a highly stable operation over 500 hours (**Figure 4-5C**). In other words, there is no deposition of solid discharge products that possibly causes clogging or physical damage on the electrode as examined from scanning electron microscopy images and X-ray diffraction patterns (**Figure 4-5D-G**). In contrast, conventional aprotic metal-CO_2 batteries have exhibited typical clogging phenomenon by the deposition of solid M_2CO_3(s) (M = Li or Na), $Al_2(C_2O_4)_3$(s) or $MgCO_3$(s) on the surface of the electrode (Zhang et al., 2015; Qie et al., 2017; Hu et al., 2016; Al Sadat and Archer, 2016; Das et al., 2013), which results in a performance drop with limited capacity. A comparison of the capacities of various batteries is provided in **Table 4-2**. Further, the pH of the CO_2-saturated NaOH solution after the 1,000 hours operation was investigated and determined to be 6.62, indicating that the pH of solution is stably maintained over 1,000 hours (**Figure 4-7**). The produced gas during operation was analyzed by

a gas chromatography (GC) which confirms that this system generates only H_2 as expected from **Equation 4** during the discharge process (**Figure 4-8**). To identify a soluble product, the aqueous solution was freeze-dried and obtained in the form of a white powder (**the inset of Figure 4-9**). The X-ray diffraction (XRD) patterns of the white powder identifies as pure $NaHCO_3$ (**Figure 4-9**), commonly known as baking soda. It is notable that the continuous enrichment of $NaHCO_3$(aq) in the aqueous media from the discharge does not affect on the discharge performance as shown in the 1,000 hours discharge profile. Therefore, CO_2 gas has been successfully captured and converted in the form of baking soda. The additional XRD profiles of the powder obtained through different drying processes are provided in **Figure 4-10**. Further, we investigated the practical CO_2 conversion efficiency through the quantitative GC analysis. As shown in **Figure 4-11**, the practical efficiency of CO_2 conversion during the discharge reaction was determined to be 47.7 %. We have determined the efficiency of CO_2 conversion during the reaction time. First, theoretical CO_2 conversion rate is determined by calculating H^+ removal rate during discharge reaction. Because one CO_2 molecule can make one H^+ molecule from the dissolution process (*i.e.*, $CO_2 + H_2O \rightarrow H^+ + HCO_3^-$) and two H^+ molecules can make one H_2 molecule (*i.e.*, $2H^+ + 2e^- \rightarrow H_2$), we can assume two CO_2 molecules can contribute to produce one H_2 molecule (100 % conversion efficiency). As shown in **Figure 4-11A**, the theoretical CO_2 conversion rate is determined at the current of 100 mA, *i.e.*, 1.39 mL min^{-1}. Then, the quantitative GC profiles of outlet CO_2 gas during discharge reaction have been examined. As shown in **Figure 4-11B**, the measurement proceeds at the inlet CO_2 flow rate of 23.0 mL min^{-1} and the outlet CO_2 flow rate was 22.34 mL min^{-1}. Accordingly, the practically converted CO_2 rate is determined, *i.e.*, 0.66 mL min^{-1}. Thus, the practical efficiencies of CO_2 conversion were calculated to be 47.7 %. Although this value is lower than the theoretical conversion rate, it is meaningful in that proves the additional CO_2 dissolution during the discharge process. It is also expected

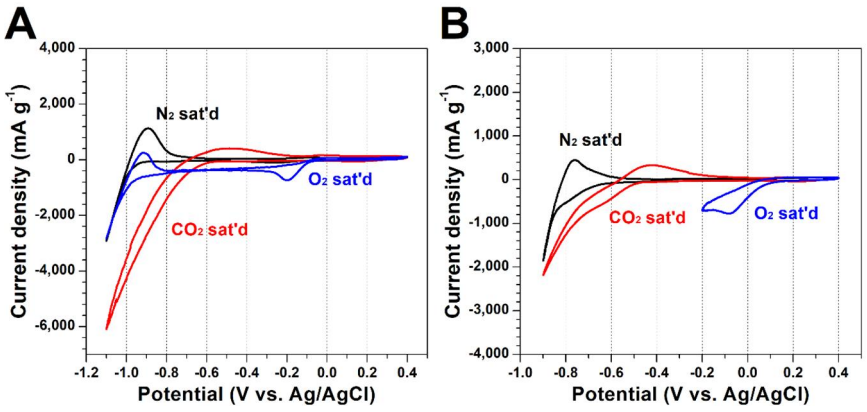

Figure 4-6 Cathodic full-cell CV profiles measured by Pt/C+IrO_2 catalyst at 0.1 mV s^{-1} in the hybrid Na-CO_2 system conducted in three-electrode configuration using Ag/AgCl. Related to Figure 3. CV profiles measured in O_2, N_2, or CO_2 saturated (A) 0.1 M NaOH (B) seawater. These profiles reveal the CO_2 dissolution could render a favorable electrochemical environment to HER.

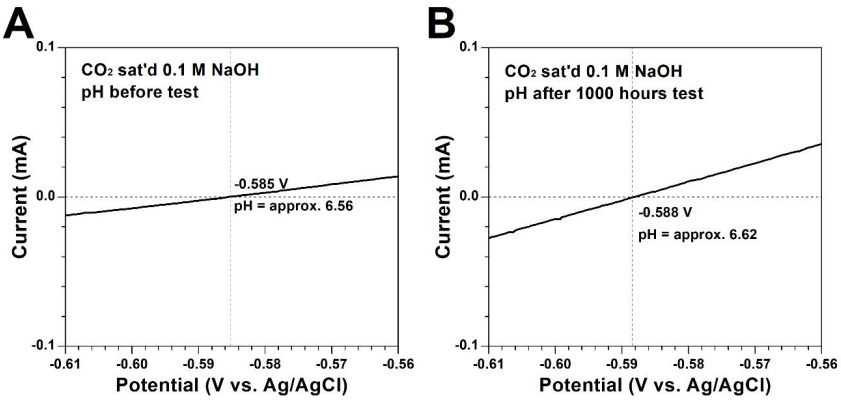

Figure 4-7 The pH of the CO_2-saturated 0.1 M NaOH solution. (A) before test and (B) after 1000 hours test.

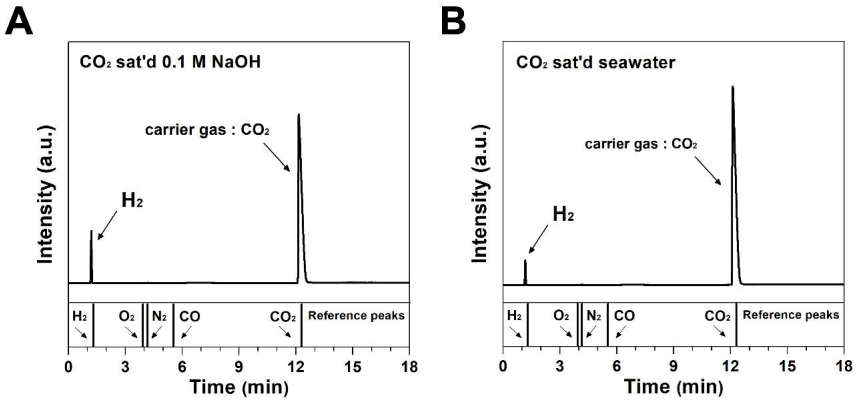

Figure 4-8 Gas chromatography (GC) profiles of generated gas during discharge process. The gas obtained during cathodic reaction proceeded in (A) CO_2 saturated 0.1 M NaOH (B) CO_2 saturated seawater.

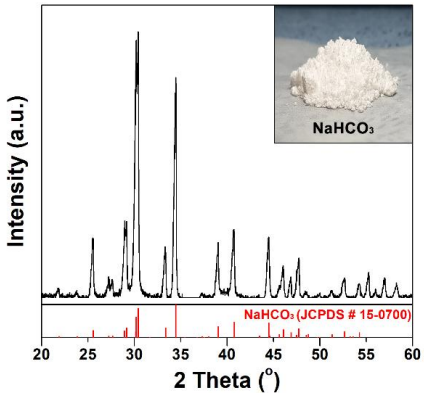

Figure 4-9 XRD profile of the solidified aqueous solution *via* freeze-drying. The inset shows the obtained white powder.

that the time that CO_2 contacts the solution (*i.e.*, it related to the depth of the solution.) will also affect the conversion rate. Although this value is lower than the theoretical conversion rate, it is meaningful in that proves the additional CO_2 dissolution during the discharge process.

Table 4-2. Comparison of various batteries capacity.

	Current density (mA g^{-1})	Catalyst loading (mg cm^{-2})	Gravimetric capacity (mAh g^{-1})	Area specific capacity (mAh cm^{-2})
This work	**200**	**2**	**210,000**	**420**
Li-CO_2 battery (Zhang et al., 2015)	50	0.27-0.45	14,723	6.5
Li-CO_2 battery (Qie et al., 2017)	300	0.3	16,006	4.8
Na-CO_2 battery (Hu et al., 2016)	1,000	0.071	60,359	42.9
Na-CO_2 battery (Das et al., 2013)	70	0.76-1.28	3,478	4.5
Mg-CO_2 battery (Al Sadat and Archer, 2016)	70	0.76-1.28	2,540	3.3
Al-CO_2 battery (Al Sadat and Archer, 2016)	70	0.5-1.0	13,322	13.3
Li-O_2 battery (Kang et al., 2006)	280	0.72	11,060	8.0
Li-ion battery (Wang et al., 2012)	280	6.66	225	1.5

4.3.4. Reversibility of hybrid Na-CO_2 cell

To confirm the reversibility of hybrid Na-CO_2 cell, an anodic charge profile (electrolysis profile) was observed. Because Na is one of the most abundant elements on earth, Na metal anode could be easily recycled through a charging process in Na ion containing aqueous solution, such as seawater. **Figure 4-12A** shows an oxidation rotating disk electrode (RDE) profile for examining whether CO_2 was reproduced during a charging process. Generally, the charging process is regarded as the opposite reaction of the discharging reaction. In this work, however, the generated H_2 gas from the discharging process is naturally removed on the surface of electrode and thus the oxidation reaction proceeds in the oxygen evolution reaction (OER) from the water oxidation (**Equation 6**).

$$2H_2O \rightarrow O_2(g) + 4H^+ + 4e^- \qquad E^o = 1.229\ V \qquad (6)$$

The oxidation curve corresponding to OER (Kim et al., 2016; Bu et al., 2017), observed in a CO_2-saturated NaOH solution near of 1.0 V vs. Ag/AgCl (from the Nernst equation, the OER potential can be calibrated by 0.0592 V × pH). Additionally, the qualitative GC profiles indicates that O_2 was generated during the oxidation process (**Figure 4-13 and 4-14**). In **Figure 4-14**, As shown in **Figure 4-13**, the GC profile reveals the gas contains O_2, CO_2, N_2. This raw data of GC intensity profiles is

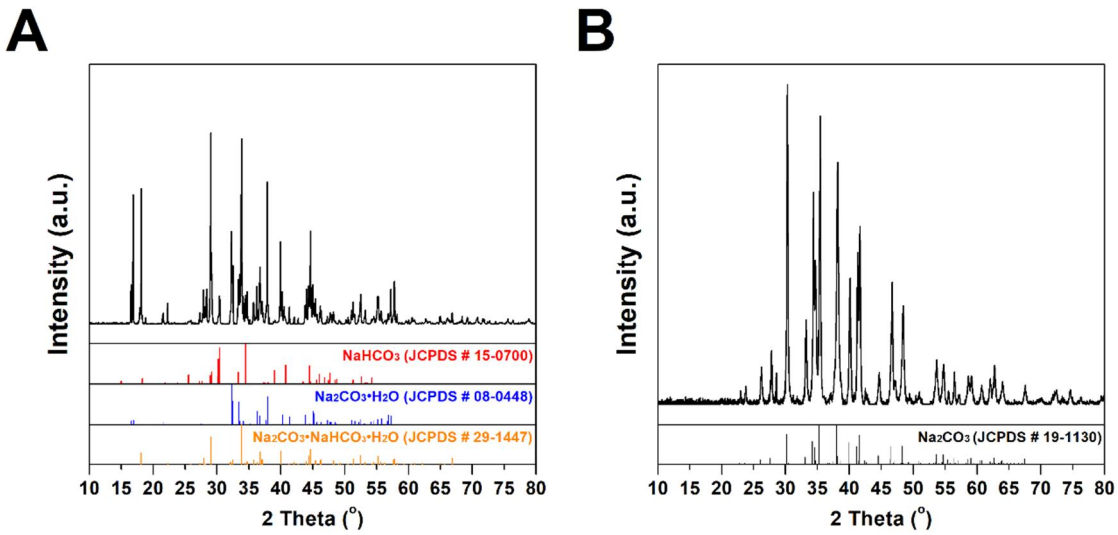

Figure 4-10 XRD profiles of the soluble product after discharge reaction obtained by various drying conditions. (A) Dried at room temperature. Because non-marine evaporites precipitate in different proportions of chemical elements from those found in the aqueous environments, three different minerals (nahcolite: $NaHCO_3$, thermonatrite: $Na_2CO_3 \cdot H_2O$, and trona: $Na_2CO_3 \cdot NaHCO_3 \cdot 2H_2O$) are naturally obtained. (B) Dried at 70 °C oven. Only Na_2CO_3 is formed when dried at high temperature.

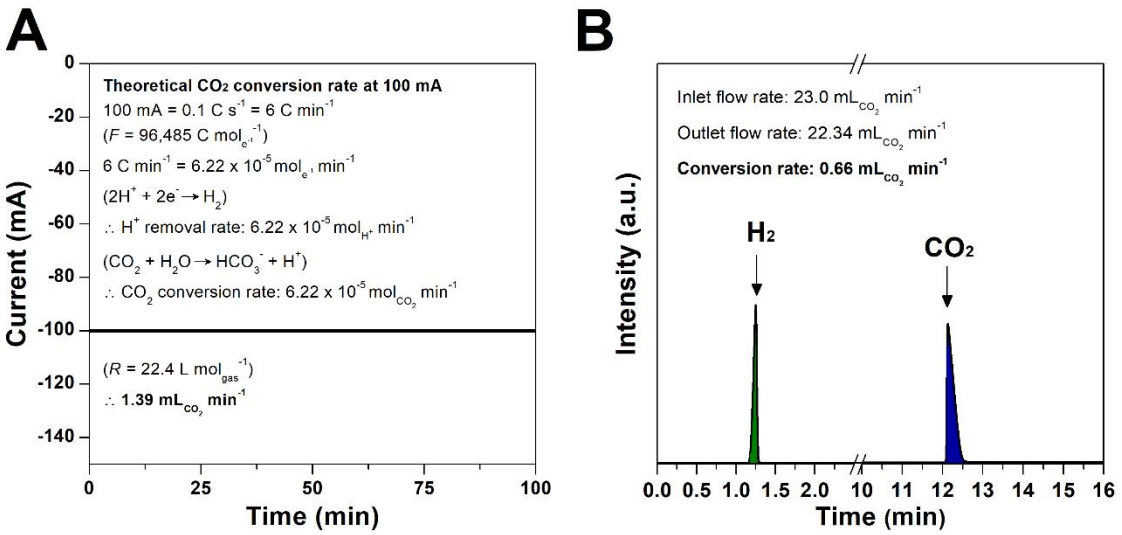

Figure 4-11 The experimental CO_2 conversion efficiency. (A) Theoretical CO_2 conversion rate at current of 100 mA. (B) The quantitative GC profiles of outlet CO_2 gas during practical measurement condition for different inlet CO_2 flow rate of 23.0 mL min^{-1}.

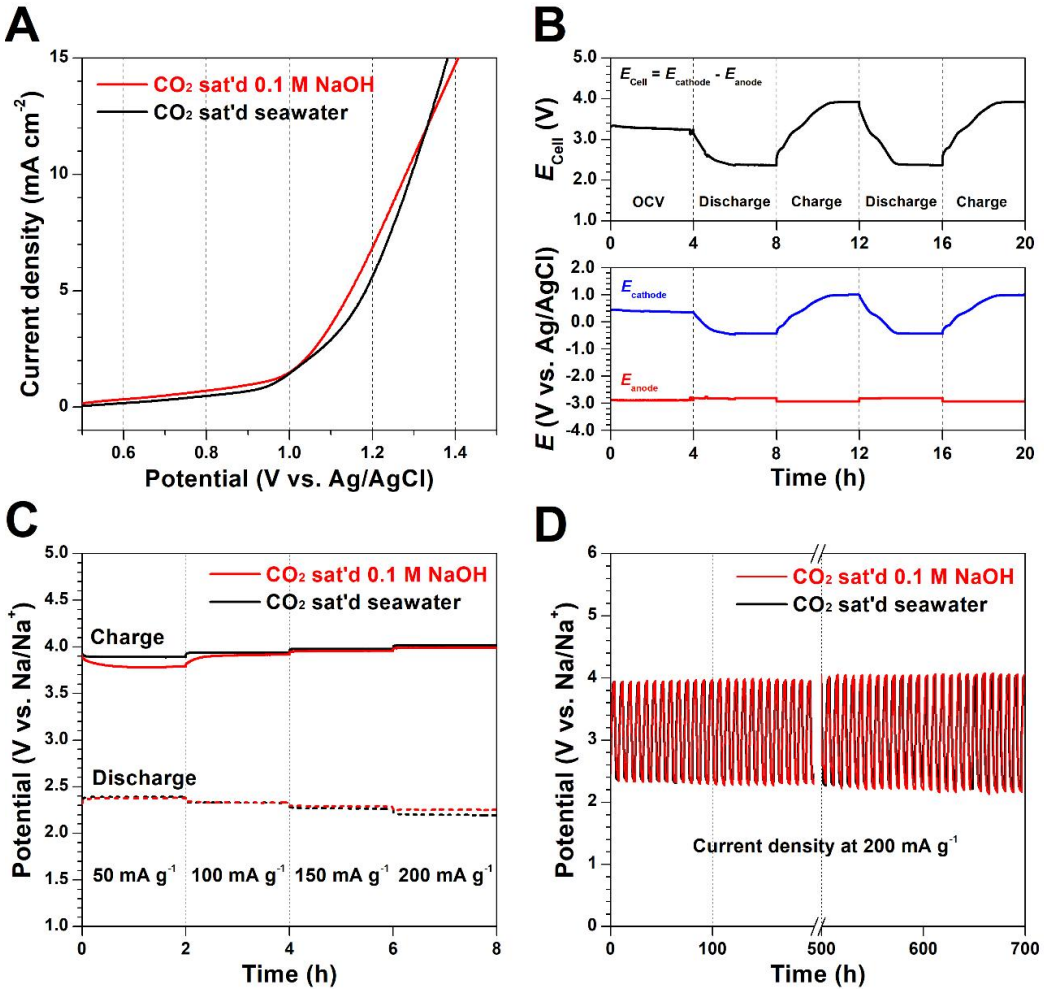

Figure 4-12 (A) Anodic RDE profile of Pt/C+IrO_2 catalyst measured in CO_2-saturated 0.1 M NaOH and seawater at 10 mV s^{-1}, where Pt as a counter electrode and Ag/AgCl electrode as a reference electrode. (B) Discharge-charge profiles measured in three-electrode configuration using Ag/AgCl reference electrode at 100 mA g^{-1}. (C) Charge-discharge profiles at various current densities under CO_2 saturated 0.1 M NaOH and seawater. (D) Cyclic charge-discharge performance measured in CO_2-saturated 0.1 M NaOH and seawater at a current density of 200 mA g^{-1} for 700 hours.

obtained and total gas, and each gas component profiles are indicated. The total gas is obtained in order of GCounts (1.25×10^9). For O_2, it obtained in almost same intensity (1.25×10^9). For CO_2, however, the intensity is obtained in 7.0×10^7, revealing the intensity is significantly smaller than that of O_2 (~ 2 order difference). Because the measuring is conducted in CO_2 purged aqueous electrolytes, the dissolved CO_2 could be generated. In the case of N_2, a bit more intensity is obtained in 3.0×10^8. Since N_2 cannot be produced in any electrochemical oxidation reactions, it is arisen from the inflow of air during measuring process. Therefore, the evolved gas during charging process is confirmed to be O_2. We also furtherly investigated the oxidation profiles in seawater, which present the typical chlorine evolution reaction (Kim et al., 2015) instead of OER (**Figure 4A**). It is noteworthy that the charging process does not generate CO_2 which had already been consumed during discharge, as opposed to the conventional metal-CO_2 battery system, which emits CO_2 during the charging process (Zhang et al.,

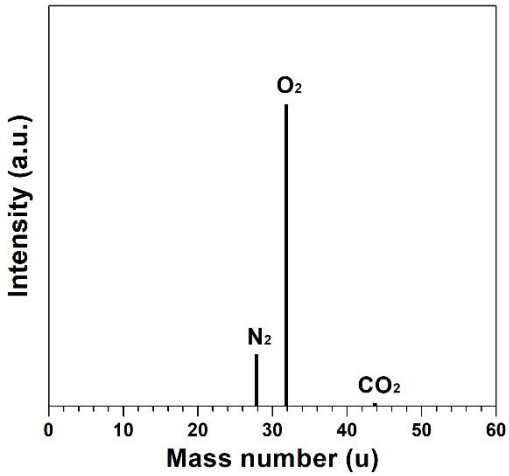

Figure 4-13 The GC profile of generated gas during the oxidation process.

2015; Qie et al., 2017; Hu et al., 2016; Al Sadat and Archer, 2016). The discharge-charge performance of this system was evaluated in the three-electrode configuration using Ag/AgCl reference electrode to closely distinguish the potential applied on the cathode and anode (**Figure 4B**). Since a cell potential (E_{cell}) is defined as a potential difference of cathode and anode ($E_{cathode}$ - E_{anode}), the potential gap decreases during discharging and increases at charging process. During repeating discharge-charge process, the cathode potential profile ($E_{cathode}$) presents discharging and charging plateau, clearly proving that this system is rechargeable. Further, the charge-discharge profiles at various current densities under CO_2-saturated NaOH solution and seawater are examined. Cyclic charge-discharge performance was evaluated to verify its reversibility and reproducibility (**Figure 4-12D**). Both of cyclic performances were highly reproducible and obtained without variations over a period of 700 hours, indicating that H_2 is stably produced utilizing CO_2 and that the cathode was kept fresh, without clogging or damage, during a repeating discharge and charge process.

4.4. Conclusions

In summary, we have devised hybrid Na-CO_2 cell utilizing CO_2 as a useful resource. This new system has three distinctive advantages. First, it uses a kinetically fast HER as a discharge reaction thanks to a spontaneous CO_2 dissolution, enabling the provision of high current compared to present aprotic system. Second, unlike conventional aprotic CO_2 batteries, where solid products are clogged on the electrodes, this system can continuously produce gas-phase hydrogen during discharge without damaging the electrode. This ability enabled highly stable performance to be achieved over 1,000 hours. Third, the proposed system has the unprecedented great advantage of not regenerating CO_2 while recycling Na metal through charging process. Therefore, this hybrid Na-CO_2 cell truly fulfills the purpose of a real CCUS technology, as it consumes CO_2 efficiently throughout the process. This novel system could potentially serve as a new CO_2 utilization technology and a stepping stone for the future utilization of renewable energy technologies.

We have devised hybrid Na-CO_2 cell utilizing carbon dioxide as a useful resource. Although we have utilized hydrogen evolution reaction as facile cathodic reaction rather than oxygen reduction reaction in aqueous electrolyte, we could not exclude that the discharge reaction of hybrid Na-CO_2 cell is relative slow rate because of the low conductivity of the ceramic NASICON electrolyte which can allow only Na^+ ion to pass through. The present work indicates the novel hydrogen generation technology from CO_2 utilization and is meaningful in that proves the additional CO_2 dissolution during the discharge process, but further work is required to improve the CO_2 conversion efficiency and power densities of the hybrid Na-CO_2 cell.

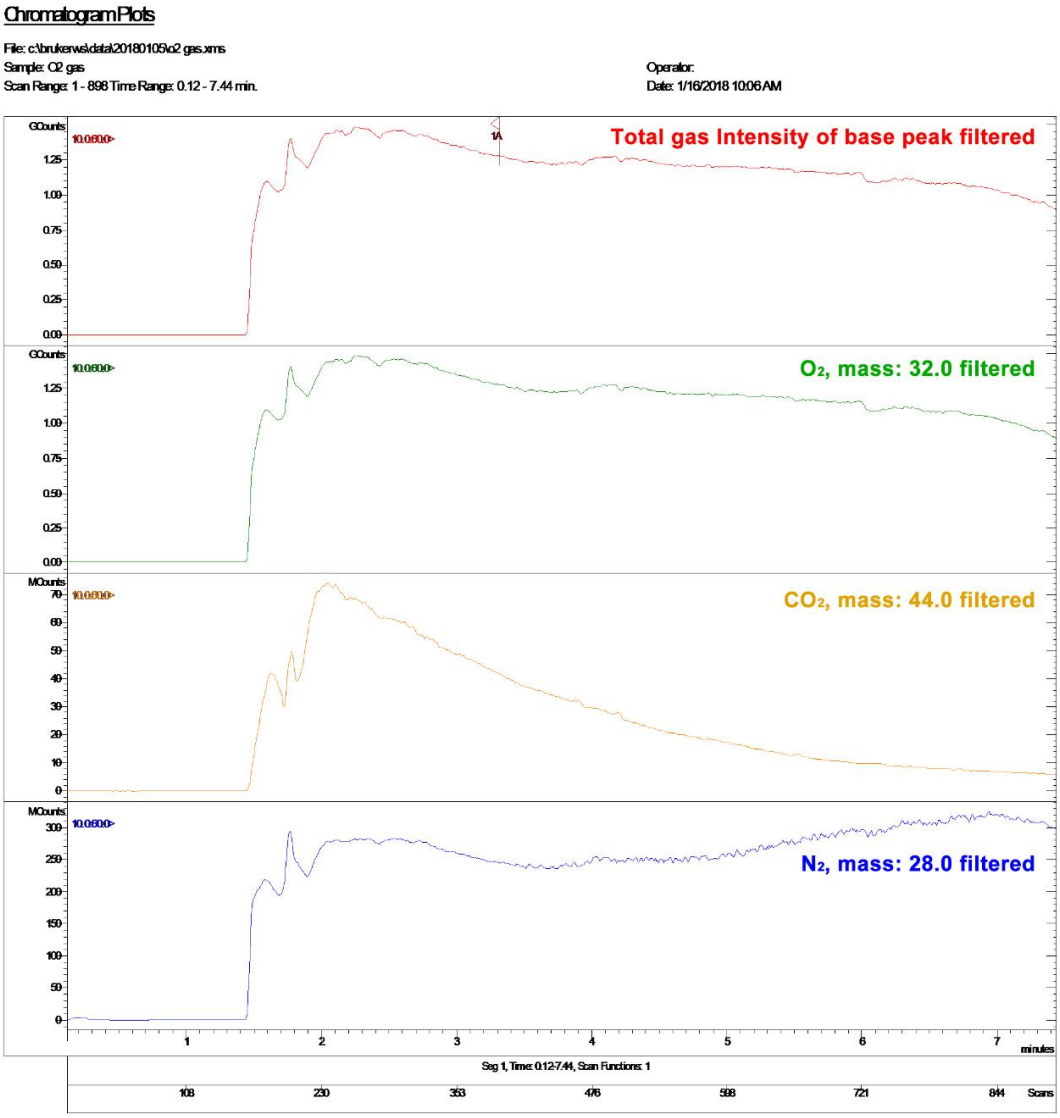

Figure 4-14 Raw data of gas chromatography profiles of evolved gas during charging process.

References

Jenkinson, D.S., Adams, D.E., and Wild, A. (1991). Model estimates of CO_2 emissions from soil in response to global warming. Nature *351*, 304-306.

Obama, B. (2017). The irreversible momentum of clean energy. Science *355*, 126-129.

Keith, D.W., Holmes, G., Angelo, D.St., and Heidel, K. (2018). A Process for Capturing CO_2 from the Atmosphere. Joule *2*, 1573-1594.

Andersen, S.O. (2017). We can and must govern climate engineering. Nature *551*, 415.

Dowell, N.M., Fennell, P.S., Shah, N., and Maitland, G.C. (2017). The role of CO_2 capture and utilization in mitigating climate change. Nat. Clim. Change *7*, 243-249.

Liu, C., Yang, B., Tyo, E., Seifert, S., DeBartolo, J., Issendorff, B.v., Zapol, P., Vajda, S., and Curtiss, L.A. (2015). Carbon dioxide conversion to methanol over size-selected Cu_4 clusters at low pressures. J. Am. Chem. Soc. *137*, 8676-8679.

Li, P.-Z., Wang, X.-J., Liu, J., Lim, J.S., Zou, R., and Zhao, Y. (2016). A triazole-containing metal-organic framework as a highly effective and substrate size-dependent catalyst for CO_2 conversion. J. Am. Chem. Soc. *138*, 2142-2145.

Angamuthu, R., Byers, P., Lutz, M., Spek, A.L., and Bouwman, E. (2010). Electrocatalytic CO_2 conversion to oxalate by a copper complex. Science *327*, 313-315.

Darensbourg, D.J. (2007). Making plastics from carbon dioxide: Salen metal complexes as catalysts for the production of polycarbonates from epoxides and CO_2. Chem. Rev. *107*, 2388-2410.

Bourzac, K. (2017). We have the technology. Nature *550*, S66-S69.

Markewitz, P., Kuckshinrichs, W., Leitner, W., Linssen, J., Zapp, P., Bongartz, R., Schreiber, A., and Müller, T.E. (2012). Worldwide innovations in the development of carbon capture technologies and the utilization of CO_2. Energy Environ. Sci. *5*, 7281-7305.

Mikkelsen, M., Jørgensen, M., and Krebs, F.C. (2010). The teraton challenge. A review of fixation and transformation of carbon dioxide. Energy Environ. Sci. *3*, 43-81.

Zhang, Z., Zhang, Q., Chen, Y., Bao, J., Zhou, X., Xie, Z., Wei, J., and Zhou, Z. (2015). The first introduction of graphene to rechargeable Li-CO_2 batteries. Angew. Chem. Int. Ed. *54*, 6550-6553.

Qie, L., Lin, Y., Connell, J.W., Xu, J., and Dai, L. (2017). Highly rechargeable lithium-CO_2 batteries with a boron- and nitrogen-codoped holey-graphene cathode. Angew. Chem. Int. Ed. *56*, 6970-6974.

Hu, X., Sun, J., Li, Z., Zhao, Q., Chen, C., and Chen, J. (2016). Rechargeable room-temperature Na-CO_2 batteries. Angew. Chem. Int. Ed. *55*, 6482-6486.

Al Sadat, W. I., and Archer, L.A. (2016). The O_2-assisted Al/CO_2 electrochemical cell: A system for CO_2 capture/conversion and electric power generation. Sci. Adv. *2*, e1600968.

Das, S.K., Xu, S., and Archer, L.A. (2013). Carbon dioxide assist for non-aqueous sodium-oxygen batteries. Electrochem. Commun. *27*, 59-62.

Noorden, R.V. (2014). A better battery. Nature *507*, 26-28.

Kwak, W.-J., Chen, Z., Yoon, C.S., Lee, J.-K., Amine, K., and Sun, Y.-K. (2015). Nanoconfinement of low-conductivity products in rechargeable sodium-air batteries. Nano Energy *12*, 123-130.

Housecroft, C.E., and Sharpe, A.G. (2005). Inorganic Chemistry 2nd edn (Pearson Prentice Hall).

Harris, D.C. (2010). Quantitative Chemical Analysis 8th edn (W. H. Freeman and Company).

Park, S.-M. Ho, S., Aruliah, S., Weber, M.F., Ward, C.A., and Venter, R.D. (1986). Electrochemical reduction of oxygen at platinum electrodes in KOH solution – temperature and concentration effects. J. Electrochem. Soc. *133*, 1641-1649.

Kim, C., Gwon, O., Jeon, I.-Y., Kim, Y., Shin, J., Ju, Y.-W., Baek, J.-B., and Kim, G. (2016). Cloud-like graphene nanoplatelets on $Nd_{0.5}Sr_{0.5}CoO_{3-}$ nanorods as an efficient bifunctional electrocatalyst for hybrid Li-air batteries. J. Mater. Chem. A *4*, 2122-2127.

Bu, Y., Gwon, O., Nam, G., Jang, H., Kim, S., Zhong, Q., Cho, J., and Kim, G. (2017). A highly efficient and robust cation ordered perovskite oxide as a bifunctional catalyst for rechargeable Zinc-air batteries. ACS Nano *11*, 11594-11601.

Mahmood, J., Li, F., Jung, S.-M., Okyay, M.S., Ahmad, I., Kim, S.-J., Park, N., Jeong, H.Y., and Baek, J.-B. (2017). An efficient and pH-universal ruthenium-based catalyst for the hydrogen evolution reaction. Nat. Nanotech. *12*, 441-446.

Xu, X., Chen, Y., Zhou, W., Zhu, Z., Su, C., Liu, M., and Shao, Z. (2016). A perovskite electrocatalyst for efficient hydrogen evolution reaction. Adv. Mater. *28*, 6442-6448.

Ahn, W., Park, M.G., Lee, D.U., Seo, M.H., Jiang, G., Cano, Z.P., Hassan, F.M., and Chen, Z. (2018). Hollow multivoid nanocuboids derived from ternary Ni-Co-Fe prussian blue analog for dual-electrolysis of oxygen and hydrogen evolution reactions. Adv. Funct. Mater. *28*, 1802129.

Wang, Z.-L., Xu, D., Xu, J.-J., and Zhang, X.-B. (2014). Oxygen electrocatalysts in metal-air batteries: from aqueous to nonaqueous electrolytes. Chem. Soc. Rev. *43*, 7746-7786.

Park, S., Vohs, J.M., and Gorte, R.J. (2000). Direct oxidation of hydrocarbon in a solid-oxide fuel cell. Nature *404*, 265-267.

Sengodan, S., Choi, S., Jun, A., Shin, T.H., Ju, Y.-W., Jeong, H.Y., Shin, J., Irvine, J.T.S., and Kim, G. (2015). Layered oxygen-deficient double perovskite as an efficient and stable anode for direct hydrocarbon solid oxide fuel cells. Nat. Mater. *14*, 205-209.

Yang, L. Wang, S., Blinn, K., Liu, M., Liu, Z., Cheng, Z., and Liu, M. (2009). Enhanced sulfur and coking tolerance of a mixed ion conductor for SOFCs: $BaZr_{0.1}Ce_{0.7}Y_{0.2-x}Yb_xO_{3-}$. Science *326*, 126-129.

Kim, J.-K., Lee, E., Kim, H., Johnson, C., Cho, J., and Kim, Y. (2015). Rechargeable seawater battery and its electrochemical mechanism. ChemElectroChem *2*, 328-332.

Chapter 5 Highly Efficient CO_2 Utilization *via* Novel Aqueous Zn or Al-CO_2 Systems for H_2 and Electricity Production

This chapter has been published and has been cited in the thesis by co-author C. Kim.

Reproduced with permission from C. Kim, J. Kim, S. Joo, Y. Yang, J. Shin, M. Liu, J. Cho, G. Kim, *Angew. Chem. Int. Ed* 2019, 58, 9506-9511.

5.1. Introduction

Carbon dioxide (CO_2), a greenhouse gas released largely by human activities, has important impact on the planet's balance of land, ocean, and air temperatures.[1] The trend of global warming is particularly alarming because it has been accelerated at an unprecedented rate in recent decades.[2] Accordingly, considerable efforts have been devoted to carbon capture, utilization, and storage/sequestration (CCUS) in an effort to reduce carbon footprint or to reuse CO_2 as a resource.[3] For instance, various chemical processes have been proposed to convert CO_2 to value-added carbon compounds such as methanol, organic materials, and plastics.[4] Also, there have been a few attempts to convert CO_2 to electrical energy using aprotic metal-CO_2 batteries.[5] The economic feasibility of the proposed conversion processes, however, is still inadequate due to low conversion efficiency.[6] Meanwhile, there is increasing global demand for hydrogen (H_2), a clean energy source, to be used as a promising alternative energy source to finite fossil fuels.[7] However, it has been pointed out that H_2 is mainly produced by a hydrocarbon thermolysis (*e.g.*, steam methane reforming) releasing a significant amount of CO_2 and an energy-intensive water electrolysis process.[8] Here we report a new zinc- or aluminum-CO_2 (Zn/Al-CO_2) system that can efficiently produce H_2 and electrical energy by consuming CO_2. The dissolution of CO_2 in an aqueous electrolyte is thermodynamically spontaneous and forms carbonic acid. By adopting kinetically efficient hydrogen evolution reaction (HER) utilizing the acidity of CO_2 as a cathodic reaction, this novel system could simultaneously generate electricity and H_2 driven by the electrochemical oxidation of Zn or Al metals. In addition, *in-operando* gas chromatograph measurements have demonstrated that our aqueous cell could perform comparable discharge rate to conventional Zn/Al-air cells with continuously utilizing CO_2. Thus, these Zn/Al-CO_2 systems have potential for efficient CO_2 removal, power and hydrogen generation in the era of pursuing a clean energy source.

5.2. Experimental

5.2.1. Catalysts preparation and characterization techniques

The 20wt.% Pt/C (Pt/C) and the few layer graphene, P-ML20, (FL-graphene) were purchased at Sigma-Aldrich and Sphere Advanced Materials Corp., respectively. $PrBa_{0.5}Sr_{0.5}Co_{1.5}Fe_{0.5}O_{5+}$ (PBSCF) was

synthesized by typical sol-gel process. Stoichiometric amounts of metal nitrate precursors and citric acid were dissolved in distilled water to form an aqueous mixed solution. An adequate amount of poly-ethylene glycol was added into the beaker after the mixture was dissolved. All chemical reactants were purchased from Sigma-Aldrich. After a viscous resin was formed, the solution was heated to 300 ^{o}C. The resultant powder was pre-calcined at 600 ^{o}C for 4 hours followed by calcination at 950 ^{o}C for 4 hours. Then, the powder was milled in a planetary ball mill (PM-200, Retsch Co., Germany) using Zr-balls at 400 rpm for 4 hours. The microstructure of the prepared catalysts was examined by scanning electron microscopy (SEM, Nova FE-SEM). The transmission electron microscopy (TEM) images were obtained using a high resolution-TEM (JEOL, JEM-2100F). The structural identification of the catalysts was conducted by X-ray powder diffraction (XRD) (Bruker diffractometer, Cu Kα radiation) at a scan rate of 1 ^{o} min^{-1}. The obtained patterns were analyzed using JADE 6.5 software. The generated gas from discharge (H_2) was collected with three-electrode configuration (Pt as a counter and Ag/AgCl as a reference electrode) in CO_2-saturated 1 M KOH and seawater by water substitution method using U-shaped tube. Then the gas was analyzed by gas chromatograph (Agilent 2820A GC instrument) with a thermal conductivity detector (TCD) and a packed column (Agilent carboxen 1000). The gas was controlled using a mass flow controller (Atovac GMC1200) and the exact volume of gas was calibrated through a bubble flow meter.

5.2.2. Half-cell analysis

Half-cell measurements were proceeded in three-electrode configuration using a platinum wire was used as both of working electrode and counter electrode with Ag/AgCl (saturated KCl filled) reference electrode in 1 M potassium hydroxide (KOH, Sigma-Aldrich Co.) aqueous solution and seawater (taken from sea of Ulsan and filtered to remove visible impurities). To estimate pH and hydrogen evolution potential, a reversible hydrogen electrode (RHE) calibration was conducted in H_2-saturated solutions where platinum wires were used as the working, counter electrodes and Ag/AgCl as a reference electrode at a scan rate of 1 mV s^{-1}. The rotating disk electrode (RDE) tests were conducted by using catalysts of Pt/C, PBSCF, and FL-graphene on RRDE-3A (ALS Co.). Each catalyst was prepared into a catalyst ink by dispersing 10 mg of the catalyst in 1 mL of a binder solution (45 : 45 : 10 = ethanol : isopropyl alcohol : 5 wt.% Nafion solution (Sigma-Aldrich Co.), volumetric ratio) followed by a bath sonication process. For PBSCF, 10 wt.% of KB (Ketjen black EC-600JD) was included as a conductive additive, *i.e.*, 9 mg of PBSCF and 1 mg of KB used. Then, RDE profiles were measured by drop-coating 5 μL of the catalyst ink onto glassy carbon disk electrode, where area is 0.1256 cm^2, at a scan rate of 5 mV s^{-1}. All half-cell profiles were iR compensated by measuring the resistance of solution (1 M KOH, CO_2-saturated 1 M KOH). All electrochemical tests were carried out using Biologic VMP3.

5.2.3. Full-cell measurements

The zinc- and aluminum-CO_2 system is tested in H-type cell. Zn and Al metal (purity higher than 99.99 %) were purchased at Alfa Aesar Co.. The system is composed of Zn or Al metal / alkaline electrolyte / glass membrane / quasi-neutral electrolyte / cathode. For the alkaline electrolyte, 6 M KOH and 4M NaOH aqueous solution was used for Zn and Al system, respectively. For glass membrane, a porous grade of G4 membrane was used. For the quasi-neutral electrolyte, CO_2-saturated 1 M KOH and seawater was used. The cathode was prepared by electro-spraying the catalyst ink onto a gas-diffusion layer (Toray carbon paper TGP-H-090, Fuel Cell Store Co.) with a loading density of 2 mg cm^{-2}. And silver wire was used as a current collector. The current density was normalized with the geometric area of the catalysts. For the calculation of practical H_2 generation and CO_2 conversion efficiency, Zn-CO_2 cell was adopted. All electrochemical tests were conducted using Biologic VMP3.

5.3. Result and discussion

5.3.1. The proposed aqueous Zn- or Al-CO_2 system and its reaction mechanism

As schematically illustrated **Figure 5-1**, the aqueous Zn- or Al-CO_2 (Zn/Al-CO_2) system uses safe, low-cost, and naturally abundant Zn and Al as the anode, which can run continuously as long as metals and CO_2 are supplied to the two electrodes, respectively. The Zn or Al metal anodes are kept in an alkaline electrolyte to allow facile and continuous electrochemical reaction. To maintain electrical neutrality within the cell, a glass membrane was employed to connect the two aqueous electrolytes. The cathodic reaction occurred under a quasi-neutral condition of CO_2-dissolved aqueous solution. To understand the complex reactions on this system from the CO_2 dissolution, the simultaneously occurring overall reaction was subdivided into the chemical reaction and the electrochemical reaction. The chemical reaction of CO_2 dissolution can be expressed as follows:

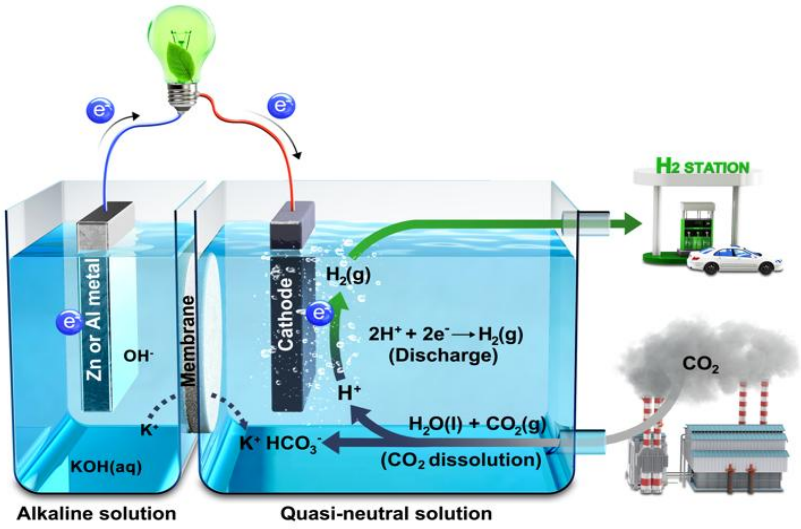

Figure 5-1 Schematic illustration of aqueous Zn- or Al-CO_2 systems and their reaction mechanism.

$$CO_2(aq) + H_2O(l) \rightleftharpoons H_2CO_3(aq), \qquad K_h = 1.70 \times 10^{-3} \qquad (1)$$

$$H_2CO_3(aq) \rightleftharpoons HCO_3^-(aq) + H^+(aq), \qquad pK_{a1} = 6.3 \qquad (2)$$

When CO_2 is purged into an aqueous solution (*e.g.*, distilled water, seawater, or KOH solution), CO_2 molecules spontaneously dissolve to form carbonic acid ($H_2CO_3(aq)$) determined by the hydration equilibrium constant[9] (K_h = 1.70 × 10^{-3} for a standard state condition in pure water) (**Eq. (1)**). Afterwards, the carbonic acid dissociates into HCO_3^- and H^+ is determined by the first acid dissociation constant[10] (pK_{a1} = 6.3) (**Eq. (2)**). Because carbonic acid is a polyprotic acid dissociating multiple steps, the second acid dissociation step (*i.e.,* $HCO_3^-(aq) \rightleftharpoons CO_3^{2-}(aq) + H^+(aq)$, pK_{a2} = 10.32) needs to be considered.[10] However, the second acid dissociation constant is significantly smaller than the first ($K_{a1} >> K_{a2}$) and is, hence, negligible for the pH calculation. This spontaneous CO_2 dissolution contributes to the acidification of the aqueous solution and lowering the pH level. The detailed CO_2 dissolution mechanism is available at **Text 1**.

The electrochemical reactions are composed of metal oxidation at the anode and hydrogen evolution on the cathode:

Anodic reactions:

$$\textit{Zn- system}: \quad Zn + 4OH^- \rightarrow Zn(OH)_4^{2-} + 2e^- \qquad E^o = -1.25\ V \qquad (3)$$

$$\textit{Al- system}: \quad Al + 3OH^- \rightarrow Al(OH)_3 + 3e^- \qquad E^o = -2.31\ V \qquad (4)$$

Cathodic reaction:

$$2H^+ + 2e^- \rightarrow H_2(g) \qquad E^o = 0.00\ V \qquad (5)$$

The anodic reaction is the electrochemical oxidation of Zn or Al metals in an alkaline electrolyte (**Eq. (3) and (4)**).[11] The cathodic reaction, hydrogen evolution reaction (HER), is closely affected by the pH of the aqueous solution (**Eq. (5)**). Unlike typical water splitting working in a strongly acidic or alkaline electrolyte, the HER in this study was proceeded in a quasi-neutral environment (pH ~7) formed by dissolving CO_2 in KOH solution or seawater. From the Nernst equation, HER potential is determined by pH and negatively shifted by 0.0592 V × pH. The acidity from CO_2 renders a favorable electrochemical reaction environment by acidifying the aqueous solution. The hydrogen evolution potential according to pH is shown in **Figure 5-2**. Then, the alkali metal bicarbonate is formed from the reaction of the dissolved bicarbonate ion and the transferred alkali metal ion to maintain the charge-neutrality of system (**Eq. (6)**).

$$HCO_3^-(aq) + K^+(aq) \rightarrow KHCO_3(aq) \qquad (6)$$

Text 1. CO_2 dissolution mechanism in an aqueous solution

The quantity of dissolved CO_2 depends on the partial pressure of CO_2 according to Henry's Law (pCO_2, atm). The partial pressure of CO_2, pCO_2, is given as 3.5×10^{-4} atm at standard state conditions (1 atm, 25°C). From Henry's law constant of 29.76 L atm mol^{-1}, the dissolved CO_2(aq) can be calculated to be 1.18×10^{-5} mol L^{-1} (**Eq. (1)**) [1].

$$CO_2(gas) \rightleftharpoons CO_2(dissolved), \quad \frac{[CO_2]}{\quad} = \frac{1}{k_H} \ (k_H = 29.76 \text{ L atm mol}^{-1}) \tag{1}$$

When dissolved CO_2(aq) hydrates, the spontaneous chemical equilibrium of CO_2(aq) hydration forms carbonic acid (H_2CO_3(aq)) determined by the hydration equilibrium constant [2] ($K_h = 1.70 \times 10^{-3}$). The concentration of H_2CO_3(aq) is determined as 1.41×10^{-8} mol L^{-1} (**Eq. (2)**).

$$CO_2(aq) + H_2O(l) \rightleftharpoons H_2CO_3(aq), \quad K_h = 1.70 \times 10^{-3} \tag{2}$$

Then, carbonic acid dissociates into HCO_3^- and H^+ as presented in **Eq. (3)**. Because the concentration of both carbonic acid and dissolved CO_2 are considered, $K_{a1} = 4.46 \times 10^{-7}$, the apparent acid dissociation constant [3], is used for the first acid dissociation step.

$$H_2CO_3(aq) \rightleftharpoons HCO_3^-(aq) + H^+(aq), \quad pK_{a1} = 6.35 \tag{3}$$

Because carbonic acid is a polyprotic acid, the second acid dissociation step (**Eq. (4)**) is also considered.

$$HCO_3^-(aq) \rightleftharpoons CO_3^{2-}(aq) + H^+(aq), \quad pK_{a2} = 10.33 \tag{4}$$

From the second acid dissociation constant of $K_{a2} = 4.69 \times 10^{-11}$, $[HCO^{3-}(aq)]$, $[CO_3^{2-}(aq)]$, and $[H^+(aq)]$ can be calculated to be 2.29×10^{-6}, 4.69×10^{-11}, and 2.29×10^{-6}, respectively. Then, the pH of the CO_2 dissolved solution is 5.64, confirming that CO_2 dissolution acidifies the dissolved solution.

However, the second acid dissociation constant is significantly smaller than the first acid dissociation constant ($K_{a1} >> K_{a2}$), hence negligible to consider the second acid dissociation step when calculating the concentration of protons in the aqueous solution. If only the first acid dissociation step was considered, the pH can be determined as 5.64. Therefore, the first acid dissociation step, *i.e.*, $H_2CO_3(aq) \rightleftharpoons HCO_3^-(aq) + H^+(aq)$, is the dominant step to raising $[H^+(aq)]$ during the CO_2 dissolution process in water.

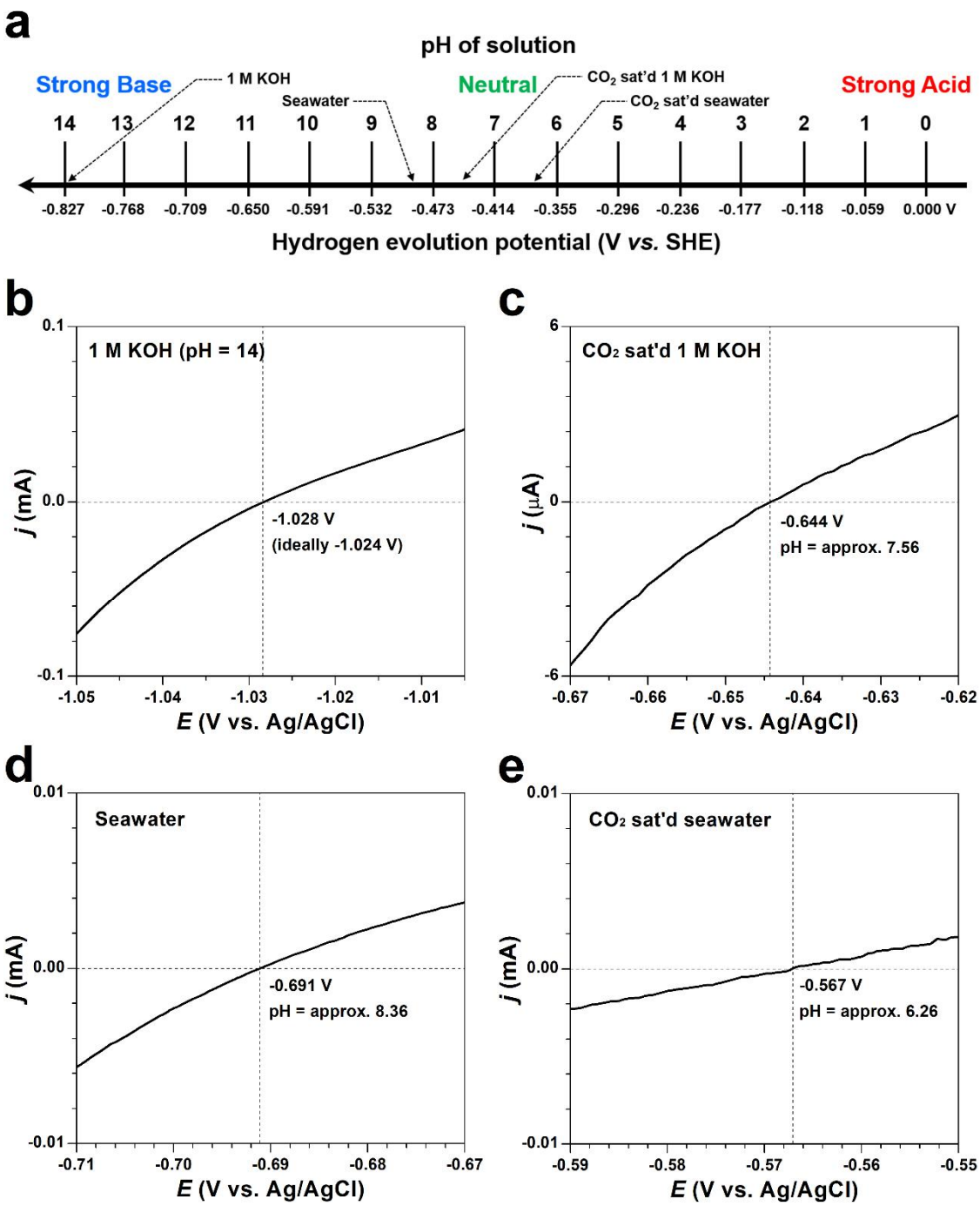

Figure 5-2 Hydrogen evolution potential according to a pH of aqueous solution. Hydrogen evolution potential is closely correlated to the pH value and follows the equation, *E* (V *vs.* SHE) = 0.000 – 0.0591 × pH and *E* (V *vs.* Ag/AgCl) = -0.197 – 0.0591 × pH. (a) Schematics diagram of hydrogen evolution potential related to pH. RHE calibration profile corresponding to hydrogen evolution potential measured in (b) 1 M KOH (c) CO_2 saturated 1 M KOH (d) seawater and (e) CO_2 saturated seawater.

5.3.2. Half-cell configured electrochemical analysis

The electrochemical profiles were closely examined on Pt-wire electrode using cyclic voltammetry (CV) (**Figure 5-3a**) under various gas saturated conditions. An apparent oxygen reduction peak appeared near -0.15 V (*vs.* Ag/AgCl) in O_2-saturated 1 M KOH, corresponding possibly to oxygen reduction reaction (ORR) on Pt electrode.[12] The typical diffusion-controlled region with the limiting current was observed near -0.4 V from O_2 mass transfer limitation in the ORR profile.[11c,12b] At the lower potential region, the steep reduction profiles were observed around -1.05 V of the O_2- and N_2-saturated conditions corresponding to typical hydrogen evolution reaction (HER).[13] In contrast, for CO_2-saturated condition, the onset potential of HER shifted positively by 0.4 V due to decreased pH from the CO_2 dissolution. It is notable that, contrary to typical ORR profile, the HER profiles present the sharply increasing reduction curves without a diffusion-controlled region. To gain in-depth insights into the electrochemical reactions, Tafel plots derived from polarization curves are also constructed (**Figure 5-3b**). Because ORR is regarded as one of the most complex electrochemical reactions, simultaneously

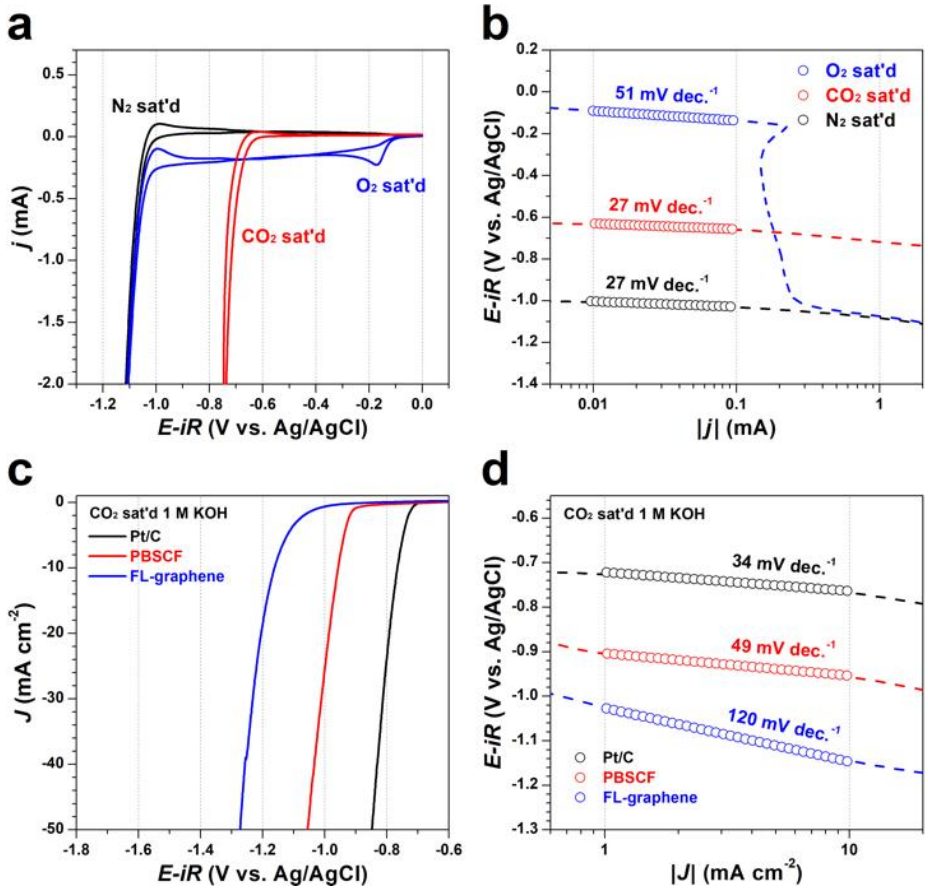

Figure 5-3 Half-cell configured reduction profiles. A reference potential is described with Ag/AgCl instead of RHE for the clarification of potential difference in a relationship between purging gases and pH. (a) Cathodic CV profiles measured in O_2, N_2, and CO_2-saturated 1 M KOH at 10 mV s^{-1}, where Pt-wire is a working and counter electrode. (b) Tafel analysis of the cathodic profiles. (c) RDE polarization curves for various catalysts measured in CO_2-saturated 1 M KOH. (d) Tafel plots derived from the RDE profiles.

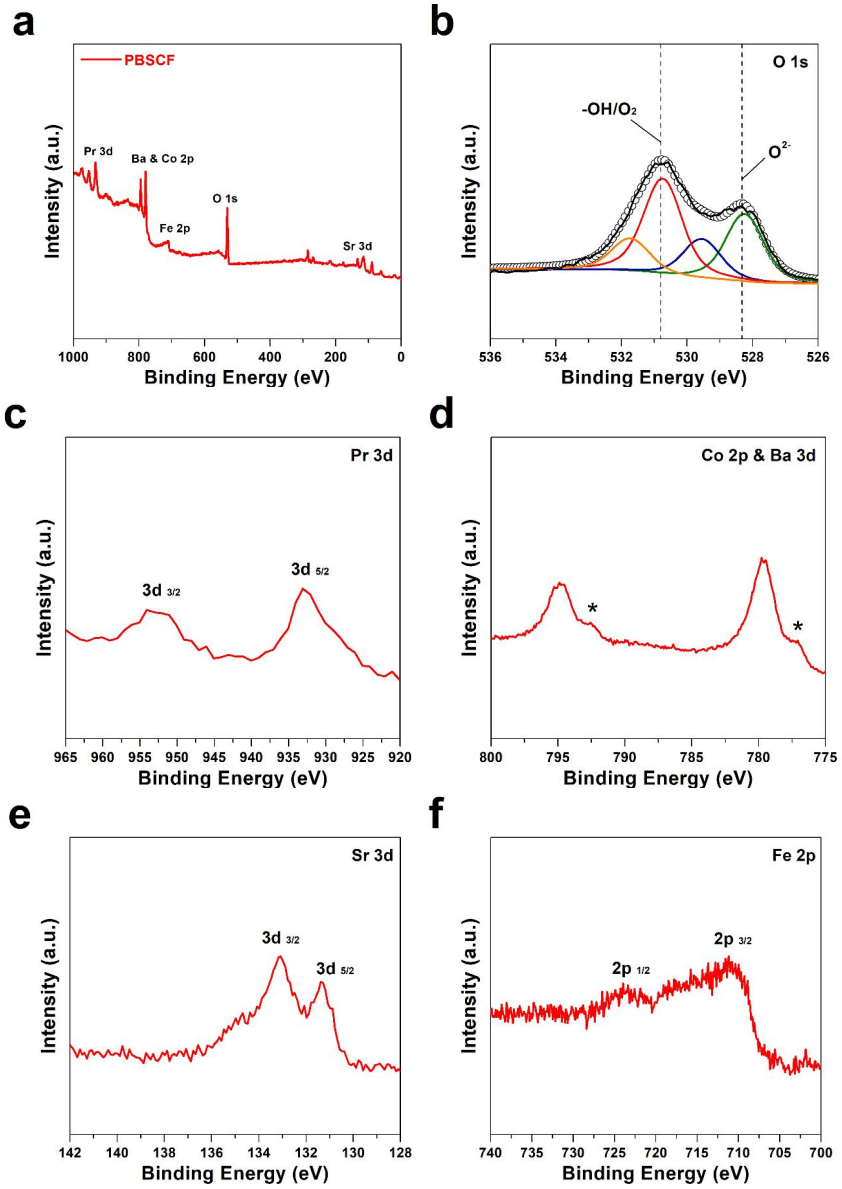

Figure 5-4 (a) XPS spectra of PBSCF; (b) O 1s, (c) Pr 3d, (d) Co 2p and Ba 3d, (e) Sr 3d, (f) Fe 2p.

involving 4 electrons with 2 reactants (O_2 and H_2O), the reaction kinetics is sluggish even on a Pt electrode as obtained to be 51 mV dec.$^{-1}$. By contrast, HER only involves 2 electrons with 1 reactant (H^+ or H_2O depending on pH) and presents a low Tafel slope of 27 mV dec.$^{-1}$, suggesting that the HER pathway is followed by the Volmer-Tafel mechanism.[13f,13g,14] Thus, this reduction reaction involving CO_2 dissolution notably contributes to the improvement of the reaction potential and kinetics, enabling adoption as a highly efficient cathodic reaction for the novel Zn- or Al-CO_2 systems.

To examine HER activities under the quasi-neutral environment for various catalysts, rotating disk electrode (RDE) polarization curves were acquired (**Figure 5-3c**) and Tafel plots were presented (**Figure 5-3d**). We adopted $PrBa_{0.5}Sr_{0.5}Co_{1.5}Fe_{0.5}O_{5+}$ (PBSCF), which reported to be active HER

catalyst in alkaline media,[13f,15] few-layer graphene (FL-graphene), which has been extensively studied as an HER catalyst in an acidic media,[14a,16] and Pt/C, commonly used as a referencing catalyst. Pt/C exhibits superior HER activity under CO_2-saturated condition with the onset potential of -0.65 V and Tafel slope of 34 mV $dec.^{-1}$, corresponding well to the value observed in Pt-wire electrode (**Figure 5-3a**) and RHE calibration profile (**Figure 5-2**). PBSCF displays active hydrogen evolution profile in the quasi-neutral environment from high lattice oxygen concentration and partially oxidized cobalt species as examined in X-ray photoelectron spectroscopy (XPS) profiles (**Figure 5-4**) with the onset potential of -0.9 V and Tafel slope of 49 mV $dec.^{-1}$, suggesting the Volmer- Heyrovsky as the HER pathway.[13f,13g,14] While FL-graphene shows a slightly negative-shifted polarization curve at -1.1 V, its current density increases rapidly owing to its defects and edges of basal plane reported as the active catalytic center for HER with the Tafel slope of 120 mV $dec.^{-1}$.[16a] These performance profiles imply significance in terms of the electrochemical reaction occurring under the quasi-neutral condition because typical water splitting is performed either in strongly acidic or alkaline electrolytes. Actually, a quasi-neutral condition (pH ~7) can provide a less corrosive environment and could allow a potential adoption of abundant and non-noble metal-based electrocatalysts. In addition, the continuous hydrogen evolution deriving a pH increase could be compensated *via* an additional dissolution of CO_2 so that the pH level remains constant.

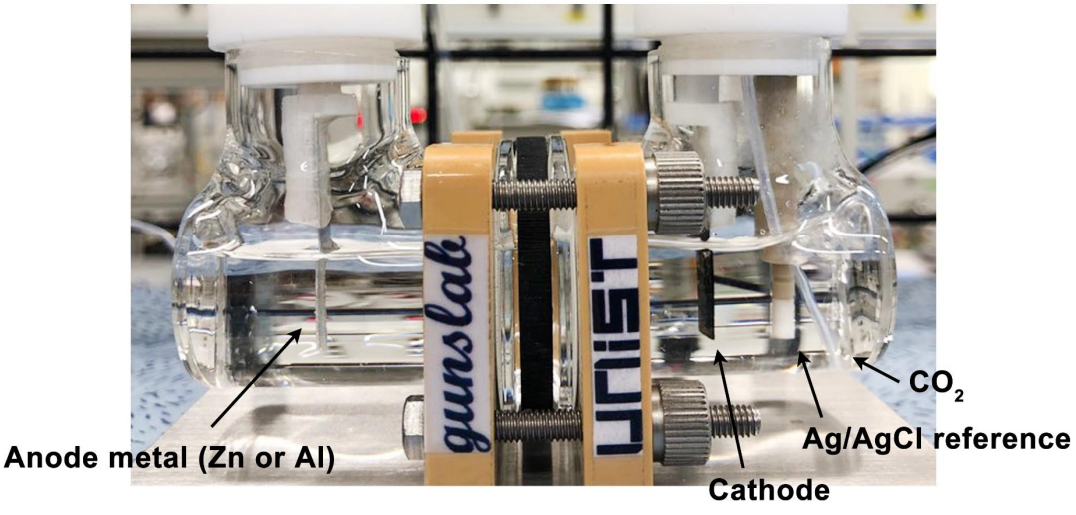

Figure 5-5 The digital photograph of Zn- or Al-CO_2 system

5.3.3. Electrochemical performances and *in-operando* quantitatively analysis

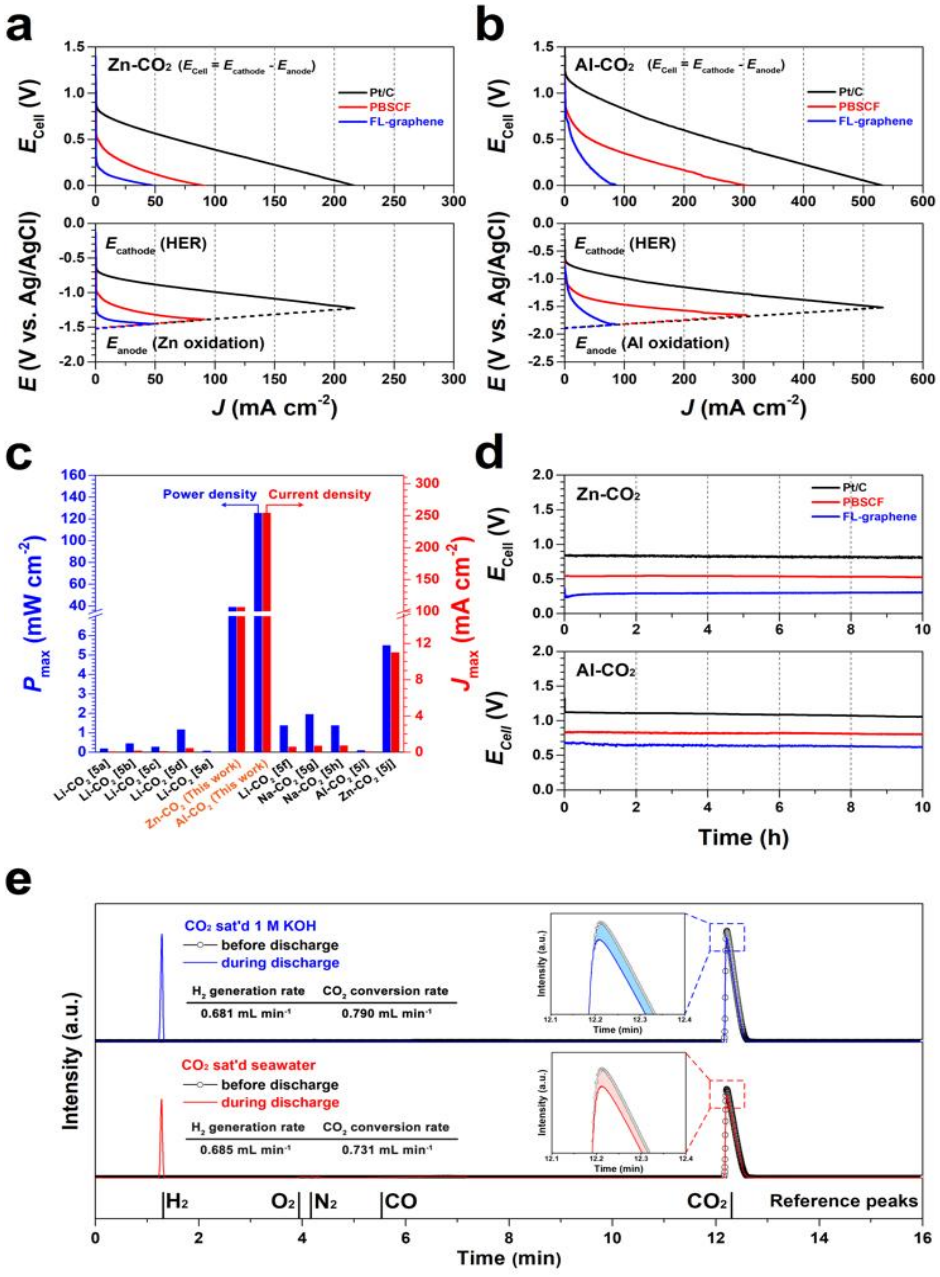

Figure 5-6 Zn- and Al-CO_2 systems performance. Full cell tests were conducted in three-electrode configuration using Ag/AgCl reference electrode. The polarization *I-V* profiles were measured under CO_2-saturated 1 M KOH for various catalysts for (a) Zn-CO_2 system and (b) Al-CO_2 system. (c) Comparison of maximum power density and corresponding current density for various metal-CO_2 cells. (d) Chronopotentiometric reduction profiles at 5 mA cm^{-2} in CO_2-saturated 1 M KOH for Zn-CO_2 system (above) and Al-CO_2 system (below). (e) The *in-operando* qualitative GC profiles of outlet CO_2 feed gas before and during discharging at 100 mA under CO_2-saturated 1 M KOH (above) and seawater (below). The enlarged areas near 12 min indicating the amount of converted CO_2 is shown as the insets.

By adopting this new reaction environment, herein the actual working performance of Zn- and Al-CO_2 systems were evaluated. The digital photograph of cell system can be seen at **Figure 5-5**. The full cell

tests were conducted in three-electrode configuration using Ag/AgCl reference electrode to distinguish the overall cell reaction into the cathodic and anodic reactions. **Figure 5-6a** presents the polarization curves for Zn-CO_2 systems based on various catalysts. The lowermost curves (dashed lines) denoted E_{anode} indicate the oxidation *I-V* profiles of Zn anode, revealing that the anode potentials are achieved reproducibly for all catalysts. The open-circuit voltage (OCV) for Pt/C is determined to be around 0.9 V from the difference between the anodic OCV (Zn oxidation potential) and the cathodic OCV (HER potential) at -1.5 V and -0.6 V *vs*. Ag/AgCl, respectively. As observed from the polarization profiles, the maximum current densities achieved were 48.3, 91.3, and 216.5 mA cm^{-2} for FL-graphene, PBSCF, and Pt/C, respectively. Notably, the maximum power density for Pt/C is measured to be 39.1 mW cm^{-2} at 106.6 mA cm^{-2}. This performance indicates that this Zn-CO_2 system has a facile and highly efficient cathodic reaction compared to the highest performance reported for the metal-CO_2 cells (*i.e.,* Zn-CO_2 cell based on CO_2-HCOOH interconversion: 5.5 mW cm^{-2} at 11 mA cm^{-2}).[5j] The polarization *I-V* profiles obtained at the various catalyst loading density and concentration of KOH solution are presented in **Figure 5-7.** It is important to note that this cell consumes CO_2 to generate not only electrical energy but also H_2 gas under the quasi-neutral condition (Note: H_2 is a byproduct during discharge

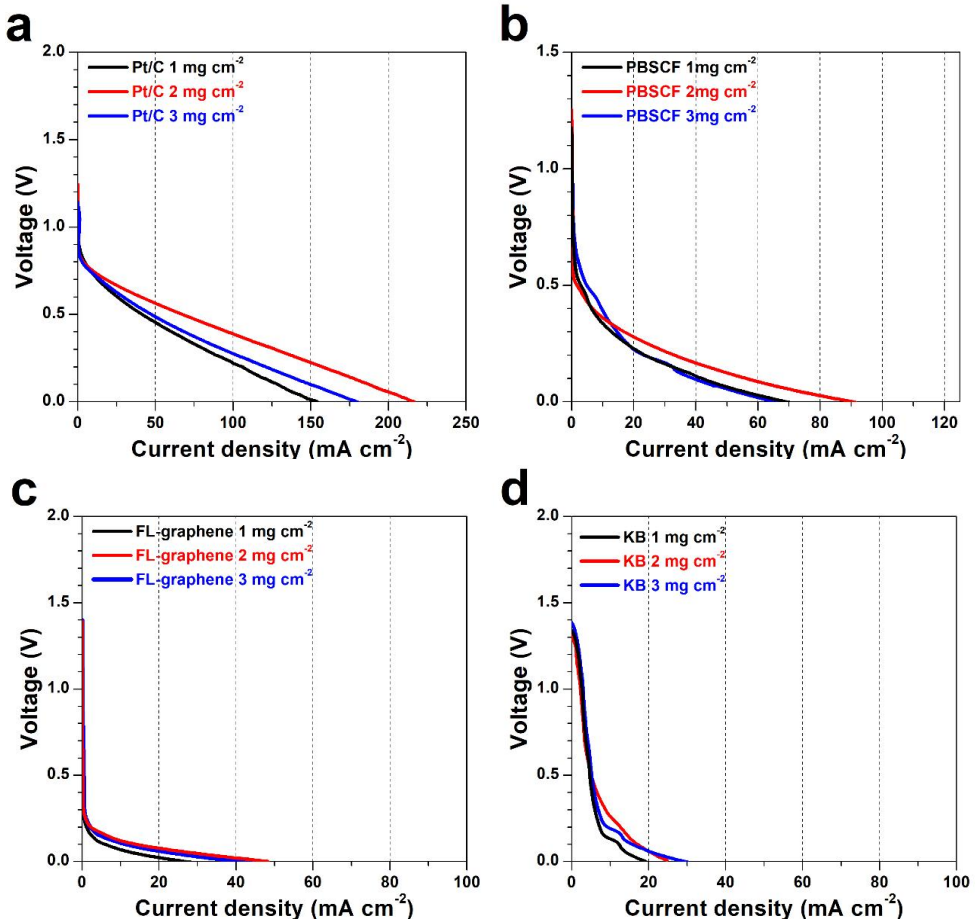

Figure 5-7 The polarization *I-V* profiles obtained at the various catalyst loading density of 1, 2, and 3 mg cm^{-2} for (a) Pt/C, (b) PBSCF, (c) FL-graphene, (d) KB.

process).

The polarization discharge curves for Al-CO_2 system are presented in **Figure 5-6b**. The Al-CO_2 system has a slightly higher OCV (1.3 V) than that of the Zn-CO_2 system (the oxidation of Al was observed at -1.9 V *vs*. Ag/AgCl). As similarly observed in the Zn-CO_2 system, the oxidation *I-V* profiles of Al anode are also achieved reproducibly for all catalysts. For the Al-CO_2 system, the maximum current densities achieved were 87.3, 305.3 and 532.1 mA cm^{-2} for FL-graphene, PBSCF, and Pt/C, respectively. Surprisingly, the highest electrochemical performance was obtained at a maximum power density of 125.4 mW cm^{-2} at 254.3 mA cm^{-2} for Pt/C catalyst, far superior to the best performance reported for the metal-CO_2 systems; *i.e.*, Zn-CO_2 cell based on CO_2-HCOOH interconversion of 5.5 mW cm^{-2} at 11 mA cm^{-2}.[5j] For direct comparison, the maximum power density (P_{max}) and the corresponding current density (J_{corr}) of various metal-CO_2 cells in the literatures[5] were presented in **Figure 5-6c**. The performances of both Zn- or Al-CO_2 systems are clearly better than those of the conventional aprotic metal-CO_2 systems[5a-5i]. Interestingly, it has been observed that the performances of our systems are comparable to those of Zn- or Al-air cells which have been actively studied as promising representatives of metal-air batteries.[11]

To investigate the stability and durability of this system, the chronopotentiometric profiles on a mechanically rechargeable Zn/Al-CO_2 system were examined at current density of 5 mA cm^{-2} (**Figure 5-6d**). For the Zn-CO_2 system, as similarly observed in the polarization profiles of **Figure 5-6a**, Pt/C, PBSCF, and FL-graphene presents 0.84, 0.54, and 0.30 V, respectively, for 10 hours. For the Al-CO_2 system tested under the same conditions, the discharge voltages were slightly higher: 1.11, 0.83, and 0.63 V for Pt/C, PBSCF, and FL-graphene, respectively. The discharge profiles measured at high current densities (10 and 50 mA cm^{-2}) more than 50 hours for Zn/Al-CO_2 systems using Pt/C are shown in

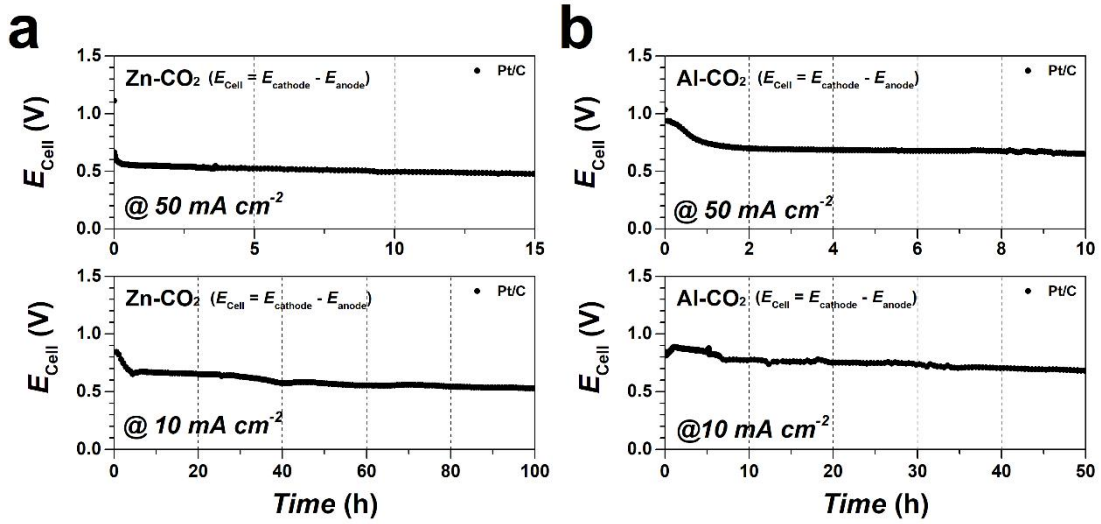

Figure 5-8 Discharge profiles measured at the current density of 10 and 50 mA cm^{-2} for (a) Zn-CO_2 and (b) Al-CO_2 cell using Pt/C catalyst. The discharge profile of Al-CO_2 cell in this figure was measured by using a low purity Al plate (Al plate, alloy 6061, Alfa-aesar Co.) rather than the high purity Al foil (99.99 %) because a self corrosion rate of thin Al foil is too fast.

Figure 5-8. It is notable that all profiles have shown in plateau without significant degradation, indicating a stable generation of a gas phase H_2 and electricity. In other words, there is no clogging or physical damage on the electrode during continuous operation as examined from scanning electron microscopy images of Pt/C, PBSCF, and FL-graphene (**Figure 5-9, 5-10, and 5-11**), unlike existing aprotic metal-CO_2 cells which have solid products, such as Li_2CO_3(s) or Na_2CO_3(s) on electrodes during discharge.[5a-5i] Also, the discharge profiles were further investigated in CO_2 dissolved seawater electrolyte, an environment similar to the natural condition for removing atmospheric CO_2 (**Figure 5-12**). The performance profiles measured in CO_2-saturated seawater for Zn- and Al-CO_2 systems were obtained at 0.77 and 1.00 V for Pt/C, respectively, indicating also active and stable performance. Consequently, this finding confirmed that the dissolution of CO_2 led to a favourable HER environment in both KOH solution and seawater.

To identify the continuity of this system, the H_2 generation and CO_2 conversion rate were simultaneously analysed by the quantitative gas chromatography (GC) measurement *in-operando* condition. The Faraday efficiency of H_2 generation and the practical CO_2 conversion efficiency were investigated. **Figure 5-6e** presents the *in-operando* quantitative GC profiles measured at a discharge current of 100 mA using CO_2-saturated 1 M KOH and seawater based on the Zn-CO_2 system configuration. During the measurement CO_2 was purged at bottom side of the electrolyte. The blue- and red-coloured areas shown in **the inset of Figure 5-6e** indicate the converted amount of CO_2 during discharging reaction in CO_2-saturated 1 M KOH and seawater, respectively. Only pure CO_2 gas was detected from the outlet gas before discharging the system. When the system is discharged, the pure H_2 was detected without any other impurities and the amount of CO_2 feed gas was decreased both under CO_2-saturated 1 M KOH and seawater as shown in **Figure 5-6e** and **Figure 5-13**. The actual amount of generated H_2 and converted CO_2 during the cell operation under CO_2-saturated 1 M KOH were measured to be 0.681 and 0.790 mL min^{-1}, respectively. Since the theoretical H_2 generation rate was calculated as 0.696 mL min^{-1} at a current of 100 mA, the Faraday efficiency of H_2 generation was determined to be 97.9 % under CO_2-saturated 1 M KOH solution, confirming the efficient H_2 generation of this system. Then, the CO_2 conversion efficiency of the *in-operando* condition was evaluated to be 56.8 % due to the theoretical CO_2 conversion rate of 1.39 mL min^{-1}. Therefore, this GC profile clearly indicates that the additional CO_2 dissolution proceeds during the discharge process. Also, the H_2 generation and CO_2 conversion rates were similarly observed under CO_2-saturated seawater (**Figure 5-6e**). The Faraday efficiency and the CO_2 conversion efficiency were 94.5 and 52.6 %, respectively. Again, these *in-operando* GC profiles clearly demonstrate that the proposed system could continuously utilize CO_2 to produce H_2 and electrical energy. Further, the reversibility of this system was investigated and the system is revealed to be rechargeable under both CO_2-saturated KOH solution and seawater.

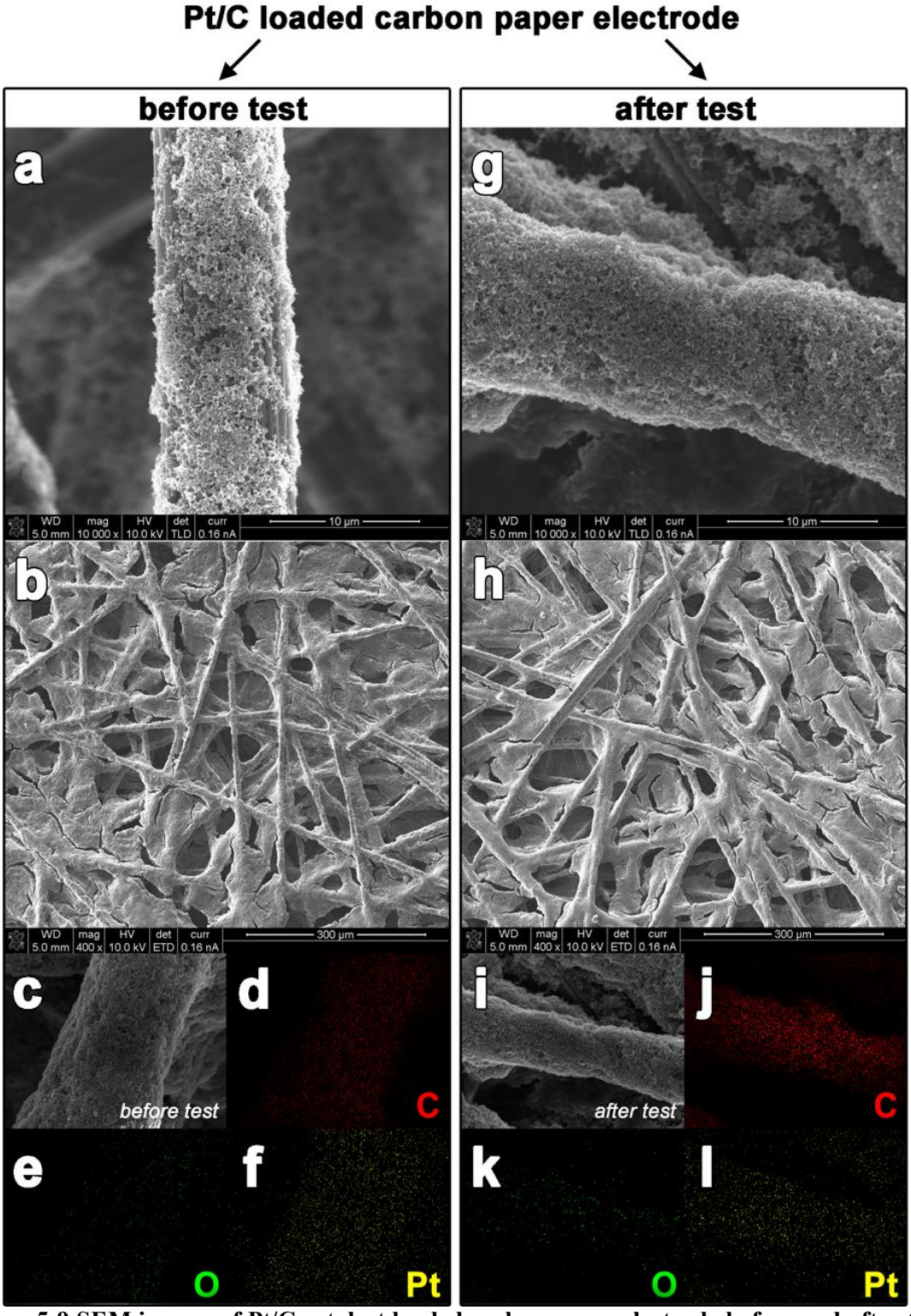

Figure 5-9 SEM images of Pt/C catalyst loaded carbon paper electrode before and after tests in Zn- and Al-CO_2 systems. (a) and (b) SEM images of Pt/C electrode before tests. (c) Energy dispersive X-ray spectroscopy (EDX) image of the electrode before tests. Corresponding elements mapping images for (d) carbon (e) oxygen and (f) platinum. (g) and (h) SEM images of Pt/C electrode after tests. (i) EDX image of the electrode before tests. Corresponding elements mapping images for (j) carbon (k) oxygen and (l) platinum.

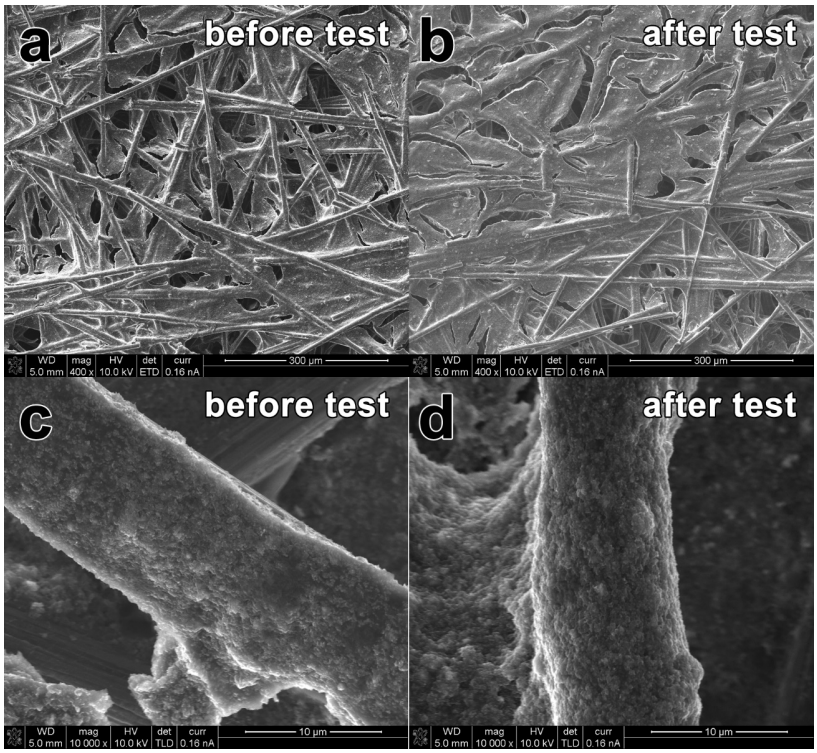

Figure 5-10 SEM images of PBSCF loaded electrode. (a) SEM image of PBSCF catalyst electrosprayed carbon paper electrode examined before a test (b) after electrochemical test. (c) and (d), enlarged images of (a) and (b), presenting PBSCF loaded carbon fiber tissue of carbon paper electrode.

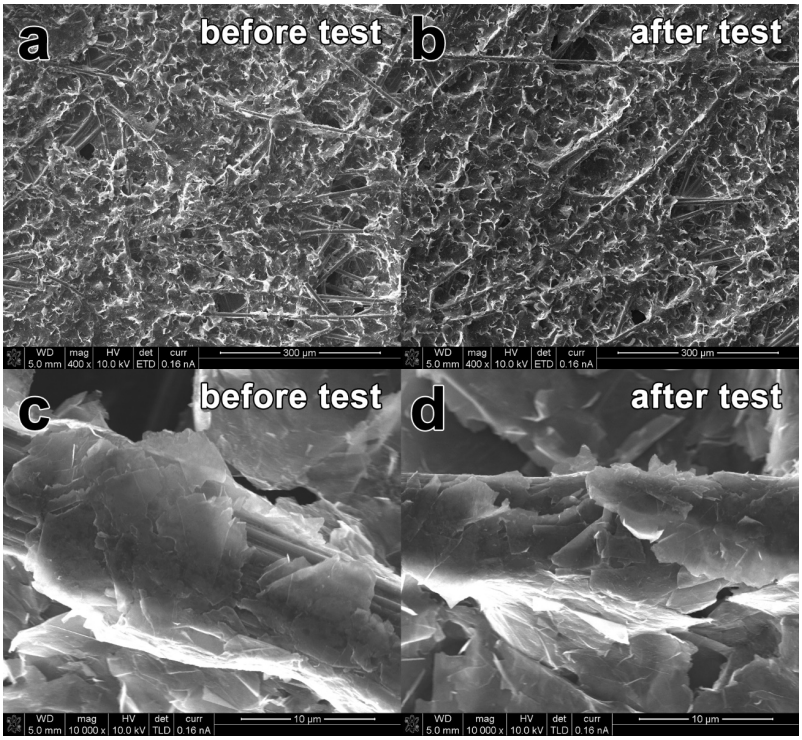

Figure 5-11 SEM images of FL-graphene loaded electrode. (a) SEM image of FL-graphene catalyst electrosprayed carbon paper electrode examined before a test, (b) after electrochemical test. (c) and (d), enlarged images of (a) and (b), presenting FL-graphene loaded carbon fiber tissue of carbon paper electrode.

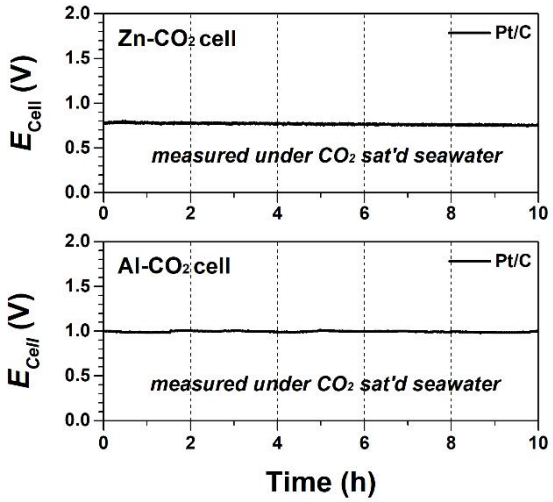

Figure 5-12 Chronopotentiometric discharge profiles of Zn- and Al-CO_2 systems measured under CO_2 saturated seawater.

5.3.4. Structural analysis of product and feed gas after long-term stability test

We examined the continuity of the system when the electrolyte is saturated with the carbonate ions. The electrochemical profiles were investigated when the system approaching the saturation condition. When discharge reaction continues, CO_2 can be further dissolved, and carbonate ions can be accumulated. Since CO_2-saturated 1 M KOH includes approximately 1 mol CO_2 in 1 L (*i.e.*, ~1 M $KHCO_3$ solution), two- or three-times accumulation of carbonate from continuous electrochemical reaction will produce 2 or 3 M $KHCO_3$ solution. Then, we investigated the solution resistance in the concentrated carbonate solution (**Figure 5-14e**) and the HER profiles **(Figure 5-14f)** to examine the effect of carbonate ion accumulation. As observed from HER profiles, the increased carbonate ions concentration in the solution preferably contributes to the increased HER activities owing to the decreased solution resistance, indicating that the system is sustainable under the concentrated carbonate conditions.

When discharge reaction continues, the pH increases due to H^+ removal due to H_2 generation, and CO_2 can be further dissolved. To understand the effect of carbonate ion accumulation on pH, the causal relationship needs to be considered first. The accumulation of carbonate ions occurs only in an environment where pH is elevated due to the continuous hydrogen evolution reaction (HER). In other words, the accumulation of carbonate ions does not affect the pH, but the increase of pH causes additional dissolution of CO_2, restoration of pH, and accumulation of carbonate ions. It can also be assumed that the maximum carbonates ion solubility is reached by a continuous electrochemical reaction. CO_2-saturated 1 M KOH includes approximately 1 mol CO_2 for 1 L (*i.e.*, ~1 M $KHCO_3$ solution). When CO_2 is dissolved 2 or 3 times more by accumulation of carbonate from continuous electrochemical reaction, then the solution concentration will be 2 or 3 M $KHCO_3$ solution. We investigated the solubility of $KHCO_3$ as shown in **Fig. S20**, which means that it is still possible to furtherly dissolve CO_2 in 1 M $KHCO_3$ solution. Thus, the effect from solubility of CO_2 can be excluded.

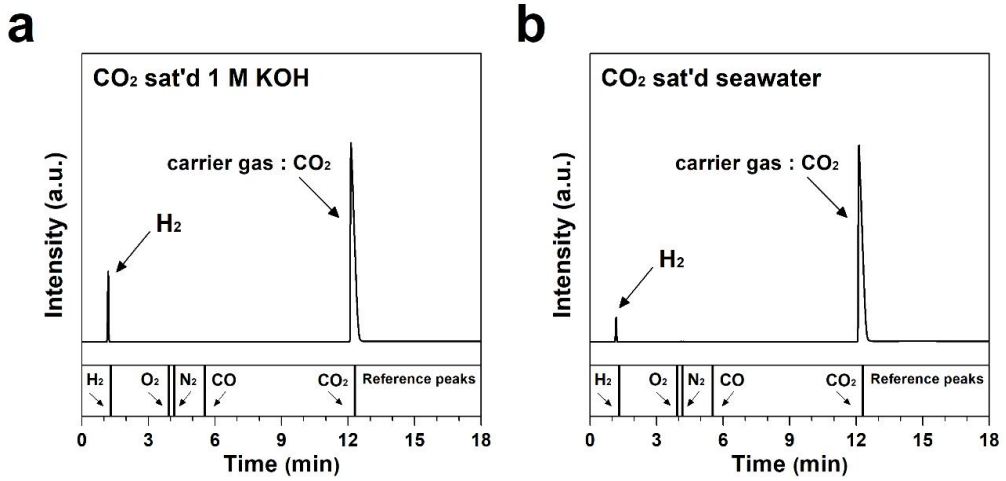

Figure 5-13 Gas chromatography (GC) profiles of generated gas during discharge process. The gas obtained during cathodic reaction proceeded in (a) CO_2 saturated 1 M KOH, (b) CO_2 saturated seawater

In terms of reaction efficiency, *i.e.*, the efficiency of HER, it can be understood as follows. Because the H_2 production rate is directly related to the magnitude of the current, the performance of the HER is influenced by the activity of the catalyst, the pH of the solution, and the resistance of the solution. The effect from the activity of the catalyst can be excluded because it depends on the catalyst itself. Thus, we have examined the pH of various $KHCO_3$ aqueous solution as shown in **Figure 5-14**.

In this regard, the continuity of CO_2 conversion and H_2 generation were investigated when the electrolyte is completely saturated with carbonate ions, *i.e.*, 3.4 M $KHCO_3$ solution (~3.4 M is known as the maximum solubility) **(Figure 5-15a)**. The red-coloured area shown in **the inset of Figure 5-15a** indicates the amount of converted CO_2 during a discharge reaction. Interestingly, H_2 generation and CO_2 conversion were still observed even the electrolyte solution is fully saturated with carbonate ion species. The H_2 generation and CO_2 conversion rate were 0.668 and 0.669 mL min^{-1}, respectively and the Faraday and CO_2 conversion efficiency were 96.3 and 48.0 %, respectively. This finding indicates that the H_2 generation by the CO_2 conversion still occurs even after the complete saturation with carbonate ions during the discharge process. Hereat, interestingly, the precipitation of a white solid product near the cathode was observed during the discharge reaction in the completely saturated electrolyte (**Figure 5-15b)**. Then, the white solid was collected by carefully filtering the aqueous electrolyte and the crystal structure was analyzed by an X-ray diffractometer **(Figure 5-15c)**. As shown in the XRD pattern, the white solid was identified as potassium bicarbonate ($KHCO_3$) containing a little amount of potassium carbonate (K_2CO_3) and the hydrate form ($K_4H_2(CO_3)_{3}\cdot_{1.5}H_2O$). Therefore, the GC profiles **(Figure 5-15a)** and the precipitation observation **(Figure 5-15b)** clearly demonstrate that CO_2 consumption is sustainable even when the system is completely saturated with carbonate ions.

The large-scale applicability of the system was confirmed using a cell system with 20 times larger scale by manufacturing the H-type cell with 1 L volume **(Figure 5-16)**. **Figure 5-16c** presents the screen

captured raw data of Zn-CO_2 cell performance measured by small H-type cell and large scaled H-type cell. The maximum current was achieved at 970 mA for the 20 times larger cell and this value is 18 times higher than the maximum current achieved by small H-type cell (*i.e.*, 54 mA). These performance profiles indicate that this cell system can be operated on a large scale. The H_2 gas being actively generated from the discharge on the large scaled cell can be seen. Besides, we have confirmed a crossover effect on the large scaled cell. This observation further supports the system is sustainable with the large scaled cell.

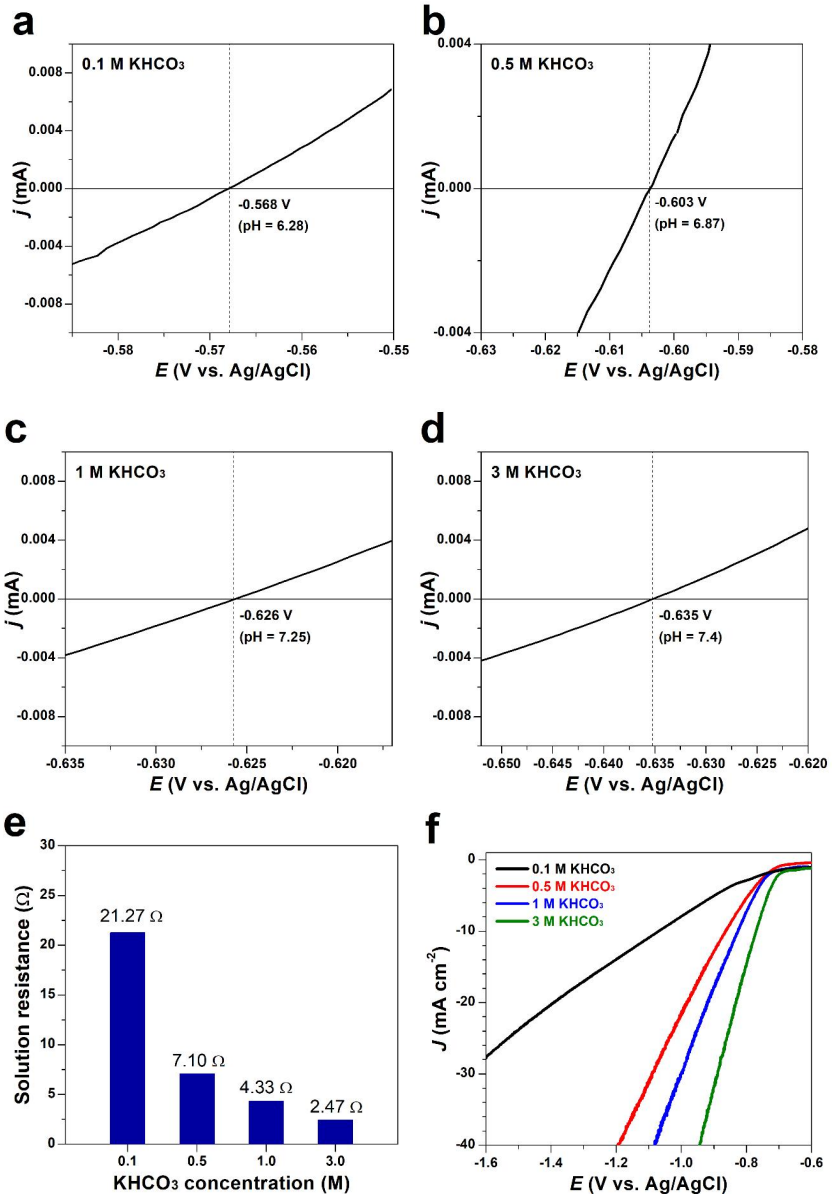

Figure 5-14 RHE calibration profiles for calculating the pH of (a) 0.1 M $KHCO_3$, (b) 0.5 M $KHCO_3$, (c) 1 M $KHCO_3$ and (d) 3 M $KHCO_3$. (e) Solution resistance value of 0.1, 0.5, 1.0, and 3.0 M $KHCO_3$ measured by electrochemical impedance spectroscopy using Pt-wire as a working and counter electrode. (f) RDE polarization curves measured at various concentration of $KHCO_3$ for Pt/C catalyst.

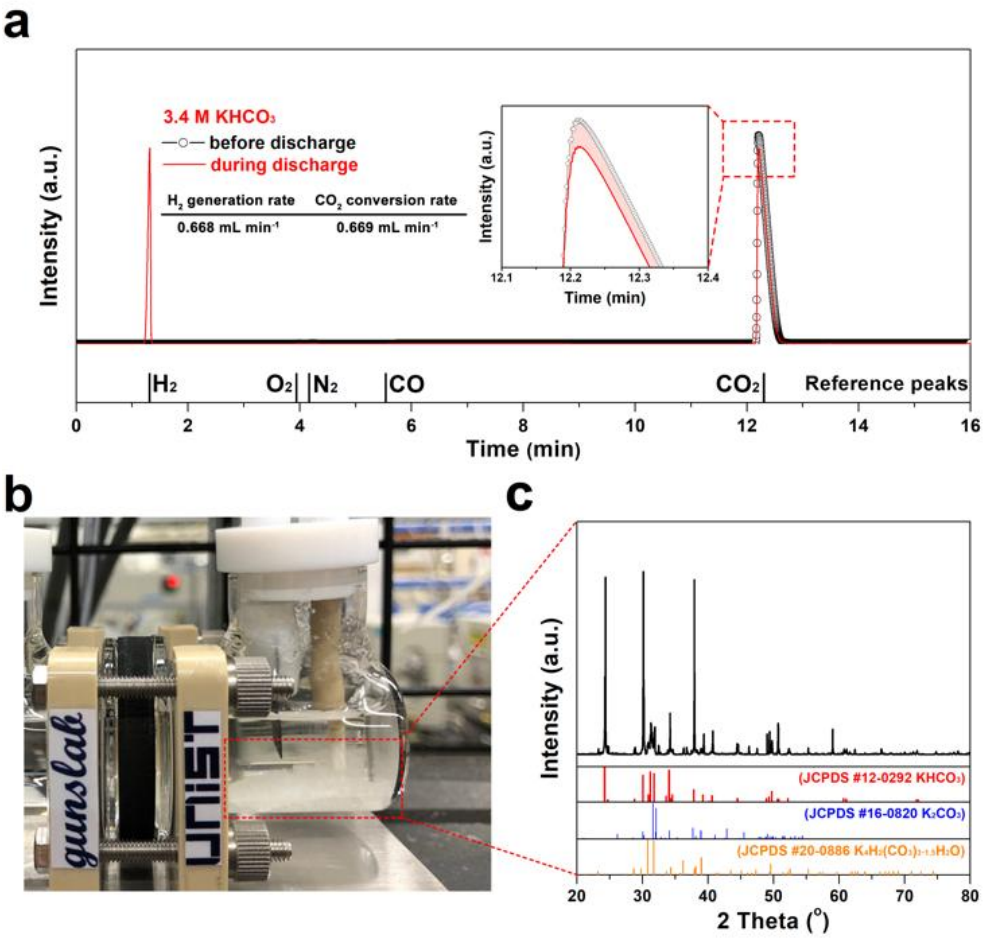

Figure 5-15 (a) The *in-operando* qualitative GC profiles of outlet CO_2 feed gas before and during discharging at 100 mA under 3.4 M $KHCO_3$ solution. The enlarged area near 12 min indicating the amount of converted CO_2 is shown as the inset. (b) A digital photograph of a precipitated white solid formed during discharging in the completely carbonate ions saturated solution. (c) the XRD profile of the precipitated white solid.

5.4. Conclusions

In summary, we have devised new Zn/Al-CO_2 systems that utilize CO_2 as a useful resource to produce electricity and hydrogen gas. As a novel electrochemical reaction, HER utilizing acidity contributed by spontaneous dissolution of CO_2, was adopted as a cathodic reaction. It simultaneously generates electrical energy and H_2 from the electrochemical oxidation of Zn and Al metals, which are abundant, low-cost, and environmentally friendly. Unlike the sluggish and difficult discharge reaction of the direct CO_2 reduction in a conventional aprotic metal-CO_2 battery, the proposed Zn- or Al-CO_2 systems adopting a novel HER utilizing CO_2 acidity have shown excellent performance of 39 and 125 mW cm^{-2}, respectively. The *in-operando* gas chromatograph measurements have demonstrated that the system could continuously operate with consuming CO_2. These proposed Zn/Al-CO_2 systems could potentially serve as a new CO_2 utilization technology in the era of pursuing a clean energy source

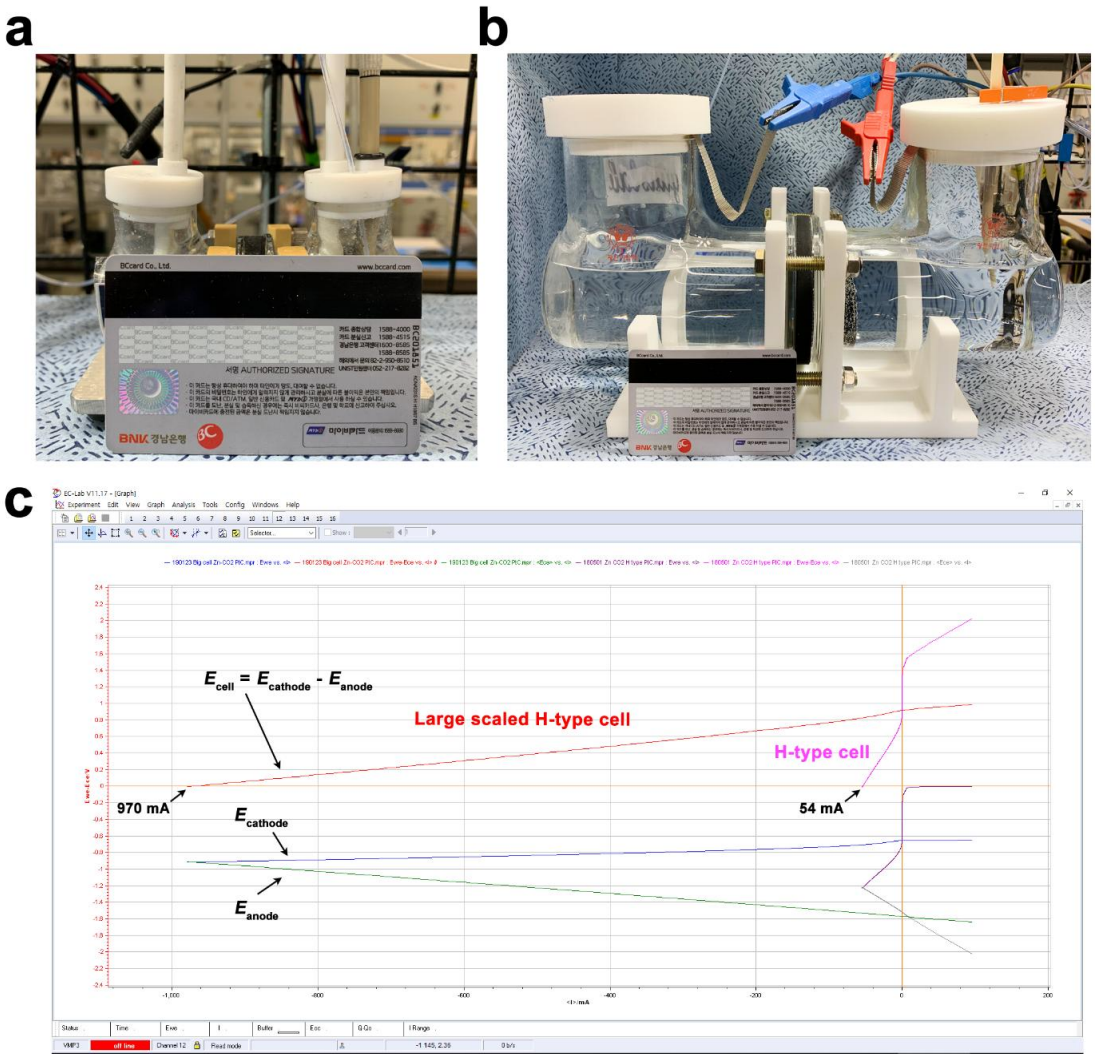

Figure 5-16 Digital photographs of (a) H-type cell used in this work, (b) newly manufactured H-type cell with 20 times larger scale. Typical credit card was presented for comparison the size of cell (Any personal information or card number is not shown). (c) Screen captured image of raw data of Zn-CO_2 cell performances measured by small H-type cell and large scaled H-type cell.

References

[1] Bu, M. Liu, J. Cho, G. Kim, *iScience* **2018**, *9,* P278-285.

[2] J.-P. Gattuso, A. Magnan, R. Billé, W. W. L. Cheung, E. L. Howes, F. Joos, D. Allemand, L. Bopp, S. R. Cooley, C. M. Eakin, O. Hoegh-Guldberg, R. P. Kelly, H.-O. Pörtner, A. D. Rogers, J. M. Baxter, D. Laffoley, D. Osborn, A. Rankovic, J. Rochette, U. R. Sumaila, S. Treyer, C. Turley, *Science*, **2015**, *349,* aac4722.

[3] a) N. M. Dowell, P. S. Fennell, N. Shah, G. C. Maitland, *Nat. Clim. Change*, **2017**, *7*, 243-249; b) K. S. Lackner, *Science*, **2003**, *300*, 1677-1678. c) J. Zhang, R. Yin, Q. Shao, T. Zhu, X. Huang, *Angew. Chem. Int. Ed.* **2019**, *58*, 5609-5613; *Angew. Chem.* **2019**, *131*, 5665-5669. d) S. Liu, J. Xiao, X. F. Lu, J. Wang, X. Wang, X. W. Lou, *Angew. Chem. Int. Ed.* 10.1002/anie.201903613; *Angew. Chem.* 10.1002/ange.201903613. e) J. J. Leung, J. A. Vigil, J. Warnan, E. E. Moore, E. Reisner, *Angew. Chem. Int. Ed.* **2019**, *58*, 1-6; *Angew. Chem.* **2019**, *131*, 1-6.

[4] a) D. J. Darensbourg, *Chem. Rev.*, **2007**, *107*, 2388-2410; b) J. Wang, G. Li, Z. Li, C. Tang, Z. Feng, H. An, H. Liu, T. Liu, C. Li, *Sci. Adv.*, **2017**, *3*, e1701290; c) R. Angamuthu, P. Byers, M. Lutz, A. L. Spek, E. Bouwman, *Science*, **2010**, *327*, 313-315.

[5] a) S. Bie, M. Du, W. He, H. Zhang, Z. Yu, J. Liu, M. Liu, W. Yan, L. Zhou, Z. Zou, *ACS Appl. Mater. Interfaces* **2019**, *11*, 5146-5151; b) L. Wang, W. Dai, L. Ma, L. Gong, Z. Lyu, Y. Zhou, J. Liu, M. Lin, M. Lai, Z. Peng, W. Chen, *ACS Omega* **2017**, *2*, 9280-9286; c) Y. Liu, R. Wang, Y. Lyu, H. Li, L. Chen, *Energy Environ. Sci.*, **2014**, *7*, 677; d) C. Li, Z. Guo, B. Yang, Y. Liu, Y. Wang, Y. Xia, *Angew. Chem. Int. Ed*. **2017**, *56*, 9126-9130; *Angew. Chem.* **2017**, *129*, 9254–9258; e) L. Qie, Y. Lin, J. W. Connell, J. Xu, L. Dai, *Angew. Chem. Int. Ed.*, **2017**, *56*, 6970-6974; *Angew. Chem.* **2017**, *129*, 7074–7078; f) Z. Zhang, Q. Zhang, Y. Chen, J. Bao, X. Zhou, Z. Xie, J. Wei, Z. Zhou, *Angew. Chem. Int. Ed.*, **2015**, *54*, 6550-6553; *Angew. Chem.* **2015**, *127*, 6650-6653; g) X. Hu, J. Sun, Z. Li, Q. Zhao, C. Chen, J. Chen, *Angew. Chem. Int. Ed.*, **2016**, *55*, 6482-6486; *Angew. Chem.* **2016**, *128*, 6592–6596; h) C. Fang, J. Luo, C. Jin, H. Yuan, O. Sheng, H. Huang, Y. Gan, Y. Xia, C. Liang, J. Zhang, W. Zhang, X. Tao, *ACS Appl. Mater. Interfaces* **2018**, *10*, 17240-17248; i) W. I. Al Sadat, L. A. Archer, *Sci. Adv.*, **2016**, *2*, e1600968; j) J. Xie, X. Wang, J. Lv, Y. Huang, M. Wu, Y. Wang, J. Yao, *Angew. Chem. Int. Ed.* **2018**, *57*, 16996-17001; *Angew. Chem.* **2018**, *130*, 17242–17247.

[6] Y. Jin, C. Hu, Q. Dai, Y. Xiao, Y. Lin, J. W. Connel, F. Chen, L. Dai, *Adv. Funct. Mater.*, **2018**, *28*, 1804630.

[7] L. Singh, Z. A. Wahid, *J. Ind. Eng. Chem.*, **2015**, *21*, 70-80.

[8] Y. Zhang, S. Zhang, H. H. Lou, J. L. Gossage, T. J. Benson, *Chem. Eng. Technol.*, **2014**, *37*, 1493-1499.

[9] C. E. Housecroft, A. G. Sharpe, *Inorganic Chemistry, 2nd ed.*, Pearson Prentice Hall, New Jersey, **2005**.

[10] D. C. Harris, *Quantitative Chemical Analysis, 8th ed.*, W. H. Freeman and Company, New York, **2010**.

[11] a) T. Wang, Z. Kou, S. Mu, J. Liu, D. He, I. S. Amiinu, W. Meng, K. Zhou, Z. Luo, S. Chaemchuen, F. Verpoort, *Adv. Funct. Mater.*, **2018**, *28*, 1705048; b) X. Han, X. Wu, C. Zhong, Y. Deng, N. Zhao, W. Hu, *Nano Energy*, **2017**, *31*, 541-550; c) Y. Bu, O. Gwon, G. Nam, H. Jang, S. Kim, Q. Zhong, J. Cho, G. Kim, *ACS Nano*, **2017**, *11*, 11594-11601; d) A. Sumboja, X. Ge, F. W. T. Goh, B. Li, D. Geng, T. S. A. Hor, Y. Zong, Z. Liu, *ChemPlusChem*, **2015**, *80*, 1341-1346; e) S. Sun, H. Miao, Y. Xue, Q. Wang, S. Li, Z. Liu, *Electrochim. Acta*, **2016**, *214*, 49-55; f) Y. Lai, Q. Wang, M. Wang, J. Li, J. Fang, Z. Zhang, *J. Electroanal. Chem.*, **2017**, *801*, 72-76; g) Z. Zhang, C. Zuo, Z. Liu, Y. Yu, Y. Zuo, Y. Song, *J. Power Sources*, **2014**, *251*, 470-475.

[12] a) S.-M. Park, S. Ho, S. Aruliah, M. F. Weber, C. A. Ward, R. D. Venter, *J. Electrochem. Soc.*, **1986**, *133*, 1641-1649; b) C. Kim, O. Gwon, I.-Y. Jeon, Y. Kim, J. Shin, Y.-W. Ju, J.-B. Baek, G. Kim, *J. Mater. Chem. A*, **2016**, *4*, 2122-2127; c) D.-G. Lee, S. H. Kim, S. H. Joo, H.-I. Ji, H. Tavassol, Y. Jeon, S. Choi, M.-H. Lee, C. Kim, S. K. Kwak, G. Kim, H.-K. Song, *Energy Environ. Sci.*, **2017**, *10*, 523-527; d) L. Liu, G. Zeng, J. Chen, L. Bi, L. Dai, Z. Wen, *Nano Energy*, **2018**, *49*, (2018).

[13] a) X. Li, S. Guo, W. Li, X. Ren, J. Su, Q. Song, A. J. Sobrido, B. Wei, *Nano Energy*, **2019**, *57,* 388-39; b) Q. Wang, Z. L. Zhao, S. Dong, D. He, M. J. Lawrence, S. Han, C. Cai, S. Xiang, P. Rodriguez, B. Xiang, Z. Wang, Y. Liang, M. Gu, *Nano Energy*, **2018**, *53*, 458-467; c) P. Hu, C. Chen, R. Zeng, J. Xiang, Y. Huang, D. Hou, Q. Li, Y. Huang, *Nano Energy*, **2018**, *50*, 376-382; d) C. Hu, L. Dai, *Adv. Mater.*, **2017**, *29*, 1604942; e) J. Zhang, L. Qu, G. Shi, J. Liu, J. Chen, L. Dai, *Angew. Chem. Int. Ed.* **2016**, *55*, 2230–2234; *Angew. Chem.*, **2016**, *128*, 2270-2274; f) X. Xu, Y. Chen, W. Zhou, Z. Zhu, C. Su, M. Liu, Z. Shao, *Adv. Mater.*, **2016**, *28*, 6442-6448; g) J. Mahmood, F. Li, S.-M. Jung, M. S. Okyay, I. Ahmad, S.-J. Kim, N. Park, H. Y. Jeong, J.-B. Baek, *Nat. Nanotech.*, **2017**, *12*, 441-446.

[14] a) Y. Li, H. Wang, L. Xie, Y. Liang, G. Hong, H. Dai, *J. Am. Chem. Soc.*, **2011**, *133*, 7296-7299; b) T. Zhang, M.-Y. Wu, D.-Y. Yan, J. Mao, H. Liu, W.-B. Hu, X.-W. Du, T. Ling, S.-Z. Qiao, *Nano Energy*, **2018**, *43*, 103-109.

[15] B. Hua, M. Li, Y.-Q. Zhang, Y.-F. Sun, J.-L. Luo, *Adv. Energy Mater.*, **2017**, *7*, 1700666.

[16] a) J. Duan, S. Chen, M. Jaroniec, S. Z. Qiao, *ACS Nano*, **2015**, *9*, 931-940; b) S. Deng, Y. Zhong, Y. Zeng, Y. Wang, Z. Yao, F. Yang, S. Lin, X. Wang, X. Lu, X. Xia, J. Tu, *Adv. Mater.*, **2017**, *29,* 1700748; c) J. Zhang, L. Dai, *Angew. Chem. Int. Ed.*, **2016**, *55*, 13296-13300; *Angew. Chem.* **2016**, *128*, 13490-13494.

Chapter 6 Indirect Surpassing CO_2 Utilization in Membrane-free CO_2 Battery

This chapter has been published.

Reproduced with permission from J. Kim, A. Seong, Y. Yang, S. Joo, C. Kim, D. H. Jeon, L. Dai, G. Kim, *Nano Energy* 2021, 82, 105741.

6.1 Introduction

Carbon cycle has long been impaired by excess CO_2 emissions since the industrial revolution [1,2]. Thus, it is essential to develop an electrochemical system to capture or convert CO_2 from the air into valuable chemicals, materials, fuels, and renewable energy [3]. Until now, however, CO_2 capture, CO_2 storage and CO_2 conversion have required significant energy inputs; it is more important than ever now to minimize the energy required for CO_2 fixation [4–9]. Metal-CO_2 batteries, consisting of a metal (*e.g.,* Li, Na, Al, and Zn) electrode and CO_2 fixation electrode with an appropriate electrolyte (*e.g.,* organic or aqueous form), are emerging as a promising technology to integrate CO_2 utilization with metal-air batteries [10,11]. In a metal- CO_2 battery, the metal component is selected depending on the properties of the electrolyte, such as its chemical stability and electrochemical activity towards the metal electrode (Figure 1). Metal-CO_2 batteries based on organic electrolytes directly convert CO_2 feed into a solid product (*e.g.*, Li_2CO_3, Na_2CO_3, or $Al_2(CO_3)_2$), which accumulates on the electrode surface to decrease the electrode electrochemical activity and hence create a limited discharge capacity [9,12–14]. During the charging process, these solid products regenerate CO_2 gas, leading to inefficient storage of CO_2 feedstock. In contrast, aqueous electrolyte-based metal- CO_2 batteries are, in principle, free from the solid product accumulation on the electrode surface to facilitate the selective generation of desired products through relatively more controllable CO_2 reactions. However, an additional membrane is needed to maintain the different electrochemical functions between anolyte and catholyte in an aqueous metal- CO_2 battery, leading to extra complexities for cell fabrication and slow kinetics associated with the poor membrane ionic conductivity [2, 4–6,15,16]. Herein, we devised a new method for efficient CO_2 utilization that overcomes the substantial barrier for charging caused by the solidified product and eliminates the complexity of the cell fabrication associated with the membrane. Contrary to previous Metal- CO_2 batteries, this work suggests the indirect utilization of CO_2 from dissolution process in neutral condition, which produce the hydrogen gas and carbonate species. Although the Zn, Al or other metal electrode (Li, Na) is difficult to obtain the stable electrochemical potential and non-explosive properties in neutral electrolyte, in this work, the magnesium-based system showed the stable electrochemical performances over 35 h at a high current density (20 mA cm^{-2}) with continuous utilization of CO_2.

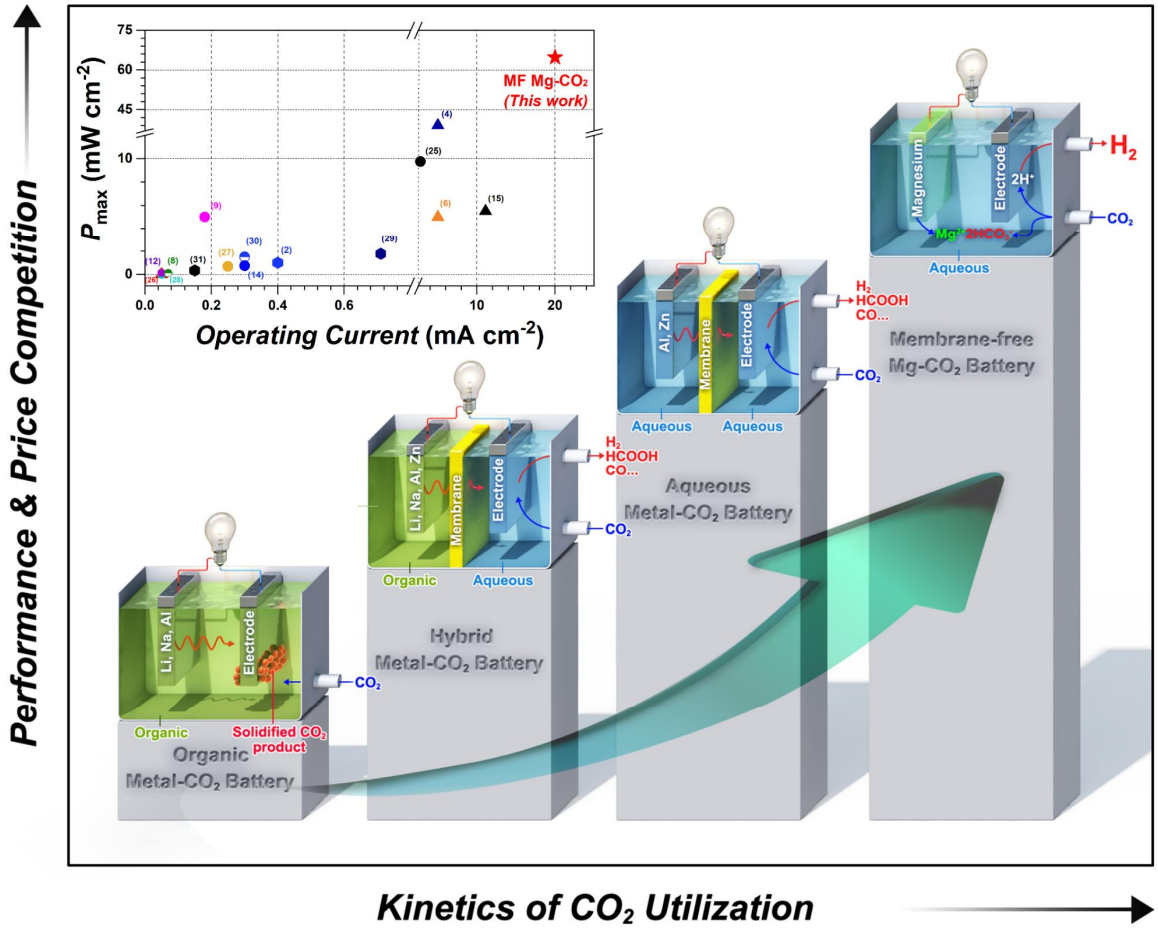

Figure 6-1 Schematic configuration and operation principle for each battery system from organic to membrane-free battery. Inset: Maximum power density (P_{max}) and operating current for various metal-CO_2 cells.Schematic illustration of aqueous Zn- or Al-CO_2 systems and their reaction mechanism.

6.2 Experimental

6.2.1 Purchasing chemicals

The 20 wt% platinum on active carbon (Pt/AC, Sigma-Aldrich Co.) and IrO2 (Sigma-Aldrich Co.) were purchased at Sigma-Aldrich. The commercial alloy metal AZ31 (96 wt% Mg, 3 wt% Al and 1 wt% Zn), AZ61 (93 wt% Mg, 6 wt% Al and 1 wt% Zn), and AZ91 (90 wt% Mg, 9 wt% Al and 1 wt% Zn) were used as Mg alloy electrode.

6.2.2 Materials synthesis

Ba0.5Sr0.5Co0.8Fe0.2O3-d (BSCF) was synthesized by typical sol-gel process. Stoichiometric amount of metal nitrate precursors and citric acid were prepared in distilled water (D.I.). An adequate amount of poly-ethylene glycol was added into a metal precursor solution and was mixed for a few hours. After a viscous resin was formed, the mixture solution was heated to 300 ◦C. The product powder was collected and calcined at 600 ◦C for 4 h followed by sintering at 950 ◦C for 4 h.

6.2.3 Characterization techniques

The solid products after the discharge process in CO_2-saturated 1 M KOH +_ _1 M NaCl were obtained through various drying process such as freeze-drying. The phase identification of the obtained products was confirmed by X-ray powder diffraction (XRD) (Bruker diffractometer, Cu Kα _radiation) at a scan rate of 1◦ _min _1. The power patterns were analyzed using JADE 6.5 software. The generated gas during discharge process was analyzed by gas chromatograph with thermal conductivity detector (GC-TCD) utilizing Argon as the carrier gas (GC-2010 Plus, SHIMADZU Co.) using H-type Cell. The gas evolved from the charging process was also collected using 450-GC chromatograph and 320-MS (Bruker Co.). The morphological analysis of the gas generation electrode before and after the discharge process in Mg- CO_2 battery was examined by scanning electron microscopy (Nova FE-SEM, FEI Co.). Fourier transform infrared (FT-IR) spectra were conducted on a Varian 670.

6.2.4 Half-cell configured electrochemical testing

To estimate pH and hydrogen evolution potential in the solution, a reversible hydrogen electrode (RHE) calibration was conducted in H2- saturated solutions where platinum wires were used as the working, counter electrodes and Ag/AgCl as a reference electrode at a scan rate of 5 mV s^{-1}. The changed pH values corresponding to the CO_2 dissolution was carried out using ORION STAR A211 (Thermo Fisher Scientific Co.). For all half-cell configured experiments, iR correction was applied by measuring the resistance of solution (1 M NaCl + 1 M KOH, CO_2-saturated 1 M NaCl + 1 M KOH). In three-electrode half-cell measurements for reductive profiles, a 20 wt% platinum on active carbon (Pt/AC) and graphite electrode were used as working electrode and counter electrode, respectively, with Ag/AgCl (saturated KCl filled) reference electrode in 1 M potassium hydroxide (KOH) and 1 M sodium chloride (NaCl, Sigma-Aldrich) in pure water. A rotating disk electrode testing was conducted by using a mixture of each catalyst on RRDE-3A (ALS Co.).

6.2.5 Electrode preparation for half-cell testing

The mixture of catalyst was prepared into a catalyst ink by dispersing 10 mg of the catalyst in 1 mL of a binder solution (45: 45: 10 =ethanol: isopropyl alcohol: 5 wt% Nafion solution (volumetric ratio) followed by a bath sonication process. The RDE profiles were measured by 5 mL of the catalyst ink drop-coated glassy carbon disk electrode, where area is 0.1256 cm2, at a scan rate of 10 mV s _1. For oxidative RRDE measurements, the commercial IrO2 was used as a catalyst. All electrochemical tests were carried out using Biologic VMP3.

6.2.6 Full-cell measurements

The membrane-free Mg- CO_2 battery is composed of Mg metal / aqueous electrolyte / gas evolution

electrode. For the aqueous electrolyte, 1 M KOH +_ _1 M NaCl were used. Full-cell tests were conducted in three-electrode configuration using Ag/AgCl reference electrode for detailed electrochemical analysis. The gas generation electrode was prepared by drop-coating the catalyst ink (Pt/C+_IrO2 ink) onto a gas-diffusion layer (Toray carbon paper, TGP-H-090, Fuel Cell Store Co.) with a loading density of 2 mg cm _2. The current density was normalized with the loading area of the catalysts. For the calculation of practical Faradaic efficiency for H2 generation, the Mg- CO_2 battery was adopted. CO_2 gas was excessively purged to prevent the lack of supplement of proton ion from CO_2 dissolution (~100 sccm). All electrochemical tests were conducted using Biologic VMP3.

6.2.7 Computational method

We have designed the electrochemical model to predict the discharge performances that are necessary for fundamental investigation. Model descriptions can be found in Figure 6-2 and the governing equations are given below. For the continuum model, the charges are conserved between the solution and solid phases, and can be expressed through the divergence of the current density as

$$\nabla \cdot i_l + \nabla \cdot i_s = 0$$

Where *il* and *is* are the current density in the liquid solution and solid phase, respectively. These are

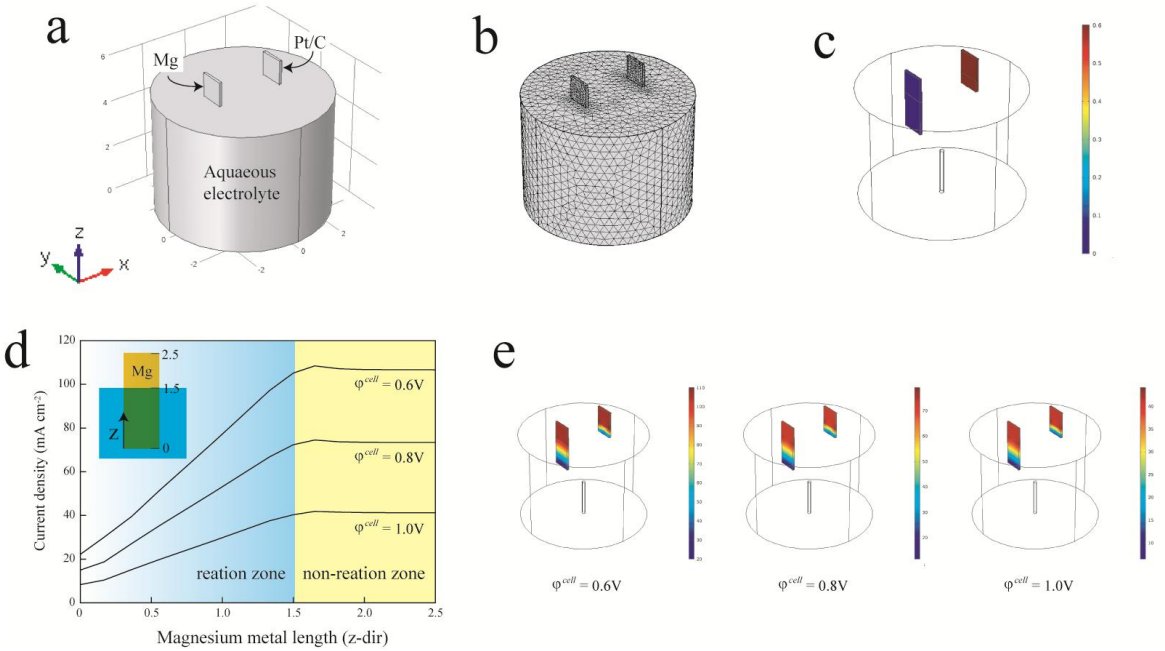

Figure 6-2 Membrane-free Mg-CO_2 battery modelling. Three-dimensional electrochemical modelling is conducted with mimicking the physical appearance of Mg-CO_2 battery system. (a) Schematic of Mg-CO_2 battery model, (b) Meshes that contain 0.1 million tetrahedral elements, (c) Electronic potential distribution at $\varphi^{cell} = 0.6V$, (d) Spatial distribution of current densities along the magnesium metal length, and (e) Corresponding current density distributions in the electrodes.

governed by Ohm's law through electronic or ionic potential

$$i_s = - \sigma_s \nabla \varphi_s$$

$$i_l = - \sigma_l \nabla \varphi_l$$

For the electrochemical reaction, the local current density between the electrode and electrolyte interface can be given by the general Butler-Volmer equation as

$$i_A = i_0 \left[exp\left(\frac{\alpha F \eta_{act}}{R_g T}\right) - exp\left(\frac{-\alpha F \eta_{act}}{R_g T}\right) \right]$$

where $i_{0,A}$ = 0.59 x 10^{10} A/m^2, $i_{0,C}$ = 0.2286 x 10^{10} A/m^2, α = 0.5.

The activation overpotential for reaction *ηact* is given by

$$\eta_{act} = \varphi_s - \varphi_l - \varphi^o$$

$$\varphi^o = \varphi_C^o - \varphi_A^o$$

In this system, the Mg^{2+} and HCO^{3-} concentrations become stable after reaching the saturation of $Mg(HCO_3)_2$(aq). Therefore, the potential drop due to concentration overpotential is not significant even with a high current density, which can be confirmed in the polarization profile of Mg- CO_2 battery. For the species transport, we employ the dilute solution theory as

$$\nabla \cdot \left(-D_i \nabla c_i - z_i u_{m,i} F c_i \nabla \varphi\right) = R_i$$

$$R_i = \frac{\nu_i i}{nF}$$

We only consider the transport of magnesium ion and hydrogen. (*i.e.*, the production of $Mg(HCO_3)_2$(aq) and transport of carbon dioxide is not modeled primarily due to the lack of knowledge for the reaction mechanism).

6.3 Result and discussion

6.3.1 The proposed battery and electrochemical mechanism

Figure 6-1 shows the newly developed membrane-free Mg- CO_2 (MF Mg- CO_2) battery in comparison with conventional organic electrolyte, aqueous electrolyte, and hybrid electrolyte metal- CO_2 batteries. The inset of Figure 6-1 displays the maximum power density (*P*max) and operating current density (mA cm^{-2}) for a direct comparison. As can be seen, the electrochemical performance of our MF Mg- CO_2 battery is clearly much better than that of previously reported metal- CO_2 batteries. In addition to free from the membrane, our MF Mg- CO_2 battery is composed of aqueous electrolyte, a magnesium (Mg) anode, and a gas-generation cathode. Unlike the conventional organic and aqueous metal- CO_2 batteries that operate through direct CO_2 reduction and evolution from the CO_2 feed gas, the MF Mg- CO_2 battery

does not directly utilize CO_2 feed gas. Instead, the MF Mg- CO_2 battery operates through spontaneous dissolution of CO_2 in an aqueous solution (Eqs. 1 and 2), followed by electrochemical oxidation of Mg and hydrogen evolution (Eqs. 3 and 4). More specifically, the indirect CO_2 utilization (dissolution) releases protons (Eqs. 1 and 2), from which hydrogen generation occurs (Eq. 4) on the cathode driven by the high negative electrochemical potential (μMg) of anodic oxidation reaction of Mg (Eq. 3) during discharge. Besides, Mg metal ion can be easily reduced by charging, leading to an efficient recharging battery system. It should be noted that the molar fraction of carbonate ions depends strongly on the pH value. This new cell electrochemical process is well-supported by fundamental studies, including the investigation of Butler-Volmer, rate of reaction at equilibrium with exchange current density, activation overvoltage/kinetics, and stoichiometric coefficient. We have also carried out simulated modeling to obtain the distribution of electronic, ionic, and spatial current potentials for a better fundamental understanding of kinetic factors of the electrochemical system, as we shall see later. CO_2 dissolution reaction:

CO_2 dissolution reaction: $CO_{2\,(aq)} + H_2O_{\,(l)} \leftrightarrow H_2CO_{3\,(aq)}$, $K_h = 1.70 \times 10^{-3}$ (1)

$H_2CO_{3\,(aq)} \leftrightarrow HCO_3^-{}_{(aq)} + H^+{}_{(aq)}$, $K_h = 6.3$ (2)

Magnesium oxidation reaction: $Mg_{(s)} \rightarrow Mg^{2+}{}_{(aq)} + 2\,e^-$, $E_a = -2.37$ V vs. SHE (3)

Hydrogen evolution reaction: $2\,H^+{}_{(aq)} + 2\,e^- \rightarrow H_{2\,(g)}$, $E_c = -0.44$ V vs. SHE (4)

During the discharge process, the proton consumption *via* Eq. 4 leads to the further spontaneous dissolution of CO_2 gas (Eq. 1, 2). This favorable cycle of the consumption and production of proton ions maintains the solution pH value at ~7.46 (Figure 6-3), leading to the formation of magnesium bicarbonate from the dissolved bicarbonate ion and oxidized Mg (Mg2+) (Eq. 5).

$$Mg^{2+}{}_{(aq)} + 2\,HCO_3^-{}_{(aq)} \rightarrow Mg(HCO_3)_{2\,(aq)} \quad (5)$$

Thus, the spontaneous fixation of CO_2 is achieved by converting CO_2 into value-added carbonate species during the operation of our MF Mg- CO_2 battery with a constant generation of electricity and hydrogen. it shows the thermodynamic energy cycle for the operation process of a MF Mg- CO_2 battery with the associated numerical data for ΔG and ΔH of CO_2 dissolution, HER, and Mg oxidation being listed in Table 6-1. When CO_2 dissolution proceeds, HCO_3^- is formed and the standard reaction enthalpy can be calculated as follows: $\Delta H^o_{r=\{}\Delta H^o_f(HCO_3^-,aq) + \Delta H^o_f(H^+,aq)\} - \Delta H^o_f(CO_2,g) + \Delta H^o_f(H^+,aq) + \Delta H^o_f(OH^-,aq)\}$. According to the thermodynamic data given in Table 6-1, the reaction enthalpy is presented to be $\Delta H^o_r = -68.49$ kJ mol^{-1}. Since $\Delta H^o_r < 0$, the CO_2 dissolution reaction is exothermic. Also, the standard reaction Gibbs energy can be determined as follows: $\Delta G^o_r = \{\Delta G^o_f(HCO_3^-,aq) + \Delta G^o_f(H^+,aq)\}$

$-\Delta G^o_f(CO_2,g) + \Delta G^o_f(H^+,aq) + \Delta G^o_f(OH^-,aq)\}$. Thus, the reaction Gibbs energy is $\Delta G^o_r = -35.17$ kJ mol^{-1}. $\Delta G^o_r < 0$ means that the CO_2 dissolution proceeds spontaneously. From this spontaneous chemical reaction of CO_2 dissolution, the pH of solution is decreased.

Table 6-1. Thermodynamic data for various substances at 298 K

Substance	*State*	ΔH^o_f (kJ mol^{-1})	ΔG^o_f (kJ mol^{-1})	S^o (J mol^{-1} K^{-1})
H^+	aq	0	0	0
OH^-	aq	-229.99	-157.24	-10.75
H_2	g	0	0	130.68
CO_2	g	-393.51	-394.36	213.6
HCO_3^-	aq	-691.99	-586.77	91.2

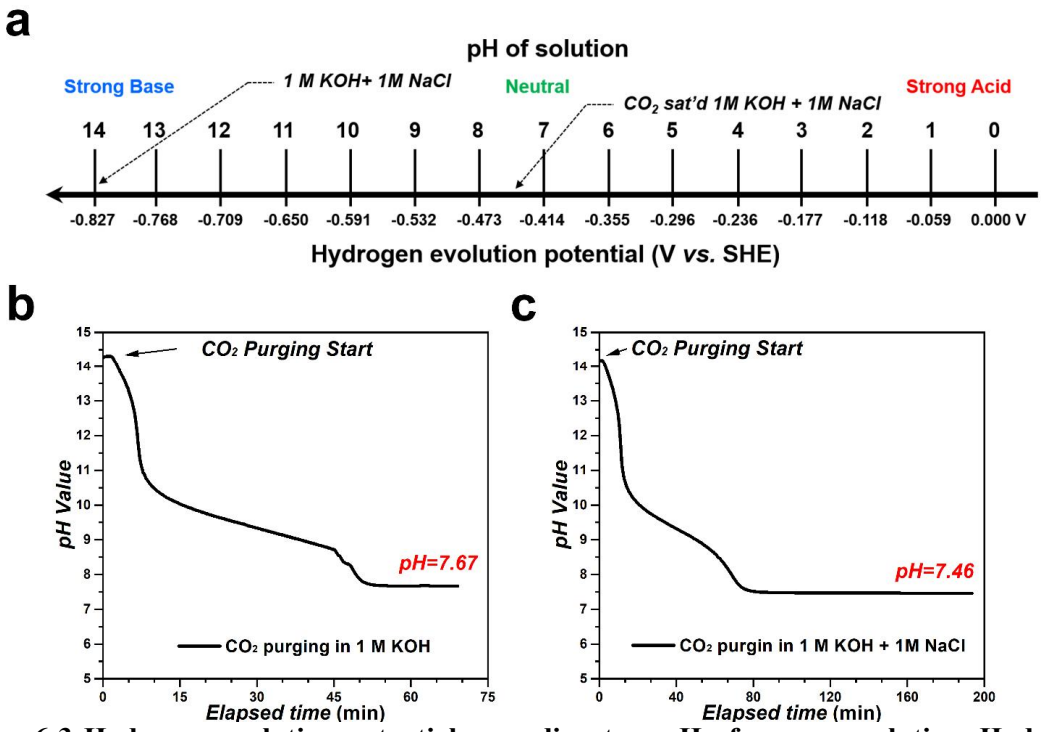

Figure 6-3 Hydrogen evolution potential according to a pH of aqueous solution. Hydrogen evolution potential is closely correlated to the pH value and follows the equation, *E* (V *vs.* SHE) = 0.000 – 0.0591 × pH and *E* (V *vs.* Ag/AgCl) = -0.197 – 0.0591 × pH. (a) Schematics diagram of hydrogen evolution potential related to pH. pH value of the solution with CO_2 purging as a function on the time aerated in (b) 1M KOH and (c) 1 M KOH + 1 M NaCl solution.

6.3.2 Half-cell configured electrochemical analysis

The electrochemical performance was measured by a rotating disk electrode (RDE) with linear sweep voltammetry (Figure 6-4a). A reference potential was made to Ag/AgCl instead of RHE for the clarification of potential difference caused by pH changes corresponding to different purging gases while platinum loaded active carbon (Pt/AC) electrocatalyst was use d for the reduction reaction. As shown in Figure 6-4a, the reduction polarization curve was observed around - 1.02 V *vs.* Ag/AgCl in the N2 saturated solution, corresponding to the typical hydrogen evolution reaction (HER). For the CO_2 saturated solution, however, the onset potential for HER positively shifted by about 0.37 V caused by

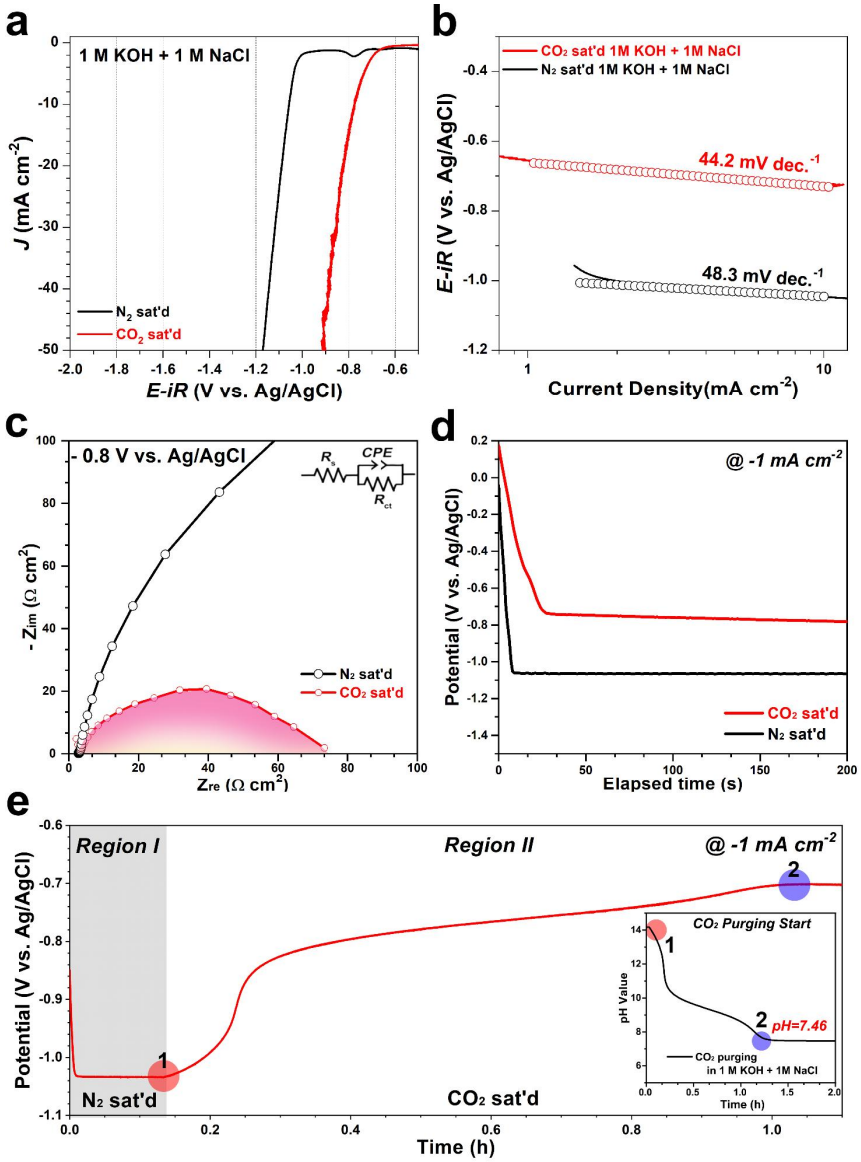

Figure 6-4 Half-cell configured reduction profiles. (a)Linear sweep voltammetry (LSV) profiles measured in N_2- and CO_2-saturated condition. (b) Tafel plots of the cathodic profiles. (c) EIS curves at - 0.8 V *vs.* Ag/AgCl in N_2- and CO_2-saturated condition. (d) Chronopotentiometry profile at - 1 mA cm^{-2} in different saturated gas. (e) The *in-operando* chronopotentiometry reduction profile from N_2-saurated to CO_2-saturated condition at - 1 mA cm^{-2}. Inset: pH value of the solution with CO_2 purging as a function on the time aerated.

the decreased pH value with the dissolution of CO_2 (Eqs. 1 and 2), as the HER potential is determined by the Nernst equation (0.0592 V x pH), leading to the facile (spontaneous) hydrogen generation. To gain further insight into the electrochemical performance under the CO_2 saturated condition, Tafel plots were obtained from polarization curves measured in both of the N_2- and CO_2-saturated solutions (Figure 6-4b), which showed a smaller slope (44.2 mV dec^{-1}) in the CO_2-saturated solution than that of the N2-saturated solution (48.3 mV dec^{-1}). Figure 6-4c shows the electrochemical impedance spectrum, from which the charge-transfer resistance (Rct) value in the CO_2-saturated solution was estimated to be 70.1 Ω cm^{-2}, a value which is significantly lower than that of the N2-saturated counterpart. These results indicate that the dissolution of CO_2 improved the electrocatalysis kinetics for the hydrogen evolution process. To confirm the onset-potential for HER, we reproduced the chronopotentiometry profiles in Figure 6-4d, which shows that the CO_2-saturated solution has a smaller overpotential for HER than that of N_2-saturated solution without any significant degradation in both cases. For demonstrating the effect of CO_2 dissolution on the hydrogen evolution, the *in-operando* chronopotentiometry reduction profile in the N_2- and CO_2- saturated solutions was presented in Figure 6-4e as a function of the time aerated with CO_2 purging. Upon the CO_2 purging in the electrolyte solution (red-colored as 1), the HER potential continuously increased with time to reach the value up to - 0.70 V *vs.* Ag/AgCl (blue-colored as 2) before leveling off. Because the HER potential is inversely proportional to the pH value of the electrolyte solution by following the Nernst equation (0.0592 V x pH), the *in-operando* chronopotentiometry reduction profile is more or less mirror imaged by the pH *vs.* time profile given in the Inset of Figure 6-4e. As can be seen from both the profiles in Figure 6-4e, it took about 1 h to reach the plateaus. Thus, 1 h was chosen as the aeration time for HER progress in CO_2-saturated electrolyte toward the Mg- CO_2 battery.

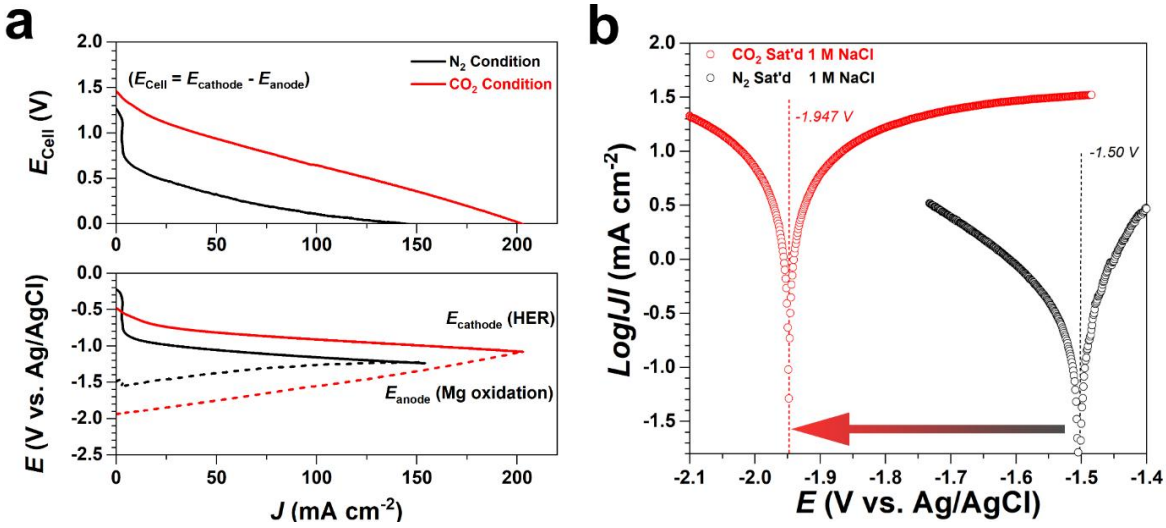

Figure 6-5 The effects of saturated condition in N_2 or CO_2 for Mg-CO_2 battery. (a) I-V profiles under N_2- or CO_2-saturated 1 M KOH and 1 M NaCl. (b) Potentiodynamic polarization for Mg at different saturated condition.

6.3.3 Full-cell performances of membrane-free Mg- CO_2 battery

To demonstrate the working performance of MF Mg- CO_2 battery, we performed a proof-of-concept experiment by constructing a cell with the three-electrode configuration shown in Figure 6-5, in which a Mg foil and Pt/C were used as the anode and cathode, respectively, along with a Ag/ AgCl reference electrode. Figure 6-6a shows the discharge polarization curves for the MF Mg- CO_2 battery, from which an open-circuit voltage (OCV) was determined to be around 1.5 V from the difference between the anodic Mg potential (- 1.95 V *vs*. Ag/AgCl) and cathodic HER potential (- 0.47 V *vs*. Ag/AgCl) with a maximum current density of 202.3 mA cm^{-2}. To investigate the effects of the dissolution of CO_2, the discharge polarization curve in N_2-saturated solution was also recorded, as shown in Figure 6-5. As expected, the values of both current density and OCV for the CO_2-saturated cell are significantly higher than those for the N_2-saturate cell, indicating improved electrochemical performance by the CO_2 dissolution. The chronopotentiometry profile of the MF Mg- CO_2 battery was measured at a current density of 20 mA cm^{-2} (Figure 6-6b), which shows a stable reduction potential (E_{cell} =~ around 1.0 V) over 35 h. Without further dissolution of CO_2 during the HER, the pH condition would be rapidly changed during the discharge process, as shown in Figure 6-7. Therefore, the stable cathodic potential in Figure 6-6b indicates that the continuous dissolution of CO_2 ensured the pH unchanged, and no clogging effects were observed during the HER process, leading to a stable cell operation performance without continuous degradation in sharp contrast to previous aprotic metal- CO_2 batteries. To gain a fundamental understanding of the electrochemical process in the MF Mg- CO_2 battery, we conducted a numerical simulation of three-dimensional electrochemical modeling. The model geometry and meshes can be found in Figure 6-2. As shown in Figure 6-6c, the simulated performance is well agreed with experimental data. Notably, the practical maximum power density was estimated to be 64.8 mW cm^{-2} at 109.7 mA cm^{-2}, which outperformed those reported metal- CO_2 cells. To investigate the contribution of each overpotential, we have analyzed the component overpotential for the total potential loss of the cell. Figure 6-6d depicts the contribution of the anode, electrolyte, and cathode overpotentials to the overall potential loss. As can be seen, the contribution of cathode overpotential is large at a low current density region, but that of electrolyte overpotential becomes dominant at a high current density region. Meanwhile, the contribution of anode overpotential is observed small, likely due to the relatively fast kinetics of Zn oxidation at the anode. The large electrolyte overpotential is primarily attributed to the low ionic conductivity of electrolyte in the aqueous solution. To further understand the potential configuration during the discharge process, the spatial distributions of electrode and electrolyte potentials were simulated at the cell voltage of 0.6, 0.8, and 1.0 V (Figure 6-6e), which show a steep decrease in the electrolyte potential from Mg metal to cathode due to the low ionic conductivity of electrolyte (CO_2 saturated 1 M KOH +_ _1 M NaCl) and a nearly constant electric potential for each of the electrodes due to their high electronic conductivity. Insights gained from these simulated results could be used to guide engineering of the electrolyte concentration and distance between the electrodes

to further improve the overall cell performance by reducing the electrolyte overpotential. To quantitatively evaluate the utilization of CO_2 and generation of H2 for the MF Mg- CO_2 battery, the amounts of generated H2 and utilized CO_2 were measured consecutively during the discharge process by the *in-operando* quantitative gas chromatography (GC) measurements (Figure 6-6f and g). It was found that the hydrogen was generated with an average Faraday efficiency of 92.0% over 70 min with an average CO_2 consumption of 1.41 mL CO_2 min^{-1} (being converted into HCO_3^-, cf. Eq. 1 and 2). Figure 6-6g shows the *in-operando* quantitative GC profiles measured at a discharge current of 200 mA in the CO_2-saturated electrolyte solution. Prior to the discharge progress, only the CO_2 peak was

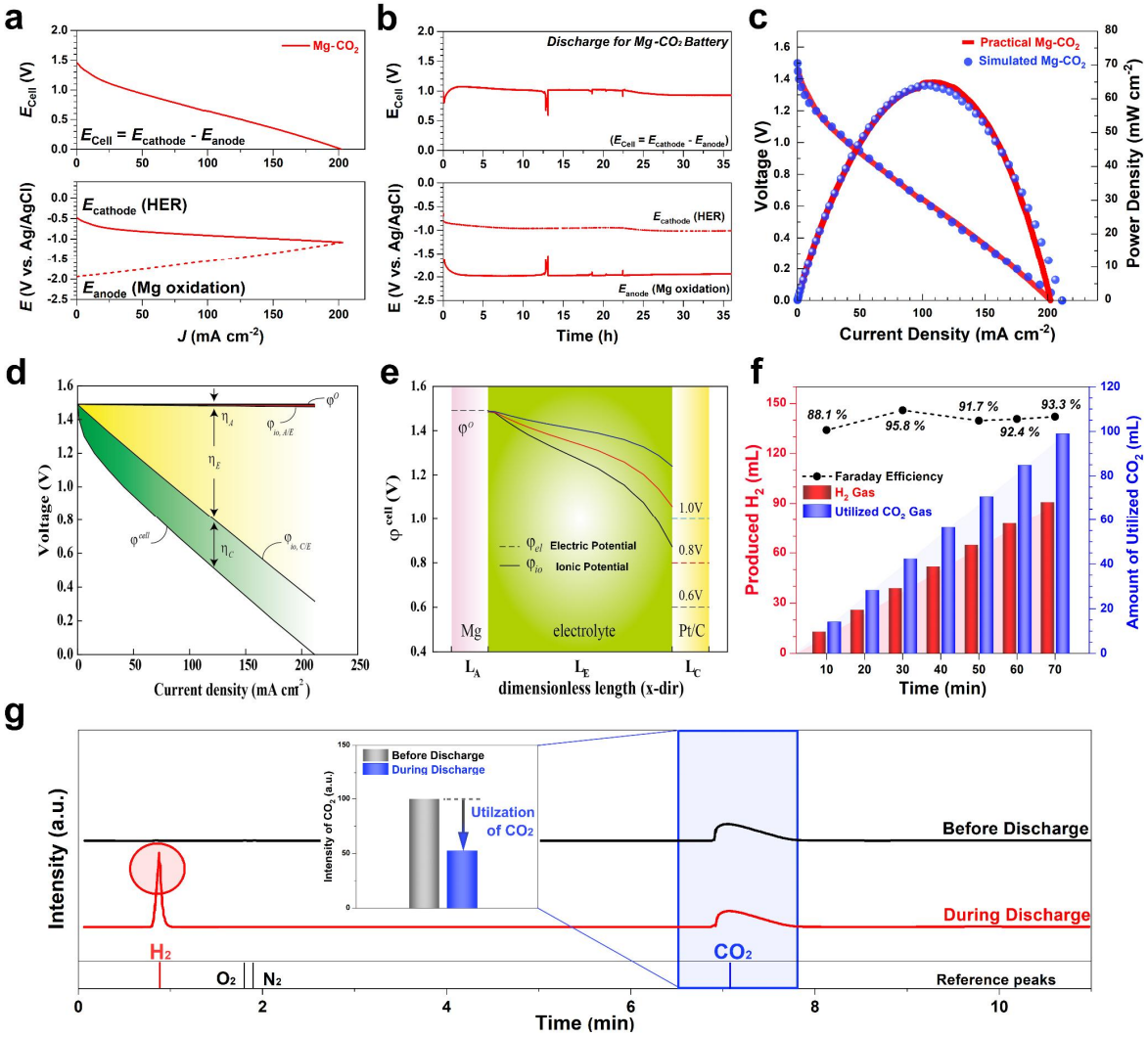

Figure 6-6 Membrane-free Mg-CO_2 Battery performance. Full-cell tests were conducted in three-electrode configuration using Ag/AgCl reference electrode. (a) Polarization curves of catalyst. (b) Chronopotentiometric reduction profiles at 10 mA cm^{-2}. (c) I-V profiles and corresponding power density of practical and simulated electrochemical performances. (d) Contribution of component overpotentials to the overall potential loss. (e) Spatial distribution of electronic and ionic potentials. (f) The amount of hydrogen production and CO_2 conversion with Faraday efficiency during consecutive discharge at 200 mA. (g) The *in-operando* qualitative GC profiles of outlet CO_2 feed gas before and during discharge at 200 mA under CO_2 saturated 1 M KOH + 1M NaCl solution.

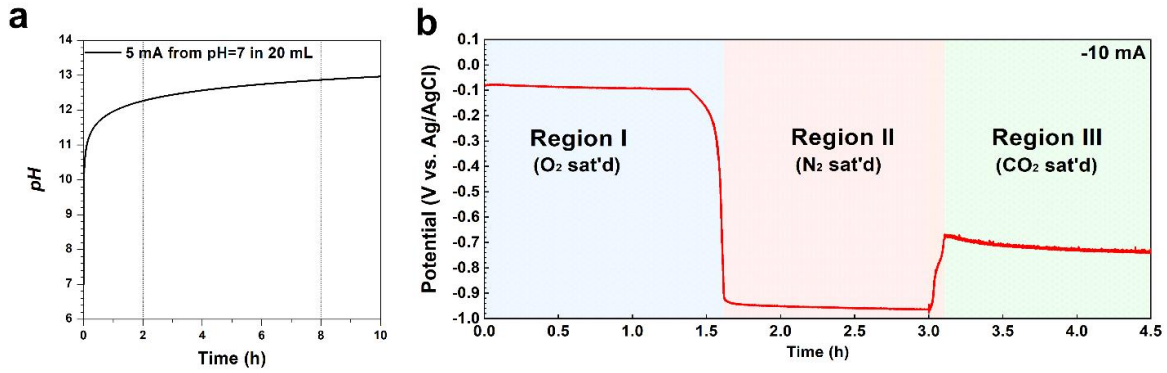

Figure 6-7 The effects of saturated condition in N_2 or CO_2 for Mg-CO_2 battery. (a) I-V profiles under N_2- or CO_2-saturated 1 M KOH and 1 M NaCl. (b) Potentiodynamic polarization for Mg at different saturated condition.

detected. During the discharge process, however, the pure H2 and excess CO_2 gas were detected, but without any other gases (*e.g.*, oxygen, nitrogen, carbon monoxide, *etc.*). The amount of utilized CO_2 gas was further investigated, as shown in the inset of Figure 6-6g, confirming the fixation of CO_2 during the discharge process. The theoretical amounts of hydrogen production and CO_2 consumption were also shown in Figure 6-8, which shows the same trend as the experimental data (Figure 6-6f). Therefore, these GC profiles clearly indicate that the utilization of CO_2 has continuously proceeded to generate pure H_2 during the discharge process.

6.3.4 Structure and morphology analysis after discharge process

After a prolonged discharge process, carbonate ion species converted from the CO_2 feed gas precipitated as a white solid product at the bottom of the MF Mg- CO_2 battery (Figure 6-9a) [2,4]. However, H2 generation and CO_2 conversion still occurred even when the electrolyte solution was fully saturated with carbonate ion species. As shown in XRD profiles (Figure 6-9b), the white solid product was identified as magnesium carbonate (MgCO3 complexed with water). Following the calculated Pourbaix phase diagram (Figure 6-10), Mg2+ is the most thermodynamically stable phase under the present operating conditions [17]. Upon full saturation of the aqueous solution of magnesium bicarbonate with carbonate ion species, however, Mg(HCO3)2(aq) ion was converted into the solid-phase MgCO3 (Eq. 6).

$$Mg^{2+}_{(aq)} + 2\ HCO_3^-{}_{(aq)} \rightarrow MgCO_{3(s)} + H_2O_{(l)} + CO_{2(g)} \quad (6)$$

The XRD pattern of the freeze-dried electrolyte after the discharge process under the N2-saturated condition was shown in Figure 6-9c, revealing magnesium hydroxide, Mg(OH)2, as the main product. We have further investigated the surfaces of the Mg electrode (Figure 6-9d and e) and gas generation

electrode (Figure 6-9f). As expected, the partial corrosion reaction of the Mg electrode surface occurred in the presence of CO_2, leading to the partial formation of carbonate products, such as Mg(OH)HCO3 and Mg2(OH)2CO3. This is a kind of carbonate species (*e.g.,* CO32- and HCO3 -), but different discharge products, as shown in Figure 6-9d and e. To avoid possible inhibition of the electrochemical oxidation of Mg metal by a protective layer of the newly-formed carbon products, we have added NaCl in the electrolyte solution to release Cl- ions to maintain the continuous oxidation of the Mg electrode under the CO_2-saturated condition as Cl- ions have been previously demonstrated to facilitate the corrosion of magnesium alloy in the presence of CO_2 [18]. The concentration of NaCl for the MF Mg-CO_2 battery was optimized according to the Ecorr *vs.* Ag/AgCl (Figure 6-11). Unlike the Mg electrode, the hydrogen gas generation electrode (Pt/AC) showed no significant change in XRD profiles before and after the discharge process, indicating no deposition of any solid discharge product on the electrode (Figure 6-9f).

6.3.5 Reversibility of membrane-free Mg- CO_2 battery

To demonstrate the reversibility of the Mg- CO_2 battery, we measured the anodic charge profile by using an electrocatalyst IrO2. Figure 6-12a shows oxidation profiles on a rotating disk electrode with or without NaCl in the electrolyte. As can be seen, the current density more rapidly increased with increasing overpotential in the CO_2-saturated 1 M KOH and 1 M NaCl electrolyte compared to CO_2-saturated 1 M KOH without NaCl. The increased current density is attributable to the chlorine evolution reaction (CER, Eq. 7) apart from the oxygen evolution reaction (Eq. 8).

$$2Cl^- \rightarrow Cl_{2(g)} + 2e^- \qquad E = 1.36\ V\ vs.\ SHE \qquad (7)$$

$$2H_2O \rightarrow O_{2(g)} + 4H^+ + 2e^- \qquad E = 0.78\ V\ vs.\ SHE \qquad (8)$$

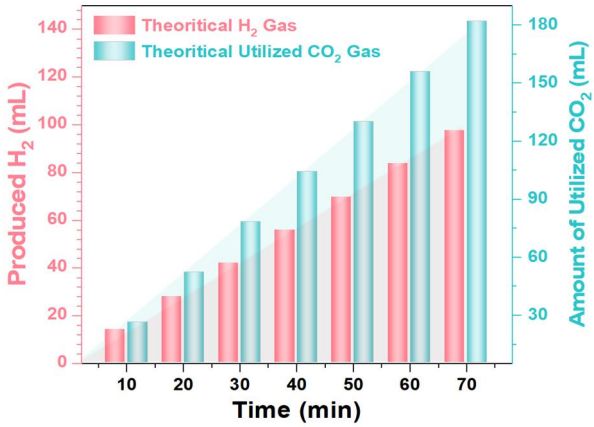

Figure 6-8 The theoretical amount of hydrogen production and CO_2 conversion at 200 mA discharge process.

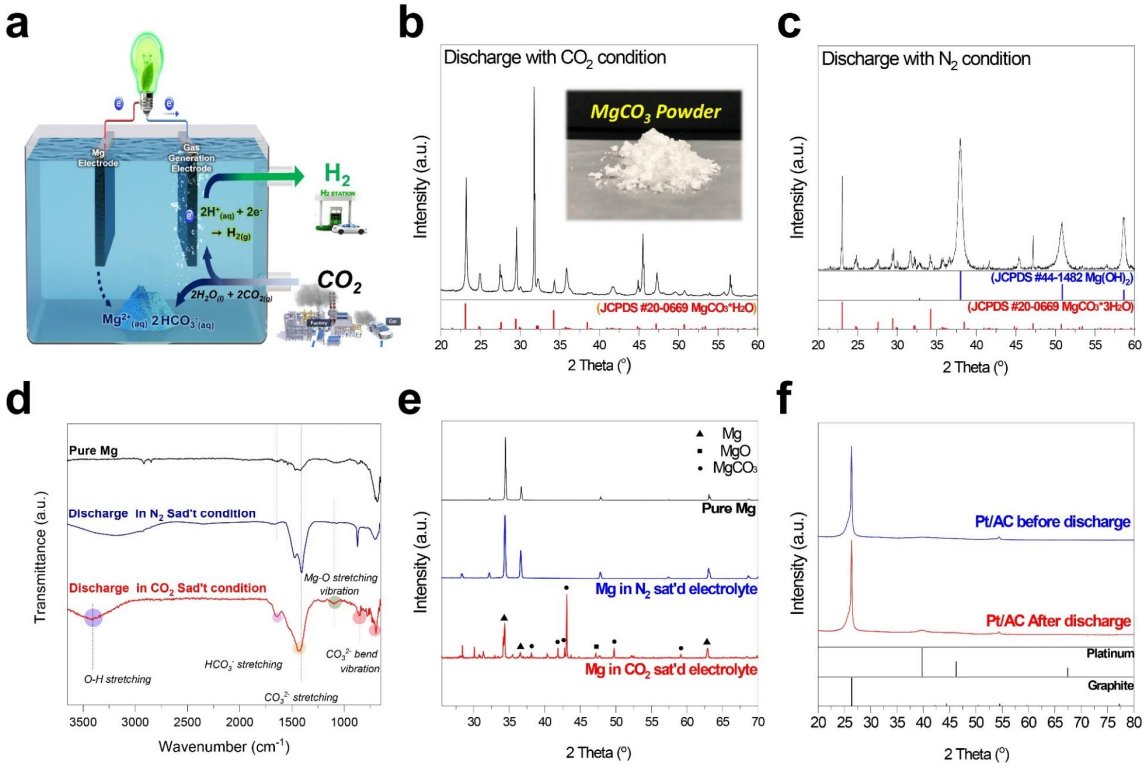

Figure 6-9 Structure and morphology analysis after discharge process. (a) Schematic illustration of MF Mg-CO_2 battery. (b and c) The XRD profile of the precipitated white solid after discharge process in CO_2 sat'd condition and N_2 sat'd condition. (d and e) The FT-IR spectra and XRD patterns of pure Mg, Mg after discharge in N_2 sat'd condition, and Mg after discharge in CO_2 sat'd condition. (f) XRD profiles of carbon paper electrode with Pt/C catalyst before and after discharge progress under CO_2 sat'd 1 M KOH + 1M NaCl solution.

As shown in the inset of Figure 6-12a, Tafel plots were derived from polarization curves for both electrolyte conditions, which show a smaller slope (47 mV dec _1) for the electrolyte containing NaCl than that for the electrolyte without NaCl (65 mV dec _1), indicating that the addition of NaCl facilitated the oxidation processes in the MF Mg- CO_2 battery. Figure 6-12b shows the charge and discharge curves for the MF Mg- CO_2 battery, along with the simulated polarization data that display a good agreement with the experimental results except for the slight decrease of charge performance at low current densities due to the well-known oxidation peak of iridium-based catalyst [19,20]. GC profiles shown in Figure 6-12c indicate that both O_2 and Cl_2 were simultaneously generated during the oxidation process. Cl^- ions in the electrolyte has led to not only stable oxidation of the Mg electrode, but also enhanced charging kinetics of the MF Mg- CO_2 battery. Furthermore, the charge-discharge performance for the MF Mg- CO_2 battery was compared to the recently reported aqueous Zn- CO_2 battery containing membrane [4]. As can be seen in Figure 6-13, our MF Mg- CO_2 battery outperformed the Zn- CO_2 battery in terms of the open circuit voltage and peak power density. The power capability of the MF Mg- CO_2 battery was tested at various current rates. As shown in Figure 6-12d (the upper

rectangle), the current density gradually raised from 5 to 40 mA cm^{-2} and reduced back to 5 mA cm^{-2}. Notably, the polarization degree did not significantly increase even when the current density increased by a factor of 8 times. Over the whole current density range from 5 to 40 mA cm^{-2} covered in this study, the charging voltage remained under 3.1 V and discharging voltage remained over 0.75 V. Also, the initial discharging voltage was nearly recovered after returning the current density to 5 mA cm^{-2}. For the further investigation of the reversibility of the gas generation electrode, the long-term cycling performance at a constant current density of 20 mA cm^{-2} was conducted. Figure 6-12d (the lower rectangle) also shows polarization curves for the metal and gas generation electrode, respectively, which displays a similar overall trend as that for the whole MF Mg- CO_2 battery. Over the 800 min (80

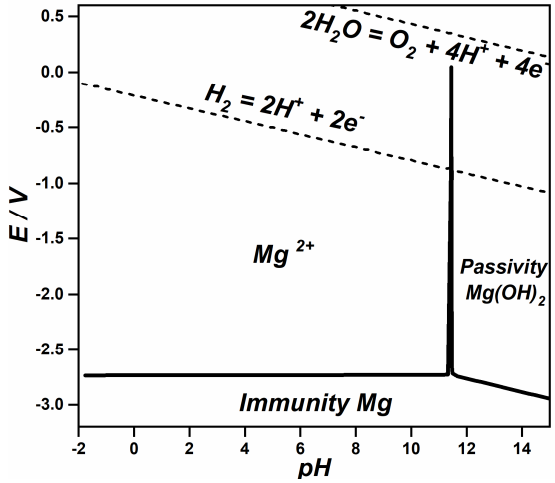

Figure 6-10 Pourbaix diagram for Mg-H_2O system at 25 °C.

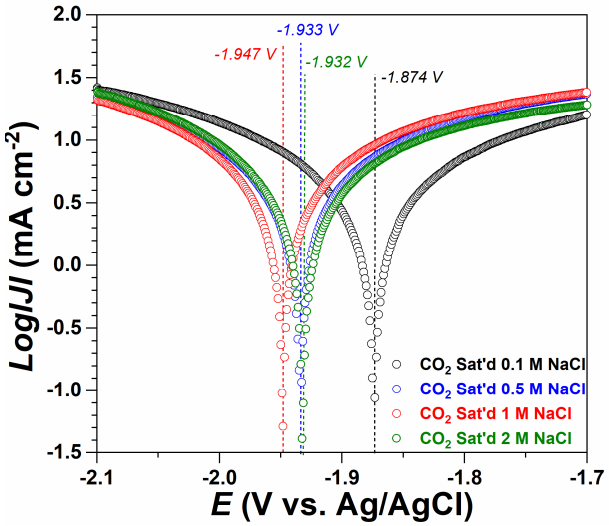

Figure 6-11 Potentiodynamic polarization for Mg electrode at different concentrations of NaCl.

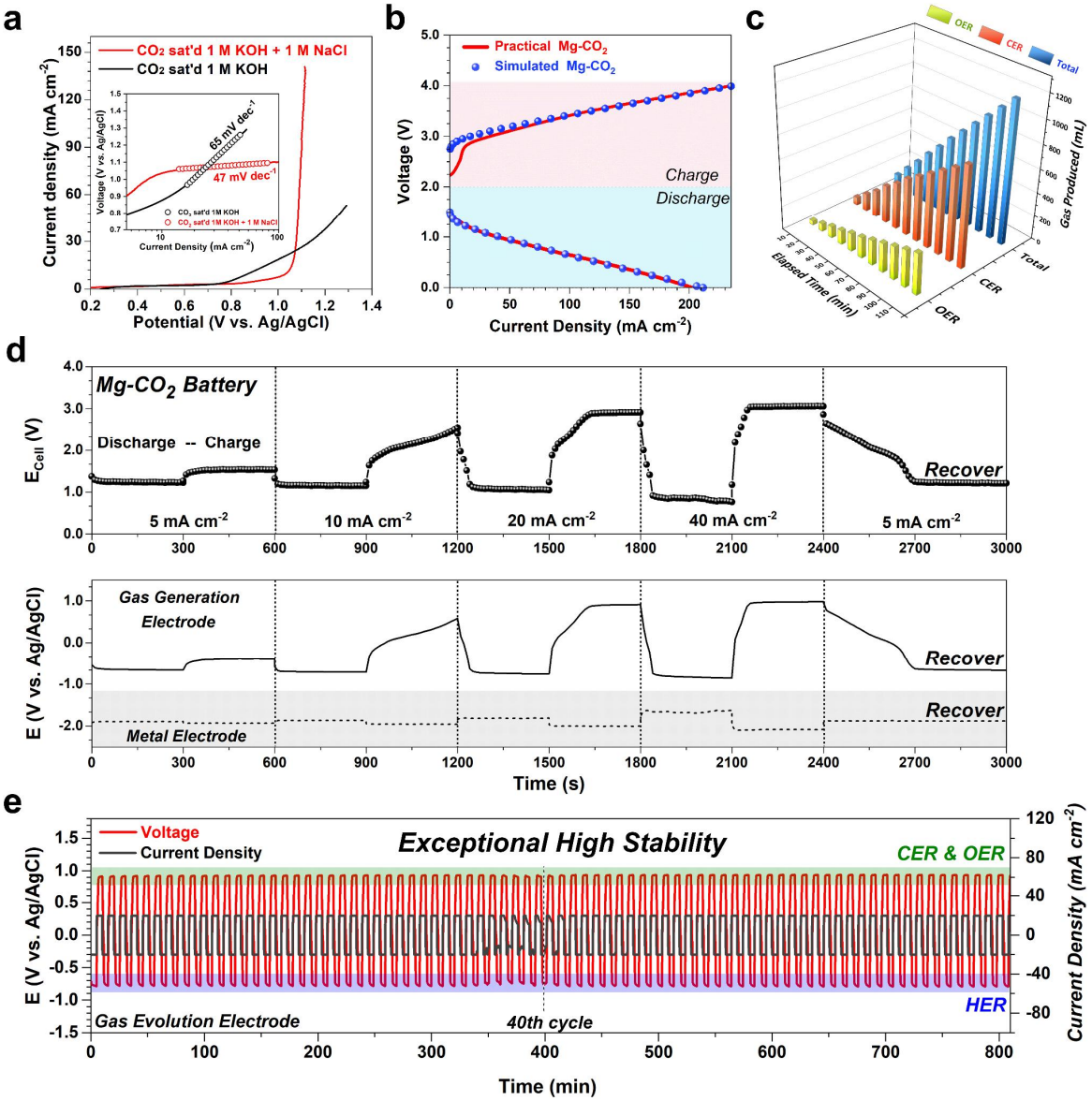

Figure 6-12 Reversibility of Membrane-free Mg-CO_2 Battery. (a) Anodic rotating disk electrode profiles of IrO_2 catalyst in CO_2 sat'd 1 M KOH with and without 1 M NaCl. Inset: Tafel plots of the anodic profiles. (b) Charge and discharge polarization curves compared between practical and simulated performances in Mg-CO_2 Battery. (c) The amount of oxygen and chlorine production during the consecutive charge at 200 mA. (d) Discharge-charge curves with different current densities in the range of 5-40 mA cm^{-2}. (e) Cycling performance of Mg-CO_2 Battery at a current density of 20 mA cm^{-2}.

discharge-charge cycles), the MF Mg- CO_2 battery exhibited outstanding cycling performance with the triple gas generation (H2/O2/Cl2) with a nearly constant charge-discharge voltage gap. The reproducibility of the Mg anode during the charging process at a constant voltage of 3.5 V was also investigated by the ICP (inductively coupled plasma) measurements. As shown in Figure 6-14, the concentration of Mg ions in the electrolyte solution gradually increased due to the partial corrosion of the Mg electrode even without charging during the initial 2 h. After charging the MF Mg- CO_2 battery, the concentration of Mg ions decreased to 47.0 mgMg L^{-1}, indicating the deposition of Mg ions back to

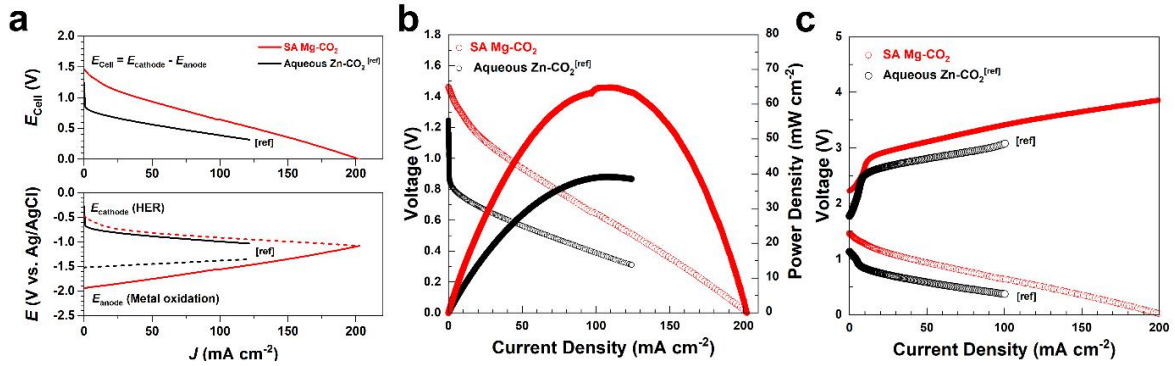

Figure 6-13 Polarization curves, I-V profiles and Charge-discharge polarization curves compared between aqueous Zn-CO_2 system and Mg-CO_2 battery.

the Mg anode (*i.e.,* the reverse reaction of Eq. 3). These results clearly demonstrate superior rate-capability and reversibility for both the metal and gas generation electrodes in the Mg- CO_2 battery. Additionally, it is worth noting that a charge process can suppress the solidification of the carbonate species (Eq. 6), leading to the improvement of CO_2 utilization efficiency per Mg. We have also used Ba0.5Sr0.5Co0.8Fe0.2O3-d (BSCF) and various Mg-based alloyed electrocatalysts for demonstrating the versatility of the MF Mg- CO_2 battery (Figure 6-15) and estimated the maximum power densities for AZ31(42.3 mW at 87 mA cm^{-2}), AZ61(43.9 mW at 112 mA cm^{-2}), and AZ91 (50.0 mW at 121 mA cm^{-2}) electrodes in Figure 6-16. Owing to the highly generic nature characteristic of the battery reactions and the associated electrocatalysts that can be used to enable the battery operation, the methodology developed in this study could be regarded as a general platform for the development of next-generation of metal- CO_2 batteries for CO_2 sequestration, value-added chemical production, clean energy generation, and beyond.

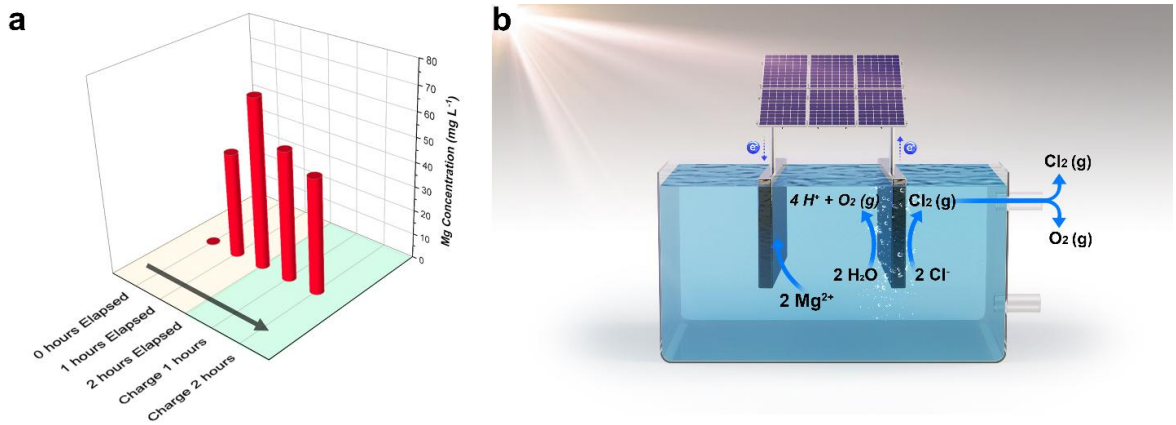

Figure 6-14 (a) Mg ion concentration in solution during charge process for Mg-CO_2 battery. (b) Schematic of charge process of battery.

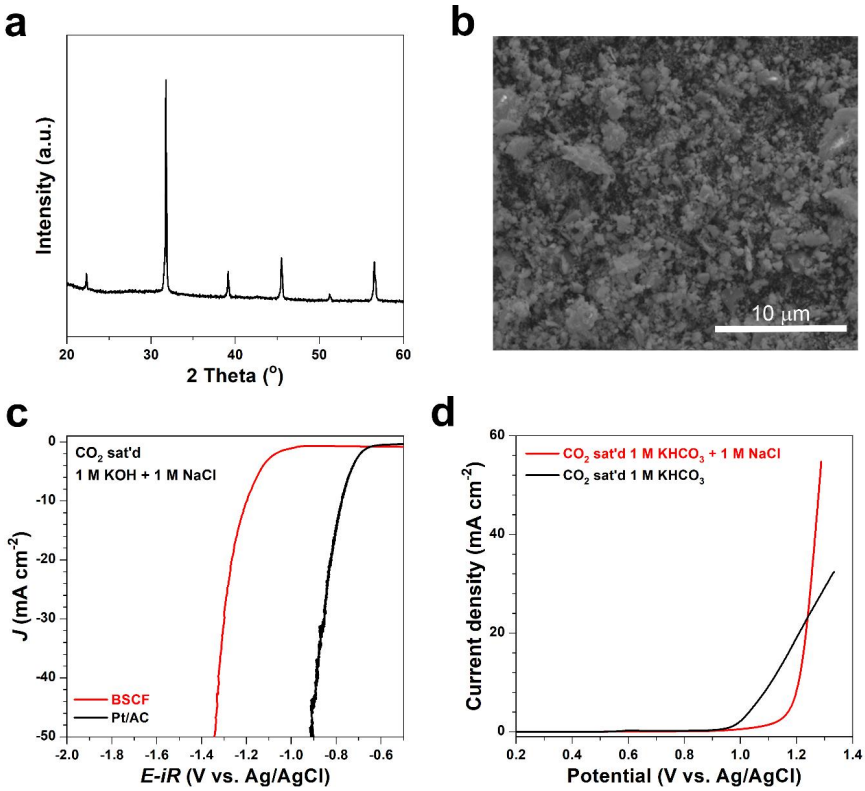

Figure 6-15 Structural and electrochemical analysis of $Ba_{0.5}Sr_{0.5}Co_{0.8}Fe_{0.2}O_{3-d}$ (BSCF). (a) X-ray diffractometer (XRD) result and (b) morphology of BSCF. (c) RDE polarization curves of each catalyst for reductive profile and (d) anodic profiles in CO_2 sat'd 1 M KOH with and without 1 M NaCl of BSCF.

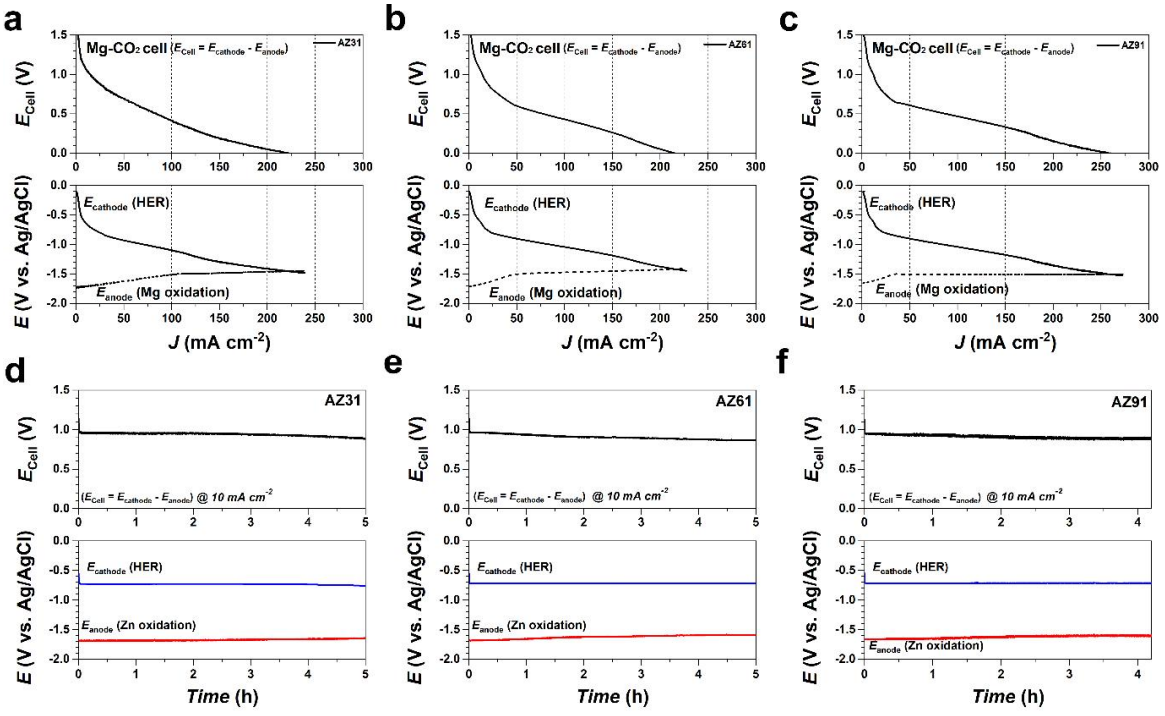

Figure 6-16 Various Mg alloy electrodes for Mg-CO_2 battery. I-V profiles and stability test using (a,d) AZ31, (b,e) AZ61, and (c,f) AZ91 alloy electrode

6.4 Conclusions

Finally, in order to translate the newly-developed laboratory-scale MF Mg- CO_2 battery technology into a commercial reality, we have envisioned an operational prototype system (Figure 6-17) that produces electricity and value-added chemicals as a cornerstone to better support sustainable human life from CO_2 and earth-abundant renewable power (*e.g.,* wind, solar, seawater). A typical process flow diagram for discharging and/or charging the MF Mg- CO_2 battery system is given in Figure 6-18. With only the discharging process for the Mg- CO_2 battery (Figure 6-18a), the produced energy was estimated to be 0.15 MJ mol^{-1} CO_2, which increased up to 0.20 MJ mol^{-1} CO_2 in conjunction with the charging process from renewable energy (*e.g.,* solar, wind, seawater) as the charging process will suppress the solidification of the carbonate species and improve the CO_2 utilization efficiency (*vide supra*). The energy requirements per mole of CO_2 at each of the processes were detailed which, together with Figure 6-17, indicate great benefits for the newly-developed MF Mg- CO_2 battery technology to produce various value-added chemicals of practical significance and electricity from CO_2 without any wasted by-products. Therefore, we have developed a promising and feasible protocol to convert harmful CO_2 into clean electricity and value-added products, opening the door to electrochemical utilization of CO_2 for future alternative technologies.

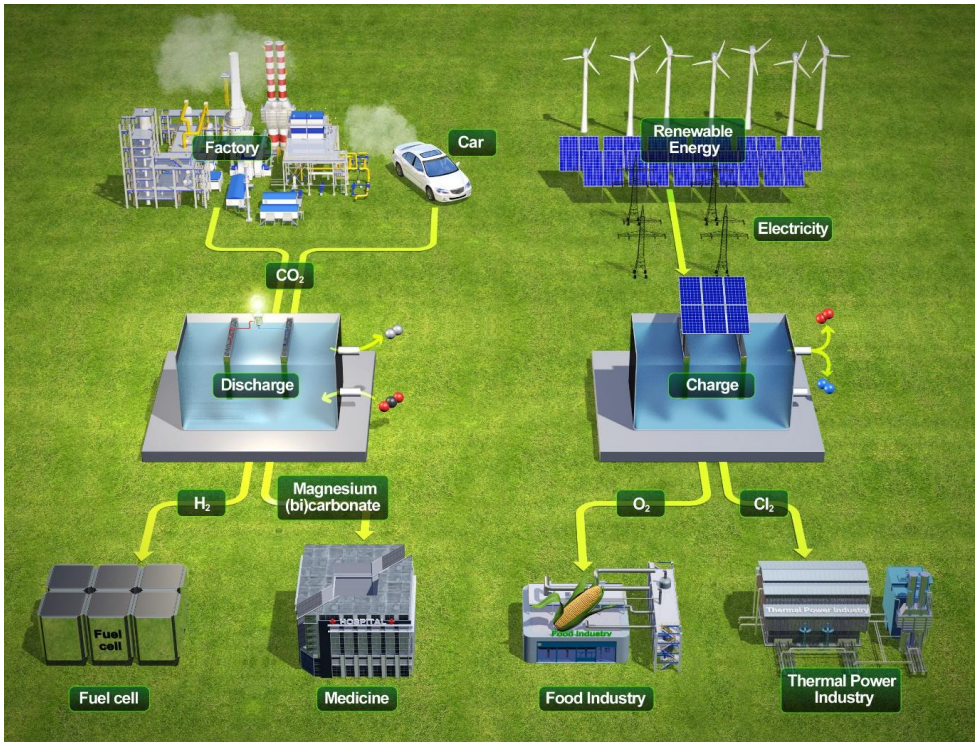

Figure 6-17 MF Mg-CO_2 battery at the crossroad to better support sustainable human life.

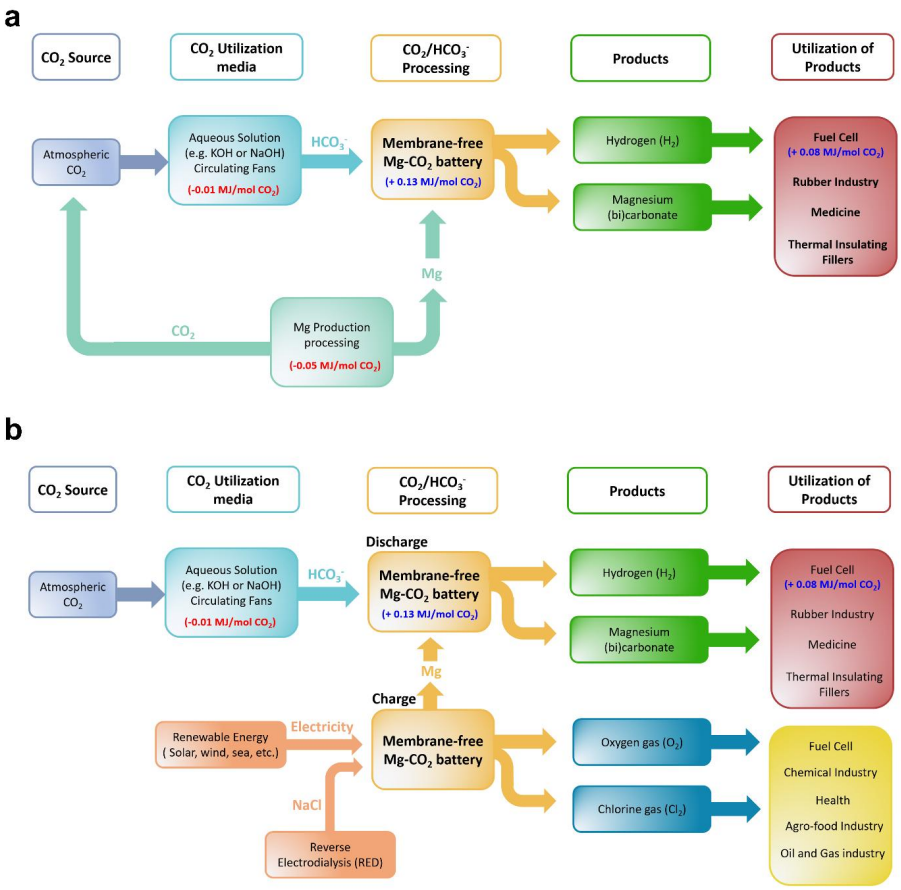

Figure 6-18 Schematic representation of processes and energy requirements (a) without charge process and (b) with charge process from renewable energy.

References

[1] F.P. García de Arquer, C.T. Dinh, A. Ozden, J. Wicks, C. McCallum, A.R. Kirmani, D.H. Nam, C. Gabardo, A. Seifitokaldani, X. Wang, Y.C. Li, F. Li, J. Edwards, L. J. Richter, S.J. Thorpe, D. Sinton, E.H. Sargent, CO_2 electrolysis to multicarbon products at activities greater than 1 A cm _2, Science 367 (2020) 661–666, https:// doi.org/10.1126/science.aay4217.

[2] C. Kim, J. Kim, S. Joo, Y. Bu, M. Liu, J. Cho, G. Kim, Efficient CO_2 utilization via a hybrid Na-CO_2 system based on CO_2 dissolution, IScience 9 (2018) 278–285, https://doi.org/10.1016/j.isci.2018.10.027.

[3] A.J. Welch, E. Dunn, J.S. Duchene, H.A. Atwater, Bicarbonate or carbonate processes for coupling carbon dioxide capture and electrochemical conversion, ACS Energy Lett. 5 (2020) 940–945, https://doi.org/10.1021/acsenergylett.0c00234.

[4] C. Kim, J. Kim, S. Joo, Y. Yang, J. Shin, M. Liu, J. Cho, G. Kim, Highly efficient CO_2 utilization via aqueous zinc– _or aluminum– CO_2 systems for hydrogen gas evolution and electricity production, Angew. Chem. Int. Ed. 58 (2019) 9506–9511, https:// doi.org/10.1002/anie.201904763.

[5] S. Lee, J.D. Ocon, Y. Il Son, J. Lee, Alkaline CO_2 electrolysis toward selective and continuous HCOO- production over SnO2 nanocatalysts, J. Phys. Chem. C 119 (2015) 4884–4890, https://doi.org/10.1021/jp512436w.

[6] X. Wang, J. Xie, M.A. Ghausi, J. Lv, Y. Huang, M. Wu, Y. Wang, J. Yao, Rechargeable Zn– CO_2 electrochemical cells mimicking two-step photosynthesis, Adv. Mater. 31 (2019), 1807807, https://doi.org/10.1002/adma.201807807.

[7] K. Wang, Y. Wu, X. Cao, L. Gu, J. Hu, A Zn– CO_2 flow battery generating electricity and methane, Adv. Funct. Mater. 30 (2020), 1908965, https://doi.org/10.1002/ adfm.201908965.

[8] W.I. Al Sadat, L.A. Archer, The O2-assisted Al / CO_2 electrochemical cell: a system for CO_2 capture / conversion and electric power generation, Sci. Adv. 2 (2016), e1600968. https://advances.sciencemag.org/content/2/7/e1600968.

[9] Y. Jin, C. Hu, Q. Dai, Y. Xiao, Y. Lin, J.W. Connell, F. Chen, L. Dai, High-performance Li- CO_2 batteries based on metal-free carbon quantum dot/holey graphene composite catalysts, Adv. Funct. Mater. 28 (2018), 1804630, https://doi. org/10.1002/adfm.201804630.

[10] Z. Xie, X. Zhang, Z. Zhang, Z. Zhou, Metal– CO_2 batteries on the road: CO_2 from contamination gas to energy source, Adv. Mater. 29 (2017), 1605891, https://doi. org/10.1002/adma.201605891.

[11] J. Xie, Z. Zhou, Y. Wang, Metal– CO_2 batteries at the crossroad to practical energy storage and CO_2 recycle, Adv. Funct. Mater. 30 (2019), 1908285, https://doi.org/ 10.1002/adfm.201908285.

[12] R. Pipes, J. He, A. Bhargav, A. Manthiram, Efficient Li- CO_2 batteries with molybdenum disulfide nanosheets on carbon nanotubes as a catalyst, ACS Appl. Energy Mater. 2 (2019) 8685–8694, https://doi.org/10.1021/acsaem.9b01653.

[13] S. Xu, S.K. Das, L.A. Archer, The Li- CO_2 battery: a novel method for CO_2 capture and utilization, RSC Adv. 3 (2013) 6656–6660, https://doi.org/10.1039/ c3ra40394g.

[14] L. Qie, Y. Lin, J.W. Connell, J. Xu, L. Dai, Highly rechargeable lithium- CO_2 batteries with a boron- and nitrogen-codoped holey-graphene cathode, Angew. Chem. Int. Ed. 129 (2017) 7074–7078, https://doi.org/10.1002/anie.201701826.

[15] J. Xie, X. Wang, J. Lv, Y. Huang, M. Wu, Y. Wang, J. Yao, Reversible aqueous zinc– CO_2 batteries based on CO_2–HCOOH interconversion, Angew. Chem. Int. Ed. 57 (2018) 16996–17001, https://doi.org/10.1002/anie.201811853.

[16] A. Asokan, C. Lim, J. Kim, O. Kwon, H. Lee, S. Joo, H.Y. Jeong, G. Kim, Carbon nanofibers encapsulated nickel-molybdenum nanoparticles as hydrogen evolution catalysts for aqueous Zn–CO_2 system, ChemNanoMat 6 (2020) 937–946, https:// doi.org/10.1002/cnma.202000099.

[17] V.S. Saji, Review of rare-earth-based conversion coatings formagnesium and its alloys, J. Mater. Res. Technol. 8 (2019) 5012–5035, https://doi.org/10.1016/j. jmrt.2019.08.013.

[18] Q. Qu, J. Ma, L. Wang, L. Li, W. Bai, Z. Ding, Corrosion behaviour of AZ31B magnesium alloy in NaCl solutions saturated with CO_2, Corros. Sci. 53 (2011) 1186–1193, https://doi.org/10.1016/j.corsci.2010.12.014.

[19] V. Pfeifer, T.E. Jones, J.J. Velasco V´elez, R. Arrigo, S. Piccinin, M. H¨avecker, A. Knop-Gericke, R. Schl¨ogl, In situ observation of reactive oxygen species forming on oxygen-evolving iridium surfaces, Chem. Sci. 8 (2017) 2143–2149, https://doi. org/10.1039/c6sc04622c.

[20] S. Kim, M. Cho, Y. Lee, Iridium oxide dendrite as a highly efficient dual electro-catalyst for water splitting and sensing of H2O2, J. Electrochem. Soc. 164 (2017) B3029–B3035, https://doi.org/10.1149/2.0061705jes.

Chapter 7 A Rigorous Electrochemical Ammonia Electrolysis Protocol with *In-operando* Quantitative Analysis

This chapter has been published and has been cited in the thesis by co-author Y. Yang.

Reproduced from ***J. Mater. Chem. A***, 2019, **9**, 11571-11579 with permission from the Chinese Chemical Society (CCS), Peking University (PKU), and the Royal Society of Chemistry.

7.1 Introduction

Owing to high capacity of hydrogen storage and environmental points of view, the ammonia (NH_3) electro-oxidation reaction has received increasing interest as advanced technology to produce hydrogen using less thermodynamic energy than water electrolysis.[1–4] Theoretically, the electrolysis of ammonia to produce nitrogen and hydrogen only requires an external voltage of 0.06 V, which is much lower than the energy needed for water electrolysis (1.23 V), leading to high theoretic energy efficiency.[5–7] According to Vitse et al., ammonia electrolysis consumes 95 % less energy than water electrolysis during producing hydrogen at mild conditions.[3] Also in terms of energy density, the ammonia contains 15.6 MJ/L of volumetric energy density which is 70 % higher than liquid hydrogen (9.1 MJ/L). Moreover, ammonia is easily condensed at ambient temperature (under 8 bar of pressure), making it suitable for transportation and storage. Consequently, the use of ammonia as a carbon-free hydrogen carrier has several advantages to succeed in widespread applications.

Ideally, the decomposition of ammonia is an attractive application for hydrogen production and comprises the reversal of the Haber-Bosch process.[4,8,9] In the liquid ammonia decomposition system, H_2O is reduced at the cathode to H_2 **(eq. 1)** while NH_3 is oxidized at the anode to N_2 **(eq. 2)**, generating the gas phase of hydrogen and nitrogen from an ammonia solution **(eq. 3)**.

Cathodic Reaction : $6H_2O + 6e^- \rightarrow 3H_2(g) + 6OH^-$ (1)

Anodic Reaction : $2NH_3(aq) + 6OH^- \rightarrow N_2(g) + 6H_2O + 6e^-$ (2)

Total Reaction : $2NH_3(aq) \rightarrow N_2(g) + 3H_2(g)$ (3)

Competitive Anodic Reaction: $6OH^- \rightarrow 3/2O_2 + 6H_2O + 6e^-$ (4)

In the liquid ammonia decomposition process, it is well-known that the anodic reaction of ammonia oxidation reaction **(eq.2)** competes with side reaction of oxygen evolution reaction **(eq. 4)**.

Herein, through *in-operando* analysis, we aim to track the real-time gas products and compare the consumption of power per hydrogen production for the ammonia electrolysis with the water-splitting during electrochemical measurements. Following this analysis, firstly ammonia decomposition can be successfully identified as H_2 and N_2 when using the most promising Pt electro-deposited electrode for this reaction in aqueous media. The well-controlled Pt electrode exhibited an exceptionally high electrochemical performance (50 mA cm^{-2} over 10 hours) in practical application. Moreover, we determine accurately the actual amount of H_2 and N_2 (or O_2) and calculate faradaic efficiency during

operation. Besides, the higher hydrogen production per power than water splitting is providing definite evidence as an efficient hydrogen production electrochemical system. However, the above discussion also disproves that the ammonia oxidation reaction (AOR) mechanism conducted on Pt electrodes are rather complicated. Therefore, we also suggested standardized protocol towards the electrochemical tendency of AOR according to the electrode synthesis process utilizing electrochemical experiments, so that the experimental results can be inferred based on the standard catalyst. The use of this viable protocol will enable more effective analysis of electrochemical systems that are focusing on the practical application of ammonia electrolysis.

7.2 Experimental

7.2.1 Electrochemical Pt deposition

The synthesis process was carried out with a three-electrode system using Biologic VMP3. The working electrode was a Ni foam (1.6 mm thickness, 99.99%, MTI Korea). A Carbon rod and Ag/AgCl served as the counter and reference electrodes, respectively. In addition, the electrodeposition of Pt on Ni foam ($1cm^2$) was performed by various cycle conditions with a voltage range from -0.4 to +0.2V (*vs.* Ag/AgCl) in 0.1 M $HClO_4$ containing H_2PtCl_6 (2 mM, Sigma-Aldrich). After that, both electrodes were dried in a vacuum oven. The optimum electrodeposition conditions were determined using CVs of electrodeposited Pt at various voltages. CP electrodeposition of Pt on Nickel foam was performed at constant current at -2 mA in 0.1 M $HClO_4$ containing 2 mM H_2PtCl_6 (Sigma-Aldrich). The electrodeposited Pt electrodes were characterized using SEM (Nova Nano SEM, FEI) and XRD (D8 Advance, Bruker).

7.2.2 Electrochemical measurements

The experiments for ammonia electrolysis were conducted using Biologic VMP3. The carbon rod and Ag/AgCl electrode (saturated KCl filled) were used as the counter electrode and the reference electrode to evaluate the electrocatalytic AOR activities. To investigate the effect of pH on ammonia oxidation, CVs were conducted in 1 M NH_3(aq) electrolytes containing various concentrations of KOH ranging from 1 M to 5 M. In addition to the effect of pH, the effect of ammonia concentration was investigated by recording CVs in 5 M KOH containing concentrations of ammonia ranging from 0.1 M to 2 M NH_3(aq). CVs were carried out at a scan rate of 20 mVs^{-1} in the region from -0.40 to 0.60 V (*vs.* Ag/AgCl). Furthermore, stability profiles were investigated at various constant current density ranging from 50 to 100 mA cm^{-2}. The obtained gas mixture was then directly subjected to analysis using a GC.

7.2.3 Gas chromatography analysis

The practical ammonia electrolysis system is composed of AOR electrode (Anode), HER electrode (Cathode), and reference electrode (Ag/AgCl) with three electrode system. The generated gas during

operating was analyzed by gas chromatograph with thermal conductivity detector (GC-TCD, controlled at 290 °C) utilizing Argon gas as the carrier gas (GC-2010 Plus, SHIMADZU Co.). The used column (controlled at 150 °C) is Micropacked column (shincarbon ST 100/120 2 m, 1 mm ID, 1/16in OD). In addition, the 1mL of sample loop (=sample volume) for GC analysis was used. Before the *in-operando* analysis, cleaning of the residue nitrogen (N_2) and oxygen (O_2) in the system is very important, because the residue N_2 & O_2 may contain substantial impurities in the faraday profiles of each gas. We have tested the residual quantity of each gas by first saturating our solution of 5 M KOH + 1 M NH_3(aq) (40 mL of electrolyte used) with Ar to remove any excess N_2 and O_2, followed by flowing 50 sccm for 1 h. A water trap before the GC instrument was placed. After Ar saturation process, all of ammonia analysis for FE was estimated with flowing 25 sccm Ar carrier gas. Although ammonia (NH_3) in the solution could be volatile, we have also checked the absence of O_2 and N_2 peak without any impurity after Ar saturation process. Each standard gas was composed with Ar gas, and was quantified from the integrated peak area. Although the electrolysis was operated in consecutive condition, the GC analyzes by a dose but not in a consecutive real-time. For sum of each produced gas, during the consecutive gas was flew into GC and out, the 1 mL (=volume of sample loop) of sample in flowing gas was analyzed every 20 min. From the FE results of each gas, we have calculated the amount of gas produced assuming that the system was operated with the identical FE between every 20 minutes.

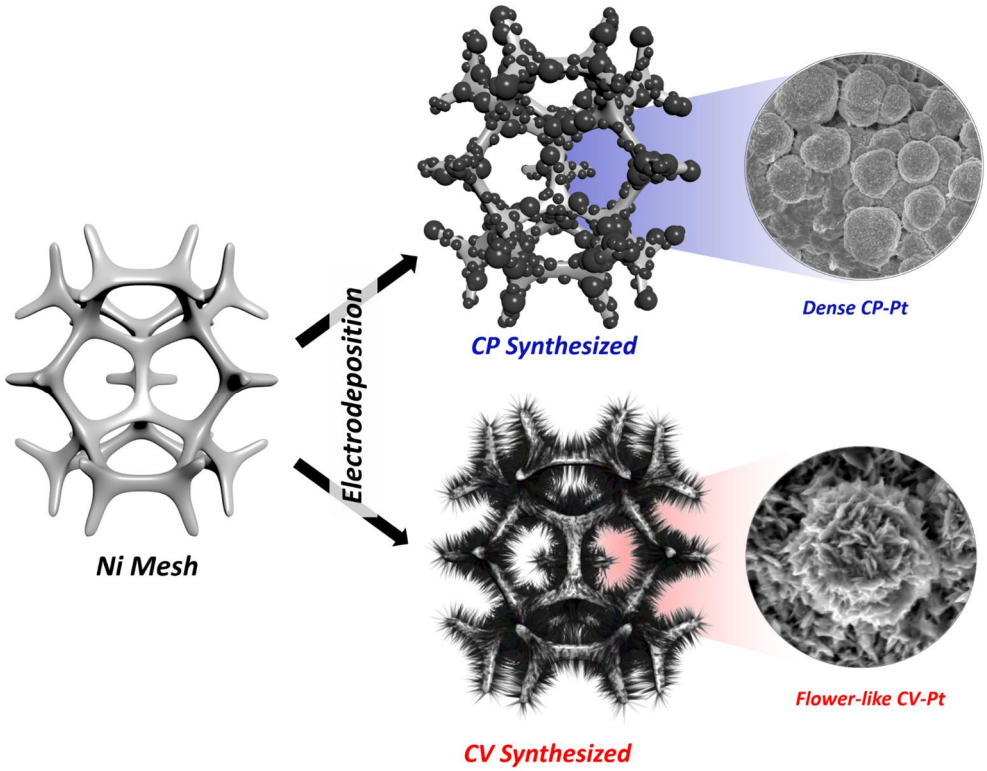

Figure 7-1 Schematic illustration of CP -Pt and CV-Pt electrodes.

7.3 Result and discussion

7.3.1 Procedure for synthesis of electrode

As shown in **Figure 7-1**, the two types of electrodeposited Pt electrodes were fabricated with a different electrochemical process (chronopotentiometric deposition *vs.* cyclic voltammetric deposition). The Pt particles were homogeneously deposited on the Nickel substrate from both processes, but different morphology.

7.3.2 Structural analysis for AOR electrode

The crystalline structure and morphology of each electrode were presented in **Figure 7-2**. In **Figure 7-2a**, the crystal structure profiles were analyzed by X-ray diffraction (XRD) measurements. On the nickel substrate, the XRD patterns featured three small polycrystalline Pt peaks as Pt(111), Pt(200), and Pt(220) at 40°, 46°, and 68°, respectively.[10–13] In Pt electrode from the cyclic voltammetric (CV) deposition process, the crystallinity of Pt improved in both Pt(111) and Pt(200) as the number of cycles was increased. With the Pt(111) and Pt(200), the average crystalline size of Pt was also investigated using the Debye-Scherrer equation (**Table 7-1**).[14–16] The average crystalline size of Pt from the CV process was about a diameter of 10 nm with independency of the cycle number of CV, which is smaller than that of Pt electrode synthesized by chronopotentiometry (CP) deposition process (diameter of ~20 nm). In **Figure 7-2b-f**, SEM profiles show the morphology of Pt on nickel substrate for CP and CV electrodes. Under chronopotentiometric deposition Pt, the agglomerated round shape dense particles with the rough surface were obtained (**Figure 7-2b**). Meanwhile, the size of Pt particles synthesized CV method in 100, 200, 400, and 500 cycles revealed smaller than that of CP method, which is well-matched with a tendency of particle size calculated from XRD.[5] Interestingly, the 400 cycle electrode showed the flower-like platinum structure on a nickel substrate, which might be attributed to the enhanced electrochemical performance with high catalytic active sites. Compared to CP synthesis, the CV acts as an alternating redox process during the cyclic process, which is involving both deposition and dissolution of Pt. The continuous redox reactions (cathodic/anodic scans) are involved in nucleation and growth of Pt particles/atoms on a nickel substrate.[17] During the reductive scan, the hydrogen (H_2) is generated on the nickel substrate following possible reactions.[18,19]

$$PtCl_6^{2-} + 2e^- \rightarrow PtCl_4^{2-} + 2Cl^- \quad (5)$$

$$PtCl_4^{2-} + 2e^- \rightarrow Pt + 4Cl^- \quad (6)$$

$$Pt + 2H^+ \rightarrow Pt(H_2)_{ads} \quad (7)$$

And then, during the oxidative scan, the further electrochemical reactions proceeded.

$$Pt(H_2)_{ads} + H_2O \rightarrow Pt(O)_{ads} + H_2(g) + 2H^+ + 2e^- \quad (8)$$

$$Pt(O)_{ads} + H_2O \rightarrow PtO_2 + 2H^+ + 2e^- \quad (9)$$

After that, during the again-reductive scan in cycle voltammetry, the reactions (10-12) proceed at low

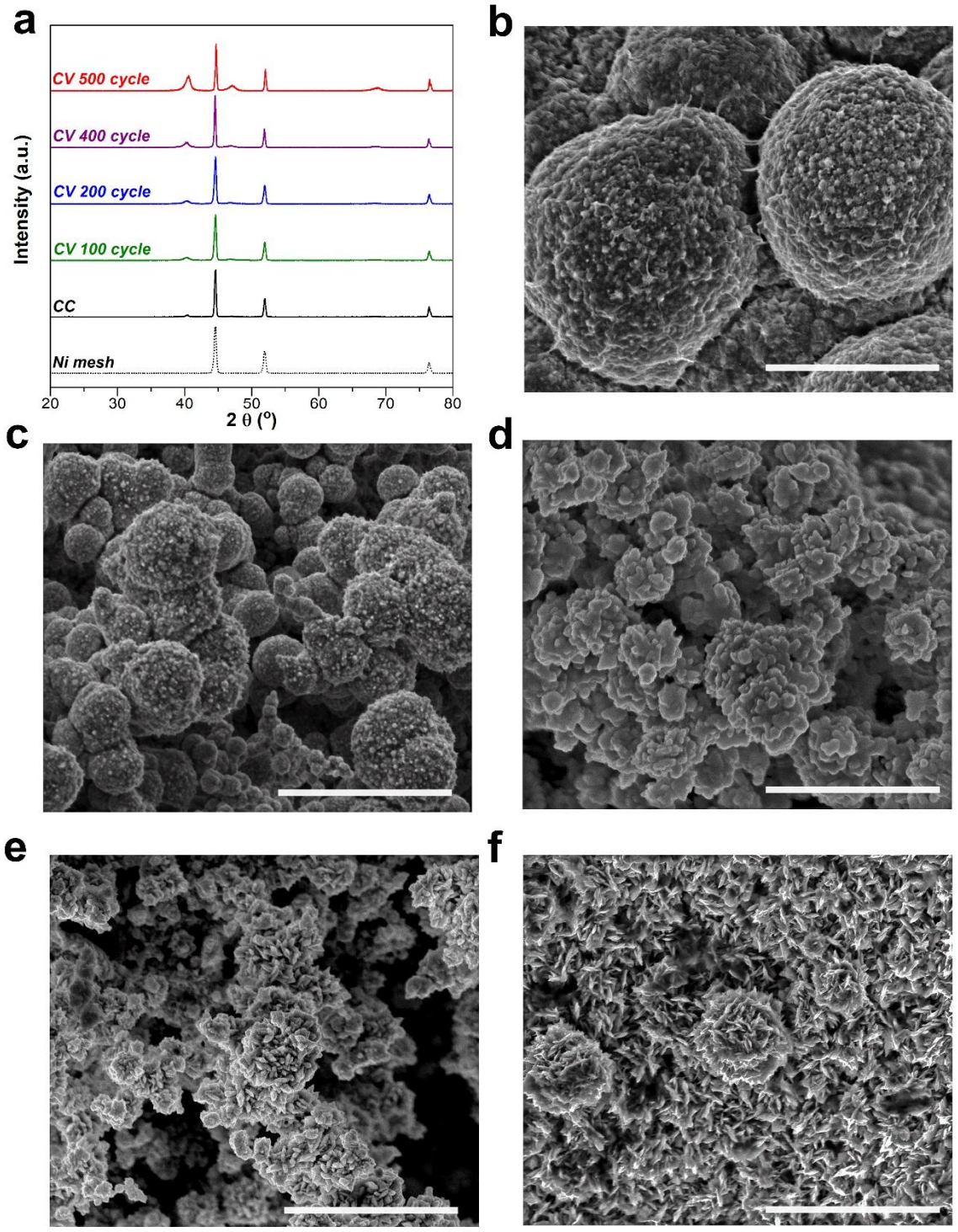

Figure 7-2 (a) XRD patterns of six samples including bare Ni mesh, and Pt-deposited Ni mesh prepared by different electrochemical processes. SEM images of electrodeposited Pt on Ni mesh (b) CP process and at various cycle number (c) 100 (d) 200 (e) 400 (f) 500 cycles. Scale bar : 1 um.

overpotential window, leading to deposition of nanoparticles/atom Pt metal on the substrate.

$$Pt(O)_{ad} + 2H^+ + 2e^- \rightarrow Pt + H_2O \qquad (10)$$

$$PtO_2 + 4H^+ + 2e^- \rightarrow Pt^{2+} + H_2O \quad (11)$$

$$Pt^{2+} + 2e^- \rightarrow Pt \text{ metal} \quad (12)$$

As suggested reaction (8), the desorption of H_2 takes place by the reaction with H_2O, which is might be attributed to flower-like morphology of Pt as shown in SEM results. Dendrite growth of Pt metal near the surface is favored due to direct generation of hydrogen bubbles off the substrate, with affects the local hydro-dynamic condition and flower-like morphology of Pt. According to the Bright-field (BF) STEM, totally different morphology between CP-Pt and 500 CV-Pt are reconfirmed (**Figure 7-3**). Moreover, TEM-EDS can be provided to confirm that the flower-like morphology belongs to Pt.

Table 7-1 FWHM and crystallite size extracted from the XRD data for electrodeposited Pt electrodes prepared with CC and CV methods

Sample	Theta (rad)	Cos θ	β, FWHM (rad)	λ, Cu Kα (nm)	Particle size (nm)
500 cycle	0.353952	0.93801	0.015374509	0.15406	10.04174
	0.411007	0.916719	0.014589506	0.15406	10.82782
	0.600044	0.825311	0.017476807	0.15406	10.04010
400 cycle	0.351353	0.938908	0.016154846	0.15406	9.547553
	0.408695	0.91764	0.01562143	0.15406	10.10240
	0.597299	0.826857	0.017461752	0.15406	10.02996
200 cycle	0.351878	0.938727	0.014104084	0.15406	10.93789
	0.410338	0.916986	0.015462694	0.15406	10.21338
	0.597159	0.826936	0.018876891	0.15406	9.27716
100 cycle	0.351971	0.938695	0.014000307	0.15406	11.01934
	0.410114	0.917075	0.017184	0.15406	9.189430
	0.597581	0.826699	0.015794198	0.15406	11.09105
CC	0.352607	0.938476	0.008769777	0.15406	17.59568
	0.409807	0.917198	0.008017641	0.15406	19.69283
	0.597907	0.826515	0.011548777	0.15406	15.17157

7.3.3 Electrochemical activieis for optimized AOR progress

To deeply evaluate the electrocatalytic activity for ammonia oxidation reaction (AOR), CP -Pt electrode and CV-Pt electrodes with the different number of CV cycles were conducted by cyclic voltammograms (CVs) in alkaline media (**Figure 7-4a**). From the CVs measurements, the CP -Pt electrode and 100 CV-Pt electrode showed a similar peak current density of 182 and 176 mA cm^{-2}, respectively. In addition, with the increased number of CV cycles, the peak current density is significantly increased and saturated by 500 cycles. After 500 cycles, as the surface grows and the structures become larger with increased surface area, the hydrodynamic stirring by the evolving H_2 is less pronounced, and the diffusion limited growth of Pt to dendritic structures is no longer favored. When this occurs, compact Pt on the flower-like Pt was deposited which might lead saturated electrochemical performance of CV electrode. The ammonia oxidation kinetics were also increased by 500 CV-Pt electrode as shown in **Figure 7-4b**. As shown in **Figure 7-5**, the AOR mass activity for 500 CV-Pt electrode was optimized as 4.37 A mg^{-1}, which is higher than that of commercial Pt/C. In addition, the 500 CV-Pt electrode of normalized

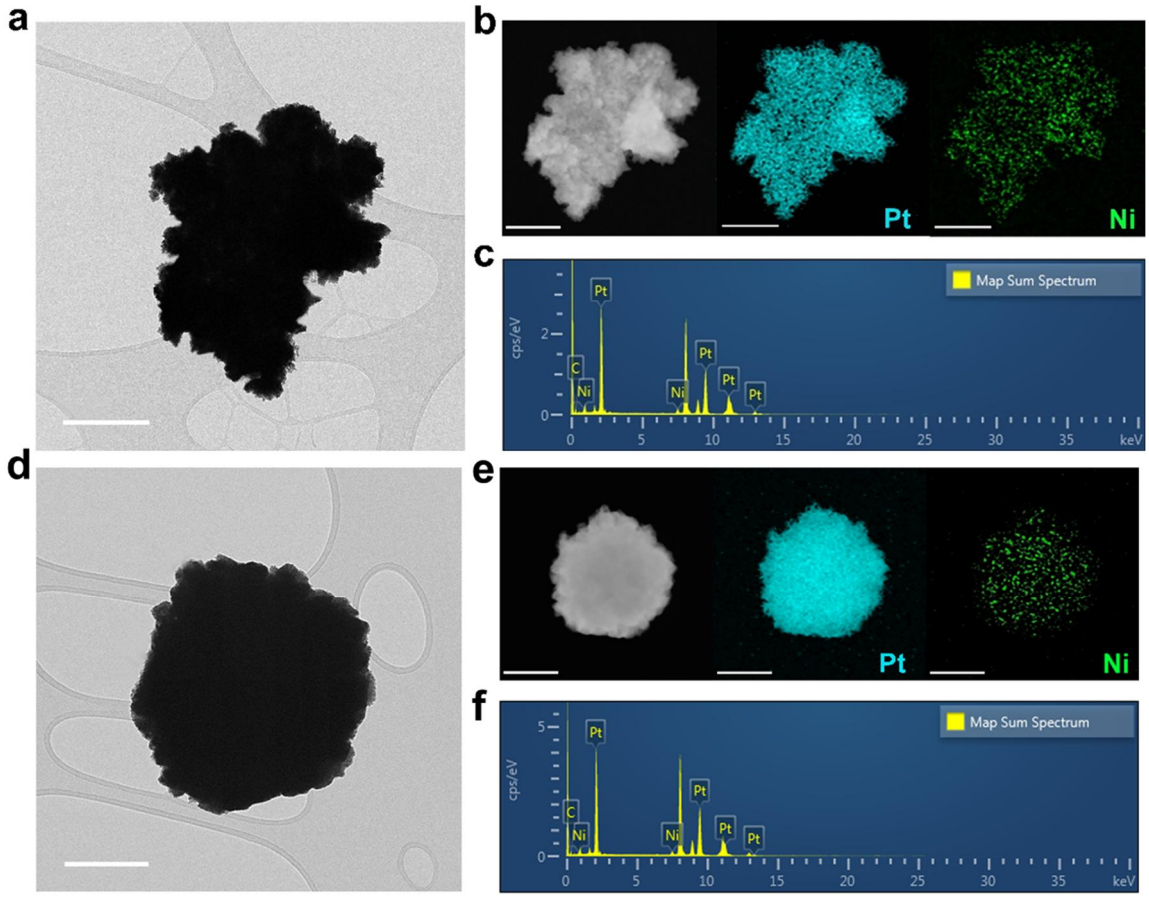

Figure 7-3 (a) Bright-field (BF) STEM image of 500 CV-Pt. (b) TEM-EDS mapping image shows flower-like morphology belongs to Pt of 500 CV-Pt. (c) EDS map spectrum of 500 CV-Pt. Scale bar : 200 nm. (d) Bright-field (BF) STEM image of CP-Pt. (e) TEM-EDS mapping image shows flower-like morphology belongs to Pt of CP-Pt. (f) EDS map spectrum of CP-Pt. Scale bar : 200 nm.

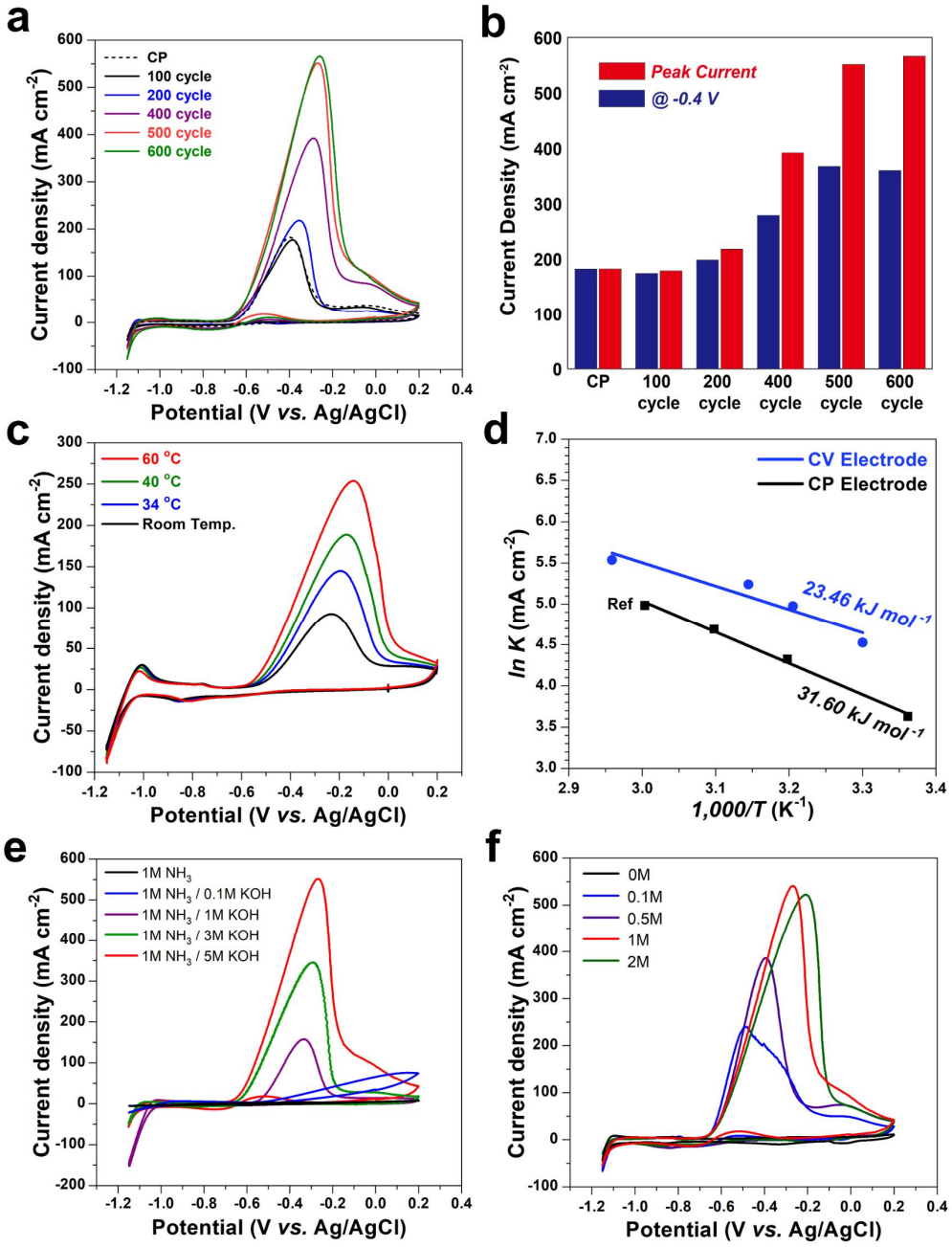

Figure 7-4 (a) CVs measured on the CV-Pt electrocatalysts in 5 M KOH / 1 M ammonia solution. (b) Comparison of peak current density at different electrodeposition process. (c) CVs of the 500 CV-Pt on carbon paper at various temperatures from 25 °C to 60 °C. (d) Arrhenius plot. The double-layer capacitance (C_{dl}) of Ref electrode is 4.86 mF cm^{-2} (e) CVs of the 500 CV-Pt electrode at various KOH concentrations from 0 M to 5 M. (f) CVs of the 500 CV-Pt electrode at various ammonia concentrations from 0 M to 2 M. All of CVs measurements are recorded at a scan rate 20 mV s^{-1}.

electrochemical performance with electrochemical surface area (ECSA) was also confirmed (**Figure 7-6** and **7**). Therefore, the CV deposition process was optimized for 500 CV-Pt electrode according to ammonia oxidation performance regarding peak current density and kinetics for AOR. In the analysis protocol for identifying promising electrocatalyst for AOR, the intrinsic catalytic activity for AOR is

needed to be investigated with the different AOR activities in various temperature conditions. In **Figure 7-4c**, CVs measurements were conducted using 500 CV-Pt on carbon paper to eliminate the activity of the nickel substrate at various temperatures in alkaline media. As the temperature increased, the peak current density for AOR is also increased. With the CVs results, we can obtain the apparent activation energy (E_a) calculated using the Arrhenius equation as follows.[20–22]

$$k = A\, e^{(-E_a/RT)}$$

where k, A, R, and T represent the reaction rate constant, frequency factor, gas constant, and temperature, respectively. Between the logarithm of current density and the reciprocal of the temperature, the linear increase of current density was confirmed with increased temperatures (**Figure 7-4d**). From the plotting data of 500 CV-Pt electrode, activation energy (E_a) for ammonia electro-oxidation was calculated as 21.26 kJ mol^{-1}, which is more favorable electrocatalyst for AOR than that of the previous Pt-based electrode (31.60 kJ mol^{-1}).[2] It is also worth noting that the activation energy for ammonia electro-oxidation is much lower than that for thermal decomposition (ca. 70-170 kJ mol^{-1}).[23,24] From the calculation of E_a for AOR, we could find the efficient electrocatalyst for AOR or evaluate the ammonia oxidation or decomposition energy in various processes.

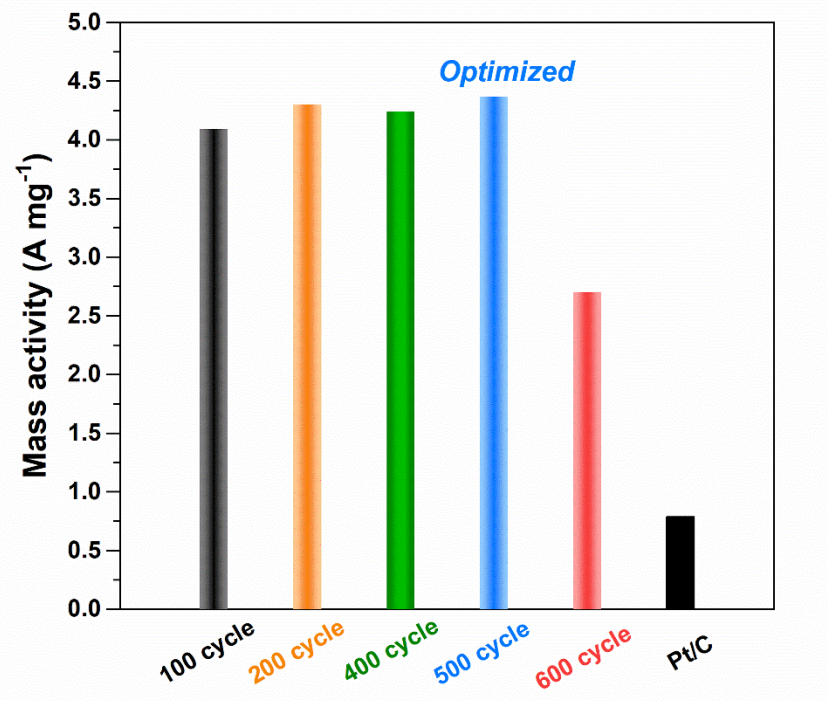

Figure 7-5 Mass activity of peak current for 100 CV-Pt, 200 CV-Pt, 400 CV-Pt, 500 CV-Pt, 600 CV-Pt, and commercial Pt/C catalyst

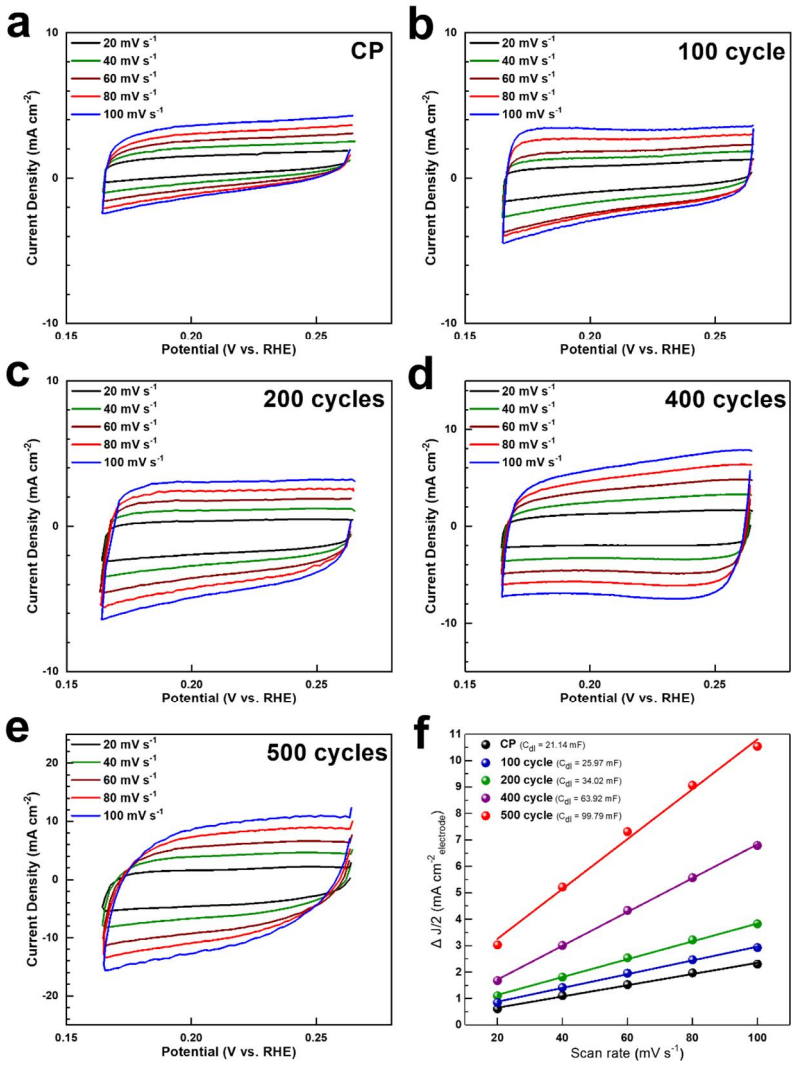

Figure 7-6 Electrochemical CV scans recorded for each electrode; Scan rates are 20, 40, 60, 80, 100, and 120 mV s-1. The selected potential range where no faradic current was observed from 0.165 to 0.265 V vs. RHE. (a) CP (b) CV-100 cycles (c) CV-200 cycles (d) CV-400 cycles (e) CV-500 cycles and (f) Capacitive current of each electrode at 0.215 V with different scan rates.

To detail investigate the catalytic activities of synthesized catalyst, the effects of not only OH^- ion concentration, but also ammonia concentration should be evaluated. In **Figure 7-4e**, the investigation for AOR was conducted in various concentrations of KOH because the KOH electrolyte was utilized as a supporting solution at both half-cell and full-cell measurements. From without KOH condition to 5 M KOH, the overpotentials for AOR were significantly reduced and the peak current densities were extremely increased. According to the above results, ammonia is easily oxidized to N_2 on Pt surface at a high concentration of KOH, which might be attributed to the facile absorption of OH^- ion at high concentration of KOH electrolyte. In addition to OH^- ion concentration dependence, the effects of ammonia concentration in the electrolyte was also investigated. **Figure 7-4f** presented that

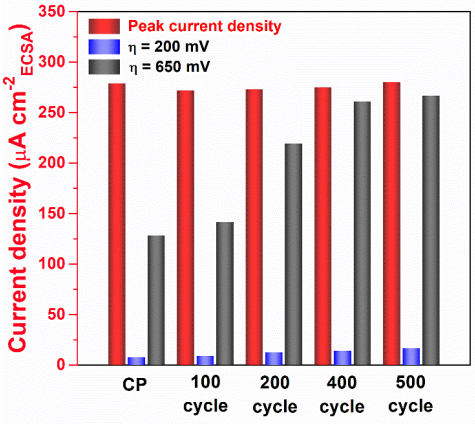

Figure 7-7 Peak current density and current density at specific potential of each electrode. h means overpotential for AOR.

the CVs measurements with a concentration of ammonia ranging from 0 M to 2 M in 5 M KOH electrolyte. As expected, at the concentration of ammonia for 0 M, there is no ammonia oxidation peak. From the 0.1 M to 1 M concentration, the ammonia oxidation peak current was gradually increased. At the 2 M concentration ammonia, however, the peak current for ammonia oxidation was slightly decreased. The decreased peak current density at 2 M ammonia electrolyte is might be attributed to metal oxidation reaction forming the metal oxynitrides that hinder the ammonia oxidation reaction.[25] Therefore, from the above electrochemical analysis, we have optimized the specific condition for 500 CV-Pt electrode for AOR as 1 M NH_3(aq) in 5 M KOH solution at 60 °C. The ammonia electrolysis in single-cell and half-cell test was operated in the optimized condition.

7.3.4 Full-cell measurements for AOR

For a practical application for ammonia oxidation and hydrogen production, we have investigated single-cell electrochemical performance containing both hydrogen evolution reaction (HER) and ammonia oxidation reaction (AOR) in **Figure 7-8**. The CV-Pt electrode with various cycles was used as anode (ammonia oxidation electrode), and Pt wire was used as a cathode for the hydrogen evolution electrode. The single-cell measurements were conducted in a three-electrode configuration using an Ag/AgCl reference electrode to detail distinguish each electrochemical reaction.[15,16,26] The stability test of the anode at various synthesized cycles ranging from 100 to 500 were conducted (**Figure 7-8a**). Among the electrocatalyst, the 500 CV-Pt electrode exhibits an excellent durability performance for 10 h at a current density of 50 mA cm^{-2}. In **Figure 7-8a**, all of the stability profiles show a potential range from 0.6 to 0.7 V in the beginning and then sharp jump to above 1.5 V as time passes. The sharp rise in cell potential occurs after a long time when the number of CV cycle is higher. From the three-electrode configuration, it is investigated that the sharp rise in cell potential was caused by the changed anodic reaction. These phenomena could be explained by competition between Equation (2) and (4) for the

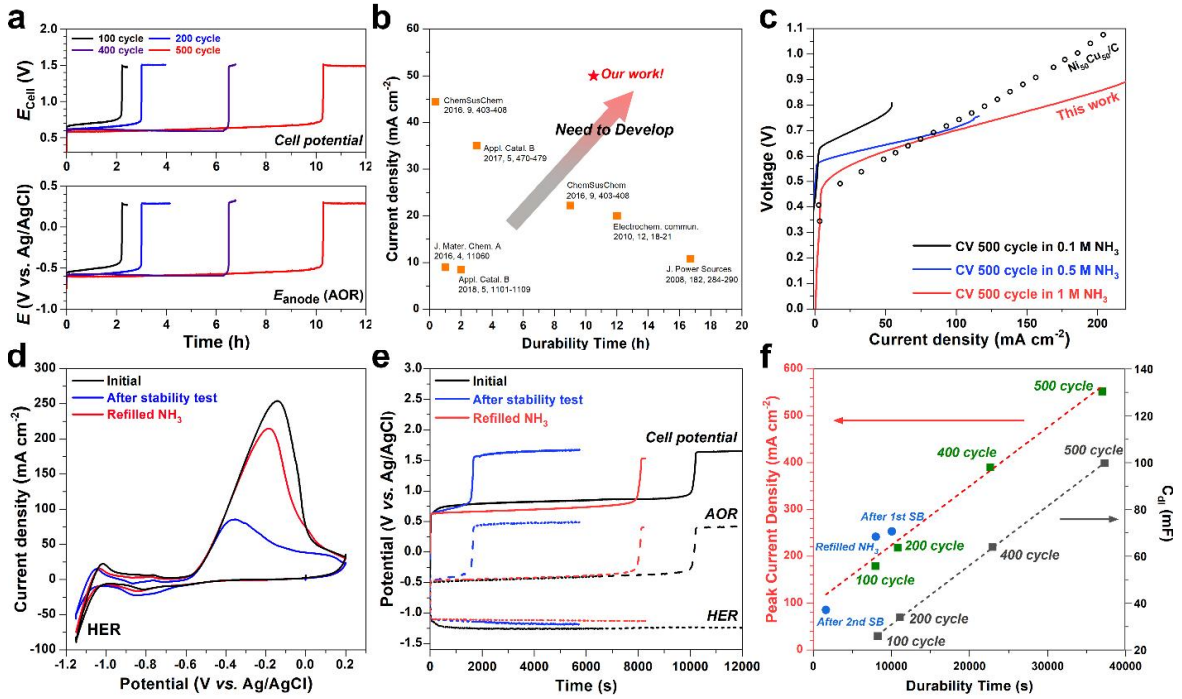

Figure 7-8 (a) Stability test of the CV-Pt electrodes at 60°C at constant current density of 50 mA cm^{-2} using 5 M KOH containing 1 M ammonia. (b) Maximum durability time and operating current density for the present work with that of previous studies for the electro-oxidation of ammonia. (c) Polarization I-V profiles of 500 CV-Pt at various ammonia concentrations (d)-(e) Relationship between peak current density in CVs and durability time. (f) Linear-tendency of durability time with ECSA and peak current density.

oxidation of NH_3(aq) and the oxidation of OH^-, respectively. At the beginning of electrolysis, sufficient ammonia is adsorbed on the catalyst surface for ammonia oxidation. As electrolysis proceeds, however, the continuously degraded and sharply raised cell voltage was detected, which is attributed to consumed ammonia sources and the poisoning effect of the Pt surface during ammonia oxidation.[3,6] For the detailed evaluation for practical application, the durability performance and I-V curve profile should be investigated as shown in **Figure 7-8b** and **c**. The stability performance at a high current density region (50 mA cm^{-2}) was achieved over 10 hours, which is excellent electrochemical durability than that of recently reported AOR electrocatalyst.[1,2,4,6,27–29] The stability performance and maximum durability time of 500 CV-Pt electrode at room temperature were also confirmed in **Figure 7-9**. In **Figure 7-8c**, I-V profiles present the electrochemical performance corresponding to different current density regions of each electrocatalyst. Because electrochemical property for different current density conditions needs to be investigated for the application in various operating conditions, the comparison has been made in both of the high and low current range. The 500 CV-Pt electrode showed low overpotential for ammonia oxidation (10 mA cm^{-2} at 0.51 V) as well as excellent ammonia oxidation performance at a high current density region (200 mA cm^{-2} at 0.85 V). From the detailed results in **Figure 7-8b** and **c**, the suitable electrocatalyst for practical application could be investigated.

The relationship between peak current density in CV tests and stability in the application as

illustrated in **Figure 7-8d-f**. The electrical stability of the electrode showed a similar trend with peak current density. After stability using the 'initial electrode', the peak current density of electrode was dramatically decreased (denoted After stability test with blue color). Corresponding to decreased peak current density, the electrode has poor stability performance in **Figure 7-8e**. However, after refilling the NH_3(aq) source in an electrolyte, both of peak current density and stability performance was increased. Interestingly, the stability performance in the practical application has linearly increased with peak current density in CV tests (**Figure 7-8f**). Furthermore, the stability performance also has a linear tendency with electrochemical surface area (ECSA) of the catalyst (**Figure 7-6**).[30,31] With these results, we concluded that the stability performance of electrocatalyst is attributed to reduced ammonia source in electrolyte as well as initial physical or electrochemical surface area, which could be treated as a capacity for preventing poisoning effect. Also, it is worth noting that we could roughly predict the stability performance from the CV profiles.

7.3.5 *In-operando* quantitative analysis with gas chromatography

To identify the composition of gas products in practical applications, *in-operando* quantitative gas chromatography (GC) measurement was conducted. Before the ammonia electrolysis with GC analysis, we have cleaned the impurity from residue gas in the system for quantitative analysis of each gas (**Figure 7-10**). As shown in **Figure 7-11a**, a systematic experiment was conducted by connecting a closed liquid ammonia decomposition device (AOR + HER) directly toward a GC instrument. With the three-electrode system, firstly, we have investigated the faraday efficiency (FE) of hydrogen production at each specific potential (**Figure 7-11b**). In the potential window from -0.25 V to 0.35 V *vs.* Ag/AgCl, the faraday efficiency of 500 CV-Pt electrode was detected at ca. average 90 %, suggesting that efficient

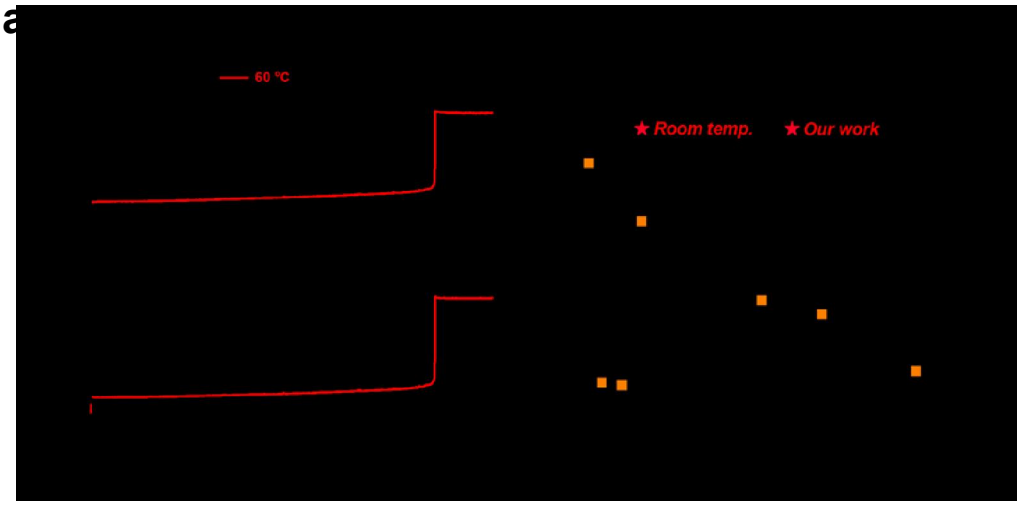

Figure 7-9 (a) Stability test of the CV-Pt electrodes at 60°C and room temperature at constant current density of 50 mA cm^{-2} using 5 M KOH containing 1 M ammonia. (b) Maximum durability time and operating current density for the present work with that of previous studies for the electro-oxidation of ammonia.

AOR activities of 500 CV-Pt electrode. Meanwhile, a separated drainage tube was utilized to determine the amount of H_2/N_2, which indicates the gas volume and molar ratio being close to 2:1 between H_2 and N_2 gas (**Figure 7-12**) at cell potential of 0.8 V. To investigate the AOR catalytic activity in consecutive condition, the chronopotentiometry measurements with *in-operando* GC analysis was conducted at a constant current of 200 mA (**Figure 7-11c-f**). A constant current was applied over 200 min and the amount of each gas generated was analyzed every 20 min using GC analysis. During the electrolysis process, the hydrogen and nitrogen gas were simultaneously produced with faraday efficiency of an average 93 % until 100 min. After the anodic reaction changed from AOR to OER, the hydrogen and oxygen gas were produced instead of nitrogen gas (**Figure 7-11c-d**). It is worthy noting that AOR and OER progress were clearly distinguished in the case of Pt based catalyst, but the working potential of AOR for non-noble metal catalysts normally overlaps with OER potential window. Therefore, it is necessary to distinguish AOR with OER through *in-operando* analysis during practical operating

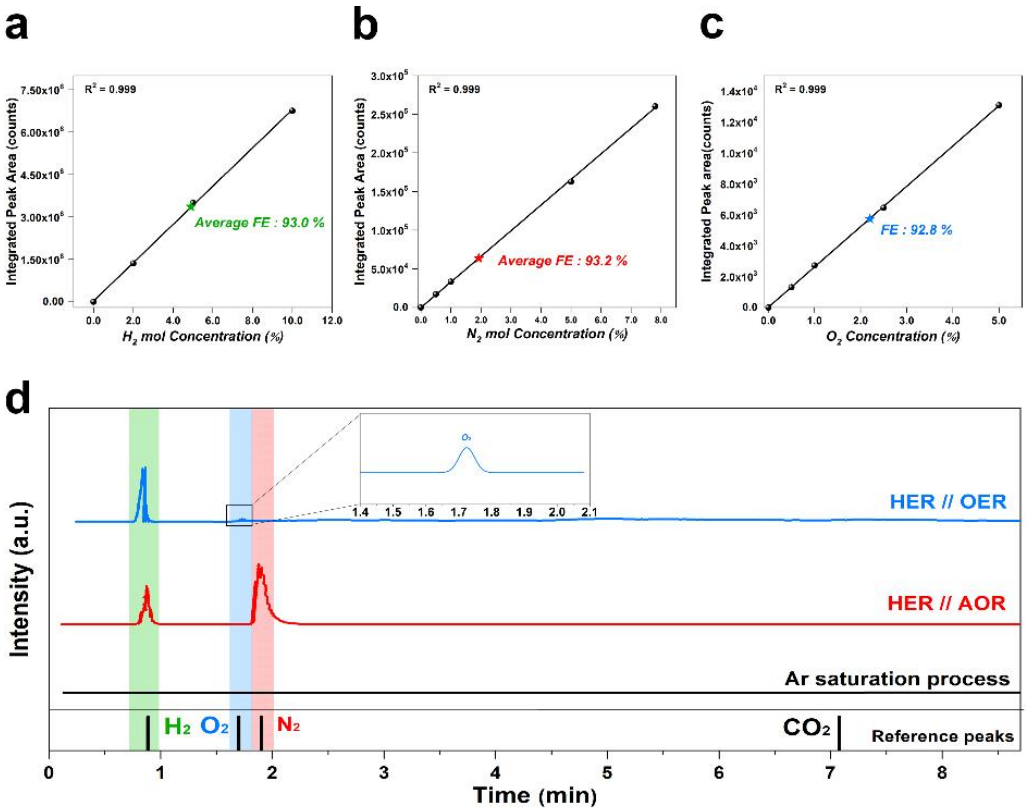

Figure 7-10 Integrated peak areas of each gas and faradaic efficiency of (a) H_2, (b) O_2, and (c) N_2. (d) GC profiles of Ar saturation process, HER/AOR, and HER//OER configuration. After Ar cleaning process, there is no residue gas in the ammonia electrolysis system.

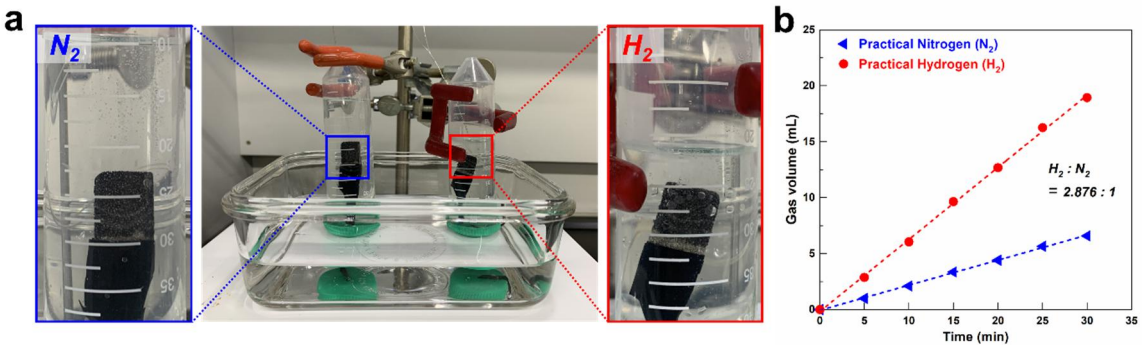

Figure 7-12 a) A digital image of the ammonia electolysis system for b) the production volume of H_2 and N_2 at 0.8V using 500 CV-Pt electrode.

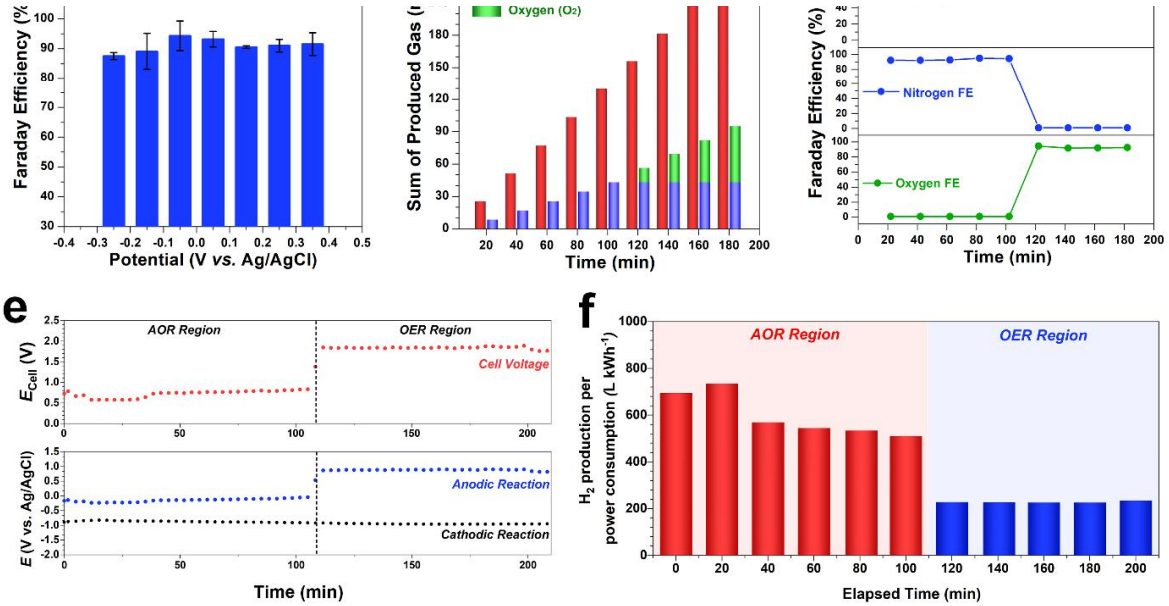

Figure 7-11 (a) Schematic diagram of the *in-operando* GC measurement using a three-electrode system. (b) Faradaic efficiency at a specific voltage (-0.25, -0.15, -0.05, 0.05, 0.15, 0.25, and 0.35V). The error bar reflects the three device results. All electrolysis in this system was operated in 1 M NH_3 in 5 M KOH solution at 60 ^{o}C. (c) The amount (mL) and (d) faradaic efficiency (%) of each produced gases during operating ammonia electrolysis time over 200 min discharge at 200 mA. (e) Chronopotentiometric profile in three electrode configuration system and (f) Hydrogen production per power consumption during consecutive discharge at 200 mA.

condition. At the same time, the overpotential for the anodic reaction was sharply increased from -0.05 V toward 0.87 V *vs.* Ag/AgCl. The changed anodic reaction leads to significantly increase energy consumption for hydrogen production as shown in **Figure 7-11f**. At the AOR region, the hydrogen production per power consumption was about 152 % higher (568.97 L_{H2} $kWh^{-1}{}_{AOR}$) than that at the OER region (225.61 L_{H2} $kWh^{-1}{}_{OER}$).[32] These results indicate that the liquid ammonia decomposition using 500 CV-Pt electrode has a strong potential for mass production of hydrogen at low-energy consumption in practical application.

7.4 Conclusions

In this study, we investigated electrodeposited Pt catalysts on various CV cycles and conducted ammonia electrolysis using practical cell. It is noteworthy that fundamental relationships between electrodeposition cycles and electrocatalytic activity about CV-Pt electrode gained from surface morphology analysis and electrochemical area. The enhanced catalytic activity of flower-like Pt particles in 500 CV-Pt electrode results in stable dehydration of NH_3(aq) (0.65 V @50mA cm^{-2}) as well as ammonia oxidation peak current. Moreover, the analyses discussed in the present work show the introduction of *in-operando* techniques has significantly affected in the AOR study. The complex AOR mechanisms, which proceeds through the continuous decomposition of NH_3(aq) into NH_2 and NH species and dimerization into N_2, are distinguished from the OER competitive reaction by the simultaneous recording of the electrocatalytic performance and quantitative gas production in real-time. We confirmed that highly pure hydrogen is produced with high faradaic efficiency (over 90%) and more than 60 % less energy consumption (1.76 Wh $L^{-1}_{H2\ with\ AOR}$) is needed compared to conventional water electrolysis (4.43 Wh $L^{-1}_{H2\ with\ OER}$). Thus, it will be required to develop the electrocatalysts using established experimental parameters and operating protocols analyses for the successful implementation of NH_3(aq) as an eco-friendly energy source.

References

[1] M. Cooper and G. G. Botte, *J. Electrochem. Soc.*, 2006, **153**, A1894.

[2] J. Gwak, M. Choun, J. Lee, *ChemSusChem*, 2016, **9**, 403–408.

[3] F. Vitse, M. Cooper, G. G. Botte, *J. Power Sources*, 2005, **142**, 18–26.

[4] D. J. Little, M. R. Smith, T. W. Hamann, *Energy Environ. Sci.*, 2015, **8**, 2775–2781.

[5] J. Gwak, M. Choun, J. Lee, *ChemSusChem*, 2016, **9**, 403–408.

[6] J. Huang, J. Cai, J. Wang, *ACS Appl. Energy Mater.*, 2020, **3**, 4108–4113.

[7] Y. Zhou, G. Zhang, M. Yu, X. Wang, J. Lv, F. Yang, *ACS Sustain. Chem. Eng.*, 2018, **6**, 8437–8446.

[8] H. Dotan, A. Landman, S. W. Sheehan, K. D. Malviya, G. E. Shter, D. A. Grave, Z. Arzi, N. Yehudai, M. Halabi, N. Gal, N. Hadari, C. Cohen, A. Rothschild and G. S. Grader, *Nat. Energy.*, DOI:10.1038/s41560-019-0462-7.

[9] K. Jiang, B. Liu, M. Luo, S. Ning, M. Peng, Y. Zhao, Y. R. Lu, T. S. Chan, F. M. F. de Groot and Y. Tan, *Nat. Commun.*, 2019, **10**, 1-9.

[10] J. Wu and H. Yang, *Acc. Chem. Res.*, 2013, **46**, 1848-1857.

[11] B. P. Vinayan and S. Ramaprabhu, *Nanoscale.*, 2013, **5**, 5109.

[12] N. Cheng, S. Stambula, D. Wang, M. N. Banis, J. Liu, A. Riese, B. Xiao, R. Li, T.-K. Sham, L.-M. Liu, G. A. Botton, X. Sun, *Nat. Commun.*, 2016, **7**, 13638.

[13] J. Kim, C. Kim, I. Y. Jeon, J. B. Baek, Y. W. Ju, G. Kim, *ChemElectroChem*, 2018, 1-7.

[14] J. Mahmood, F. Li, S.-M. Jung, M. S. Okyay, I. Ahmad, S.-J. Kim, N. Park, H. Y. Jeong, J.-B. Baek, *Nat. Nanotechnol.*, 2017, **12**, 441-446.

[15] J. Kim, Y. Yang, A. Seong, H. J. Noh, C. Kim, S. Joo, A. Cho, L. Zhang, J. Zhou, J. Q. Wang, J. W. Han, J. Mahmood, J. B. Baek, G. Kim, *J. Mater. Chem. A*, 2020, **8**, 14927-14934.

[16] Y. Yang, J. Kim, C. Kim, A. Seong, O. Kwon, J. H. Lee, I. Kristanto, L. Zhang, J. Zhou, J. Q. Wang, J. B. Baek, S. K. Kwak, G. Kim, *Nano Energy*, 2020, **76**, 105114.

[17] J. N. Tiwari, S. Sultan, C. W. Myung, T. Yoon, N. Li, M. Ha, A. M. Harzandi, H. J. Park, D. Y. Kim, S. S. Chandrasekaran, W. G. Lee, V. Vij, H. Kang, T. J. Shin, H. S. Shin, G. Lee, Z. Lee, K. S. Kim, *Nat. Energy*, 2018, **3**, 773-782.

[18] G. Jerkiewicz, G. Vatankhah, J. Lessard, M. P. Soriaga, Y. S. Park, *Electrochim. Acta*, 2004, **49**, 1451–1459.

[19] B. E. Conway, *J. Electroanal. Chem.*, 2002, **524-525**, 4-19.

[20] S. Choi, S. Park, J. Shin, G. Kim, *J. Mater. Chem. A Mater. energy Sustain.*, 2015, **3**, 6088-6095.

[21] M. Palcut, R. Knibbe, K. Wiik, T. Grande, *Solid State Ionics*, 2011, **202**, 6-13.

[22] S. Kim, A. Jun, O. Kwon, J. Kim, S. Yoo, H. Y. Jeong, J. Shin, G. Kim, *ChemSusChem*, 2015,

8, 3153-3158.

[23] A. K. Hill and L. Torrente-Murciano, *Int. J. Hydrogen Energy*, 2014, **39**, 7646-7654.

[24] J. L. Cao, Z. L. Yan, Q. F. Deng, Y. Wang, Z. Y. Yuan, G. Sun, T. K. Jia, X. D. Wang, H. Bala and Z. Y. Zhang, *Int. J. Hydrogen Energy*, 2014, **39**, 5747–5755.

[25] A. C. A. De Vooys, M. T. M. Koper, R. A. Van Santen, J. A. R. Van Veen, *J. Electroanal. Chem.*, 2001, **506**, 127–137.

[26] C. Kim, J. Kim, S. Joo, Y. Yang, J. Shin, M. Liu, J. Cho, G. Kim, *Angew. Chemie Int. Ed.*, DOI:10.1002/anie.201904763.

[27] H. Zhang, Y. Wang, Z. Wu, D. Y. C. Leung, *Energy Procedia*, 2017, **142**, 1539–1544.

[28] B. K. Boggs, G. G. Botte, *Electrochim. Acta*, 2010, **55**, 5287–5293.

[29] N. M. Adli, H. Zhang, S. Mukherjee, G. Wu, *J. Electrochem. Soc.*, 2018, **165**, J3130–J3147.

[30] X. Xu, Y. Chen, W. Zhou, Z. Zhu, C. Su, M. Liu, Z. Shao, *Adv. Mater.*, 2016, 6442–6448.

[31] A. Seong, J. Kim, O. Kwon, H. Y. Jeong, R. J. Gorte, J. M. Vohs, G. Kim, *Nano Energy*, 2020, **71**, 104564.

[32] D. H. Kweon, M. S. Okyay, S. J. Kim, J. P. Jeon, H. J. Noh, N. Park, J. Mahmood, J. B. Baek, *Nat. Commun.*, 2020, **11**, 1-10.

Chapter 8 General conclusions and outlook

8.1 General conclusions and outlook

Electrochemical catalysts and electrochemical devices are essential fields for the next-generation eco-friendly energy society. In order to progress from a fossil fuel-based energy society to an eco-friendly fuel-based energy society, numerous studies and efforts are being made. There are still many obstacles to replacing fossil fuel-based energy, but it is undeniable that we are progressing slowly but step by step towards an environmentally friendly energy society. Technology and science must advance in a direction that benefits all living things as well as humans. From this point of view, during the graduate period, my research was conducted focusing on eco-friendly energy production field using sustainable fuels in atmospheric or vast fuels to replace fossil fuel-based energy. Starting with research on the utilization of hydrogen and oxygen, research on a device that can produce energy using carbon dioxide was conducted as a next step. It was expected that the newly engineered carbon dioxide utilization device could help to solve the global climate problem and energy problem at the same time. In addition, for a faster transition to a hydrogen society, the next research was conducted on a technology that can mass-produce hydrogen using ammonia. In future research, I plan to study a new electrochemical device that can mass-produce hydrogen using nitrogen in the atmosphere. It is hoped that using these two devices, ammonia production equipment through nitrogen and hydrogen production equipment through ammonia, will be able to truly lay the groundwork for the era of a hydrogen society.

It is hoped that all these research could be of a small contribution to the accompaniment of everyone who is slowly but step by step for a better society.

List of Publications

14. Yejin Yang,† **Jeongwon Kim,†** Hyoi Jo, Arim Seong, Minzae Lee, Hyung-Ki Min, Myung-gi Seo, Youngheon Choi, and Guntae Kim*
"A rigorous electrochemical ammonia electrolysis protocol with *in-operando* quantitative analysis" ***J. Mater. Chem. A*** 9, 11571-11579 (2021)

13. **Jeongwon Kim**, Arim Seong, Yejin Yang, Sangwook Joo, Changmin Kim, Dong Hyup Jeon,* Liming Dai,* and Guntae Kim*
"Indirect surpassing CO_2 utilization in membrane-free CO_2 Battery" ***Nano Energy*** 82, 105741 (2021)

12. Yejin Yang,† **Jeongwon Kim,†** Changmin Kim, Arim Seong, Ohhun Kwon, Jeong Hyeon Lee, Imanuel Kristanto, Linjuan Zhang, Jing Zhou, Jian-Qiang Wang, Jong-Beom Baek *, Sang Kyu Kwak *, and Guntae Kim *
"Edge-selective decoration with ruthenium at graphitic nanoplatelets for efficient hydrogen production at universal pH" ***Nano Energy*** 76, 105114 (2020)

11. **Jeongwon Kim**, Yejin Yang, Arim Seong, Hyuk-Jun Noh, Changmin Kim, Sangwook Joo, Ara Cho, Linjuan Zhang, Jing Zhou, Jian-Qiang Wang, Jeong Woo Han, Javeed Mahmood*, Jong-Beom Baek*, and Guntae Kim*
"Identifying the electrocatalytic active sites of a Ru-based catalyst with high Faraday efficiency in CO2-saturated media for an aqueous Zn-CO_2 system" ***J. Mater. Chem. A.*** 8, 14927-14934 (2020)

10. Arunchander Asokan,† Chaehyun Lim,† **Jeongwon Kim,†** Ohhun Kwon, Hansol Lee, Sangwook Joo, Hu Young Jeong, and Guntae Kim*
"Carbon nanofibers encapsulated nickel-molybdenum nanoparticles as hydrogen evolution catalysts for aqueous Zn-CO_2 system" ***ChemNanoMat.*** 6, 937-946 (2020)

9. Arim Seong,† **Jeongwon Kim,†** Ohhun Kwon, Hu Young Jeong, Raymond J. Gorte,* John M. Vohs,* and Guntae Kim*
"Self-reconstructed Interlayer derived by in-situ Mn diffusion from $La_{0.5}Sr_{0.5}MnO_3$ via atomic layer deposition for an efficient bi-functional electrocatalyst" ***Nano Energy*** 71, 104564 (2020)

9. Changmin Kim,† **Jeongwon Kim,†** Sangwook Joo, Yejin Yang, Jeeyoung Shin, Meilin Liu, Jaephil Cho*, and Guntae Kim*

"Highly Efficient CO_2 Utilization *via* Novel Aqueous Zn- or Al-CO_2 Systems for H_2 and Electricity Production" ***Angew. Chem. Int. Ed.*** 58, 9506-9511 (2019)

7. **Jeongwon Kim**, Ohhun Gwon, Ohhun Kwon, Javeed Mahmood, Changmin Kim, Yejin Yang, Hansol Lee, Jong Hoon Lee, Hu Young Jeong, Jong-Beom Baek*, and Guntae Kim*
"Synergistic Coupling Derived Cobalt Oxide with Nitrogenated Holey Two-Dimensional Matrix as an Efficient Bifunctional Catalyst for Metal–Air Batteries" ***ACS Nano.*** 13, 5502-5512 (2019)

6. Changmin Kim,† **Jeongwon Kim,†** Sangwook Joo, Yunfei Bu, Meilin Liu, Jaephil Cho,* and Guntae Kim*
"Efficient CO utilization via a hybrid Na-CO system based on CO dissolution " ***iScience***. 9, 278-285 (2018)

5. **Jeongwon Kim,†** Changmin Kim,† In-Yup Jeon, Jong-Beom Baek, Young-Wan Ju,* and Guntae Kim*
" A New Strategy for Outstanding Performance and Durability in Acidic Fuel Cells: A Small amount Pt Anchored on Fe,N co-Doped Graphene Nanoplatlets" ***ChemElectroChem.*** 5, 2857-2862 (2018)

4. Hansol Lee, Ohhun Gwon, Chaehyun Lim, **Jeongwon Kim,** Oyunbileg Galindev* and Guntae Kim*
" Advanced electrochemical properties of $PrBa_{0.5}Sr_{0.5}Co_{1.9}Ni_{0.1}O_{5+d}$ as a bifunctional catalyst for rechargeable zinc-air batteries" ***ChemElectroChem.*** 6, 3154-3159 (2019)

3. Arunchander Asokan, Hansol Lee, Ohhun Gwon, **Jeongwon Kim**, Ohhun Kwon, and Guntae Kim*
" Insight into the effect of nickel doping on ZIF-Derived oxygen reduction reaction catalysts for zinc-air batteries" ***ChemElectroChem***. 6, 1213-1224 (2019)

2. Changmin Kim,† Seona Kim,† Ohhun Kwon, **Jeongwon Kim**, and Guntae Kim*
" Polypyrrole Assisted Co_3O_4 Anchored Carbon Fiber as a Binder Free Electrode for Seawater Batteries" ***ChemElectroChem***. 6, 136-140 (2019)

1. Arim Seong,† Junyoung Kim,† **Jeongwon Kim**, Seona Kim, Sivaprakash Sengodan, Jeeyoung Shin, and Guntae Kim*
"Influence of Cathode Porosity on High Performance Protonic Ceramic Fuel Cells with $PrBa_{0.5}Sr_{0.5}Co_{1.5}Fe_{0.5}O_{5+\delta}$ Cathode" **J. Electrochem. Soc.** 165 F1098-F1102 (2018)

Acknowledgments

I would like to express my appreciation to many people for their help to complete my degree. First and foremost, I would like to thank my Ph. D. advisor, Prof. Guntae Kim, you have been a tremendous mentor for me. Through the graduate period with you, I could learn about research as well as consider the career for my whole life.

Additionally, I would like to express my gratitude to my committee members, Prof. Jaephil Cho, Prof. Youngkook Kwon, Prof. Sang Kyu Kwak, and Prof. Ikwhang Chang for their generous advice and encouragement.

I also thank our group members of 'gunslab'.
I would like to thank Prof. Sivaprakash Sengodan, Dr. Seonyoung Yoo, Prof. Sihyuk Choi, Dr. Areum Jun, Dr. Junyoung Kim, Dr. Seona Kim, Dr. Sangwook Joo, Dr. Changmin Kim, Dr. Chaehyun Lim, Dr. Ohhun Kwon, Dr. Arunchander Asokan, Dr. Donghwi Jeong, Gihyeon Kim, Seungtae Lee, Hyunmin Kim, Arim Seong, Yejin Yang, Hyojae Hwang, Sewon Pyo, Minseo Kim, Hyoi Jo, Jinkyung Oh, Dang Thi Kim Ngoc, Eunyoung Cho, Yeongbae jeon, Prof. Jeeyoung Shin, Prof. Young-Wan Ju, Prof. Yongwook Shin, and Prof. Yunfei Bu. In particular, I would like to convey my personal appreciation and my thanks to CO_2 research team members for allowing me to be able to consider and spend time together. I sincerely wish you may the wind be at your back.

In addition, I also want to express my gratitude to my friends, Euijong Kim, Taejin Kim, Jungwoo Nam, and Dong-Hyeon Yang who have always been able to share peaceful comfort and happiness in many things in my whole life. Furthermore, I would like to say big thanks to friends, Halim Kang, Do Hyung Kweon, Jong-Pil Jeon, Wonjoo Jin, Yong-Hyeok Lee, Jeong Hun Kim, and Woo Jin Byun, who were considerate even though they were busy and were able to share their research life together. I hope that the steps towards will be a path as a valuable journey together in the future.

And lastly, I would like to appreciate my parents, my younger brother, lover, and a beloved one sharing every moment of my life. Without your trust and sacrifice, my efforts so far would not have been possible. On the journey after graduation, I will also make a life worthy of the name you called me.

Jeongwon Kim